Some Numerical Investigations in Cosmology

Anthony Walters

Supervised by: **Prof. A. Weltman &**
Prof. C. Hellaby

Department of Mathematics and Applied Mathematics
University of Cape Town

This dissertation is submitted for the degree of
Doctor of Philosophy in Applied Mathematics

October 2017

Declaration

I hereby declare that except where specific reference is made to the work of others, the contents of this dissertation are original and have not been submitted in whole or in part for consideration for any other degree or qualification in this, or any other university. Part I of this dissertation is my own work in collaboration with my supervisor C. Hellaby, and contains nothing which is the outcome of work done in collaboration with others. Part II is the result of collaboration with my supervisor A. Weltman and MSc student E. Platts, as well as A. Padilla, D. Stefanyzian and T. Wilson at the University of Nottingham. The contents of chapter 10 is a review of the work by the Nottingham group, while chapter 11 is my own contribution. See footnotes therein.

Anthony Walters
October 2017

Acknowledgements

I would like to express my sincere gratitude to a number of people for helping to make this thesis possible. First and foremost, to my supervisors, Prof. Amanda Weltman and Prof. Charles Hellaby, for their continuous support and guidance throughout the course of my PhD studies. These have been an illuminating few years. To my fellow students and post-docs, thanks for the engaging discussion and fun we have shared, especially all the hours spent solving riddles at the blackboard. And, of course, thanks to my family and friends, who have always had my back throughout the course of my studies.

Abstract

Numerical simulations have become an indispensable tool for understanding the complex non-linear behaviour of many physical systems. Here we present two numerical investigations in cosmology. The first is posed in the context of inhomogeneous exact solutions to General Relativity. We lay out a formalism for calculating observables in an arbitrary spacetime, for an arbitrary placed observer. In particular, we calculate the area distance, redshift and transverse motion across the observer's sky. We apply our method to the Szekeres metric, and develop code in MATLAB to implement it. We successfully demonstrate that the code works for the FLRW and LT special cases, and then investigate some Szekeres models with no spherical symmetry. The second project is posed in the context of chameleon gravity. Recently, it was argued that the conformal coupling of the chameleon to matter fields created an issue for early universe cosmology. As standard model degrees of freedom become non-relativistic in the early universe, the chameleon is attracted towards a "surfing" solution, so that it arrives at the potential minimum with too large a velocity. This leads to rapid variations in the chameleon's mass and excitation of high energy modes, casting doubts on the classical treatment at Big Bang Nucleosynthesis. We propose the DBI chameleon, a consistent high energy modification of the chameleon theory that dynamically renders it weakly coupled to matter during the early universe thereby avoiding the breakdown of calculability . We demonstrate this explicitly with numerical simulations.

Table of contents

List of figures

List of tables

Part I

Modelling Cosmic Flows

Chapter 1

Introduction

Since its publication a little over a century ago, Einsteins theory of General Relativity (GR) remains central to our understanding of gravitational phenomena. It has been observationally verified in the Solar System to high precision [1], and has become the bedrock upon which most cosmological models are build. Around the time of its publication Einstein realised it predicted the existence of gravitational waves, and so their recent detection [2] is yet another remarkable confirmation of the theory. The Einstein Field Equations (EFEs) are hard to solve in full generality as they represent a system of 10 coupled partial differential equations, and so typically one must make some assumptions about the symmetries of the spacetime before proceeding. In the case of cosmological solutions, the standard assumptions of isotropy and homogeneity point toward the Friedmann-Lemaître-Robertson-Walker (FLRW) geometry as a good description of the Universe on large scales. And it has become standard practice in mainstream cosmology to analyse to interpret observations in this context.

However, we know this is not the full picture. On scales $\sim 10 - 100$ h^{-1}Mpc, observations indicate that the late Universe is largely comprised of gravitationally bound structures, like galaxies and galaxy clusters, which form a complex web of filaments, sheets and knots, surrounding large voids [3]. Evidently there is lots of inhomogeneous structure to the Universe, and exactly how each these structures contribute to the global expansion, averaging out to give FLRW, is the subject of ongoing study [4–7]. Nonetheless, on very large scales (~ 100 h^{-1}Mpc) observations of the Large Scale Structure (LSS) do seem to indicate a transition to statistical homogeneity [8], thus justifying FLRW assumptions (although the exact scale down to which one can trust these assumptions is debated [9–12]). Lacking an alternative prescription for the small scales, it has become common in many analyses to extend

the FLRW assumptions below the scale of statistical homogeneity when interpreting data.

Challenging this paradigm, there have been a number of suggestions in the literature of anisotropy in the Hubble flow [13–17]. Although these have yet to be solidly confirmed on large scales, it is certain the structures that are known to exit must have some effect on smaller scales. Similarly, the near alignment of dipole, quadrupole and octopole moments of the CMB may be due to the effect of some LSS [18]. The bulk flow of galaxies has been debated in the literature for some time now, and the measurement of peculiar velocities is considered one of the best ways to map the LSS out to distances a of few 100 h^{-1}Mpc. Such a measurements are done in a few ways. One can infer the velocity field using the Tully-Fisher relation [19], the luminosity of type 1a supernovae [20, 21], and by using CMB data combined with a catalogue of X-ray sources, searching for evidence of the kinetic Sunyaev-Zeldovich effect [22, 23]. All of these approaches have detected bulk flows on large scales. Wether or not these flows converge to the CMB rest frame, and are consistent with what one expects in the current cosmological paradigm, remain a topic of debate [24–29].

It is therefore of considerable interest to investigate how inhomogeneities of different sizes and shapes would affect the observed Hubble flow and patterns of peculiar velocities. While perturbation theory is well suited to statistical analysis of fluctuations, and extensive work has gone into to quantifying the effects of inhomogeneity on lensing and the distance redshift relation [30–34], the use of exact inhomogeneous solutions is more appropriate for building specific models and analysing particular observational features. Our interest here is in determining observation, particularly the transverse velocity field, for a given observer in a given inhomogeneous spacetime metric. That is, we aim to use a known inhomogeneous solution to the EFEs to construct a particular model, and then see what observations follow, and how they change. In a sense this is the opposite to the Observational Cosmology approach [35–42] and the related Metric of the Cosmos approach [43–47] and Inverse Problem approach [48–57]. There one defines coordinates based on the observer's past null cone (PNC), with incoming rays labelled by observed sky angles and time, with the aim of using observations to reconstruct the spacetime metric.

Of all the inhomogeneous exact solutions used in cosmology today, perhaps the most popular is the Lemaître-Tolman (LT) model. First published in 1933 by Lemaître [58, 59], and then by Tolman [60] and later popularised by Bondi [61], it has since found numerous applications in the fields of astrophysics and cosmology. It is a spherically symmetric non-static solution to the EFEs with a dust source, and can be thought of

as an assembly of concentric spherical mass shells, each with their own evolution. Soon after his publication of the LT solution, Lemaître [62] used it in an attempt to explain the formation of the "nebulae", and with some success — he showed that, with the appropriate choice of initial mass distribution, a comoving region around the origin can re-collapse, whilst the surrounding region will keep expanding forever. Following in this line of work, there have been a number of further studies into structure formation using this model [63, 64], including the development of useful model construction procedures [65, 66, 63, 67] , as well as numerous studies into the various effects of differential expansion and light propagation [68–73]. These investigations are however limited by the symmetry of the solution, and do not allow one to model non-spherical structures.

An interesting family of inhomogeneous exact solutions that goes beyond spherical symmetry are those found by Szekeres [74], in 1975. In general, these models have no symmetries (i.e. no killing-vectors [75]) and are defined by six arbitrary metric functions, representing five degrees of freedom to model inhomogeneity. They are perhaps the most sophisticated exact dust solutions that contain FLRW as a special case, and offer exciting prospects for modelling fairly complex cosmic structures. There are two classes of Szekeres models, the LT-type ($\beta_{,z} \neq 0$ or Class I) and the Kantowski-Sachs (KS) type ($\beta_{,z} = 0$ or Class II)[1] It has been shown that any interior region of LT-type quasi-spherical Szekeres spacetime can be matched to the exterior Schwarzschild solution, even though the interior metric has no symmetry. Since the Schwarzschild solution does not contain any gravitational radiation, this implies that such Szekeres models do not radiate, and consequently proves the existence of configurations of collapsing dust clouds that have no symmetry and do not produce gravitational waves [78–80]. This result was later generalised to all Szekeres models [81]. Goode & Wainwright [82, 83] introduced a different representation of the Szekeres solutions in which many properties of both subfamilies can be considered together[2]. Furthermore, this formulation facilitates the separation of 'exact perturbations' from background FLRW dynamics. To facilitate the building of interesting Szekeres models, a number of model construction procedures have been proposed [85–87].

The evolution of non-spherical structure and its impact on light propagation has only recently become the subject of serious investigation, and Szekeres models are well suited for such studies. They have been used to study large scale structure [88, 89] and coarse-graining [90, 91], model an arbitrary matter distribution along one line of sight [92], and interpret luminosity distance and CMB observations [93–97], amongst other

[1] For a comprehensive review of the two classes of Szekeres models, see §19.6 in [76] or, for a more historical account, see §2.4 in [77].

[2] The KS-Type was later shown to be a regular limit of the LT-Type [84]

things. In [98] exact solutions, both LT and Szekeres, were used to study the precision of ray standard ray tracing techniques. By comparing results from a perturbative approach with those from the exact solutions, it was shown that including non-spherical structures can have a marked effect on the ray path and resulting observables. Since these solutions are so well suited to modelling exact non-spherical structures, we choose to adopt them in the implementation of our framework for calculating observables.

The outline on this part of the thesis is as follows; We review some basic properties of the Szekres model in §2. This is followed by our framework for calculating observables in §3, along with its application to the Szekeres metric. We then outline the numerical implementation and simulation results in §4, and conclude in §5.

Chapter 2

Szekeres Models

First published in 1975, the Szekeres solution [74, 99] offers a wide range of possibilities to model structure in the Universe. It is an exact, irrotational dust solution to the EFEs that has conformally flat $t = \text{const.}$ hypersurfaces [100], emits no gravitational radiation [78], and in general has no symmetries [75].

Six metric functions fully specify the model and offer five physical degrees of freedom to model inhomogeneity. For certain choices of these functions the metric can assume the form of any one of a number of interesting special cases, such as Datt-Kantowski-Sachs, Vaiydia, Ellis, LT and FLRW metrics. That the latter is contained within the Szekeres metric is important, as it allows one the ability to model inhomogeneous structure on an FLRW "background", which is useful for comparison with the standard perturbative approach.

2.1 The Metric and its Arbitrary Functions

The line element of the Szekeres metric (in units where $G = c = 1$) can be written as

$$ds^2 = -dt^2 + \frac{(R' - R\frac{E'}{E})^2}{\epsilon + f}dr^2 + \frac{R^2}{E^2}(dp^2 + dq^2), \tag{2.1}$$

where $' \equiv \frac{\partial}{\partial r}$, $R = R(t, r)$ is referred to as the "areal" radius (as it is, in some cases, related to the area of constant-(t, r) 2-surfaces), $E = E(r, p, q)$ encodes deviations away from (some kind of) symmetry, $f = f(r)$ is the energy/curvature function, and the parameter $\epsilon = \{-1, 0, 1\}$ controls the shape of the constant-(t, r) 2-surfaces. The functions R and f have important similarities with the LT metric, which will be

outlined at the end of this section. $E(r, p, q)$ can be written as

$$E(r, p, q) = \frac{S}{2}\left[\left(\frac{p-P}{S}\right)^2 + \left(\frac{q-Q}{S}\right)^2 + \epsilon\right] \tag{2.2}$$

where $S = S(r)$, $P = P(r)$ and $Q = Q(r)$ are three more arbitrary functions, which have natural interpretations in the Riemann projection of the following section.

The source term on the right of the EFEs is described by an energy-momentum tensor for a pressure free perfect fluid (i.e. dust),

$$T^{ab} = \rho u^a u^b \tag{2.3}$$

where ρ is the energy density and u^a is the 4-velocity field, which is assumed to be comoving with the coordinates such that $u^a = \delta^a_t$. With this, and the EFEs, one arrives at an expression for the energy density

$$\kappa\rho = \frac{2\left[M' - 3M\left(\frac{E'}{E}\right)\right]}{R^2\left[R' - R\left(\frac{E'}{E}\right)\right]}, \tag{2.4}$$

and an equation of motion for the areal radius,

$$\dot{R}^2 = f + \frac{2M}{R} + \frac{\Lambda}{3}R^2, \tag{2.5}$$

where $M = M(r)$ is an arbitrary function related to the integrated energy density, and Λ is the cosmological constant (should one include it in the EFEs). This equation is analogous to the Friedmann equation in FLRW, except that M and f are now free functions of coordinate "radius", r. Solutions to (2.5) can be written in an exact parametric form when $\Lambda = 0$. They are

Hyperbolic ($f > 0$)

$$R = \frac{M}{f}(\cosh\eta - 1) \tag{2.6}$$

$$(\sinh\eta - \eta) = \frac{f^{3/2}(t - t_b)}{M} \tag{2.7}$$

Parabolic ($f = 0$)

$$R = M\frac{\eta^2}{2} \tag{2.8}$$

$$\frac{\eta^3}{6} = \frac{t - t_b}{M} \tag{2.9}$$

$$\Rightarrow R = \left(\frac{9M(t - t_b)^2}{2}\right)^{1/3} \tag{2.10}$$

Elliptic ($f < 0$)

$$R = \frac{M}{(-f)}(1 - \cos\eta) \tag{2.11}$$

$$(\eta - \sin\eta) = \frac{(-f)^{3/2}(t - t_b)}{M} \tag{2.12}$$

where $t_b = t_b(r)$ is an integration constant referred to as the "bang-time" - it gives the coordinate time at which a particular worldline emerges from the initial singularity, when $R = 0$. From this one can see that $f(r)$, which encodes the local geometry[1], also determines wether a worldline at a particular r-value will follow a hyperbolic, parabolic, or elliptic evolution. The first two expand forever, and the last eventually recollapses to form a final singularity. For hyperbolic and parabolic evolutions the phase parameter ranges between $0 \leq \eta \leq \infty$, while for elliptic evolutions one has $0 \leq \eta \leq 2\pi$ (from bang to crunch).

Furthermore, R' can be written as [102]

$$R' = \left(\frac{M'}{M} - \frac{f'}{f}\right)R - \left[t_b' + \left(\frac{M'}{M} - \frac{3f'}{2f}(t - t_b)\right)\right]\dot{R}, \tag{2.13}$$

which will later prove to be a useful expression. Since it's valid for all three evolution types it will simplify some of the numerics.

Of the six metric functions, we collectively refer to $\{M, f, t_b\}$ as the LT metric functions, because these are common to LT models and have exactly the same interpretation in Szekeres when $\epsilon = +1$. Specifically, $M(r)$ is the mass enclosed in a sphere of radius r. However when $\epsilon \neq 1$, $M(r)$ has no obvious interpretation as the constant-(t, r) 2-surfaces are not spherical. The interpretation of f and t_b is the same

[1]The orthonormal components of the Riemann tensor of the r-p-q 3-spaces is related to f by ${}^3R_{(p)(q)(p)(q)} = -f/R$ [101]. In FLRW models the kind of geometry and evolution type is a global property, whereas in LT and Szekeres models it depends on the sign of f, and can vary with r.

in all cases. The three arbitrary function contained in $E(r,p,q)$, namely $\{S,P,Q\}$, are unique to Szekeres models.

2.2 The p-q Geometry

The geometry of the constant-(t,r) 2-surfaces is controlled by the value of ϵ. This is understood because, depending on the value of ϵ, $(dp^2+dq^2)/E^2$ is a stereographic/Riemann projection of a unit 2-sphere, plane or 2-hyperboloid onto the p-q plane. The applicable transformations are shown below.
$\epsilon=+1$, either:

$$\left(\frac{p-P}{S}\right)=\cot\left(\frac{\theta}{2}\right)\cos(\phi)\qquad\left(\frac{q-Q}{S}\right)=\cot\left(\frac{\theta}{2}\right)\sin(\phi)\tag{2.14}$$

or

$$\left(\frac{p-P}{S}\right)=\tan\left(\frac{\theta}{2}\right)\cos(\phi)\qquad\left(\frac{q-Q}{S}\right)=\tan\left(\frac{\theta}{2}\right)\sin(\phi)\tag{2.15}$$

$\epsilon=0$:

$$\left(\frac{p-P}{S}\right)=\left(\frac{2}{\theta}\right)\cos(\phi)\qquad\left(\frac{q-Q}{S}\right)=\left(\frac{2}{\theta}\right)\sin(\phi)\tag{2.16}$$

$\epsilon=-1,\quad E>0$:

$$\left(\frac{p-P}{S}\right)=\coth\left(\frac{\theta}{2}\right)\cos(\phi)\qquad\left(\frac{q-Q}{S}\right)=\coth\left(\frac{\theta}{2}\right)\sin(\phi)\tag{2.17}$$

$\epsilon=-1,\quad E<0$:

$$\left(\frac{p-P}{S}\right)=\tanh\left(\frac{\theta}{2}\right)\cos(\phi)\qquad\left(\frac{q-Q}{S}\right)=\tanh\left(\frac{\theta}{2}\right)\sin(\phi)\tag{2.18}$$

Each of these transformations map θ-ϕ to p-q surfaces, where (θ,ϕ) are the coordinates on the sphere, plane or pseudo-sphere. In the $\epsilon=+1$ case either of (2.14) or (2.15) is sufficient to map the entire p-q plane onto the sphere, with the angular coordinates covering the usual range $0\le\theta\le\pi$ and $0\le\phi\le2\pi$. In the $\epsilon=0$ case there is only one relevant transformation, the planar projection (2.16). It maps the entire p-q plane onto the θ-ϕ plane, with $0\le\theta\le\pi$ and $0\le\phi\le2\pi$. This can

be thought of as a mapping from a semi-infinite cylinder onto a plane [101]. When $\epsilon = -1$ the situation is slightly different. Both of the transformations (2.17) and (2.18) are required to cover the whole p-q plane, with $0 \leq \theta \leq \infty$ and $0 \leq \phi \leq 2\pi$. Now constant-r 'shells' are two-sheeted hyperboloids, with θ positive on one sheet and negative on the other. In the $\epsilon = \{0, -1\}$ cases, θ is interpreted as a measure of 'distance' down the cylinder/hyperboloid, rather than an angle. For nice illustrations of the three projections see the figures in [81].

After transforming from (p, q) to (θ, ϕ) coordinates the resulting 2-metrics then take the form

$$\epsilon = +1, \qquad ds^2 = R^2(d\theta^2 + \sin^2(\theta)d\phi^2) \tag{2.19}$$

$$\epsilon = 0, \qquad ds^2 = R^2(d\theta^2 + \theta^2 d\phi^2) \tag{2.20}$$

$$\epsilon = -1, \qquad ds^2 = R^2(d\theta^2 + \sinh^2(\theta)d\phi^2) \tag{2.21}$$

which makes their geometry more familiar.

2.3 Deviations from Symmetry - $E(r,p,q)$

The function $E(r,p,q)$ encodes deviations away from spherical/planar/pseudo-spherical symmetry (depending on the value of ϵ), specifically via the function E'/E. In order to get a feeling for how this works it is instructive to investigate the general behaviour of E'/E, and thus the behaviour of both E and E', which we do below.

2.3.1 The $E = 0$ Locus

The function $E(r,p,q)$ has circular symmetry in the p-q plane about the point $(p, q) = (P, Q)$, and since both $P = P(r)$ and $Q = Q(r)$, the point of symmetry can vary with r. Setting (2.2) to zero gives the locus of points where $E = 0$, which is

$$(p - P)^2 + (q - Q)^2 = -\epsilon S^2. \tag{2.22}$$

In the $\epsilon = +1$ case the locus (2.22) does not exist, and $E > 0$ everywhere in the p-q plane. When $\epsilon = 0$ the locus is a single point located at $(p, q) = (P, Q)$, and $E > 0$ everywhere else. When $\epsilon = -1$ (2.22) is the equation for a circle centred at $(p, q) = (P, Q)$. In this case one has $E > 0$ outside the circle and $E < 0$ inside [101].

2.3.2 The $E' = 0$ Locus

Taking the derivative of (2.2) with respect to r and setting it to zero gives the locus of points where $E' = 0$. This gives

$$\left[p - \left(P - P'\frac{S}{S'}\right)\right]^2 + \left[q - \left(Q - Q'\frac{S}{S'}\right)\right]^2 = S^2\left(\frac{P'^2 + Q'^2}{S'^2} + \epsilon\right) \tag{2.23}$$

which is the equation of a circle centred at the point $(p, q) = (P - P'S/S', Q - Q'S/S')$ in the p-q plane, with radius $S\sqrt{(P'^2 + Q'^2)/S'^2 + \epsilon}$. When $S' > 0$ one has $E' < 0$ inside the circle and $E' > 0$ outside [103]. In the $\epsilon = \{0, +1\}$ cases the locus always exists, and in the $\epsilon = -1$ case it will only exist if one has

$$S'^2 < P'^2 + Q'^2. \tag{2.24}$$

It has been shown that if both the loci (2.22) and (2.23) exist, then they will always intersect [101].

2.3.3 General Behaviour of E'/E

The loci (2.22) and (2.23) described above create extrema in the function E'/E. One expects this function will be zero at the $E' = 0$ locus and divergent at the $E = 0$ locus, except possibly at the intersection of the two where one has $E'/E = 0/0$. This however is only possible in $\epsilon = \{-1, 0\}$ models, where both loci can exist. In $\epsilon = +1$ models one has $E > 0$ everywhere and so E'/E does not diverge anywhere. In addition, the $E'/E = 0$ locus will be the same as in (2.23), with $E'/E > 0$ outside the circle and $E'/E < 0$ inside the circle when $S' > 0$.

2.4 Foliating the 3-space

From the metric (2.1) one can see that at any particular value of (t, r), each p-q 2-surface (whose geometry is determined by the value of ϵ) is multiplied by a factor of $R(t, r)$. Thus, the r-p-q 3-space is foliated by 2-surfaces whose geometry is determined by ϵ and whose curvature scale is related to R. Since the g_{rr} component of the metric is sensitive to p-q variations via E'/E, these surfaces are interpreted as being arranged non-symmetrically relative to one another. This 'non-concentricity' is why the various families of Szekeres models have *quasi-* in front their names. Table 2.1 summarises the impact of ϵ on the various spatial foliations and naming conventions.

ϵ	constant-(t, r) 2-surfaces	Model Name
$+1$	sequence of Riemann spheres	quasi-spherical
0	sequence of Riemann planes	quasi-planar
-1	sequence of right Riemann hyperboloids	quasi-pseudospherical

Table 2.1 **The Effect of** ϵ - Showing the shape of constant-(r, t) 2-surfaces and the associated model name for the various values of ϵ

The requirement that the metric retain Lorentzian signature further restricts the possible spatial foliations. If g_{rr} is to remain positive it follows that $\epsilon \geq -f$ must then always hold (see §2.6), and thus the evolution type restricts the type of 2-surfaces that are permitted to foliate the spatial sections. The possibilities are summarised below, in Table 2.2.

Evolution Type	f	ϵ	Permissible 2-surfaces
Hyperbolic	> 0	$+1, 0, -1$	spherical, planar, pseudo-spherical
Parabolic	$= 0$	$+1, 0$	spherical, planar
Elliptic	$\geq -1, < 0$	$+1$	spherical

Table 2.2 **Permissible Spatial Foliations** - Showing the permissible 2-surfaces of constant-(t, r) that can foliate a spatial section, for a given evolution type

The area of a constant-(t, r) 2-surface is found by integrating over the entire p-q 2-metric. It is given by

$$A = R^2 \int\int \frac{dpdq}{E^2}. \tag{2.25}$$

When $\epsilon = +1$ one finds $A = 4\pi R^2$, the area of a sphere. This is why R is often referred to as the *areal* radius. In this case $M(r)$ is interpreted as being the gravitational mass enclosed within a sphere of radius r. However, in the $\epsilon = \{-1, 0\}$ cases, the constant-(t, r) 2-surfaces are not closed and the integral (2.25) is infinite, which makes the interpretation of $M(r)$ less clear.

2.5 Curvature Singularities

The Kretschmann scalar is a quadratic invariant of the spacetime and is divergent at a curvature singularity. In the Szekeres family of models, when $\Lambda = 0$, it is given by [101]

$$\mathcal{K} = R^{abcd}R_{abcd} = \kappa^2\left(\frac{4}{3}\rho_{AV}^2 - \frac{8}{3}\rho_{AV}\rho + 3\rho^2\right) \tag{2.26}$$

where

$$\kappa\rho_{AV} \equiv \frac{6M}{R^3} \tag{2.27}$$

is referred to as the 'internal average' density, and R^{abcd} is the Riemann tensor associated with (2.1). This is clearly divergent anywhere the density diverges. In general this occurs on two hyper-surfaces, namely where $R = 0$ (associated with the bang/crunch) and where $R' = 0$ (associated with shell crossings).

2.5.1 Bang and Crunch

In Szekeres models all worldlines experience a bang or crunch singularity, and in some cases both. Hyperbolic and parabolic worldlines are either forever expanding away from the bang or collapsing to toward the crunch (in the time reverse case). Elliptical worldlines expand away from the bang, reach a maximum, and then begin collapse toward the crunch. These events occur at $t = t_b$ and $t = t_b + 2\pi M f^{-3/2}$ respectively. In all cases such events occur on space-like surfaces.

2.5.2 Shell Crossings

Shell crossings occur when an inner constant-r 'shell' of matter passes though an outer one, causing the density (2.4) and curvature (2.26) diverge. Since the 'radial' coordinate is comoving with the matter it becomes degenerate at such loci. This occurs where

$$R' - R\frac{E'}{E} = 0 \tag{2.28}$$

provided

$$M' - 3M\frac{E'}{E} \neq 0 \neq \epsilon + f \tag{2.29}$$

These situations have been extensively investigated in [103] for the $\Lambda = 0$ case, and conditions on the arbitrary functions to avoid such divergences were given. They are summarised Table 2.3 for the $\epsilon = +1$ case and Table 2.4 for the $\epsilon = -1$ case. The shell

crossing conditions for $\epsilon = 0$ models require $S' = 0 = P' = Q'$, and so do not allow for deviations from planar symmetry.

ϵ	R'	f	M', f', t'_b	S', P', Q'
$+1$	> 0	all	$M' \geq 0$	$\frac{\sqrt{(S')^2+(P')^2+(Q')^2}}{S} \leq \frac{M'}{3M}$
		≥ 0	$f' \geq 0$ $t'_b \leq 0$ but not all 3 equalities at once	$\frac{\sqrt{(S')^2+(P')^2+(Q')^2}}{S} \leq \frac{f'}{2f}$ (no condition where $f = 0$)
		< 0	$\frac{2\pi M}{(-f)^{3/2}}\left(\frac{M'}{M} - \frac{3f'}{2f}\right) + t'_b \geq 0$ $t'_B \leq 0$ but not all 3 equalities at once	
	$= 0$ $R'' > 0$ neck	-1	$M' = 0$, $f' = 0$, $t'_b = 0$ $f = -1$ for no surface layer $\frac{2\pi M}{(-f)^{3/2}}\left(\frac{M''}{M} - \frac{3f''}{2f}\right) + t''_b \geq 0$ $t''_b \leq 0$	$S' = 0$, $P' = 0$, $Q' = 0$ $\frac{\sqrt{(S'')^2+(P'')^2+(Q'')^2}}{S} \leq \frac{M''}{3M}$
	$= 0$ $R'' < 0$ belly		$M' = 0$, $f' = 0$, $t'_b = 0$ $f = -1$ for no surface layer $\frac{2\pi M}{(-f)^{3/2}}\left(\frac{M''}{M} - \frac{3f''}{2f}\right) + t''_b \leq 0$ $t''_b \leq 0$	$S' = 0$, $P' = 0$, $Q' = 0$ $-\frac{\sqrt{(S'')^2+(P'')^2+(Q'')^2}}{S} \geq \frac{M''}{3M}$
	< 0	all	$M' < 0$	$-\frac{\sqrt{(S')^2+(P')^2+(Q')^2}}{S} \geq \frac{M'}{3M}$
		≥ 0	$f' < 0$ $t'_b \geq 0$ but not all 3 equalities at once	$-\frac{\sqrt{(S')^2+(P')^2+(Q')^2}}{S} \geq \frac{f'}{2f}$ (no condition where $f = 0$)
		< 0	$\frac{2\pi M}{(-f)^{3/2}}\left(\frac{M'}{M} - \frac{3f'}{2f}\right) + t'_b \leq 0$ $t'_b \geq 0$ but not all 3 equalities at once	

Table 2.3 **Quasi-spherical Szekeres No Shell Crossing Conditions** - The necessary and sufficient conditions on M', f', t'_b, S', P' and Q' to completely avoid shell crossings in $\Lambda = 0$ quasi-spherical Szekeres models.

2.6 Keeping Things Regular

Some further conditions on the arbitrary functions are required in order to ensure the model is well behaved everywhere. For the metric (2.1) to retain a Lorentzian signature one requires that $g_{ii} > 0$, where $i = 1, 2, 3$ and the repeated index does not

ϵ	R'	f'	S'	M', f', t'_b, P', Q'
-1	>0	≥ 0	$ES'>0$	$(S')^2>(P')^2+(Q')^2$ $\frac{M'}{3M}\geq -\frac{\sqrt{(S')^2-(P')^2-(Q')^2}}{S}$ $\frac{f'}{2f}\geq -\frac{\sqrt{(S')^2-(P')^2-(Q')^2}}{S}$ $t'_b\leq 0$
	$=0$	$=1$	$S'=0$	$M'=0\ ,\quad f'=0\ ,\quad t'_b=0$ $P'=0\ ,\quad Q'=0$
	<0	≥ 1	$ES'<0$	$(S')^2>(P')^2+(Q')^2$ $\frac{M'}{3M}\leq +\frac{\sqrt{(S')^2-(P')^2-(Q')^2}}{S}$ $\frac{f'}{2f}\leq +\frac{\sqrt{(S')^2-(P')^2-(Q')^2}}{S}$ $t'_b\geq 0$

Table 2.4 **Quasi-pseudospherical Szekeres No Shell Crossing Conditions** - The necessary and sufficient conditions on M', f', t'_b, S', P' and Q' to completely avoid shell crossings in $\Lambda=0$ quasi-pseudospherical Szekeres models.

imply summation. From the rr-component, this implies that

$$\epsilon \geq -f, \tag{2.30}$$

with the equality only occurring where $R'-RE'/E=0$. Thus, the permissible constant-(t,r) spatial foliations are limited by the local geometry via f. See table 2.2 for details.

In addition, at the origin of the metric coordinates, regularity conditions require that the density (2.4) and curvature (2.26) do not diverge, and their time evolution is a smooth continuation of their immediate neighbourhood. Imposing these conditions one finds the resulting conditions on the arbitrary functions are [103]

$$\begin{aligned} &M\sim R^3, \qquad f\sim R^2, \\ &S\sim R^n, \qquad P\sim R^n, \qquad Q\sim R^n, \qquad 0\leq n\leq 1. \end{aligned} \tag{2.31}$$

Since $\epsilon=-1$ models do not permit an origin, and in $\epsilon=0$ models only asymptotic approach to $f=0$ is possible [81], the above expression only applies to the $\epsilon=1$ case. With these conditions satisfied, along with the shell crossing conditions in tables 2.3 and 2.4, the model will be well defined everywhere.

2.7 Some Special Cases

By making specific choices for the arbitrary functions, the Szekeres metric can reduce to number of interesting sub-cases. Here we highlight two such cases.

2.7.1 Lemaître-Tolman

The LT metric is the spherically symmetric special case of the quasi-spherical Szekeres model. The line element is [58]

$$ds^2 = -dt^2 + \frac{R'^2}{1+f}dr^2 + R^2 d\Omega^2. \tag{2.32}$$

By making the substitutions

$$\begin{aligned} \epsilon = +1, \qquad & S = P = Q = \text{const.} \\ \Rightarrow E = \text{const.} \qquad & \Rightarrow E'/E = 0. \end{aligned} \tag{2.33}$$

into the Szekeres metric (2.1) one recovers the LT metric (2.32). Indeed, LT also contains an number of interesting sub-cases, all of which are contained within quasi-spherical Szekeres models. Some of these include the metrics of Schwarzchild [104], Vaidya [105, 106] and Kantowski-Sachs [107].

2.7.2 Dust Friedmann-Lemaître-Roberson-Walker

Perhaps the most important special case of the Szekeres model is the dust FLRW metric, as this has become the standard metric used to model the cosmos (to zeroth order). It is homogeneous and isotropic, and also a special case of the LT metic. The metric is given by

$$ds^2 = -dt^2 + a^2(t)\left[\frac{dr^2}{1-kr^2} + r^2 d\Omega^2\right], \tag{2.34}$$

where $a(t)$ is the scale factor and k is the curvature parameter, either -1, 0 or 1. By choosing the LT metric functions to be

$$\begin{aligned} M &= M_0 r^3 \ , \qquad\qquad M_0 \equiv \frac{\kappa \rho_0 a_0^3}{6} \ , \\ f &= -kr^2 \ , \\ t_b &= \text{const}, \\ \epsilon &= +1 \ , \end{aligned} \tag{2.35}$$

where subscript-0 refers to quantities at the present time, one recovers the FLRW metric (2.34). It is also possible to recover the FLRW geometry in the $\epsilon = \{0, -1\}$ cases too, and thus the constant-(t, r) 2-surfaces need not be spherical. For $\epsilon = -1$ models, the $k = -1$ FLRW special case is found by setting [81]

$$\begin{aligned} M &= M_0 \cosh^3(r) \\ f &= \cosh^2(r) \\ t_b &= \text{const} \ . \end{aligned} \tag{2.36}$$

Since regularity conditions require $f \geq -\epsilon$, the $\epsilon = -1$ case does not contain the $k = \{0, +1\}$ FLRW special cases. In all the cases above, one recovers FLRW, regardless of the behaviour of the Szekeres metric functions $S(r)$, $P(r)$ and $Q(r)$. If they are not constant, it just amounts to a coordinate transformation.

Chapter 3

Cosmic Observables in Arbitrary Spacetimes

Determining the evolution of cosmic observables in an arbitrary spacetime is a highly non-trivial task. This is primarily because successive emission events coming from some source will not necessarily follow the same spatial path to the observer. While tracing a light ray back from a single observation event to an emission event is relatively straightforward, knowing the arrival direction of a subsequent event from that same source is not clear, given that spacetime is non-symmetric and dynamical. It is essential to know these paths for one to calculate observables such as redshift, area distance and the apparent motion across the observer's sky. It would appear that this boils down to a boundary value problem, involving lots of ray tracing, and some 'shooting' methods, to determine the appropriate arrival directions. In order to avoid such a hefty numerical exercise, we propose a method which gives the instantaneous rate of change of observables, such as bulk flow patterns as a function of redshift. This can then be implemented in numerical ray tracing codes to calculate the desired observables down the past null cone (PNC)[1]. Actually tracking the evolution of observed properties of given sources is left for future work.

[1]In the literature there are existing methods for calculating observables down an observer's PNC in an exact way [108–111], however, these methods are formulated using tensor equations which are not necessarily well suited to numerical implementation. Our method is designed to facilitate numerical implementation. Additionally, our method calculates the proper motion of a source across the observer's sky, which is not done in the other methods.

3.1 Overview of the Method/Setup

We consider an observer O, with 4-velocity u^a_o, who sets up PNC coordinates

$$\hat{x}^\alpha = (\tau, \chi, \vartheta, \varphi) \tag{3.1}$$

centred on her own position. We assume the metric describes spacetime inhomogeneities up to some level of accuracy, and set the observer to be comoving with the local mean flow. This is a simplification. In practice, observer's motions will not coincide with the Hubble flow. For example, in the context of a FLRW model, observations indicate that there are proper motions of ~ 600km/s about the Hubble flow. However, the idea here is to investigate how cosmic flows might be modelled, and so we ignore observer proper motions and the internal kinematics of galaxies. At any observer O the arriving set of light rays form a 3-parameter congruence of null geodesics with tangent vector k^a. A natural way to label light rays is with the time of observation in O's frame, and the galactic latitude and longitude (or right ascention and declination). Thus, anything that O sees in a particular direction will be labeled with the same sky coordinates (ϑ, φ), and the time of observation τ. With this, emission events in spacetime are mapped to observation times and sky coordinates by Lie dragging the observer's $(\tau, \vartheta, \varphi)$ coordinates down the light rays of the PNC (See figure 3.1 for an illustration of the set-up). By this construction the $(\tau, \vartheta, \varphi)$ coordinates are constant along each incoming null geodesic. The only natural "distance" down the light ray is redshift, z, since the distance of the source and emission time are not measurable[2]. However, z is not guaranteed to be monotonically increasing down the ray [112], so this is not a suitable choice to complete our coordinate system. Moreover, we need to integrate down the light rays relative to some parameter and so it makes sense to construct the affine parameter χ. Thus the null tangent vector becomes

$$k^a = \frac{\mathrm{d}x^a}{\mathrm{d}\chi} \ , \quad k^a k_a = 0, \tag{3.2}$$

which we use along with χ to complete the coordinate system. We propagate this basis down the observer's PNC, assuming a given metric, as follows

i) choose a set of reference directions at the observer and calculate the PNC coordinates $(\tau, \chi, \vartheta, \varphi)$ in the vicinity of the observer

[2]The intrinsic size/luminosity of galaxies is not know, but the intrinsic (lab frame) emission frequencies of certain atomic/molecular transitions is known. Given a few lines, the redshift is easily calculated by comparison with standard galaxy spectra.

ii) solve for the path of the light ray

iii) Lie drag the observer's coordinates and basis vectors down the ray

We now deal with each of these steps in the following sections. The remainder of this section will deal with calculations down a single ray, which will be extended to all rays in the PNC.

3.2 Constructing the Observer's Basis

For a given metric g_{ab}, and coordinates x^a, we specify the observer's worldline, O, and locally set up an othonormal tetrad (ONT) $\overline{\mathbf{e}}_i$ with $\overline{\mathbf{e}}_0$ in the direction of the observer's 4-velocity. That is

$$\overline{\mathbf{e}}_i\Big|_o = \left[\overline{e}_i{}^a\, \boldsymbol{\partial}_a\right]_0 , \tag{3.3}$$

where $\boldsymbol{\partial}_a$ are the coordinate basis vectors and the components $\overline{e}_i{}^a$ define the new basis $\overline{\mathbf{e}}_i$. As mentioned in the previous section, we expect that O will be comoving with the fluid flow, but we do not assume it here. Since one can always define a Local Inertial Frame (LIF) in which the Christoffel symbols vanish at first order in the neighbourhood of any one point, there will be coordinates $\overline{x}^e$ in the neighbourhood of O in which $\overline{x}^0 = \overline{\tau}$, the observer's proper time. While it is not guaranteed that these will form a coordinate basis, we can construct one from $\overline{\mathbf{e}}_i$ and their first derivatives at O. We then convert the ONT $\overline{\mathbf{e}}_j$ into more natural basis for observations at O — a spherical basis $\tilde{\mathbf{e}}_n$, with coordinates $\tilde{x}^m = (\tilde{\tau}, \tilde{r}, \tilde{\vartheta}, \tilde{\varphi})$ [3]. Imposing that the $\overline{\mathbf{e}}_1$, $\overline{\mathbf{e}}_2$ & $\overline{\mathbf{e}}_3$ basis vectors be aligned the directions of $(\vartheta, \varphi) = (\pi/2, 0)$, $(\vartheta, \varphi) = (\pi/2, \pi/2)$ & $\vartheta = 0$, we find

$$\begin{aligned}
\tilde{\mathbf{e}}_{\tilde{\tau}} &= \overline{\mathbf{e}}_0 \\
\tilde{\mathbf{e}}_{\tilde{r}} &= \sin\tilde{\vartheta}\cos\tilde{\varphi}\,\overline{\mathbf{e}}_1 + \sin\tilde{\vartheta}\sin\tilde{\varphi}\,\overline{\mathbf{e}}_2 + \cos\tilde{\vartheta}\,\overline{\mathbf{e}}_3 \\
\tilde{\mathbf{e}}_{\tilde{\vartheta}} &= \tilde{r}\cos\tilde{\vartheta}\cos\tilde{\varphi}\,\overline{\mathbf{e}}_1 + \tilde{r}\cos\tilde{\vartheta}\sin\tilde{\varphi}\,\overline{\mathbf{e}}_2 - \tilde{r}\sin\tilde{\vartheta}\,\overline{\mathbf{e}}_3 \\
\tilde{\mathbf{e}}_{\tilde{\varphi}} &= -\tilde{r}\sin\tilde{\vartheta}\sin\tilde{\varphi}\,\overline{\mathbf{e}}_1 + \tilde{r}\sin\tilde{\vartheta}\cos\tilde{\varphi}\,\overline{\mathbf{e}}_2 ,
\end{aligned} \tag{3.4}$$

where $\tilde{r}$ is a proper radius from O and $\tilde{\mathbf{e}}_{\tilde{r}}$ is a spacelike unit vector pointing outwards from O and orthogonal to $\tilde{\mathbf{e}}_{\tilde{\tau}}$, $\tilde{\mathbf{e}}_{\tilde{\vartheta}}$, $\tilde{\mathbf{e}}_{\tilde{\varphi}}$. Next we convert to a null radial basis vector by

[3] This basis is of course degenerate at the observer, where $\tilde{r} = 0$.

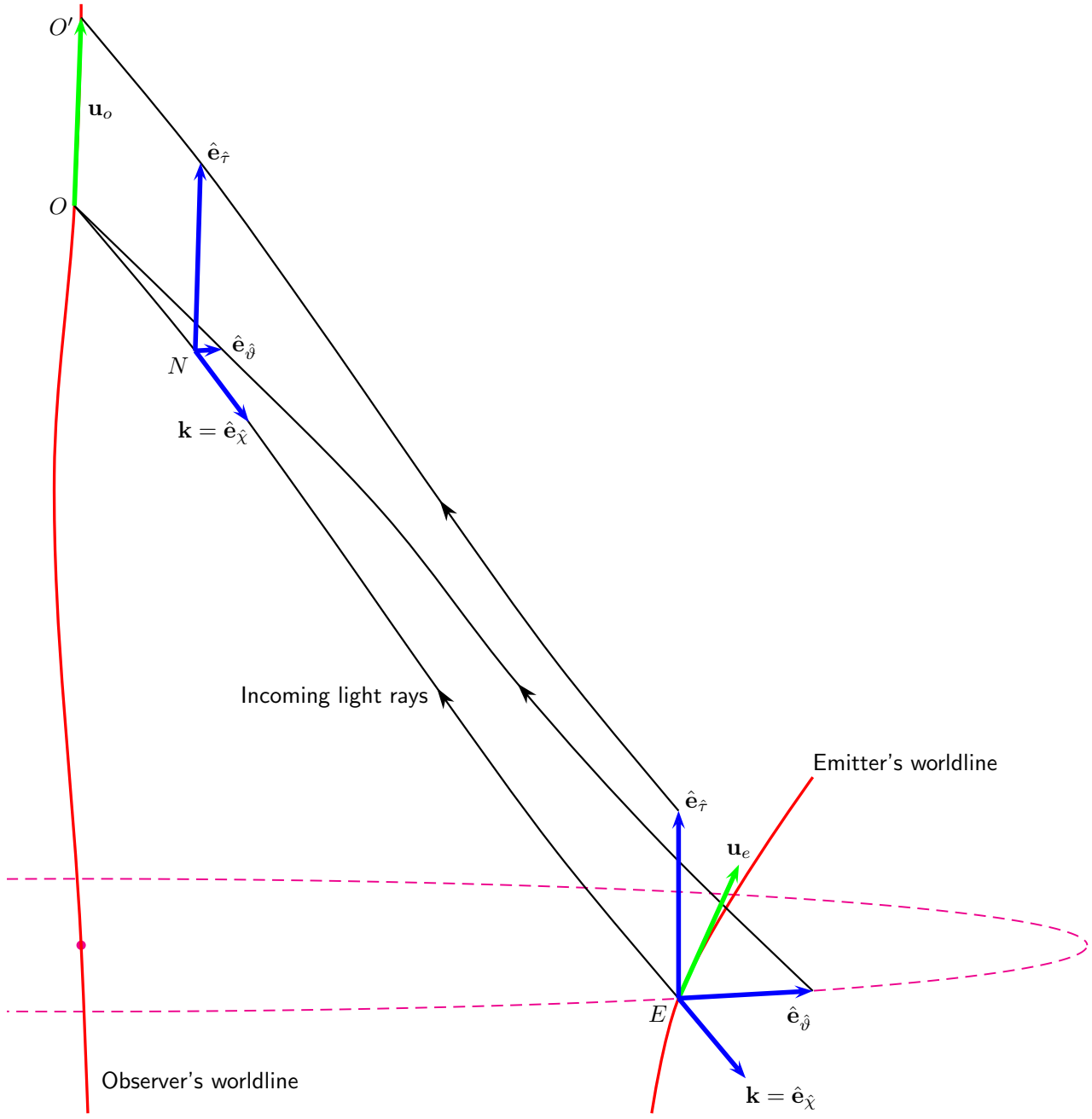

Fig. 3.1 **Illustration of the Observer's Coordinate Basis** The observation time and angles on the sky, $(\hat{\tau}, \hat{\vartheta}, \hat{\varphi})$, are propagated down the PNC from an observation event, along with the affine parameter, $\hat{\chi}$, as the fourth coordinate. The solid red lines are the worldlines of the observer and emitter, labeled O and E. The solid black line are light rays emanating from E and arriving at O. *Image credit: C Hellaby*

writing

$$\hat{\tau} = \tilde{r} + \tilde{\tau} \ , \quad \hat{\chi} = \tilde{r} \qquad \leftrightarrow \qquad \tilde{\tau} = \hat{\tau} - \hat{\chi} \ , \quad \tilde{r} = \hat{\chi} \ , \tag{3.5}$$

which gives our observer's basis, associated with coordinates $\hat{x}^i = (\hat{\tau}, \hat{\chi}, \hat{\vartheta}, \hat{\varphi})$ [4]. We find

$$\begin{aligned}
\hat{\mathbf{e}}_{\hat{\tau}} &= \tilde{\mathbf{e}}_{\tilde{\tau}} = \overline{\mathbf{e}}_0 \\
\hat{\mathbf{e}}_{\hat{\chi}} &= -\tilde{\mathbf{e}}_{\tilde{\tau}} + \tilde{\mathbf{e}}_{\tilde{r}} = -\overline{\mathbf{e}}_0 + \sin\hat{\vartheta}\cos\hat{\varphi}\,\overline{\mathbf{e}}_1 + \sin\hat{\vartheta}\sin\hat{\varphi}\,\overline{\mathbf{e}}_2 + \cos\hat{\vartheta}\,\overline{\mathbf{e}}_3 \\
\hat{\mathbf{e}}_{\hat{\vartheta}} &= \tilde{\mathbf{e}}_{\tilde{\vartheta}} = \hat{\chi}\cos\hat{\vartheta}\cos\hat{\varphi}\,\overline{\mathbf{e}}_1 + \hat{\chi}\cos\hat{\vartheta}\sin\hat{\varphi}\,\overline{\mathbf{e}}_2 - \hat{\chi}\sin\hat{\vartheta}\,\overline{\mathbf{e}}_3 \\
\hat{\mathbf{e}}_{\hat{\varphi}} &= \tilde{\mathbf{e}}_{\tilde{\varphi}} = -\hat{\chi}\sin\hat{\vartheta}\sin\hat{\varphi}\,\overline{\mathbf{e}}_1 + \hat{\chi}\sin\hat{\vartheta}\cos\hat{\varphi}\,\overline{\mathbf{e}}_2 \ .
\end{aligned} \tag{3.6}$$

Since these expressions are written in terms of the orthonormal tetrad they apply in any spacetime, with the metric dependance contained in $\overline{\mathbf{e}}_i$. These are now the basis vectors that are to be propagated down the observer's PNC[5]. Once this has been done they provide the transformation between metric coordinates and Observer's coordinates,

$$\hat{e}^{\alpha}{}_{c} = \frac{\partial \hat{x}^{\alpha}}{\partial x^{c}} \ , \qquad \hat{e}_{\alpha}{}^{c} = \frac{\partial x^{c}}{\partial \hat{x}^{\alpha}} \ , \tag{3.7}$$

from which we calculate the observables. We will see in §3.4.1 that what we actually need is not $\hat{e}_{\alpha}{}^{a}$ but its inverse $\hat{e}^{\alpha}{}_{a}$, obtained via

$$\hat{e}^{\alpha}{}_{a}\,\hat{e}_{\beta}{}^{a} = \delta^{\alpha}_{\beta} \qquad \leftrightarrow \qquad \hat{e}^{\alpha}{}_{b}\,\hat{e}_{\alpha}{}^{a} = \delta^{a}_{b} \ . \tag{3.8}$$

A summary of our conventions for the various coordinate systems is given in Table 3.1.

3.3 The Propagation Equations

Here we lay out the various differential equations (DEs) and their initial conditions which are required in order to calculate the observables we are interested in. Throughout the course of this text we will refer to them collectively as the propagation equations.

[4] Note that in this construction $\hat{\tau}$ labels particular past null cones.

[5] These basis vectors are reminiscent of the fluid-ray tetrad of [42], except $\hat{\mathbf{e}}_{\hat{\tau}}$ is not the local fluid 4-velocity

Coordinate System/Basis	"Coordinates"	Basis	Index Symbols
coordinates of given metric	x^a	$\boldsymbol{\partial}_b$	$a, b, c, \cdots$
ONT near O	$\overline{x}^i$	$\overline{\mathbf{e}}_j$	$i, j, k, \cdots$
observer's natural coords near O	$\tilde{x}^m = (\tilde{\tau}, \tilde{r}, \tilde{\vartheta}, \tilde{\varphi})$	$\tilde{\mathbf{e}}_n$	$m, n, o, \cdots$
observer's PNC coords	$\hat{x}^\alpha = (\hat{\tau}, \hat{\chi}, \hat{\vartheta}, \hat{\varphi})$	$\hat{\mathbf{e}}_\beta$	$\alpha, \beta, \gamma, \cdots$

Table 3.1 **Notation Conventions for the Various Coordinate Systems** Each set of basis vectors are denoted by different accents (overbar, tile, hat) and have corresponding sets of greek/latin letters for the index symbols.

3.3.1 Solving for the Light Cone

The observer's PNC is found by propagating k^a outward from O using the null geodesic equation. The path of the light ray in the direction of k^a is then given by

$$\frac{\delta k^a}{\delta \hat{\chi}} \equiv k^b \nabla_b k^a = 0 \ , \qquad k^a k_a = 0 \ , \tag{3.9}$$

where k^a is the null tangent vector given in (3.2), and $\hat{\chi}$ is the affine parameter along the ray. This form is however not amenable to numerical calculations since it contains an absolute derivative. Expanding (3.9) in terms of total derivatives we find the familiar form

$$\frac{\mathrm{d}k^a}{\mathrm{d}\hat{\chi}} = -k^b \Gamma^a{}_{bc} k^c \ , \qquad k^a = \frac{\mathrm{d}x^a}{\mathrm{d}\hat{\chi}}. \tag{3.10}$$

Now this can be integrated numerically. Since this is a second order DE we need two initial conditions, namely, a starting point, $[x^a]_o$, and an initial direction $[k^a]_o$. Now, by the construction in the previous section we will have $k^b = \mathrm{d}x^b/\mathrm{d}\hat{\chi} = \hat{e}_{\hat{\chi}}{}^b$ (see §A.2 where this is made explicit), and so the initial condition $[k^a]_o$ follows straight from (3.6) and the choice of ray direction, $(\hat{\vartheta}, \hat{\varphi})$, namely

$$[\mathbf{k}]_o = \hat{\mathbf{e}}_{\hat{\chi}} = -\overline{\mathbf{e}}_0 + \sin\hat{\vartheta}\cos\hat{\varphi}\,\overline{\mathbf{e}}_1 + \sin\hat{\vartheta}\sin\hat{\varphi}\,\overline{\mathbf{e}}_2 + \cos\hat{\vartheta}\,\overline{\mathbf{e}}_3 \ . \tag{3.11}$$

This ensures that in an orthonormal frame the initial value of $k^a = (-1, 1, 0, 0)$. The initial position is unconstrained, and can be chosen at will. This can now be integrated as a system of eight coupled first order ODEs.

3.3.2 Propagating the Basis Vectors

Beyond the vicinity of O, we define the observer's coordinates by labelling each light ray with its initial $(\hat{\tau}, \hat{\chi}, \hat{\vartheta}, \hat{\varphi})$ values and Lie dragging the $\hat{\mathbf{e}}_\alpha$ down each ray. Since the condition for a coordinate basis is that the commutator of every basis vector be zero, our observer's basis should remain a coordinate basis. In principle, they should obey

$$\begin{aligned} [\mathbf{e}_{\hat{\chi}}, \mathbf{e}_\alpha] &= \mathcal{L}_{\mathbf{k}} \hat{\mathbf{e}}_\alpha = 0, \\ \rightarrow \quad k^b \partial_b \hat{e}_\alpha{}^a - \hat{e}_\alpha{}^b \partial_b k^a &= 0. \end{aligned} \tag{3.12}$$

Substituting the definition (3.2) into the first term, and rearranging, then gives a ODE for the components in terms of the affine parameter along the ray,

$$\frac{\mathrm{d}}{\mathrm{d}\hat{\chi}} \hat{e}_\alpha{}^a = \hat{e}_\alpha{}^b \partial_b k^a \ . \tag{3.13}$$

However, solving this expression requires one to have knowledge of the transverse derivative $\partial_b k^a$, which would be an extra numerical calculation, and so we choose to find another formulation. Since $\mathbf{k}$ obeys the null geodesic equation (3.10), the Lie derivative of a vector along $\mathbf{k}$ (3.12) is equivalent to the geodesic deviation equation, and thus the basis vectors can be propagated with

$$\frac{\delta^2 \hat{e}_\alpha{}^a}{\delta \hat{\chi}^2} = -R^a{}_{bcd}\, k^b\, \hat{e}_\alpha{}^c\, k^d \ , \tag{3.14}$$

where $\delta^2/\delta\hat{\chi}^2$ is the absolute derivative along $\hat{\chi}$ and $R^a{}_{bcd}$ is the Riemann tensor associated with our given metric. Typically the components of the Riemann tensor (and Christoffel symbols) can be calculated analytically, and so (3.14) avoids the extra numerical calculation associated with the transverse derivative in (3.13). However, we pay the price of having to solve a higher order DE. The interpretation of the propagated basis vectors now becomes clear, $\{\hat{\mathbf{e}}_{\hat{\tau}}, \hat{\mathbf{e}}_{\hat{\vartheta}}, \hat{\mathbf{e}}_{\hat{\varphi}}\}$ are deviation vectors linking nearby light rays. In order to numerically integrate the components of $\hat{e}^a_\alpha$ along k^b we must convert the absolute derivative in (3.14) into a total derivative. That is, we want an ODE of the form $\mathrm{d}^2\hat{e}_\alpha{}^c/\mathrm{d}\hat{\chi}^2$. After some calculation (see appendix A) we find

$$\frac{\mathrm{d}^2 \hat{e}_\alpha{}^a}{\mathrm{d}\hat{\chi}^2} = -k^b \left(2\Gamma^a{}_{bc} \frac{\mathrm{d}\hat{e}_\alpha{}^c}{\mathrm{d}\hat{\chi}} + \hat{e}_\alpha{}^c k^d \Gamma^a{}_{db,c} \right) \ , \tag{3.15}$$

where $_{,c} \equiv \partial/\partial x^c$. Since the Christoffel symbols are built from derivatives of the metric, contractions in (3.15) will contain second derivatives of the metric functions. We now

have a set of four second-order vector DEs, each of which require two initial conditions, $[\hat{\mathbf{e}}_\alpha]_o$ and $[\mathrm{d}\hat{\mathbf{e}}_\alpha/\mathrm{d}\hat{\chi}]_o$, which we consider in turn. For $[\hat{\mathbf{e}}_{\hat{\tau}}]_o$ we require that it coincide with $\mathbf{u}_o$, so that $\hat{\tau}$ is the observer's proper time. Thus we have

$$\lim_{\hat{\chi}\to 0} e_{\hat{\tau}}{}^c = u_o^c \ . \tag{3.16}$$

An expression for $[\mathrm{d}\hat{\mathbf{e}}_{\hat{\tau}}/\mathrm{d}\hat{\chi}]_o$ can be found by considering two $\mathbf{k}$ vectors, one at O and one slightly further along the observer's worldling at O' (see Figure 3.1). Once the direction of $\mathbf{k}$ has been chosen at O, the one at O' must "point" in the same direction, as perceived by the observer. Therefore it is constructed by Fermi transport of $\mathbf{k}$ along $\mathbf{u}_o$

$$\left.\frac{\delta k^a}{\delta\tau}\right|_{\hat{\chi}=0} = \Big[u_o^b\nabla_b k^a - k_b a_o^b u_o^a + k_b u_o^b a_o^a\Big]_{\hat{\chi}=0} = 0 \ , \tag{3.17}$$

where a_o^a is the observer's proper acceleration, which, with the help of (3.16), can be written

$$\begin{aligned} a_o^c &= u_o^d\nabla_d u_o^c \\ &= \Big[\hat{e}_{\hat{\tau}}{}^d\nabla_d\hat{e}_{\hat{\tau}}{}^c\Big]_{\hat{\chi}=0} \ . \end{aligned} \tag{3.18}$$

Using (3.16) and (3.13) with $\alpha = \hat{\tau}$, we expand the covariant derivative in (3.17) and rearrange to give the second initial condition for $\hat{\mathbf{e}}_{\hat{\tau}}$, namely

$$\left.\frac{\mathrm{d}\hat{e}_{\hat{\tau}}{}^a}{\mathrm{d}\chi}\right|_{\hat{\chi}=0} = \Big[-\hat{e}_{\hat{\tau}}{}^b\Gamma^a{}_{bc}k^c + k_b a_o^b\hat{e}_{\hat{\tau}}{}^a - k_b\hat{e}_{\hat{\tau}}{}^b a_o^a\Big]_{\hat{\chi}=0} \ . \tag{3.19}$$

If the observer is geodesic $a_o{}^b = 0$, Fermi transport becomes equivalent to parallel transport, and (3.19) reduces to

$$\left.\frac{\mathrm{d}\hat{e}_{\hat{\tau}}{}^a}{\mathrm{d}\chi}\right|_{\hat{\chi}=0} = \Big[-\hat{e}_{\hat{\tau}}{}^b\Gamma^a{}_{bc}k^c\Big]_{\hat{\chi}=0} \ . \tag{3.20}$$

For the angular basis vectors $\hat{\mathbf{e}}_{\hat{\vartheta}}$ & $\hat{\mathbf{e}}_{\hat{\varphi}}$, the origin limits of the third and fourth of (3.6) give the first initial conditions. We find

$$\begin{aligned}\hat{\mathbf{e}}_{\hat{\vartheta}}\Big|_{\hat{\chi}\to 0} &= \lim_{\hat{\chi}\to 0}\left[\hat{\chi}\cos\hat{\vartheta}\cos\hat{\varphi}\,\overline{\mathbf{e}}_1 + \hat{\chi}\cos\hat{\vartheta}\sin\hat{\varphi}\,\overline{\mathbf{e}}_2 - \hat{\chi}\sin\hat{\vartheta}\,\overline{\mathbf{e}}_3\right] \\ &= 0\ ,\end{aligned} \tag{3.21}$$

and similarly

$$\begin{aligned}\hat{\mathbf{e}}_{\hat{\varphi}}\Big|_{\hat{\chi}\to 0} &= \lim_{\hat{\chi}\to 0}\left[-\hat{\chi}\sin\hat{\vartheta}\sin\hat{\varphi}\,\overline{\mathbf{e}}_1 + \hat{\chi}\sin\hat{\vartheta}\cos\hat{\varphi}\,\overline{\mathbf{e}}_2\right] \\ &= 0\ .\end{aligned} \tag{3.22}$$

And the derivatives of (3.21) & (3.22) then give the second set of ICs,

$$\left.\frac{\mathrm{d}e_{\hat{\vartheta}}{}^a}{\mathrm{d}\hat{\chi}}\right|_{\hat{\chi}\to 0} = \left.\frac{\partial k^a}{\partial\hat{\vartheta}}\right|_{\hat{\chi}\to 0} = \left[\cos\hat{\vartheta}\cos\hat{\varphi}\,\overline{e}_1{}^a + \cos\hat{\vartheta}\sin\hat{\varphi}\,\overline{e}_2{}^a - \sin\hat{\vartheta}\,\overline{e}_3{}^a\right]_{\hat{\chi}=0}, \tag{3.23}$$

and

$$\left.\frac{\mathrm{d}e_{\hat{\varphi}}{}^a}{\mathrm{d}\hat{\chi}}\right|_{\hat{\chi}\to 0} = \left.\frac{\partial k^a}{\partial\hat{\varphi}}\right|_{\hat{\chi}\to 0} = \left[-\sin\hat{\vartheta}\sin\hat{\varphi}\,\overline{e}_1{}^a + \sin\hat{\vartheta}\cos\hat{\varphi}\,\overline{e}_2{}^a\right]_{\hat{\chi}=0}\ . \tag{3.24}$$

Thus, our set of initial conditions for (3.15) are (3.16), (3.19), (3.21), (3.22), (3.23) and (3.24). In terms of components, this is a system of 16 coupled second-order ODEs, with 32 initial conditions. These will be applied to a specific metric and ONT in §3.5

3.4 Observables

3.4.1 Redshift and the Apparent Motion of a Source

By our construction both the apparent motion of a source and its redshift can be thought of as instantaneous rates of change, and derived from our propagated basis vectors. Since the coordinates $(\hat{\tau}, \hat{\vartheta}, \hat{\varphi})$ have been Lie dragged down the light rays and the basis for the observer's coordinate system are deviation vectors, one can easily

relate the emitter to the source with

$$\begin{aligned}\left[\frac{\mathrm{d}\hat{x}^\beta}{\mathrm{d}\hat{\tau}}\right]_o &= \left[\frac{\mathrm{d}\hat{x}^\beta}{\mathrm{d}\hat{\tau}}\right]_e \qquad\qquad \beta \neq \hat{\chi} \\ &= \left[\frac{\partial \hat{x}^\beta}{\partial x^a}\frac{\mathrm{d}x^a}{\mathrm{d}\tau_e}\frac{\mathrm{d}\tau_e}{\mathrm{d}\hat{\tau}_e}\right] \\ &= \frac{\left[\hat{e}^\beta{}_a u^a\right]_e}{(1+z)} \ , \end{aligned} \tag{3.25}$$

where τ_e is the source proper time, $\hat{\tau}_o$ is the observer's proper time, and $\hat{\tau}_e$ is its extension down the PNC. Here we introduced the redshift from the definition $(1+z) \equiv \lambda_o/\lambda_e = \mathrm{d}\hat{\tau}/\mathrm{d}\tau_e$. Setting $\beta = \hat{\tau}$ in (3.25) and rearranging then gives and expression for the redshift

$$1 + z = [\hat{e}^{\hat{\tau}}_a u^a]_e \ . \tag{3.26}$$

The motion of a source across the observer's sky is just the rate of change of observed angle with respect to observer time, and thus, setting $\beta = \{\hat{\vartheta}, \hat{\varphi}\}$ in (3.25) gives the apparent motion

$$\left.\frac{\mathrm{d}\tilde{\vartheta}}{\mathrm{d}\tilde{\tau}}\right|_o = \frac{\left[\hat{e}^{\hat{\vartheta}}{}_a u^a\right]_e}{(1+z)} \tag{3.27}$$

$$\left.\frac{\mathrm{d}\tilde{\varphi}}{\mathrm{d}\tilde{\tau}}\right|_o = \frac{\left[\hat{e}^{\hat{\varphi}}{}_a u^a\right]_e}{(1+z)} \ . \tag{3.28}$$

Clearly, the basis vectors, once propagated, have to be inverted numerically, using (3.8).

3.4.2 Area Distance

In GR there are a number of notions of distance, each with a different interpretation. Some of these include redshift, luminosity distance, light travel time, affine distance, diameter distance etc. The angular diameter distance is based on the intuitive idea that objects which are further away from an observer appear smaller, and is thus defined as the diameter of an object divided by the angle it spans at the observer. This seems an obvious measure to construct from our propagated basis since they relate changes at the emitter to the observer. However, the angular diameter distance is subject to aberration in non-symmetric spacetimes — if there is any shearing of the

ray bundle, the axis along which one measures/defines the diameter and corresponding angle becomes important[6]. In contrast, the cross-sectional area of an infinitesimally thin bundle has an invariant meaning [111], and for this reason we choose to construct the area distance. It is defined as

$$d_A{}^2 = \frac{\mathrm{d}A}{\mathrm{d}\Omega_0}, \tag{3.29}$$

where dA is the physical area spanned by a source and Ω_0 is the solid angle subtended at the observer by the incoming light rays. With this definition the area distance is equivalent to the diameter distance when there is no shearing of the ray bundle. Now, consider a bundle of rays spanned by observer angles $d\hat{\vartheta}$ and $d\hat{\varphi}$. The solid angle of this bundle (at the observer) is simply

$$\mathrm{d}\Omega_0 = \sin\hat{\vartheta}\mathrm{d}\hat{\vartheta}\mathrm{d}\hat{\varphi}. \tag{3.30}$$

An object which that spans $\mathrm{d}\Omega_0$ at the observer will have a physical area given by the norm of the wedge product of the local vectors describing the size of the emitter [110]. In our notation this is

$$\mathrm{d}A = \left|\left((\hat{\mathbf{e}}_{\hat{\vartheta}}\cdot\hat{\mathbf{e}}_{\hat{\vartheta}})\,(\hat{\mathbf{e}}_{\hat{\varphi}}\cdot\hat{\mathbf{e}}_{\hat{\varphi}}) - (\hat{\mathbf{e}}_{\hat{\vartheta}}\cdot\hat{\mathbf{e}}_{\hat{\varphi}})^2\right)\right|^{1/2}\mathrm{d}\hat{\vartheta}\mathrm{d}\hat{\varphi}. \tag{3.31}$$

Dividing this result by (3.30) gives the area distance

$$d_A{}^2 = \frac{\left|\left((\hat{\mathbf{e}}_{\hat{\vartheta}}\cdot\hat{\mathbf{e}}_{\hat{\vartheta}})\,(\hat{\mathbf{e}}_{\hat{\varphi}}\cdot\hat{\mathbf{e}}_{\hat{\varphi}}) - (\hat{\mathbf{e}}_{\hat{\vartheta}}\cdot\hat{\mathbf{e}}_{\hat{\varphi}})^2\right)\right|^{1/2}}{\sin\hat{\vartheta}}\ . \tag{3.32}$$

Unlike the redshift and apparent motion, the area distance does not require the duals of the propagated basis vectors.

3.5 Observer Basis in Szekeres

We place an observer at an arbitrary spacetime position in the coordinates of the metric (t, r, p, q), and assume the observer and all emitters are comoving with the coordinates,

[6] We succeeded in deriving an expression for the angular diameter distance which agreed nicely with FLRW analytic solutions, however, this expression failed for non-symmetric spacetimes. At this point we realised the area distance is a better measure.

$u^a_o = 0 = u^a_e$. For such an observer O, the ONT for (2.1) is

$$\overline{e}_0{}^a = \begin{pmatrix} 1 \\ 0 \\ 0 \\ 0 \end{pmatrix} , \qquad \overline{e}_1{}^a = \begin{pmatrix} 0 \\ \frac{\sqrt{\epsilon+f}}{\left(R' - \frac{RE'}{E}\right)} \\ 0 \\ 0 \end{pmatrix} , \qquad \overline{e}_2{}^a = \begin{pmatrix} 0 \\ 0 \\ \frac{E}{R} \\ 0 \end{pmatrix} , \qquad \overline{e}_3{}^a = \begin{pmatrix} 0 \\ 0 \\ 0 \\ \frac{E}{R} \end{pmatrix} . \tag{3.33}$$

From this we see that orientation of the newly constructed basis is aligned with the metric basis at O, that is $\{\overline{\mathbf{e}}_0, \overline{\mathbf{e}}_1, \overline{\mathbf{e}}_2, \overline{\mathbf{e}}_3\} = \{\overline{\mathbf{e}}_t, \overline{\mathbf{e}}_r, \overline{\mathbf{e}}_p, \overline{\mathbf{e}}_q\}$. Figure 3.2 shows this alignment and the observer's sky angles $\{\hat{\vartheta}, \hat{\varphi}\}$ relative to these directions. For a

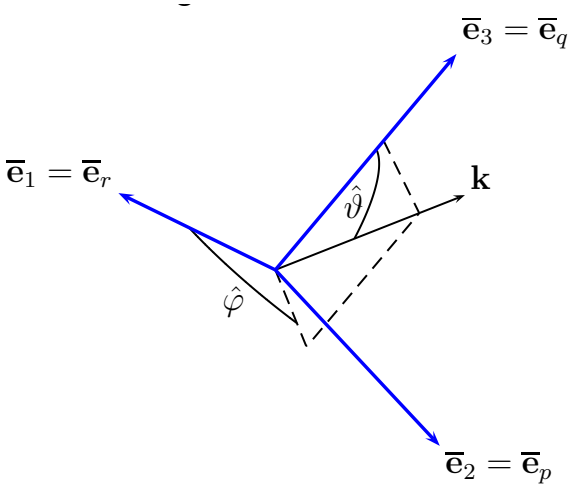

Fig. 3.2 **Observer's reference directions and ray angles in Szekeres**

particular observation direction we find the initial PNC basis vectors from (3.33) ,

using (3.6) for the components of $\overline{e}^a_i$, and taking the limit as $\hat{\chi} \to 0$. This gives[7]

$$
\begin{aligned}
\hat{e}_{\hat{\tau}}{}^a &= \begin{pmatrix} 1 \\ 0 \\ 0 \\ 0 \end{pmatrix} , \\
\hat{e}_{\hat{\chi}}{}^a &= \begin{pmatrix} -1 \\ \sin\hat{\vartheta}\cos\hat{\varphi}\frac{\sqrt{\epsilon+f}}{\left(R'-\frac{RE'}{E}\right)} \\ \sin\hat{\vartheta}\sin\hat{\varphi}\frac{E}{R} \\ \cos\hat{\vartheta}\frac{E}{R} \end{pmatrix} , \\
\hat{e}_{\hat{\vartheta}}{}^a &= \begin{pmatrix} 0 \\ \hat{\chi}\cos\hat{\vartheta}\cos\hat{\varphi}\frac{\sqrt{\epsilon+f}}{\left(R'-\frac{RE'}{E}\right)} \\ \hat{\chi}\cos\hat{\vartheta}\sin\hat{\varphi}\frac{E}{R} \\ -\hat{\chi}\sin\hat{\vartheta}\frac{E}{R} \end{pmatrix} \qquad \to \qquad \hat{e}_{\hat{\vartheta}}{}^a\Big|_{\hat{\chi}=0} = \begin{pmatrix} 0 \\ 0 \\ 0 \\ 0 \end{pmatrix} , \\
\hat{e}_{\hat{\varphi}}{}^a &= \begin{pmatrix} 0 \\ -\hat{\chi}\sin\hat{\vartheta}\sin\hat{\varphi}\frac{\sqrt{\epsilon+f}}{\left(R'-\frac{RE'}{E}\right)} \\ \hat{\chi}\sin\hat{\vartheta}\cos\hat{\varphi}\frac{E}{R} \\ 0 \end{pmatrix} \qquad \to \qquad \hat{e}_{\hat{\vartheta}}{}^a\Big|_{\hat{\chi}=0} = \begin{pmatrix} 0 \\ 0 \\ 0 \\ 0 \end{pmatrix} . \qquad (3.34)
\end{aligned}
$$

[7]Note that by (3.11) the initial k^a is the $\hat{e}_{\hat{\chi}}{}^a$ given in (3.34).

Clearly these results agree with (3.16), (3.21) & (3.22). The initial derivatives of (3.34) (except for $\hat{e}^a_{\hat{\chi}}$) are found by using (3.33) in (3.19), (3.23) & (3.24),

$$\left.\frac{\mathrm{d}}{\mathrm{d}\hat{\chi}}\hat{e}_{\hat{\tau}}{}^a\right|_{\hat{\chi}=0} = \begin{pmatrix} 0 \\ \dfrac{-\sqrt{\epsilon+f}\,(\dot{R}'-\dot{R}E'/E)}{(R'-RE'/E)^2}\sin\hat{\vartheta}\cos\hat{\varphi} \\ \dfrac{-\dot{R}E}{R^2}\sin\hat{\vartheta}\sin\hat{\varphi} \\ \dfrac{-\dot{R}E}{R^2}\cos\hat{\vartheta} \end{pmatrix}_O ,$$

$$\left.\frac{\mathrm{d}}{\mathrm{d}\hat{\chi}}\hat{e}_{\hat{\vartheta}}{}^a\right|_{\hat{\chi}=0} = \begin{pmatrix} 0 \\ \cos\hat{\vartheta}\cos\hat{\varphi}\frac{\sqrt{\epsilon+f}}{(R'-RE'/E)} \\ \cos\hat{\vartheta}\sin\hat{\varphi}\frac{E}{R} \\ -\sin\hat{\vartheta}\frac{E}{R} \end{pmatrix}_O ,$$

$$\left.\frac{\mathrm{d}}{\mathrm{d}\hat{\chi}}\hat{e}_{\hat{\varphi}}{}^a\right|_{\hat{\chi}=0} = \begin{pmatrix} 0 \\ -\sin\hat{\vartheta}\sin\hat{\varphi}\frac{\sqrt{\epsilon+f}}{(R'-RE'/E)} \\ \sin\hat{\vartheta}\cos\hat{\varphi}\frac{E}{R} \\ 0 \end{pmatrix}_O . \tag{3.35}$$

The initial derivative of $\hat{e}^a_{\hat{\chi}}$ is much more messy, but follows directly from the null geodesic equation. By using (3.33) in (3.10) we expand contractions with MAPLE and

write out the components

$$\left.\frac{\mathrm{d}}{\mathrm{d}\hat{\chi}}\hat{e}_{\hat{\chi}}{}^{t}\right|_{\hat{\chi}=0} = \left[-\left(\frac{(\dot{R}' - \dot{R}E'/E)}{(R' - RE'/E)} - \frac{\dot{R}}{R}\right)\sin^2\hat{\vartheta}\cos^2\hat{\varphi} - \frac{\dot{R}}{R}\right]_O \tag{3.36}$$

$$\begin{aligned}\left.\frac{\mathrm{d}}{\mathrm{d}\hat{\chi}}\hat{e}_{\hat{\chi}}{}^{r}\right|_{\hat{\chi}=0} = \Bigg[& \frac{\sqrt{\epsilon+f}}{(R' - RE'/E)}\Bigg\{\frac{2(\dot{R}' - \dot{R}E'/E)}{(R' - RE'/E)}\sin\hat{\vartheta}\cos\hat{\varphi} \\ & + \frac{2E}{(R' - RE'/E)}\sin\hat{\vartheta}\cos\hat{\varphi}\left[\left(\frac{E'_p}{E} - \frac{E'E_p}{E^2}\right)\sin\hat{\vartheta}\sin\hat{\varphi} + \left(\frac{E'_q}{E} - \frac{E'E_q}{E^2}\right)\cos\hat{\vartheta}\right]\Bigg\} \\ & + \frac{(\epsilon+f)}{(R' - RE'/E)}\Bigg\{\frac{1}{R}(1 - \sin^2\hat{\vartheta}\cos^2\hat{\varphi}) \\ & - \frac{(R'' - (R'E' + RE'')/E + RE'^2/E^2)}{(R' - RE'/E)^2}\sin^2\hat{\vartheta}\cos^2\hat{\varphi}\Bigg\} \\ & + \frac{2f'}{(R' - RE'/E)^2}\sin^2\hat{\vartheta}\cos^2\hat{\varphi}\Bigg]_O\end{aligned} \tag{3.37}$$

$$\begin{aligned}\left.\frac{\mathrm{d}}{\mathrm{d}\hat{\chi}}\hat{e}_{\hat{\chi}}{}^{p}\right|_{\hat{\chi}=0} = \Bigg[& -\frac{2E\sqrt{\epsilon+f}}{R^2}\sin^2\hat{\vartheta}\cos\hat{\varphi}\sin\hat{\varphi} + \frac{2\dot{R}E}{R^2}\sin\hat{\vartheta}\sin\hat{\varphi} + \frac{2EE_q}{R^2}\sin\hat{\vartheta}\sin\hat{\varphi}\cos\hat{\vartheta} \\ & + \frac{EE_p}{R^2}(\sin^2\hat{\vartheta}\sin^2\hat{\varphi} - \cos^2\hat{\vartheta}) - \frac{E^2}{RB}\left(\frac{E'_p}{E} - \frac{E'E_p}{E^2}\right)\sin^2\hat{\vartheta}\cos^2\hat{\varphi}\Bigg]_O\end{aligned} \tag{3.38}$$

$$\begin{aligned}\left.\frac{\mathrm{d}}{\mathrm{d}\hat{\chi}}\hat{e}_{\hat{\chi}}{}^{q}\right|_{\hat{\chi}=0} = \Bigg[& -\frac{2E\sqrt{\epsilon+f}}{R^2}\sin\hat{\vartheta}\cos\hat{\vartheta}\cos\hat{\varphi} + \frac{2\dot{R}E}{R^2}\cos\hat{\vartheta} + \frac{2EE_p}{R^2}\sin\hat{\vartheta}\cos\hat{\vartheta}\sin\hat{\varphi} \\ & - \frac{EE_q}{R^2}(\sin^2\hat{\vartheta}\sin^2\hat{\varphi} - \cos^2\hat{\vartheta}) - \frac{E^2}{RB}\left(\frac{E'_q}{E} - \frac{E'E_q}{E^2}\right)\sin^2\hat{\vartheta}\cos^2\hat{\varphi}\Bigg]_O\end{aligned} \tag{3.39}$$

The commutation coefficients, the Christoffel symbols and their partial derivatives are calculated using GRTensor & Maple. See appendix B for the commutation coefficients.

Chapter 4

Numerical Simulations

We develop code in MATLAB to generate sky maps of the cosmological observables as a function of redshift, as seen by an arbitrarily placed observer in the Szekeres spacetime, according to the method described in §3. First the user must specify the spacetime and observing position. Analytic expressions for the six Szekeres metric functions are input into the function *input_funcs.m* (up to and including third derivatives), and the coordinate position of the observer, x^a, into the main script, *sz_skymap.m*. Then, for a particular direction of the observer's sky, $(\hat{\theta}, \hat{\phi})$, the observer's basis vectors, $\hat{e}^a_\alpha$ and corresponding initial conditions are calculated using *obs_basis_setup.m*. Numerical solutions to the propagation equations (3.10) (3.14), along a particular line of sight, are then calculated. For this we use the MATLAB function *ode45.m*, which uses an adaptive Runge-Kutta algorithm to approximate the solution to an ODE. Once the components of $\hat{e}^a_\alpha$ along k^b are known, the observables are calculated using *redshift.m*, *apparent_motion.m* and *area_distance.m*. Since the affine distance down any ray is not a physical observable, comparing observables on χ = const. surfaces is not meaningful. Instead we interpolate the value of the area distance and apparent motion on predefined redshift slices, and from that generate sky maps. For a flowchart of the program structure see Figure 4.1, and for a list of the various functions, and their usage, see Appendix C.

4.1 Expressions for the Numerics

Expressions are often written in a form that is convenient for symbolic manipulations but problematic for explicit numerical calculation. Execution time and/or accuracy considerations often dictate that they must be rewritten in a form better suited to the implementation.

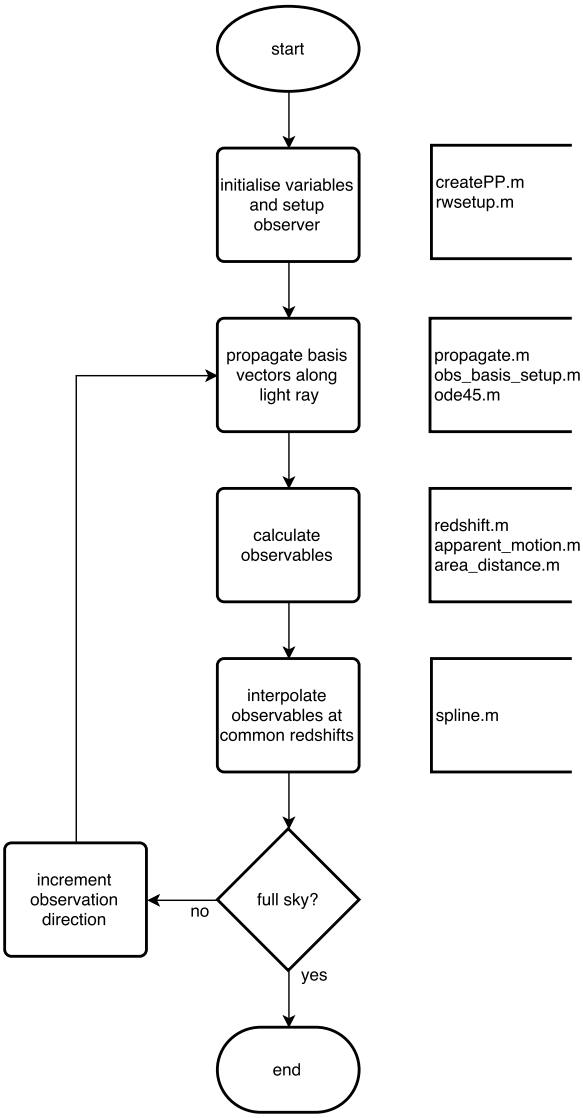

Fig. 4.1 **Flowchart for the Program** A schematic view of the program structure, and the names of the functions called at each step. The structure is a simple loop over all the $\{\tilde{\vartheta}, \tilde{\varphi}\}$ directions, with most of the details hidden in the block labelled "propagate basis vectors along light ray".

4.1.1 Propagation Equations

When inspecting the propagation equations we see that all the Christoffel symbols and their partial derivatives are needed, as one expects from an equation involving a contraction with the Riemann tensor. For this we used MAPLE with GRTensorII to calculate all of the components in terms of the Szekeres metric functions. At this point one can in principal proceed with numerical integration of (3.10) and (3.15). However, we find that numerical evaluation of the tensor contractions leads to instabilities in the solutions[1], and thus we decide to further simplify the propagation equations. Again, using MAPLE and GRTensorII, we expand out all contractions with Christoffel symbols and their derivatives in (3.15), and then simplify. These give the geodesic deviation equation directly in terms of the metric function and their derivatives. Cancellations have now happened at the symbolic level, avoiding any numerical cancellation of identical terms. We find this greatly improves the stability of the solutions. These expressions are however quite unwieldy, so we omit them here.

4.1.2 Solving for $R(t, r)$

From (2.10) we see that in parabolic regions $R(t, r)$ is straightforward to calculate since it can be written explicitly in terms of t and the metric functions $M(r)$ and $t_b(r)$. However, in hyperbolic/elliptic regions $R(t, r)$ is given by parametric equations involving the phase parameter, which are not invertible — see (2.6) (2.11). One must therefore interpolate the value of η from (2.7) or (2.12) at a given (t, r), and then use that η in (2.6) (2.11) to determine $R(t, r)$. For this we use the MATLAB function *spline*. In the elliptic case the range of η is finite and thus a linearly spaced vector of η-values over $[0, 2\pi]$ is a suitable range over which to interpolate the spline function. In the hyperbolic case the situation is different. The range of η is $[0, \infty)$, which is clearly not a feasible range over which to interpolate a spline function. We choose to compactify this range by making the substitution

$$T = \tanh \eta, \tag{4.1}$$

[1] We expect this instability is due to the cancellation of (near) identical terms in the contraction, since the Christoffel symbols are symmetric in the last two indices. Originally we wrote functions to compute the components of Γ^a_{bc} and $\Gamma^a_{bc,d}$, with which we numerically expanded the contractions in (3.15). From this we spotted the instability.

which allows us to write (2.6) and (2.7) in the form

$$R = \frac{M}{f}\left[(1-T^2)^{-1/2} - 1\right], \tag{4.2}$$

$$\frac{T}{\sqrt{1-T^2}} - \text{acosh}(1-T^2)^{-1/2} = \frac{f^{3/2}(t-t_b)}{M}. \tag{4.3}$$

Now the range over which to define the spline curve is finite, with $T = [0, 1)$ corresponding to the full range of η values. In order to avoid numerical divergences when $T = 1$ we choose a linearly spaced vector of T-values over $[0, 0.99999]$, and then perform spline interpolation on (4.3).

4.1.3 Near-Parabolic Expressions

For near parabolic evolutions, denoted NP, corresponding to small $\eta^2 f$, cancellation of near identical terms in the exact parametric expressions for $R(t, r)$ introduce large numerical errors.[2]. To avoid this we define a fat borderline region, that is close to or exactly parabolic, with which we use a series expansion for R. A series for R, which is valid for both hyperbolic and elliptic evolutions, can be written [101]

$$R = R_2 s^2 \left(1 + V - \frac{3V^2}{7} + \frac{23V^3}{63} - \frac{U}{4} - \frac{1894V^4}{4851} + \frac{UV}{11} + \frac{3293V^5}{7007} + \frac{45V^2U}{2002} + ...\right), \tag{4.4}$$

where

$$R_2 = \left(\frac{9M}{2}\right)^{1/3}, \quad V = \frac{fs^2}{10}\left(\frac{9}{2M^2}\right)^{1/3}, \quad U = \frac{\Lambda s^6}{3}, \quad s = (t-a)^{1/3}. \tag{4.5}$$

Since there is no known "proof of convergence" for series expansions, we choose the criterion for which (4.4) is used rather than (2.6) (2.7) (2.11) (2.12) to be when V is sufficiently small. And this sets the width of our fat borderlines. A suitable changeover value for V is determined empirically by plotting the ratio $R_{\text{exact}}/R_{\text{series}}$ alongside V, and looking for the region where there is reasonable agreement between the two expression. In Figure 4.2 we show the results for a model which has a borderline at $r = 0.5$. We find $V \lesssim 1.5 \times 10^{-3}$ is a suitable criterion to use the series expansion. With this, and using (4.5), we can write the NP criterion directly in terms of the metric

[2]This includes near the bang/crunch surfaces

functions as

$$\frac{|f|^{3/2}(t-t_b)}{M} < \frac{20}{6} V_{\text{border}}^{3/2} \ , \tag{4.6}$$

where $V_{\text{border}} = 1.5 \times 10^{-3}$, the value of V at the borderline.

4.1.4 Derivatives of $R(t, r)$

Expressions for the derivatives of R follow straight from (2.5) and (2.13), and can be written such that they are valid for all evolution types. The first and second partial time derivatives of R follows straight from (2.5). Setting $\Lambda = 0$ and taking the square root gives

$$\dot{R} = \sqrt{\frac{2M}{R} + f} \ , \tag{4.7}$$

and taking the partial derivative with respect to t gives

$$\ddot{R} = -\frac{M}{R^2} \ , \tag{4.8}$$

where we used (4.7) to eliminate $\dot{R}$. The third time derivative is not needed since $\dot{R}$ does not appear in the metric. The mixed partials are found by taking the first and second radial derivative of (4.7), which gives

$$\dot{R}' = \frac{1}{\dot{R}} \left(\frac{M'}{R} + \frac{f'}{2} - \frac{MR'}{R^2} \right) \ , \tag{4.9}$$

and

$$\begin{aligned} \dot{R}'' = &-\frac{1}{2} \frac{(-2M''R + 2MR'' - f''R^2 - 2f'RR')}{R^{3/2}(2M + fR)^{1/2}} + \frac{3}{4} \frac{(-2M'R + 2MR' - f'R^2)\, R'}{R^{5/2}(2M + fR)^{1/2}} \\ &+ \frac{1}{4} \frac{(-2M'R + 2MR' - f'R^2)\,(2M' + f'R + fR')}{R^{3/2}(2M + fR)^{3/2}}, \end{aligned} \tag{4.10}$$

after some manipulation. Taking the partial derivative of (4.8) with respect to r then gives

$$\ddot{R}' = \frac{2MR'}{R^3} - \frac{M'}{R^2}, \tag{4.11}$$

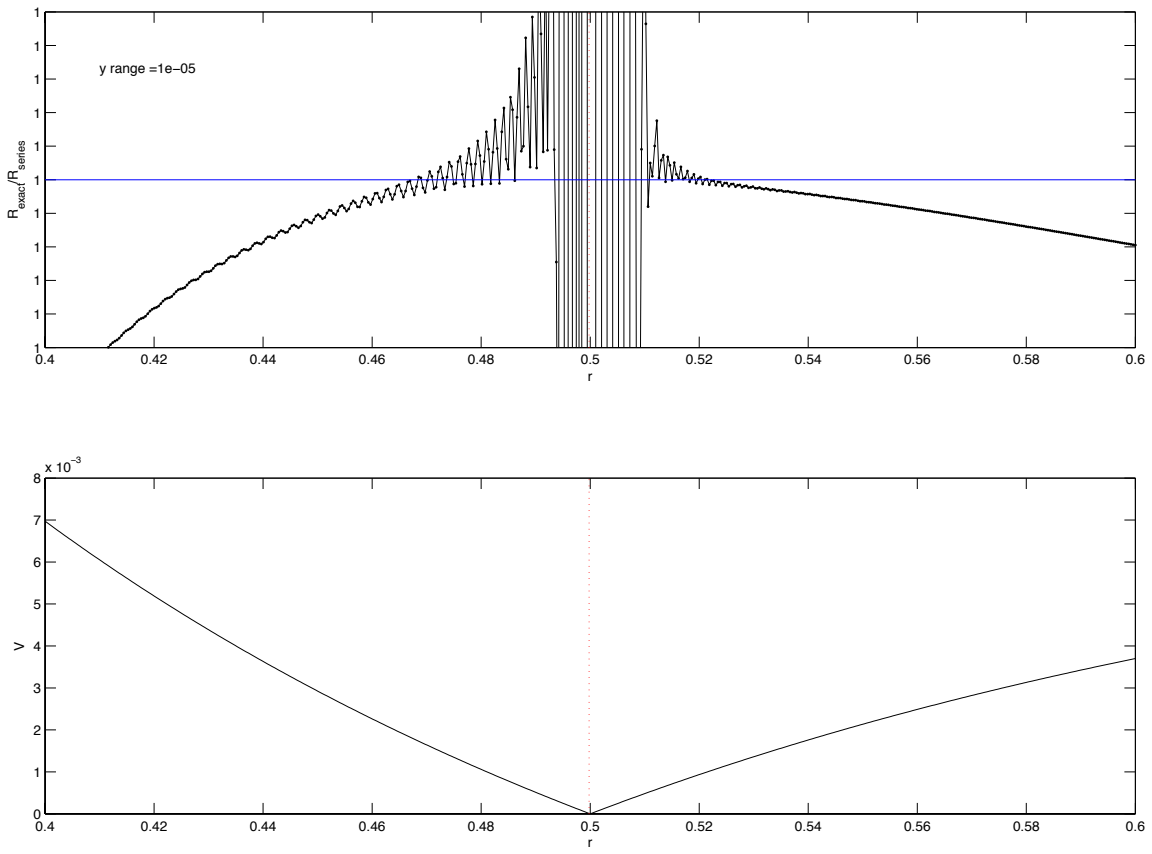

Fig. 4.2 **Comparison of a series expansion of R with the exact expression.** The top panel shows the ratio $R_{\text{exact}}/R_{\text{series}}$ for a model which has a parabolic borderline at $r = 0.5$. The wild oscillations around the borderline are due to cancellation of near identical terms in the exact expression for R. Some way away from the borderline, the slow divergence of $R_{\text{exact}}/R_{\text{series}}$ away from unity is due to the series expansion breaking down. Somewhere in between, where there is reasonable agreement, is the "sweet spot" which will define how fat a borderline to use. The bottom panel shows the corresponding value of V, which we can use for the near parabolic criterion.

which is still a relatively compact expression. Radial derivatives can be found from a useful expression for R' (2.13) which is also valid for all evolution types, however things begin to get messy. Taking the first and second radial derivative of (2.13), we find

$$\begin{aligned} R'' = &\left[\frac{M''}{M} - \frac{M'^2}{M^2} - \frac{f''}{f} + \frac{f'^2}{f^2}R + \frac{M'}{M} - \frac{f'}{f}\right] R' - \left[\left(\frac{M''}{M} - \frac{M'^2}{M^2} - \frac{3}{2}\frac{f''}{f} + \frac{3}{2}\frac{f'^2}{f^2}\right)(t-t_b)\right. \\ &\left. - \left(\frac{Mr'}{M} - \frac{3}{2}\frac{f'}{f}\right)t_b' + t_b''\right]\dot{R} - \left[t_b' + \left(\frac{M'}{M} - \frac{3}{2}\frac{f'}{f}\right)(t-t_b)\right]\dot{R}', \end{aligned} \tag{4.12}$$

and

$$\begin{aligned} R''' = &\left(\frac{M'''}{M} - 3\frac{M'M''}{M^2} + 2\frac{M'^3}{M^3} - \frac{f'''}{f} + 3\frac{f'f''}{f^2} - 2\frac{f'^3}{f^3}\right)R \\ &+ 2\left(\frac{M''}{M} - \frac{M'^2}{M^2} - \frac{f''}{f} + \frac{f'^2}{f^2}\right)R' + \left(\frac{M'}{M} - \frac{f'}{f}\right)R'' \\ &- \left[t_b''' + \left(\frac{M'''}{M} - 3\frac{M'M''}{M^2} + 2\frac{M'^3}{M^3} - \frac{3}{2}\frac{f'''}{f} + \frac{9}{2}\frac{f'f''}{f^2} - 3\frac{f'^3}{f^3}\right)(t-t_b)\right. \\ &\left. -2\left(\frac{M''}{M} - \frac{M'^2}{M^2} - \frac{3}{2}\frac{f''}{f} + \frac{3}{2}\frac{f'^2}{f^2}\right)t_b' - \left(\frac{M'}{M} - \frac{3}{2}\frac{f'}{f}\right)t_b''\right]\dot{R} \\ &- 2\left[t_b'' + \left(\frac{M''}{M} - \frac{M'^2}{M^2} - \frac{3}{2}\frac{f''}{f} + \frac{3}{2}\frac{f'^2}{f^2}\right)(t-t_b) - \left(\frac{M'}{M} - \frac{3}{2}\frac{f'}{f}\right)t_b'\right]\dot{R}' \\ &- \left[t_b' + \left(\frac{M'}{M} - \frac{3}{2}\frac{f'}{f}\right)(t-t_b)\right]\dot{R}''. \end{aligned} \tag{4.13}$$

All the above expressions (4.7) (4.8) (4.9) (4.10) (4.11) (2.13) (4.12) (4.13) are valid for all three evolution types, including NP regions, provided one uses the appropriate expression for R.

4.1.5 Derivatives of $E(r,p,q)$

The partial derivatives of E are straightforward to calculate from the definition (2.2). Using Mathematica we find the radial derivatives to be

$$E' = -\frac{(p-P)P'}{S} - \frac{(p-P)^2 S'}{2S^2} - \frac{(q-Q)Q'}{S} - \frac{(q-Q)^2 S'}{2S^2} + \frac{\epsilon S'}{2} \ , \tag{4.14}$$

$$\begin{aligned} E'' = {} & (p-P)\left(\frac{2P'S'}{S^2} - \frac{P''}{S}\right) + (p-P)^2\left(\frac{(S')^2}{S^3} - \frac{S''}{2S^2}\right) + \frac{(P')^2}{S} \\ & + (q-Q)\left(\frac{2Q'S'}{S^2} - \frac{Q''}{S}\right) + (q-Q)^2\left(\frac{(S')^2}{S^3} - \frac{S''}{2S^2}\right) + \frac{(Q')^2}{S} + \frac{\epsilon S''}{2} \ , \end{aligned} \tag{4.15}$$

$$\begin{aligned} E''' = {} & (p-P)\left(-\frac{P^{(3)}}{S} + \frac{3P''S'}{S^2} + P'\left(\frac{3S''}{S^2} - \frac{6(S')^2}{S^3}\right)\right) \\ & + (p-P)^2\left(-\frac{3(S')^3}{S^4} - \frac{S^{(3)}}{2S^2} + \frac{3S'S''}{S^3}\right) - \frac{3(P')^2 S'}{S^2} + \frac{3P'P''}{S} \\ & + (q-Q)\left(-\frac{Q^{(3)}}{S} + \frac{3Q''S'}{S^2} + Q'\left(\frac{3S''}{S^2} - \frac{6(S')^2}{S^3}\right)\right) \\ & + (q-Q)^2\left(-\frac{3(S')^3}{S^4} - \frac{S^{(3)}}{2S^2} + \frac{3S'S''}{S^3}\right) - \frac{3(Q')^2 S'}{S^2} + \frac{3Q'Q''}{S} + \frac{1}{2}S^{(3)}\epsilon \ . \end{aligned} \tag{4.16}$$

Since E is invariant under the redefinition $\{p,P\} \to \{q,Q\}$, so are the partial derivatives. To avoid unnecessary duplication, we show only the p derivatives. We find

$$\begin{aligned} E_{,p} &= \frac{p-P}{S} \\ E_{,pp} &= \frac{1}{S} \\ E'_{,p} &= -\frac{P'}{S} - \frac{(p-P)S'}{S^2} \ , \\ E'_{,pp} &= -\frac{S'}{S^2} \\ E''_{,p} &= (p-P)\left(\frac{2(S')^2}{S^3} - \frac{S''}{S^2}\right) - \frac{P''}{S} + \frac{2P'S'}{S^2} \end{aligned} \tag{4.17}$$

4.1.6 Dual Basis Components and Observables

Expressions for the observables described in §3.4.1 do not directly involve the propagated basis vectors, $\hat{e}^a_\alpha$, but rather their duals, $\hat{e}^\alpha_a$. Since these dual basis vectors must satisfy (3.8), in order to compute them numerically one must perform matrix inversion. This

quickly becomes computationally expensive if one wishes to calculate observables at every affine distance down a ray, and in all directions on the observer's sky. We avoid this by calculating the inverse of a general 4×4 matrix in Mathematica, and using result to write the dual basis components explicitly in terms of the original basis components. The expressions for each of the components of dual basis components are quite lengthy so we omit them here, but one can get an idea from the redshift expression. Assuming the emitter is co-moving with the coordinates ($u^a = \delta^a_t$), the redshift is just the $\hat{e}^\tau_t$ component of the dual. In terms of the original basis, we find

$$\begin{aligned}1+z =&(\hat{e}^r_\chi \hat{e}^q_\phi \hat{e}^p_\theta - \hat{e}^q_\chi \hat{e}^r_\phi \hat{e}^p_\theta - \hat{e}^r_\chi \hat{e}^p_\phi \hat{e}^q_\theta + \hat{e}^p_\chi \hat{e}^r_\phi \hat{e}^q_\theta + \hat{e}^q_\chi \hat{e}^p_\phi \hat{e}^r_\theta - \hat{e}^p_\chi \hat{e}^q_\phi \hat{e}^r_\theta)/(\hat{e}^q_\chi \hat{e}^t_\phi \hat{e}^r_\tau \hat{e}^p_\theta \\ &- \hat{e}^q_\chi \hat{e}^r_\phi \hat{e}^t_\tau \hat{e}^p_\theta - \hat{e}^p_\chi \hat{e}^t_\phi \hat{e}^r_\tau \hat{e}^q_\theta + \hat{e}^p_\chi \hat{e}^r_\phi \hat{e}^t_\tau \hat{e}^q_\theta - \hat{e}^q_\chi \hat{e}^t_\phi \hat{e}^p_\tau \hat{e}^r_\theta + \hat{e}^p_\chi \hat{e}^t_\phi \hat{e}^q_\tau \hat{e}^r_\theta + \hat{e}^q_\chi \hat{e}^p_\phi \hat{e}^t_\tau \hat{e}^r_\theta \\ &- \hat{e}^p_\chi \hat{e}^q_\phi \hat{e}^t_\tau \hat{e}^r_\theta + \hat{e}^t_\chi (\hat{e}^r_\phi \hat{e}^q_\tau \hat{e}^p_\theta - \hat{e}^q_\phi \hat{e}^r_\tau \hat{e}^p_\theta - \hat{e}^r_\phi \hat{e}^p_\tau \hat{e}^q_\theta + \hat{e}^p_\phi \hat{e}^r_\tau \hat{e}^q_\theta + \hat{e}^q_\phi \hat{e}^p_\tau \hat{e}^r_\theta - \hat{e}^p_\phi \hat{e}^q_\tau \hat{e}^r_\theta) \\ &+ \hat{e}^q_\chi \hat{e}^r_\phi \hat{e}^p_\tau \hat{e}^t_\theta - \hat{e}^p_\chi \hat{e}^r_\phi \hat{e}^q_\tau \hat{e}^t_\theta - \hat{e}^q_\chi \hat{e}^p_\phi \hat{e}^r_\tau \hat{e}^t_\theta + \hat{e}^p_\chi \hat{e}^q_\phi \hat{e}^r_\tau \hat{e}^t_\theta + \\ &+ \hat{e}^r_\chi (-\hat{e}^t_\phi \hat{e}^q_\tau \hat{e}^p_\theta + \hat{e}^q_\phi \hat{e}^t_\tau \hat{e}^p_\theta + \hat{e}^t_\phi \hat{e}^p_\tau \hat{e}^q_\theta - \hat{e}^p_\phi \hat{e}^t_\tau \hat{e}^q_\theta - \hat{e}^q_\phi \hat{e}^p_\tau \hat{e}^t_\theta + \hat{e}^p_\phi \hat{e}^q_\tau \hat{e}^t_\theta)) \end{aligned} \tag{4.18}$$

Fortunately much simplification is possible when the apparent motion is calculated. Applying the same method to the apparent motion (3.28), we find

$$\left.\frac{\mathrm{d}\tilde{\vartheta}}{\mathrm{d}\tilde{\tau}}\right|_o = \frac{-\hat{e}^r_\chi \hat{e}^q_\tau \hat{e}^p_\theta + \hat{e}^q_\chi \hat{e}^r_\tau \hat{e}^p_\theta + \hat{e}^r_\chi \hat{e}^p_\tau \hat{e}^q_\theta - \hat{e}^p_\chi \hat{e}^r_\tau \hat{e}^q_\theta - \hat{e}^q_\chi \hat{e}^p_\tau \hat{e}^r_\theta + \hat{e}^p_\chi \hat{e}^q_\tau \hat{e}^r_\theta}{\hat{e}^r_\chi \hat{e}^q_\phi \hat{e}^p_\theta - \hat{e}^q_\chi \hat{e}^r_\phi \hat{e}^p_\theta - \hat{e}^r_\chi \hat{e}^p_\phi \hat{e}^q_\theta + \hat{e}^p_\chi \hat{e}^r_\phi \hat{e}^q_\theta + \hat{e}^q_\chi \hat{e}^p_\phi \hat{e}^r_\theta - \hat{e}^p_\chi \hat{e}^q_\phi \hat{e}^r_\theta}. \tag{4.19}$$

and

$$\left.\frac{\mathrm{d}\tilde{\varphi}}{\mathrm{d}\tilde{\tau}}\right|_o = \frac{-\hat{e}^r_\chi \hat{e}^q_\phi \hat{e}^p_\tau + \hat{e}^q_\chi \hat{e}^r_\phi \hat{e}^p_\tau + \hat{e}^r_\chi \hat{e}^p_\phi \hat{e}^q_\tau - \hat{e}^p_\chi \hat{e}^r_\phi \hat{e}^q_\tau - \hat{e}^q_\chi \hat{e}^p_\phi \hat{e}^r_\tau + \hat{e}^p_\chi \hat{e}^q_\phi \hat{e}^r_\tau}{\hat{e}^r_\chi \hat{e}^q_\phi \hat{e}^p_\theta - \hat{e}^q_\chi \hat{e}^r_\phi \hat{e}^p_\theta - \hat{e}^r_\chi \hat{e}^p_\phi \hat{e}^q_\theta + \hat{e}^p_\chi \hat{e}^r_\phi \hat{e}^q_\theta + \hat{e}^q_\chi \hat{e}^p_\phi \hat{e}^r_\theta - \hat{e}^p_\chi \hat{e}^q_\phi \hat{e}^r_\theta}, \tag{4.20}$$

The function *redshift.m* was written to calculate (4.18), and *apparent_motion.m* to calculate (4.20) (4.19). Now the improvement becomes clear. These functions exploit MATLAB's ability to 'vectorise' calculations, so one can pass the output of the integrator (which is a 'vector' in MATLAB language) directly to the function, and the observables along a single line of sight are computed in parallel.

4.1.7 Propagating Near the Poles

It is clear from the last of (3.6) that the $\hat{\mathbf{e}}_{\hat{\varphi}}$ basis vector is degenerate at the poles of the observer's coordinates, where $\hat{\vartheta} = \{0, \pi\}$. This prevents numerical propagation at the pole. Moreover, near the pole $\hat{\mathbf{e}}_{\hat{\varphi}}$ becomes very small compared to the other propagated vectors. To avoid issues of integrating objects vastly different in magnitude,

with the same integrator tolerance, we decide to rescale the $\hat{\mathbf{e}}_{\hat{\varphi}}$ near the poles. We propagate

$$\hat{\mathbf{e}}_{\hat{\varphi}\mathrm{mod}} = \hat{\mathbf{e}}_{\hat{\varphi}} \sin^{-1}\hat{\vartheta}, \tag{4.21}$$

which is not small near the poles. The $\sin^{-1}\hat{\vartheta}$ correction is divergent at the poles, compensating for the small $\sin\hat{\vartheta}$ part in $\hat{\mathbf{e}}_{\hat{\varphi}}$. Then, once the basis are propagated, we remove the correction by multiplying by $\sin\hat{\vartheta}$ before calculating observables. Since this is a constant factor for each ray direction the numerical integration remains valid.

4.2 FLRW Background Setup

It will be useful specify a FLRW model for a couple of reasons. Firstly, for testing purposes. If we are to verify that the output of the program is correct, we need to compare it known analytic solutions, for which FLRW solutions are an obvious choice. Secondly, if we want to model some structure in the Universe, it may be desirable to first specify the background FLRW model, which gives an idea of scales and allows onto specify exact perturbations to the model in a meaningful way.

Choosing the metric functions to be (2.35) reduces the Szekeres metric (2.1) to the FLRW metric. Then, choosing an observer epoch, t_0, and the corresponding relative size of the scale factor, S_0, fully specifies the model. Essentially the energy content of the model are implied by specifying its expansion history. It is however not obvious what geometry will result from such a model setup procedure. Since we wish to experiment with various geometries, we choose to specify the model in terms of matter density fraction, Ω_m, and present day value of the Hubble parameter, H_0, instead of t_0 and S_0. The other parameters of the model are then [101]

$$\begin{aligned} \Omega_k &= 1 - \Omega_m, \\ k &= -\mathrm{sign}(\Omega_k) \\ s_0 &= \begin{cases} \text{arbitrary} & \text{if} \quad k = 0 \\ \frac{1}{H_0}\sqrt{\frac{-k}{\Omega_k}} & \text{if} \quad k \neq 0 \end{cases} \\ M_0 &= \Omega_m H_0^2 S_0^3/2 \end{aligned} \tag{4.22}$$

In contrast to [101], we find that the initial time is given by $t_0 = \frac{2}{3H_0}$ if and only if $k = 0$. For evolutions with $k \neq 0$ one must interpolate the value of η_0 in (2.6) (2.11) and then use that η_0 in (2.7) (2.12) to find t_0. In the elliptic case the evolution equation

(2.11) is symmetric about $\eta = \pi$, and thus the interpolation of η_0 on $[0, 2\pi]$ becomes degenerate. However, this is resolved by realising that the phase of evolution of such a model is related to the sign of H_0. If $H_0 > 0$ then the model is in the expansion phase, and $0 < \eta < \pi$ and conversely if $H_0 < 0$ the model is contracting and $\pi < \eta < 2\pi$. The initial time is then found by rearranging (2.12) and substituting in the FLRW metric functions (2.35), which gives

$$t_0 = M_0(\eta_0 - \sin\eta_0). \tag{4.23}$$

In the hyperbolic case we again need to define the spline curve over a compactified range, as in §4.1.2, by re-expressing (2.7) in terms of the parameter $T = \tanh\eta$. Now interpolation of T_0 on $[0, 1)$ is sufficient to cover all η values. Having determined the initial value T_0, the initial time can then be written

$$t_0 = M_0\left[\frac{T_0}{(1-T_0^2)^{1/2}} - \mathrm{acosh}((1-T_0^2)^{-1/2})\right]. \tag{4.24}$$

The function *rwsetup.m* was written to perform the calculations.

4.3 Verifying the Output

In order to verify that the program in working correctly, and that we can trust the output, we perform an number of consistency checks and convergence tests. Firstly we check that the output is self-consistent, agreeing with what we expect from our construction, and also that it is consistent with known analytic solutions. In general, solutions the propagation equations (3.10) (3.15) are highly non-trivial, and have not been solved analytically. analytic solutions against which to compare the output are limited to a few highly symmetric special cases of the Szekeres metric. Most notable in the cosmological context are the FLRW solutions, of which many can easily be solved analytically. However, care must be taken when working with components, as the FLRW special case of Szekeres is written in funny coordinates.

4.3.1 Consistency of $\mathbf{k}$ and $\hat{\mathbf{e}}_\chi$

Although $\mathbf{k}$ is propagated with (3.10) and $\hat{\mathbf{e}}_{\hat{\chi}}$ with (3.15), theoretically their solutions must be the same. We make this explicit in §A.2. Thus, by our construction both $\hat{\mathbf{e}}_\chi$ and $\mathbf{k}$ must be null everywhere along a ray, and their components equal. Some obvious consistency checks for the numerics, then, are to compute the magnitudes of $\hat{\mathbf{e}}_\chi$ and $\mathbf{k}$,

as well as the difference in their components, and ensure they are suitably small. That is

$$k^a g_{ab} k^b \lesssim \varepsilon, \quad \hat{e}^a_\chi g_{ab} \hat{e}^b_\chi \lesssim \varepsilon, \quad k^a - \hat{e}^a_\chi \lesssim \varepsilon, \tag{4.25}$$

where ε is the expected cumulative errors associated with the integrator. Should they be larger than this, it would signal an inconsistency between the solutions to (3.10) and (3.15). This is a useful self-consistency check for the program, as it can be done in any Szekeres model, even the highly inhomogeneous ones, where analytic solutions are not available for comparison. Once we verify the residual is suitably small, convergence can also be checked. Doing a number of runs of the program while holding all the input parameters fixed except for the integrator tolerance, allows one to see how the residuals scale. If they decrease with integrator tolerance this give some indication that propagation equations are consistent, and the solutions to them are approaching the correct result.

4.3.2 FLRW Checks

The FLRW special case is an obvious test to do since, analytic solutions to the propagation equations can be calculated explicitly, which allows one to check that the components of the propagated vectors are correct. We solve the propagation equations (3.10) (3.6) explicitly for the RW metric

$$ds^2 = -dt^2 + s(t)^2 \left(\frac{dr^2}{(1-kr^2)} + r^2\, d\Omega^2 \right) , \qquad d\Omega^2 = d\theta^2 + \sin^2\theta\, d\phi^2 , \tag{4.26}$$

by choosing the metric functions of the forms (2.35). For simplicity, we choose the observer to be at the centre $r = 0$; a more general result may be obtained by a displacement of the these simpler results. For the 3 RW cases, we list the scale factor, the incoming radial null vector, the past null geodesic path, the affine parameter χ, the redshift, and the diameter distance. The magnitude of the null vector k^a is set by

$[k^b h^a_b]_o = [k^b(\delta^a_b + u^a u_b)]_o = (0,1,0,0)$.

$$k=0: \qquad s = At^{2/3}\ , \quad A \text{ arbitrary} \tag{4.27}$$

$$\hat{r} = \frac{3}{A}\left(t_0^{1/3} - t^{1/3}\right) \tag{4.28}$$

$$k^a = \frac{K_0}{s}\left[-1, \frac{\sqrt{1-kr^2}}{s}, 0, 0\right] = \frac{K_0}{At^{2/3}}\left[1, \frac{-1}{At^{2/3}}, 0, 0\right] \tag{4.29}$$

$$\hat{\chi} = \frac{3A}{5K_0}\left\{t_0^{5/3} - t^{5/3}\right\} \tag{4.30}$$

$$K_0 = s_0 = At_0^{2/3} \tag{4.31}$$

$$1+z = \frac{t_0^{2/3}}{t^{2/3}} \tag{4.32}$$

$$d_D = 3t^{2/3}\left(t_0^{1/3} - t^{1/3}\right) \tag{4.33}$$

$$k=+1: \qquad s = A(1-\cos\eta)\ , \quad t = A(\eta - \sin\eta)\ , \quad A = \frac{\kappa\rho_0 s_0^3}{6} \tag{4.34}$$

$$\hat{r} = \sin(\eta_0 - \eta)\ , \quad t_0 = A(\eta_0 - \sin\eta_0) \tag{4.35}$$

$$k^a = \frac{K_0}{s}\left[-1, \frac{\cos(\eta_0-\eta)}{s}, 0, 0\right] = \frac{K_0}{A(1-\cos\eta)}\left[1, \frac{-\cos(\eta_0-\eta)}{A(1-\cos\eta)}, 0, 0\right] \tag{4.36}$$

$$\hat{\chi} = \frac{A^2}{2K_0}\Big\{3(\eta_0-\eta) + \sin\eta_0(\cos\eta_0 - 4) - \sin\eta(\cos\eta - 4)\Big\} \tag{4.37}$$

$$K_0 = s_0 = A(1-\cos\eta_0) \tag{4.38}$$

$$1+z = \frac{(1-\cos\eta_0)}{(1-\cos\eta)} \tag{4.39}$$

$$d_D = A(1-\cos\eta)\sin(\eta_0-\eta) \tag{4.40}$$

$$k=-1: \qquad s = A(\cosh\eta - 1)\ , \quad t = A(\sinh\eta - \eta)\ , \quad A = \frac{\kappa\rho_0 s_0^3}{6} \tag{4.41}$$

$$\hat{r} = \sinh(\eta_0 - \eta)\ , \quad t_0 = A(\sinh\eta_0 - \eta_0) \tag{4.42}$$

$$k^a = \frac{K_0}{s}\left[-1, \frac{\cosh(\eta_0-\eta)}{s}, 0, 0\right] = \frac{K_0}{A(\cosh\eta-1)}\left[1, \frac{-\cosh(\eta_0-\eta)}{A(\cosh\eta-1)}, 0, 0\right] \tag{4.43}$$

$$\hat{\chi} = \frac{A^2}{2K_0}\Big\{3(\eta_0-\eta) + \sinh\eta_0(\cosh\eta_0 - 4) - \sinh\eta(\cosh\eta - 4)\Big\} \tag{4.44}$$

$$K_0 = s_0 = A(\cosh\eta_0 - 1) \tag{4.45}$$

$$1+z = \frac{(\cosh\eta_0 - 1)}{(\cosh\eta - 1)} \tag{4.46}$$

$$d_D = A(\cosh\eta - 1)\sinh(\eta_0 - \eta) \tag{4.47}$$

In all cases, it is obvious that the angular deviation vectors are $\mathbf{e}_{\hat{\vartheta}} \propto \boldsymbol{\partial}_{\hat{\vartheta}}$, $\mathbf{e}_{\hat{\varphi}} \propto \boldsymbol{\partial}_{\hat{\varphi}}$, i.e.

$$e_{\hat{\vartheta}}{}^a = [0, 0, \Theta_0, 0] \ , \qquad \Theta_0 \text{ constant} \ , \tag{4.48}$$

$$e_{\hat{\varphi}}{}^a = [0, 0, 0, \Phi_0] \ , \qquad \Phi_0 \text{ constant} \ , \tag{4.49}$$

where $\Theta_0 = 1 = \Phi_0$ for $e_{\hat{\vartheta}}{}^a$ and $e_{\hat{\varphi}}{}^a$ to be standard observer-angle basis vectors, and we already have

$$e_{\hat{\chi}}{}^a = k^a = \frac{\hat{s}_0}{\hat{s}} \left[-1, \frac{\sqrt{1 - k\hat{r}^2}}{\hat{s}}, 0, 0 \right] \ . \tag{4.50}$$

The above deviation vectors (4.48)-(4.50) solve both forms of the null geodesic deviation equation (3.14) & (3.15) trivially. The $\hat{\tau}$ deviation vector, however, is not at all obvious. We find

$$e_{\hat{\tau}}{}^a = \left[\frac{s_0}{s} - \frac{\dot{s}_0 \int_t^{t_0} s \, dt}{s_0 s}, \sqrt{1 - kr^2} \left(\frac{1}{s_0^2} - \frac{s_0}{s^2} + \frac{\dot{s}_0 \int_t^{t_0} s \, dt}{s_0 s^2} \right), 0, 0 \right] \ , \tag{4.51}$$

and as required $e_{\hat{\tau}}{}^a \to u_o^a$ at the origin, where $\hat{t} = t_0$. Consequently, for the initial conditions on the χ derivatives, as $\chi \to 0$, we find

$$\frac{\mathrm{d}e_{\hat{\tau}}{}^a}{\mathrm{d}\hat{\chi}} \to \left[0, \frac{-\dot{s}_0}{s_0^2}, 0, 0 \right] \tag{4.52}$$

$$\frac{\mathrm{d}e_{\hat{\chi}}{}^a}{\mathrm{d}\hat{\chi}} \to \frac{\dot{\hat{s}}_0}{\hat{s}_0} \left[-1, \frac{2}{s_0}, 0, 0 \right] \tag{4.53}$$

$$\frac{\mathrm{d}e_{\hat{\vartheta}}{}^a}{\mathrm{d}\hat{\chi}} = [0, 0, 0, 0] \tag{4.54}$$

$$\frac{\mathrm{d}e_{\hat{\varphi}}{}^a}{\mathrm{d}\hat{\chi}} = [0, 0, 0, 0] \ . \tag{4.55}$$

Note that index a here indicates standard RW coordinates, so the above do not agree with (3.35), which are for Szekeres coordinates. Our numerical procedure for solving (3.15) should agree with these analytic solutions, (4.48)-(4.51), when the Szekeres arbitrary functions are set to (2.35). In practice it is easier to calculate the magnitudes

as functions of $\hat{\chi}$,

$$k^a g_{ab} k^b = e_{\hat{\chi}}{}^a g_{ab} e_{\hat{\chi}}{}^b = 0 \tag{4.56}$$

$$e_{\hat{\vartheta}}{}^a g_{ab} e_{\hat{\vartheta}}{}^b = \Theta_0^2 \hat{s}^2 \hat{r}^2 \tag{4.57}$$

$$e_{\hat{\varphi}}{}^a g_{ab} e_{\hat{\varphi}}{}^b = \Phi_0^2 \hat{s}^2 \hat{r}^2 \sin^2 \hat{\vartheta} \tag{4.58}$$

$$e_{\hat{\tau}}{}^a g_{ab} e_{\hat{\tau}}{}^b = \frac{\hat{s}^2}{\hat{s}_0^2} - 2 + \frac{2\hat{\dot{s}}_0}{\hat{s}_0^2} \int_{\hat{t}}^{t_0} s \, dt \ , \tag{4.59}$$

because this avoids transforming (4.48), (4.49) & (4.51) to an off-centre observer and then transforming to Szekeres coordinates. Similarly, our numerical calculations for d_D and z should agree with (4.32), (4.33), (4.39), (4.40), (4.46), & (4.47). Obviously we expect zero flow too,

$$\frac{\mathrm{d}\hat{\vartheta}}{\mathrm{d}\hat{\tau}} = 0 = \frac{\mathrm{d}\hat{\varphi}}{\mathrm{d}\hat{\tau}} \ . \tag{4.60}$$

However, there are also a few simple checks on directions as well. Referring to (3.33) for the FLRW-Szekeres case, a ray pointing away from the "origin" will be in the pure r direction, so a $\hat{\vartheta}$ displacement ($\hat{\mathbf{e}}_{\hat{\vartheta}}$) will be in the pure q direction, and $\hat{\varphi}$ displacement ($\hat{\mathbf{e}}_{\hat{\varphi}}$) will be in the pure p direction. For a ray along the p direction, a $\hat{\vartheta}$ displacement will be in the pure q direction, and $\hat{\varphi}$ displacement will be in the pure r direction. For a ray along the q direction, a $\hat{\vartheta}$ displacement will be in the pure r direction if $\hat{\varphi} = 0$, in the pure p direction if $\hat{\varphi} = \pi/2$. These relations should be preserved as one integrates outwards.

In addition, we numerically solve two versions of the FLRW radial null geodesic equation, and compare with the program output. This gives some idea of how efficient the numerical integration of the Szekeres equations are. Also, we expect these solutions to agree with the program output for an observer located away from origin, while some of the analytic solutions assume the observer is at the origin. The first pair of equations is obtained by expanding the null geodesic equation (3.10) into its individual components and substituting in the non-zero Christoffel symbols, which gives

$$\frac{dk^t}{d\chi} = -(k^r)^2 \left(\frac{s\dot{s}}{1 - kr^2} \right), \tag{4.61}$$

$$\frac{dk^r}{d\chi} = -2k^t k^r \left(\frac{\dot{s}}{s} \right) - (k^r)^2 \left(\frac{kr}{1 - kr^2} \right). \tag{4.62}$$

For the second pair we partially decouple (4.61) from (4.62) by substituting in the relation between dt and dr, obtained by setting $d\theta = d\phi = 0$ in the FLRW line element (4.26), essentially encoding that the path is radial. This gives

$$\frac{dk^t}{d\chi} = -(k^t)^2 \left(\frac{\dot{s}}{s}\right), \tag{4.63}$$

$$\frac{dk^r}{d\chi} = -(k^r)^2 \left[\frac{2\dot{s}(1-kr^2)^{1/2} + kr}{1-kr^2}\right]. \tag{4.64}$$

One can see that (4.63) is entirely decoupled from the r coordinate, however (4.64) is not decoupled from t, since it contains an $\dot{s}(t)$ term. For all of (4.61) - (4.64) we write the function *scalefactor.m* to return the value of $s(t)$ and its derivative.[3]

Clearly there is only one on-sky direction in the Szekeres model which will correspond to the purely radial direction in the FLRW special case. By examining the second of (3.34) one can see that by setting $(\hat{\theta}, \hat{\phi}) = (\pi/2, 0)$ will give a tangent vector, k^a, with only t and r components. This implies that, in the FLRW special case, the observer's coordinate system (hatted) is oriented in such a way that $(\hat{\theta}, \hat{\phi}) = (\pi/2, \pi)$ always points toward the origin.

4.3.3 LT Checks

Beyond FLRW, general analytic solutions to the propagation equations become highly non-trivial, and in the LT special case, for an arbitrary placed observer, such solutions are not known. Thanks to spherical symmetry of the model some consistency checks are possible. Any off-centre observer in any LT spacetime must see axial symmetry on the sky, with the axis of symmetry aligned with the direction of the origin. Thus, any observable or scalar quantity (not coordinate components) along any two rays separated by the same angle from the symmetry axis should be identical.

4.4 Results

4.4.1 Model Setups

Using the numerical code we have developed we simulate a few Szekeres model setups, which are listed below. These models are not intended to be realistic, but rather are used to check the program and start to explore how observations in Szekeres models

[3]Fat borderline equations must also be used for $s(t)$, see §4.1.3

appear. In all cases we check that the applicable shell crossing conditions are satisfied in the regions of interest. We use geometric units, in which time units are $T = 9.79$ Gyr, length units are $L = 3$ Gpc, and mass units are $M = 6.26 \times 10^{22}\ M_\odot$. In all of the cases below we choose the absolute tolerance of the integrator to be $= 10^{-12}$ and the relative tolerance $= 10^{-9}$.

Run #1a Spatially open FLRW special case of quasi-spherical Szekeres with S,P & Q constant. We choose metric functions given by (2.33) & (2.35) where M_0 is given by (4.22) with $H_0 = 72$ km.s.Mpc^{-1} and $\Omega_m = 0.8$. We place the observer near the origin, at $x^a = (1, 10^{-3}, 0, 0)$. We solve the propagation equations (3.10) (3.15) with $\{\hat{\vartheta}, \hat{\varphi}\} = \pi/2, 0$, corresponding to a ray directed in the increasing-r direction. In addition, we also solve FLRW radial null geodesics (4.61) (4.62) and (4.63) (4.64) numerically, and compare with the Szekeres results.

Run #1b Spatially open FLRW special case of quasi-spherical Szekeres with S,P & Q varying. We place the observer at $x^a = (0.96.1, 0, 0)$, and choose the metric functions and parameters as we did in run #1a, except for S, P & Q for which we choose the functional forms

$$S(r) = \frac{S_0 + S_\infty C_1 r}{1 + C_1 r}\ , \qquad P(r) = \frac{P_0 + P_\infty C_1 r}{1 + C_1 r}\ , \qquad Q(r) = \frac{Q_0 + Q_\infty C_1 r}{1 + C_1 r} \tag{4.65}$$

which allows us to choose the asymptotic values of each function easily. We choose parameter values to be

$$C_1 = 2.1, \quad S_0 = 1, \quad S_\infty = 9, \quad P_0 = 0, \quad P_\infty = 4, \quad Q_0 = 0, \quad Q_\infty = -2. \tag{4.66}$$

We place the observer at $x^a = (0.96, 1, 0.7, 5)$. Now the symmetry in $p - q$ coordinates is broken, but the observables should remain isotropic.

Run #1c FLRW special case of quasi-pseudo-spherical Szekeres with $\{S, P, Q\}$ variation. We choose metric functions of the form (2.36) and (4.65), and place the observer at $x^a = (1, 2, 0, 0)$. Now the constant-(t, r) 2-surfaces are hyperboloids of constant density. Again, the observables should remain isotropic.

Run #2a Spatially closed LT special case of quasi-spherical Szekeres with underdensity at $r = 0$. We place the observer at $x^a = (0.86, 0.3, 5, 0.7)$, and choose metric functions given by (2.33) and (2.35), except for $M(r)$, for which we choose the functional

form

$$M(r) = M_0 r^3 + \delta M(r) \ , \qquad \delta M(r) = \frac{C_2 r^3}{C_3 + C_4 r^3} \tag{4.67}$$

with parameter values

$$M_0 = \ 2.94, \quad C_2 = 100 \ , \quad C_3 = 1 \ , \quad C_4 = 10^5. \tag{4.68}$$

With this choice the mass perturbation is zero at the origin, goes like $\sim r^3$ near $r = 0$, and asymptotically approaches $C_2/C_4 = 10^{-3}$. The value of M_0 which defines the 'background' FLRW model is given by (4.22) with $H_0 = 72$ km.s.Mpc^{-1} and $\Omega_m = 1.5$.

Run #2b Spatially open LT special case of quasi-spherical Szekeres with overdensity. We choose the simulation parameters exactly as in run #2a, except with $\Omega_m = 0.85$.

Run #3a Quasi-spherical Szekeres with S, P, Q variation (no symmetry). We choose LT metric functions of the form

$$M(r) = \frac{r^3(M_0 + M_\infty C_5 r)}{1 + C_5 r} \ , \qquad f(r) = \frac{r^2(f_0 + f_\infty C_6 r)}{1 + C_6 r} \ , \qquad t_b(r) = \frac{t_{b0} + t_{b\infty} C_7 r^2}{1 + C_7 r^2} \tag{4.69}$$

with the parameters

$$\begin{gathered} C_5 = 2 \ , \quad C_6 = 1.6 \ , \quad C_7 = \ 1.8 \ , \\ M_0 = 10 \ , \quad M_\infty = 20 \ , \quad f_0 = 1 \ , \quad f_\infty = 3 \ , \quad t_{b0} = -1 \ , \quad t_{b\infty} = -2, \end{gathered} \tag{4.70}$$

and Szekeres metric functions as in (4.65) with the parameters (4.66) and $\epsilon = +1$.

Run #3b Quasi-pseudo-spherical Szekeres with S, P, Q variation (no symmetry). For this run we choose all the metric functions as in run #3a, except we investigate the case where space is foliated by hyperboloids, and thus we choose $\epsilon = -1$.

4.4.2 Discussion

The simulation runs described in the previous section are arranged into three distinct groups. All FLRW results are grouped in Run #1, LT results in Run #2 and fully inhomogeneous Szekeres results in Run # 3.

In Run #1a we compare analytic solutions with the results of integrating a single FLRW radial null geodesic, in both Szekeres and standard FLRW coordinates, and perform some consistency checks. We check magnitude of $\mathbf{k}$ and $\hat{\mathbf{e}}_{\hat{\chi}}$, shown in Figure 4.3, and verify they are both effectively null, as desired. We also verify that the components of $\mathbf{k}$ and $\hat{\mathbf{e}}_{\hat{\chi}}$ are consistent. Expressions for diameter distance and area distance are compared in Figure 4.4, and both agree, as expected for FLRW. The redshift is compared with analytics in Figure 4.5. After interpolation, the area distance vs. redshift relation is constructed, shown in Figure 4.6. All observables agree with analytic solutions, within the expected numerical error.

In Run #1b we extend the model from Run #1a by adding S, P & Q variation, and propagate 200 rays down the PNC, equally spaced in $(\hat{\vartheta}, \hat{\varphi})$[4], out to $z = 3$. On each ray we interpolate the observables on common redshift slices, and stack the results. The apparent motion vs. redshift relation for each ray, stacked and plotted in Figure 4.7, is numerically zero, as desired. The area distance vs. redshift relation, and residuals, are shown Figure 4.8. For all FLRW runs we find the residual error scales with the integrator tolerance. The results from Run #1c are qualitatively very similar to the previous FLRW runs, and so we omit the plot. However, since the coordinates are highly non-symmetric, this is a significant test of the full program suite.

In Run #2a we explore a LT model with a central void, that asymptotically approaches FLRW. We construct the "LT density contrast", $(\delta\rho = \rho_{LT}(r) - \rho_\infty)/\rho_\infty$, where ρ_∞ is the asymptotic LT density. This has approximately the same interpretation as in perturbation theory, since this model asymptotically approaches FLRW (no dipole variation), and so is useful for interpreting plots. In figure 4.9 we plot this quantity on five different slices of constant t, namely $t = t_0\{0.2, 0.4, 0.6, 0.8, 1\}$. The top panel is plotted as a function of radial coordinate, r, and the bottom as a function of the areal radius, $R(t, r)$, which can be related to physical units. In both plots we see that as time progresses (curves purple through black), the void evolves, expanding and becoming less dense. In this run we placed the observer at $r = 0.3$, which corresponds to the rightmost point in the top plot. The position of the observer varies with time in the bottom plot, corresponding to the rightmost point of each curve, marked with a cross. In the bottom panel we see that the void is ~ 1 Gpc away from the observer, on the spacelike $t = t_0$ hypersurface. The density along each line of sight is shown at the top of Figure 4.10, and the relative difference between each ray and a reference ray is shown below it. The reference ray is directed toward the pole of the observer's

[4]This choice does not equally space rays over the 2-sphere, but rather, it prefers the poles. This is not desirable, but sufficient for our current needs. We leave for future work to implement an algorithm which equally spaces rays over the observer's celestial sphere

coordinates, and so it only sees the FLRW background density. Thus the relative difference can be thought of as a density contrast, as before. The bottom of figure 4.10 has a feature at $z \approx 0.5$, where some rays begin to pass though a compensating overdensity and then the central under-density. Those rays that are directed closer toward the origin feel the void 'sooner' and for longer, as one might expect for a central feature. The area distance redshift relation for each line of sight is shown at the top of figure 4.11. The bottom panel shows the difference between each ray and a reference ray near the pole (which should behave close to one in a FLRW background). The features echo those in the plot of the density, except this a cumulative effect. The ray which passes deepest through the void shows the biggest deviation even after it has exited the void. In the language of perturbation theory, this would include effects like gravitation redshift and magnification. One can see the area distance is affected at the percent level, by a void that reaches a density contrast of $\delta\rho \approx -0.2$ at late times. The apparent motion is shown in figure 4.12, with the $\hat{\vartheta}$-motion in top panel, and the $\hat{\varphi}$-motion in the bottom. Both plots also show features induced by the void. The most affected rays have tangential flow rates reaching 1.5 miliarcseconds per year at a redshift around $z \approx 0.6$, and then decreasing as the rays pass beyond the void into the FLRW "background". The flow does not go away entirely however, as it is also an integrated effect. The evolution of intervening structure will affect the light path, and thus the apparent motion of a source. Figure 4.13 shows full sky maps of the area distance on two redshift slices, namely $z = 0.3$ and $z = 0.7$. In both slices (and all others not shown) we see axial symmetry on the sky, as expected for an off centre observer in a spherically symmetric spacetime. As in figure 4.11, we see the effect of the void is to increase the area distance for a given redshift. The apparent motion on the same two slices is shown in figure 4.14. Again, we see axial symmetry, as expected. The flow that is diverging away from the axis of symmetry is associated with the expanding void, which confirms what we expect to see. Further away there is flow toward the axis of symmetry. This is due to the observer having a slight motion relative to the background.

Moving beyond spherical symmetry, we investigate some Szekeres models with dipole variation. In run #3a we consider a strongly inhomogeneous quasi-spherical Szekeres model, where the spatial sections are foliated with 2-spheres which have a density dipole. The evolution of the LT-density is shown in figure 4.15 as a function of comoving radial coordinate (top), and areal radius (bottom). The observer is placed at $r = 1$, corresponding to the rightmost point in the top plot, and the crosses in the bottom plot. In both plots we see a central over-density that is expanding and

becoming less dense with cosmic time. This however does not show the structure of the inhomogeneity caused by the dipole variation. As we did for run #2a, we plot the line of sight density, figure 4.15, area distance, figure 4.17 and apparent motion, figure 4.18, as a function of redshift. We see that some rays pass through some relatively overdense regions. Also, there is some considerable cosmic flow across the sky, with the apparent motion reaching tens of arcseconds per year. The observer's sky maps of the area distance, figure 4.19 and apparent motion, figure 4.20, both show asymmetric structure, as we expect for a Szekeres model with $\{S, P, Q\}$ variation. At $z = 1$ the area distance looks like its close to spherical symmetry, with a small off-axis structure, but by $z = 3$ the intervening inhomogeneity has produced a large crescent shape in the map. The divergent flow pattern around the central axis is due to the central overdensity that is expanding, but it also contains some substructure due to the inhomogeneity. The flow at the very centre is not symmetric. All these seem consistent with what one might expect to see in a Szekeres model. For a more intuitive picture of the LT and Szekeres runs, see the schematics in figure 4.21. In these we contrast the spherically symmetric LT results with the $\epsilon = +1$ Szekeres models. Deviations away from spherical symmetry cause an off-centre observer to no longer see axial symmetry on the sky, with flow towards the overdensy is enhanced. The results from run #3b are qualitatively very similar to those of #3a and so we do not show them here.

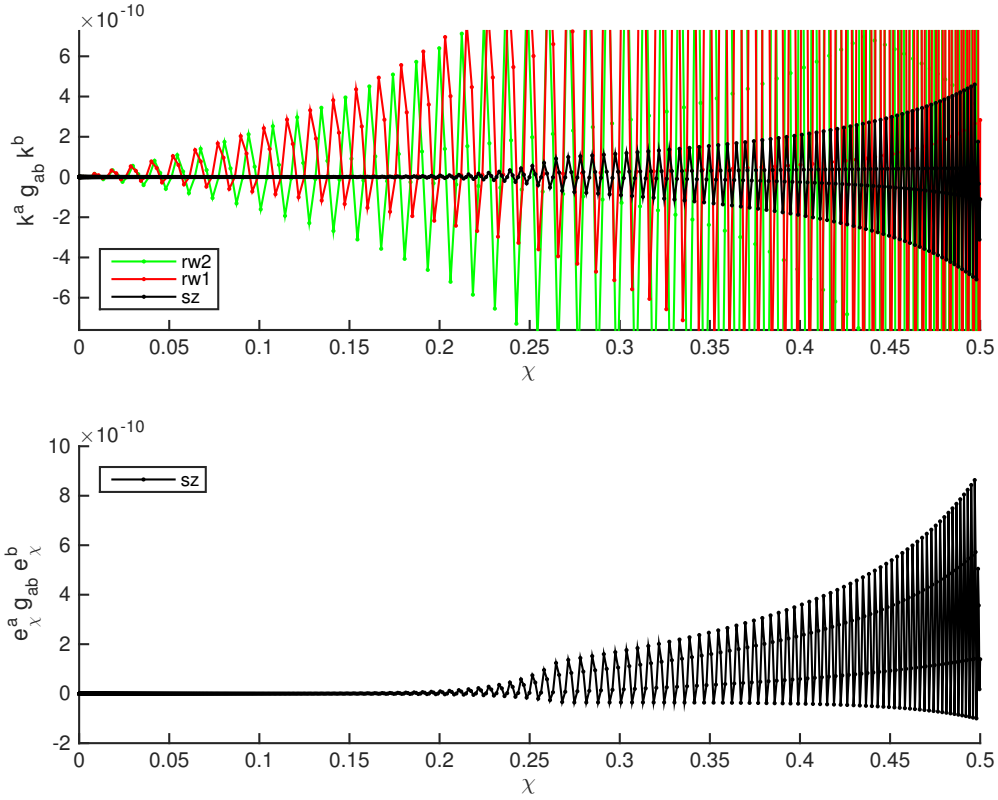

Fig. 4.3 **Magnitude of k and $\hat{\mathbf{e}}_{\hat{\chi}}$ from Run#1a** The top panel shows the nullness/magnitude of **k** versus $\hat{\chi}$, for three different forms of the null geodesic equation, along a single line of sight. The red and green curves are the result of numerically integrating (4.61) (4.62) and (4.63) (4.64), respectively, and the black curve is the result from (3.10) with (2.1). In all cases the integrator tolerance was set to the same values. All curves have growing oscillations about zero, but the solution in Szekeres coordinates does a better job of staying null. The bottom panel shows the nullness of $\hat{\mathbf{e}}_{\hat{\chi}}$, which also has growing modes. All the curves however remain within the expected cumulative error of the integrator.

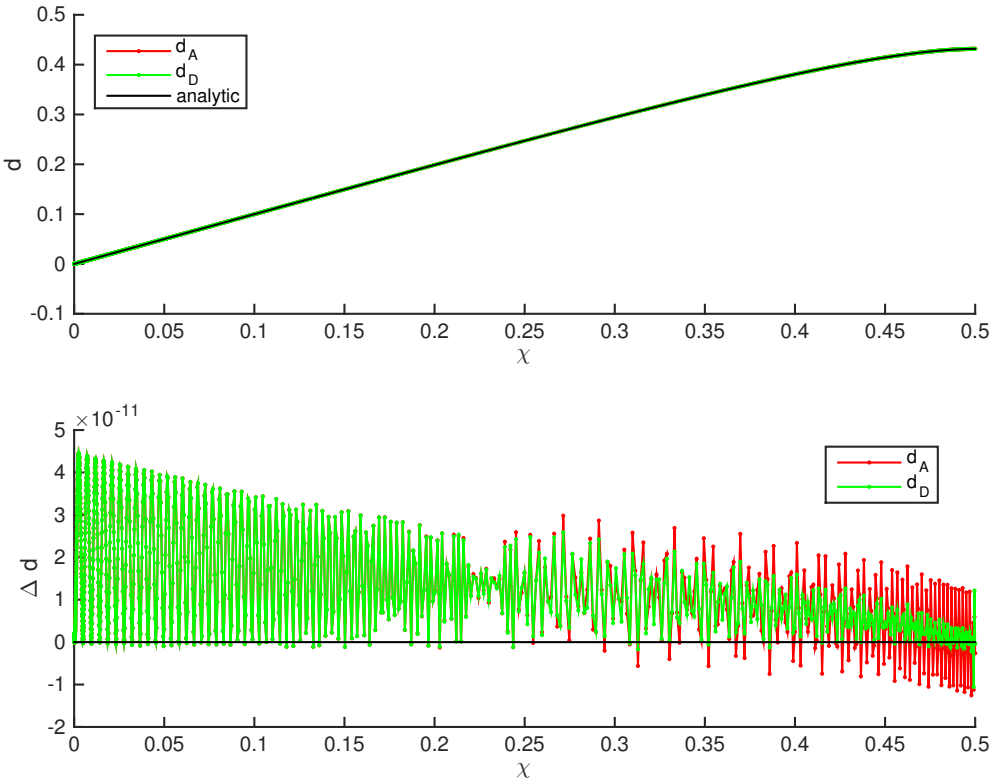

Fig. 4.4 **Distance Measures from Run#1a** Top panel shows the both the area distance (red curve) and diameter distance (green curve) alongside the FLRW analytic solution (4.47), for a single radially directed ray. The curves are indistinguishable. As expected in FLRW, the area distance and the diameter distance are identical. The bottom panel shows the difference between the numerical results and the analytic solution. Numerical errors in both solutions are well within the integrator tolerance.

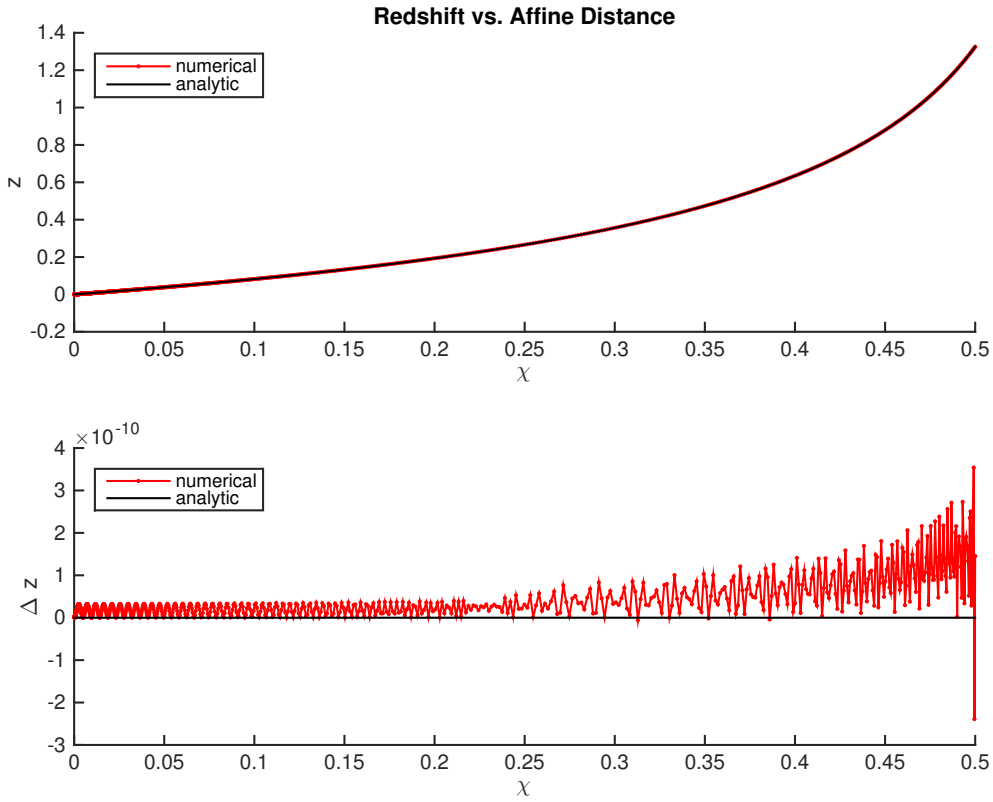

Fig. 4.5 **Redshift from Run#1a** The top panel shows the redshift versus $\hat{\chi}$ for a single radially directed ray. The red curve is the numerical result from (4.18), and the black is the analytic solution (4.46). Redshift begins to grow rapidly with $\hat{\chi} \gtrsim 0.35$. The difference between the two curves is plotted below. The numerical error oscillated on one side of the analytic solution, and begins to grow around $\hat{\chi} \gtrsim 0.25$, but remains within the tolerance of the integrator.

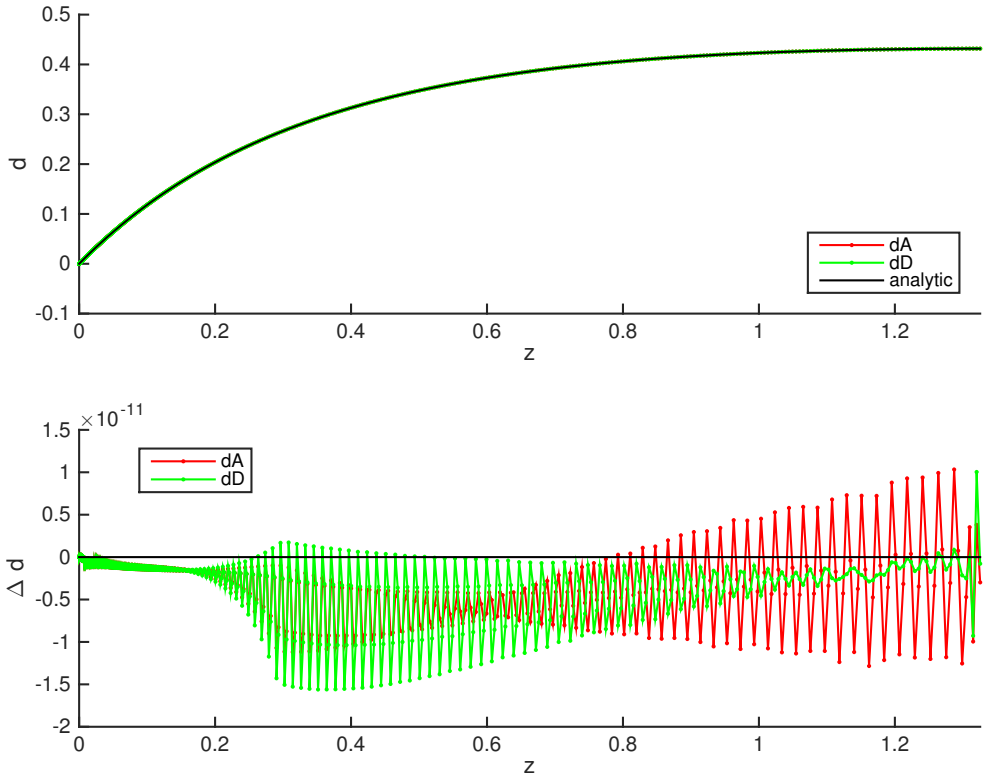

Fig. 4.6 **Distance-Redshift Relation from Run#1a** The top panel shows comparison of the area distance and the diameter distance plotted against redshift. As expected in FLRW, they agree with each other. And the residuals are acceptably small.

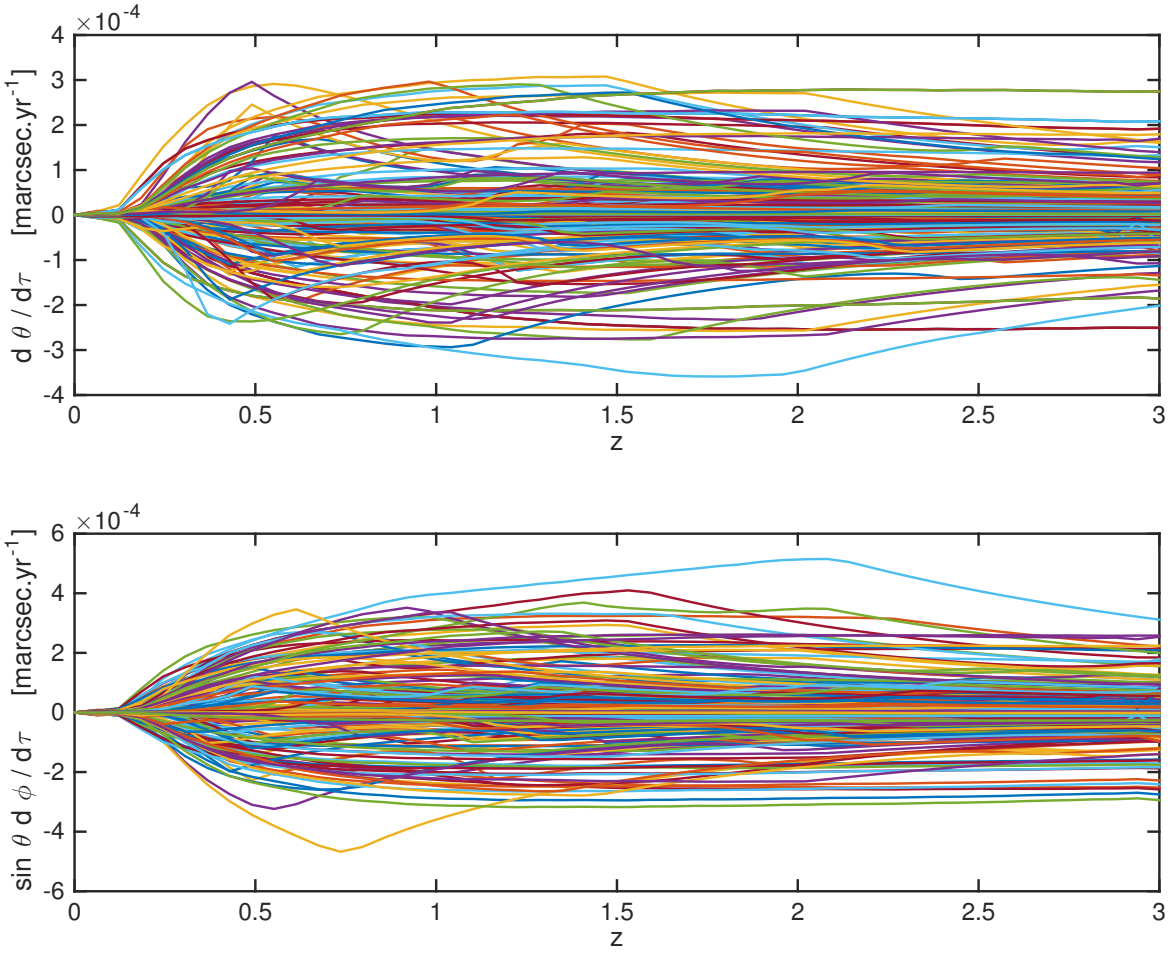

Fig. 4.7 **Apparent Motion versus Redshift Run #1b** The *top panel* shows the dA vs. z for all 200 lines of sight from Run #1b. Lines are coincident, as expected in FLRW spacetime. The *bottom panel* shows the difference between these and the analytic solution. All error are within the relative tolerance of the integrator, and scale accordingly.

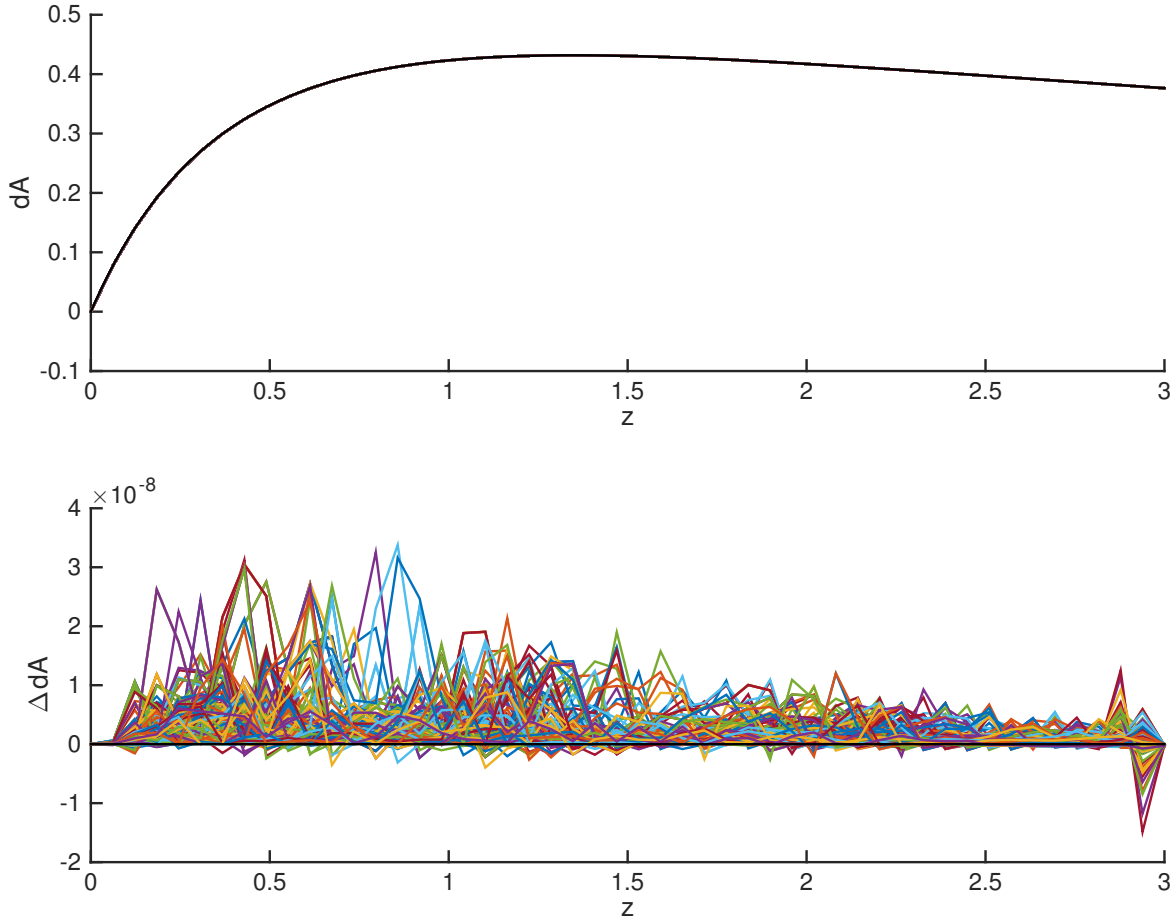

Fig. 4.8 **Area Distance versus Redshift from Run #1b** *Top panel* shows the dA vs. z for all 200 lines of sight from Run #1b. Lines are coincident, as expected in FLRW spacetime. The *bottom panel* shows the difference between these and the analytic solution. All error are within the relative tolerance of the integrator, and scale accordingly.

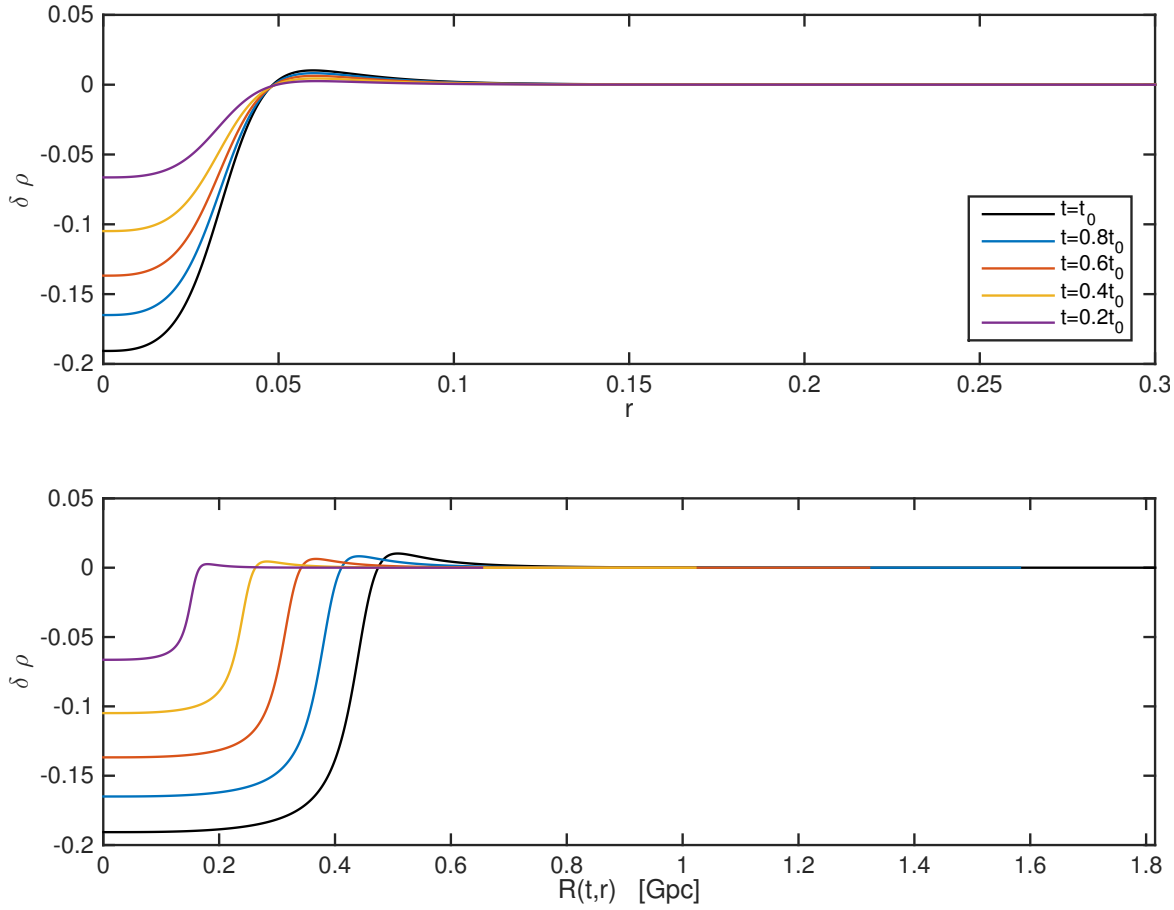

Fig. 4.9 **Late time density contrast from Run #2a** The top panel show the LT density contrast at $t = t_0$ as a function of comoving radial coordinate, and the bottom panel shows the same as a function of areal radius. In this run we place the observer at $r = 0.3$, corresponding to the rightmost point in the top plot, and the right end of each curve in the bottom plot

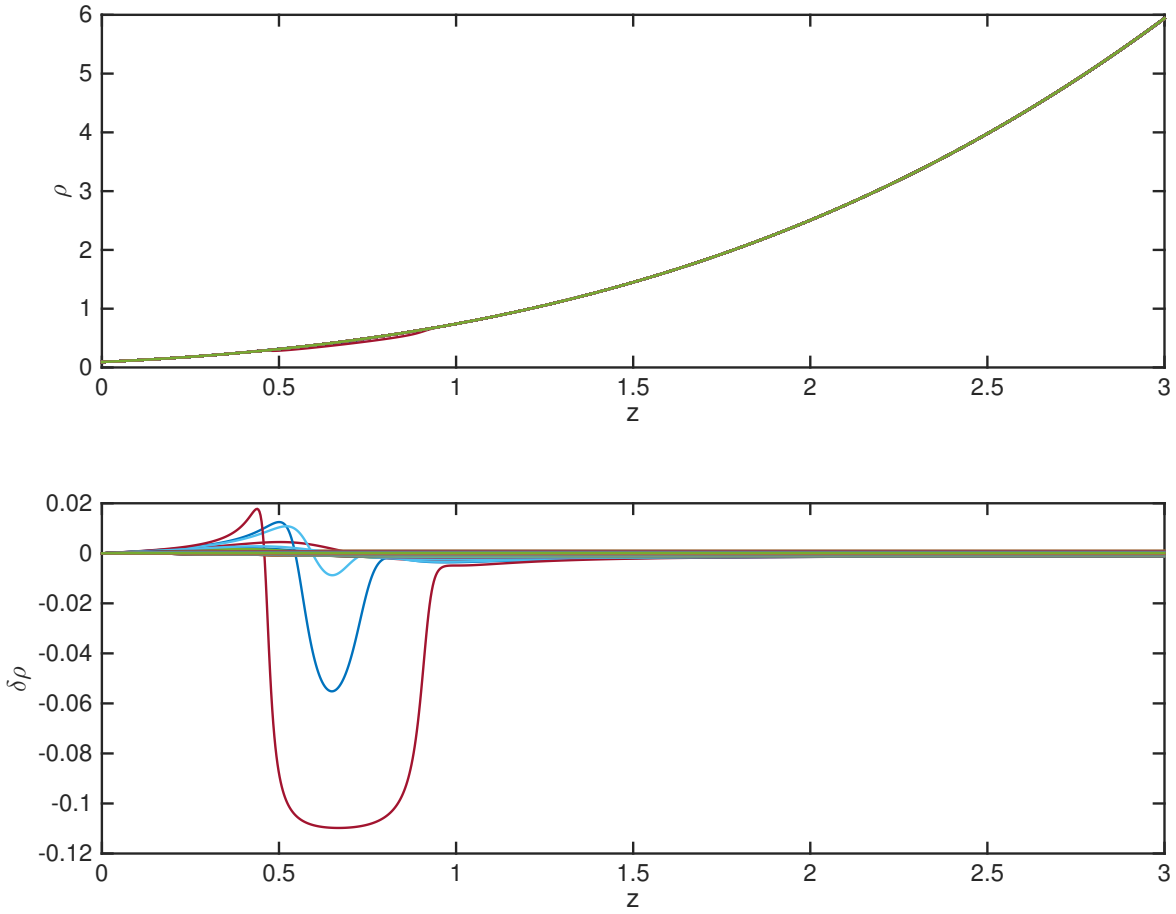

Fig. 4.10 **Line of sight density from Run#2a** Top panel shows the density along each line of sight, and the bottom plot shows the relative difference between each ray and a reference ray near the pole. A few rays pass through a under-dense region near $r = 0$. This can be seen in the bottom plot at $z \approx 0.6$. The reference ray does not see the void, since its toward the pole, and thus the density along its line of sight is approximately the FLRW background density. This means the $\delta\rho$ has the standard cosmological interpretation, approximately.

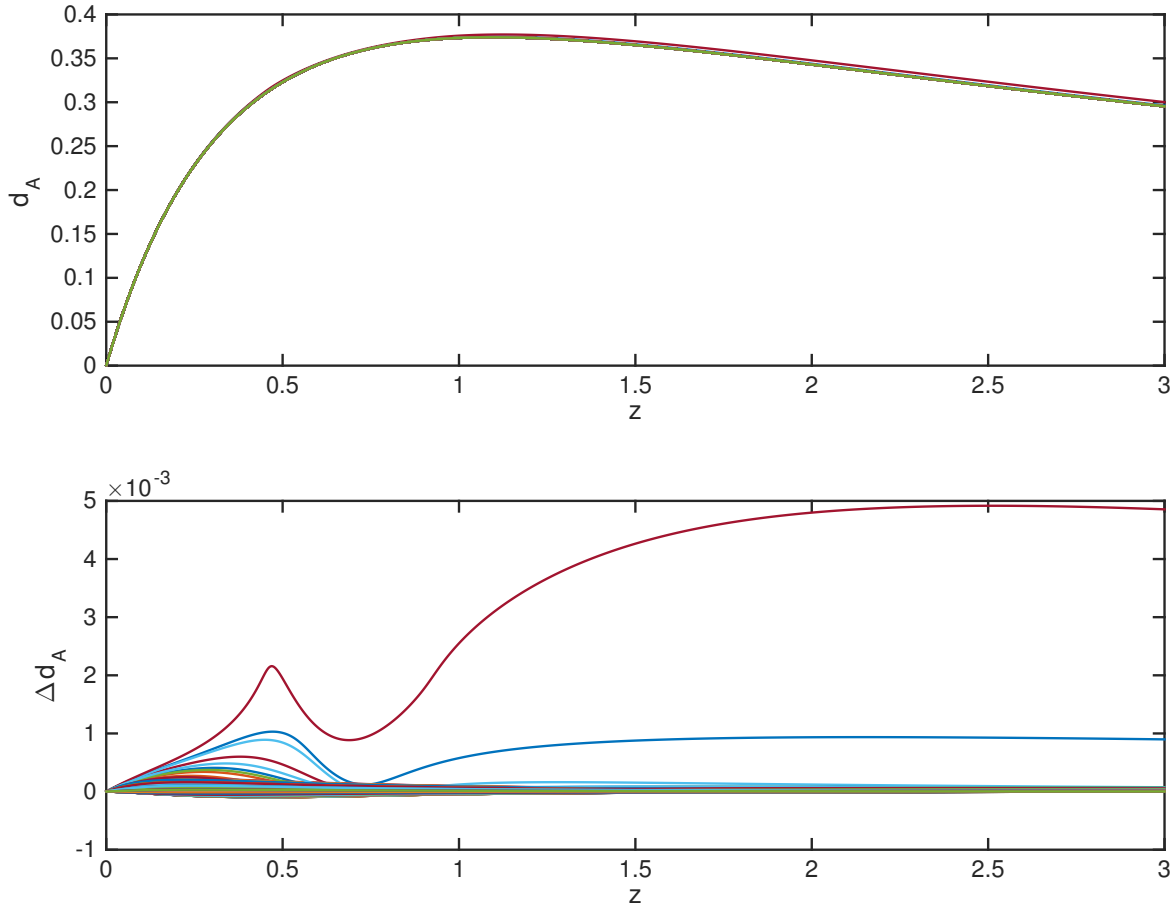

Fig. 4.11 **Area distance from Run#2a** Top panel shows the area distance vs. redshift and the bottom plot shows the difference between each ray and a reference ray near the pole. Some of the ray pass through an under-dense region. This feature can be seen in the bottom plot at $z \approx 0.6$.

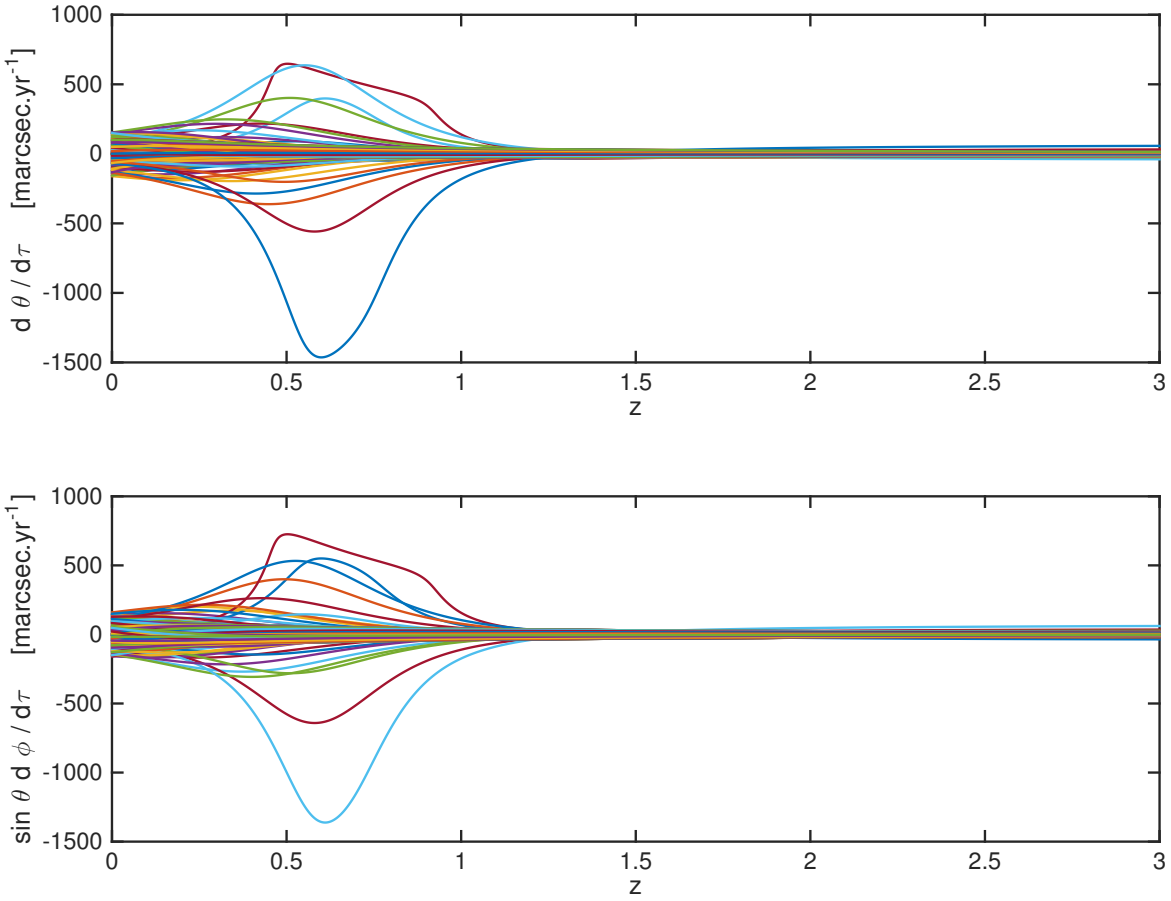

Fig. 4.12 **Apparent from Run#2a** The top panel shows the motion in the $\hat{\vartheta}$-direction and the bottom panel show the notion in the $\hat{\varphi}$-direction. The feature in Figures 4.10 and 4.11 can be seen in the both plots at $z \approx 0.6$. This corresponds to flow away from the centre of the void. At its maximum, the flow rate reaches ~ 1.5 arcseconds per year.

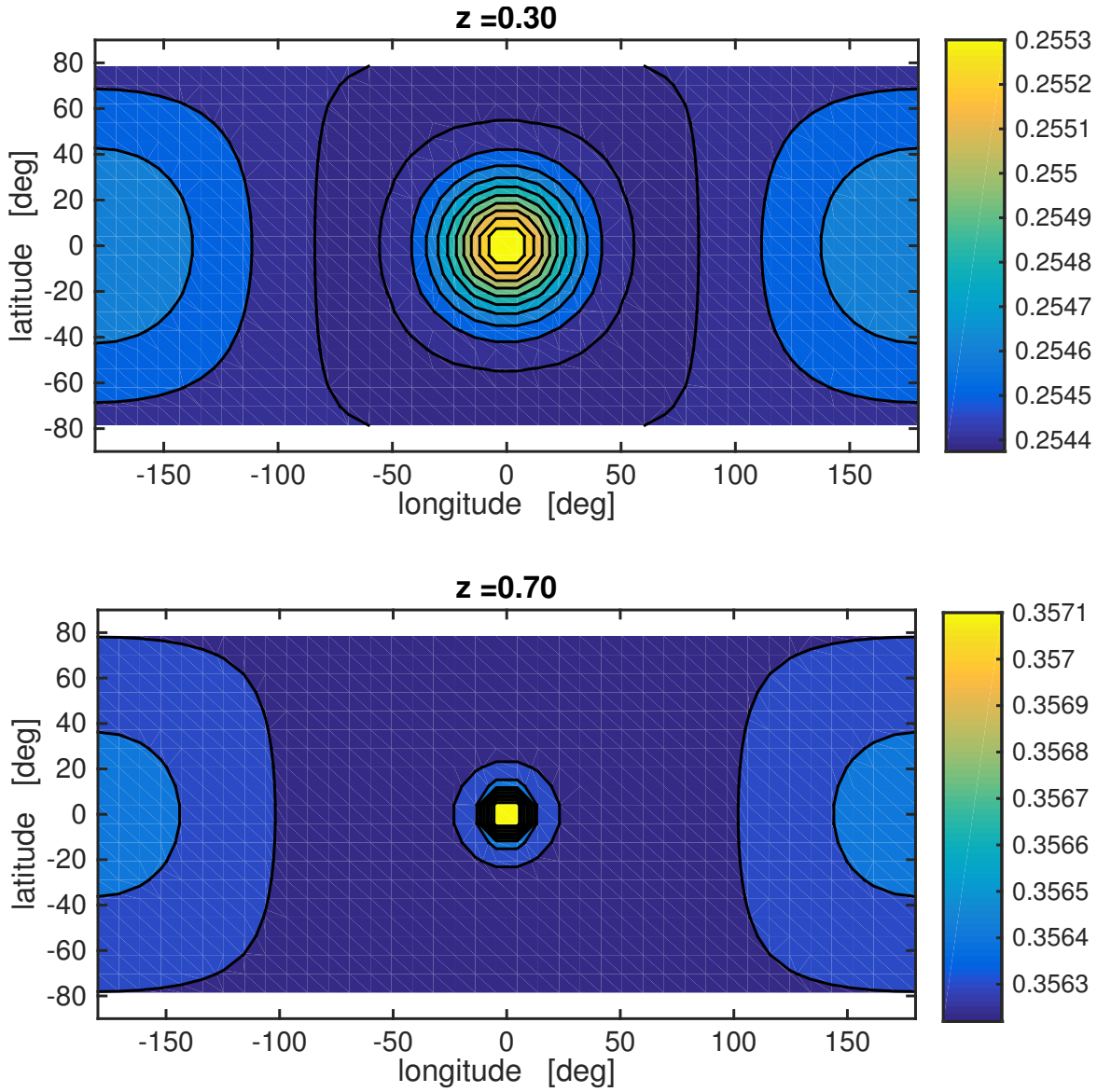

Fig. 4.13 **Redshift slice of area distance from Run#2a**Top panel shows the area distance over the observer's sky, at $z = 0.3$, and the bottom shows the same at $z = 0.7$. The observer's $(\hat{\vartheta}, \hat{\varphi})$ coordinates have been transformed to latitude and longitude with the $(0, 0)$ aligned with the decreasing r direction at the observer.

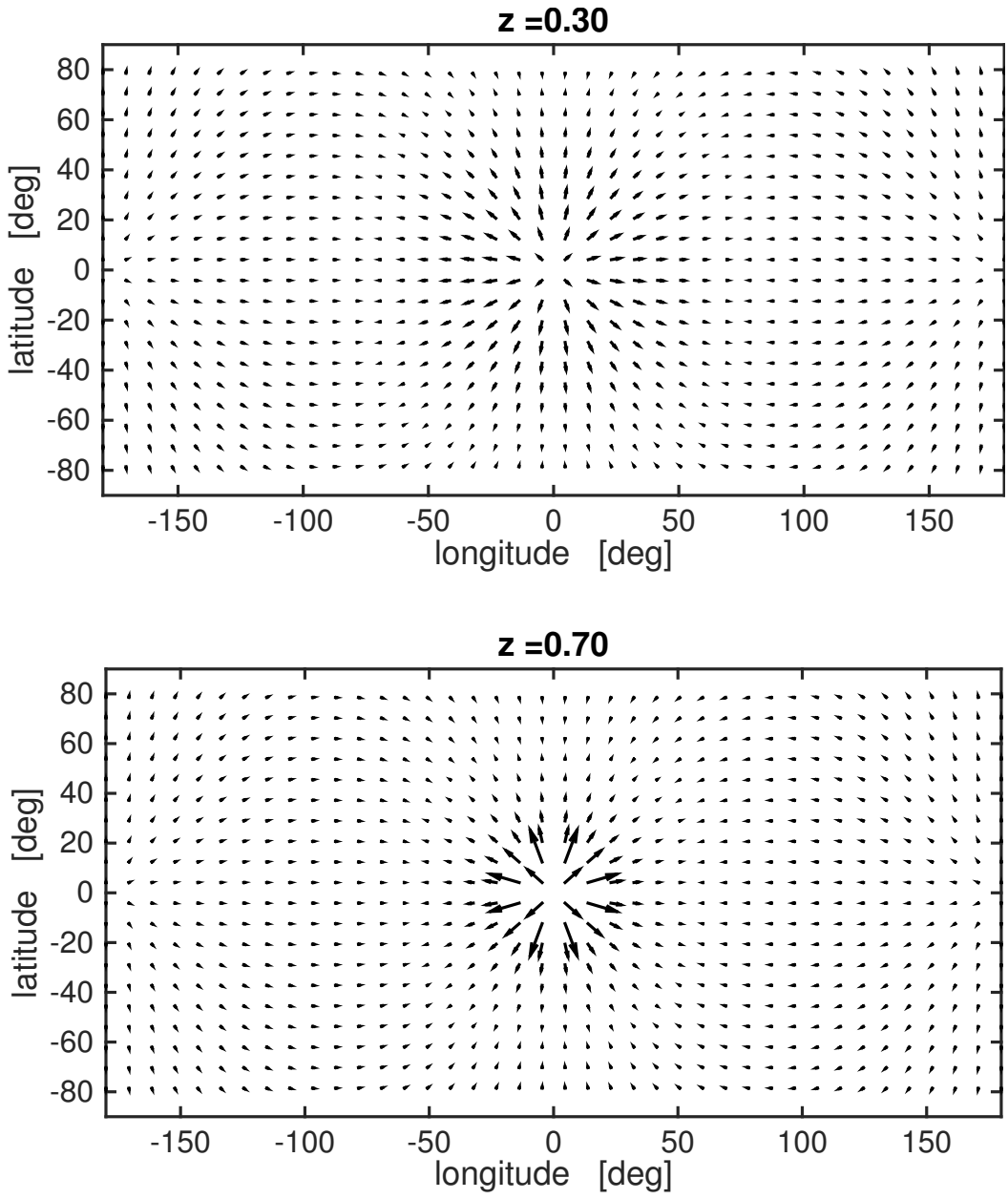

Fig. 4.14 **Flow pattern from Run#2a** Top panel shows the apparent motion over the observer's sky at $z = 0.3$, and the bottom shows the same at $z = 0.7$. The observer's $(\hat{\vartheta}, \hat{\varphi})$ coordinates have been transformed to latitude and longitude with the $(0, 0)$ aligned with the decreasing r direction at the observer.

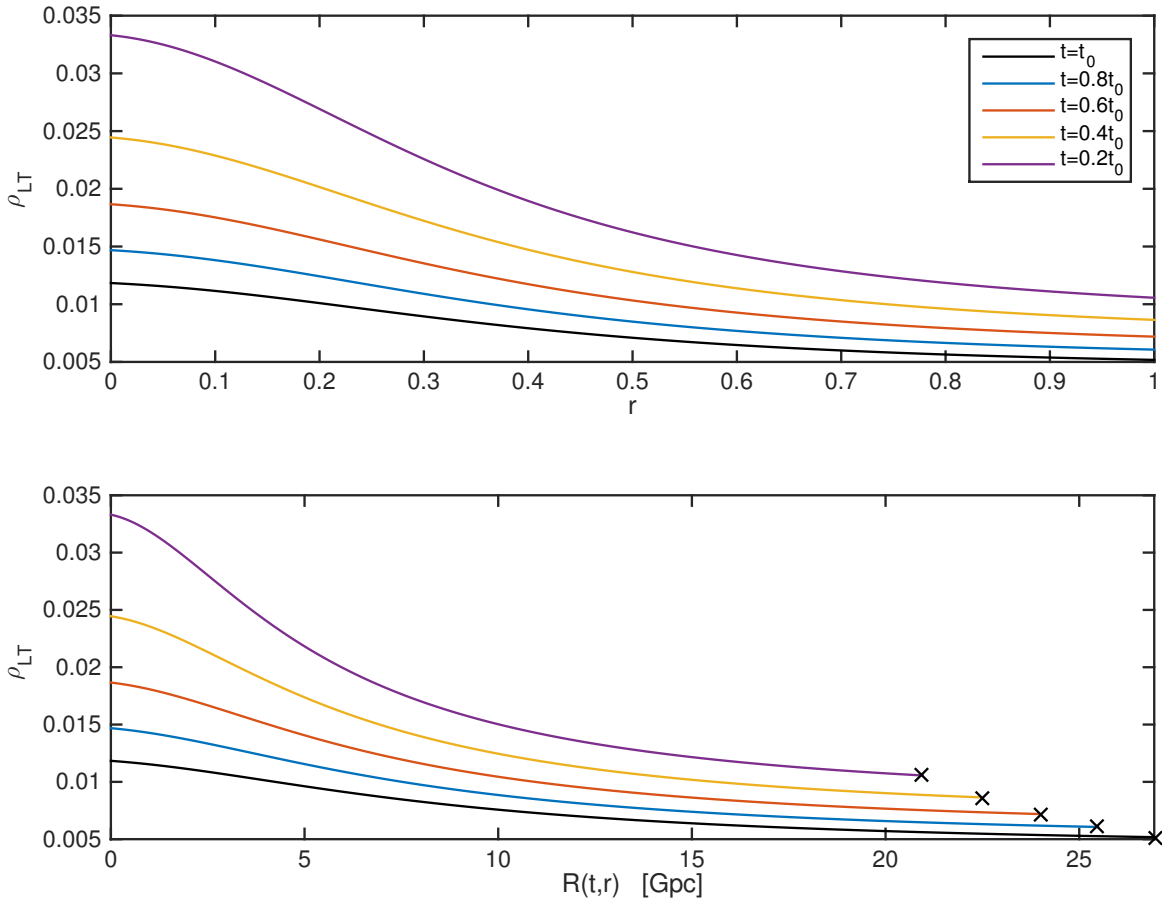

Fig. 4.15 **Late time density contrast from Run #3a** The top panel show the LT density contrast at $t = t_0$ as a function of comoving radial coordinate, and the bottom panel shows the same as a function of areal radius. In this run we place the observer at $r = 0.3$, corresponding to the rightmost point in both plots.

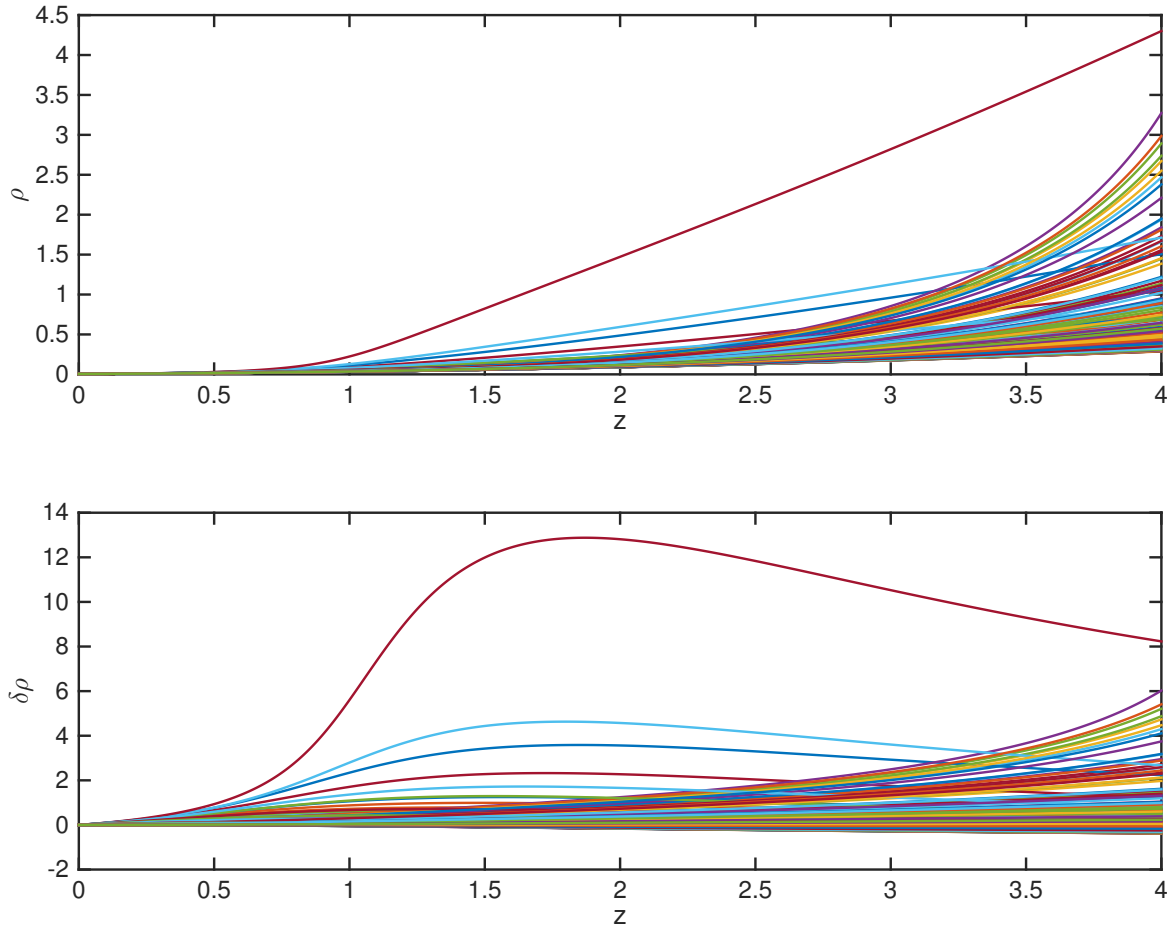

Fig. 4.16 **Line of sight density from Run#3a** Top panel shows the density along each line of sight, and the bottom plot shows the relative difference between each ray and a reference ray near the pole. A few rays pass through a under-dense region near $r = 0$. This can be seen in the bottom plot at $z \approx 0.6$. The reference ray does not see the void, since its toward the pole, and thus the density along its line of sight is approximately the FLRW background density. This means the $\delta\rho$ has the standard cosmological interpretation, approximately.

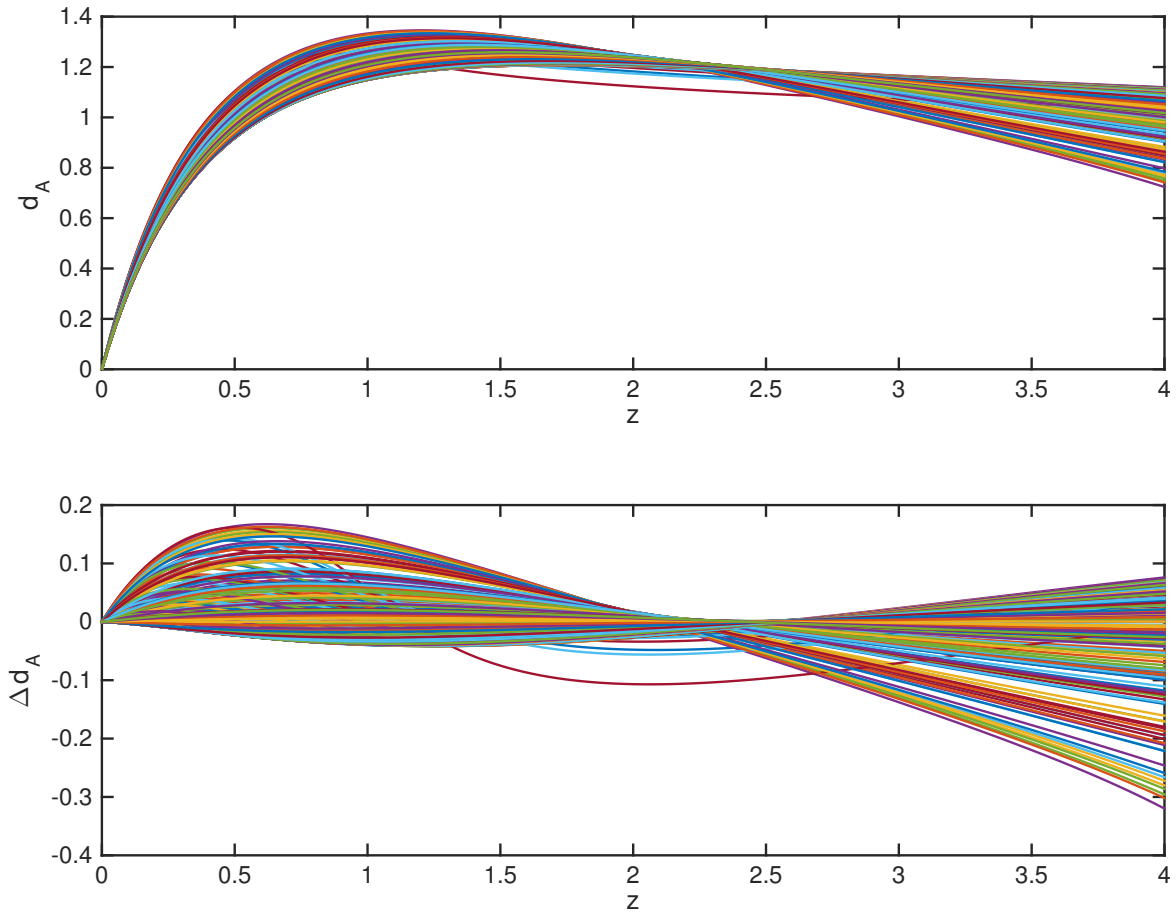

Fig. 4.17 **Area distance from Run#3a** Top panel shows the area distance vs. redshift and the bottom plot shows the difference between each ray and a reference ray near the pole. Some of the ray pass through an under-dense region. This feature can be seen in the bottom plot at $z \approx 0.6$.

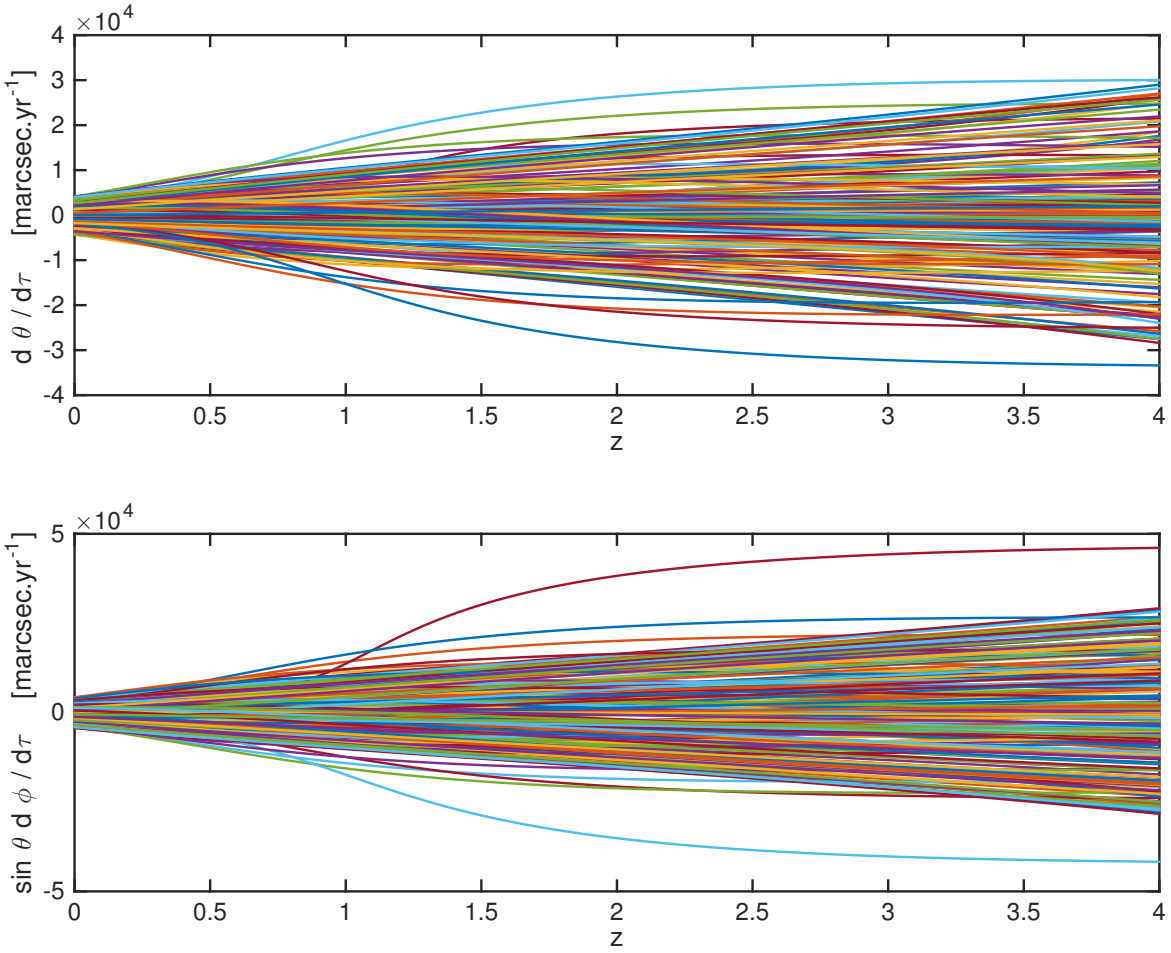

Fig. 4.18 **Apparent from Run#3a** The top panel shows the motion in the $\hat{\vartheta}$-direction and the bottom panel show the notion in the $\hat{\varphi}$-direction. The feature in Figures 4.10 and 4.11 can be seen in the both plots at $z \approx 0.6$. This corresponds to flow away from the centre of the void. At its maximum, the flow rate reaches ~ 1.5 arcseconds per year.

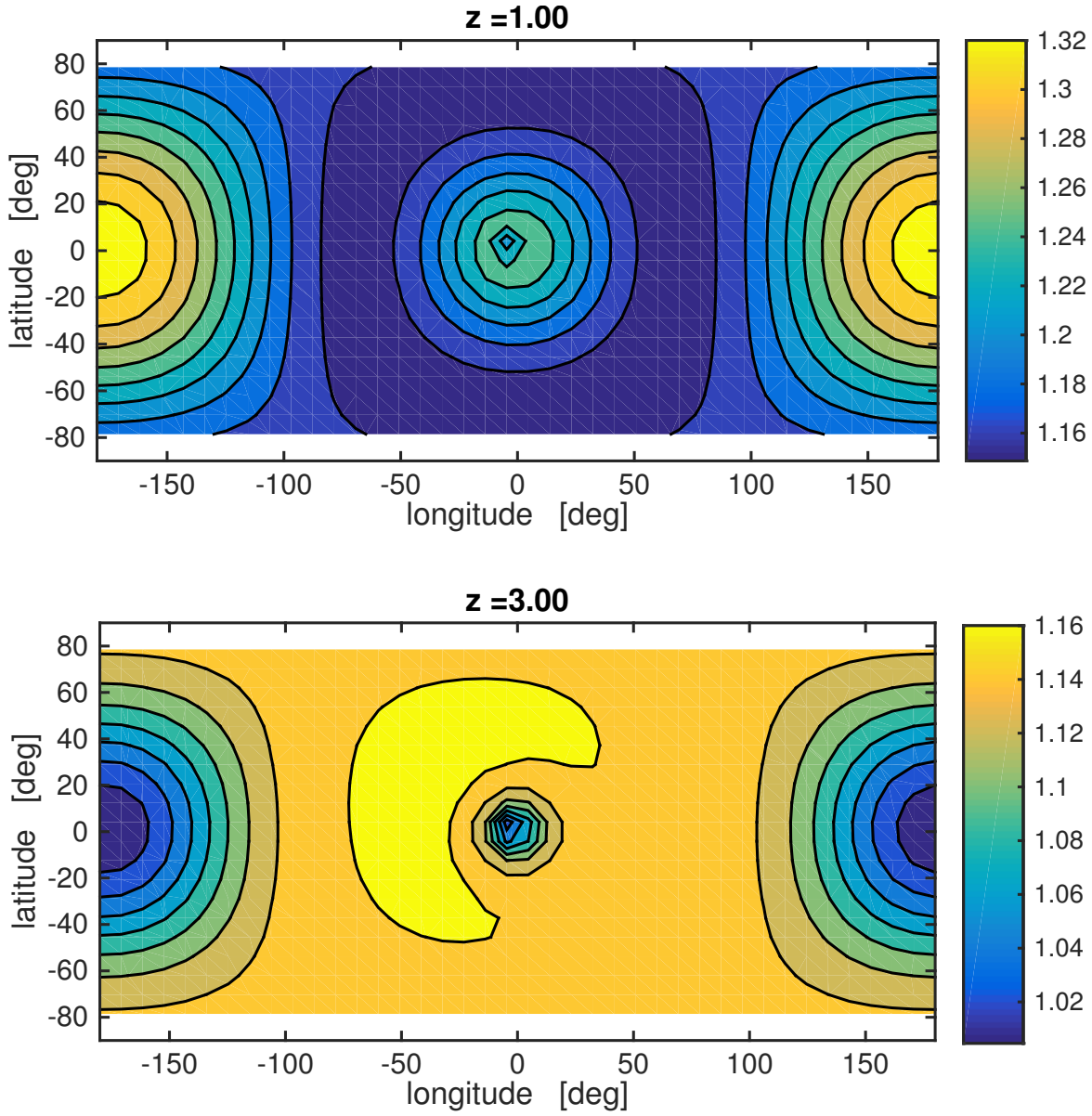

Fig. 4.19 **Redshift slice of area distance from Run#3a**Top panel shows the area distance over the observer's sky at $z = 0.3$, and the bottom shows the same at $z = 0.7$. The observer's $(\hat{\vartheta}, \hat{\varphi})$ coordinates have been transformed to latitude and longitude with the $(0, 0)$ aligned with the decreasing r direction at the observer.

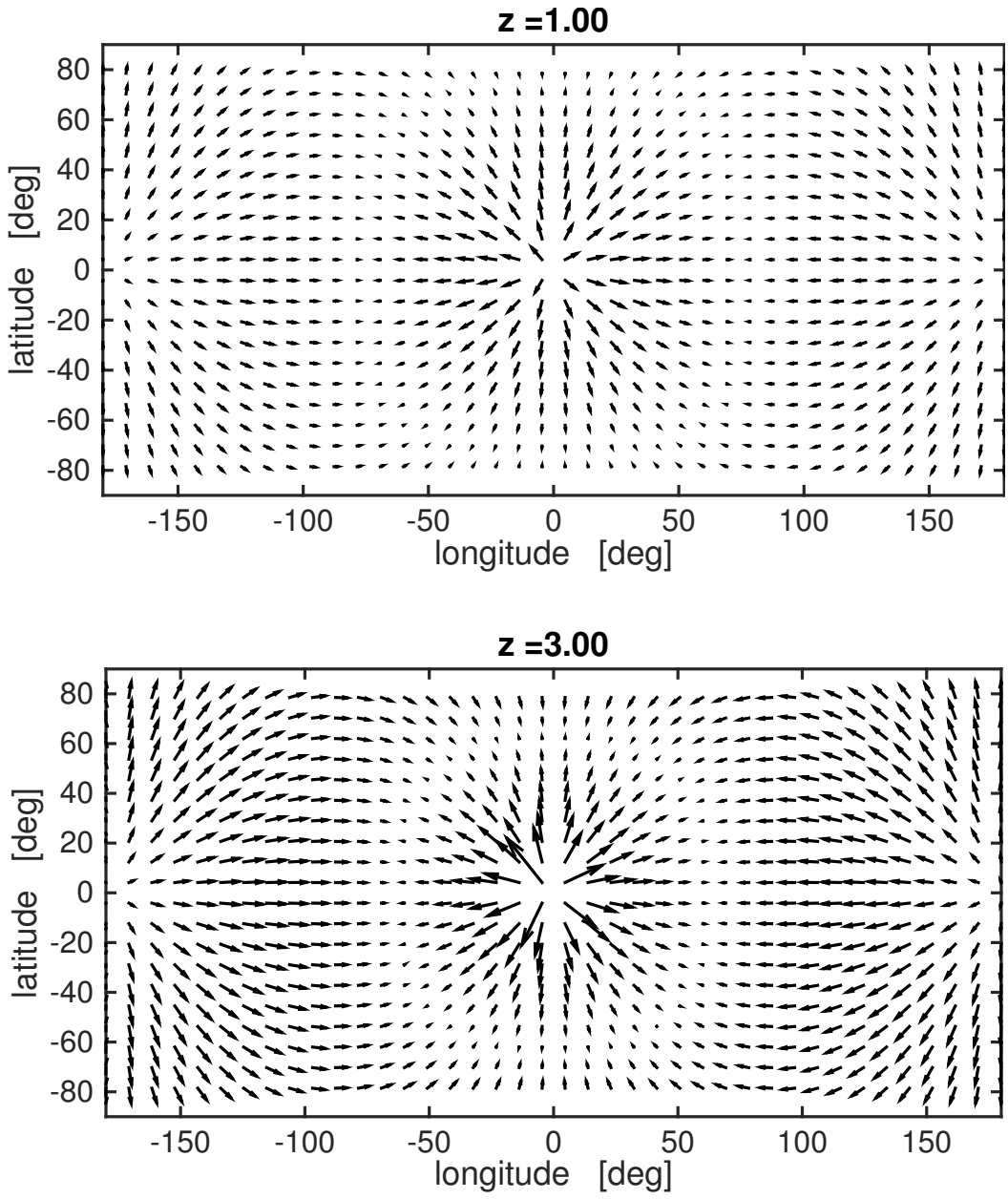

Fig. 4.20 **Flow pattern from from Run#3a** Top panel shows the apparent motion over the observer's sky at $z = 0.3$, and the bottom shows the same at $z = 0.7$. The observer's $(\hat{\vartheta}, \hat{\varphi})$ coordinates have been transformed to latitude and longitude with the $(0, 0)$ aligned with the decreasing r direction at the observer.

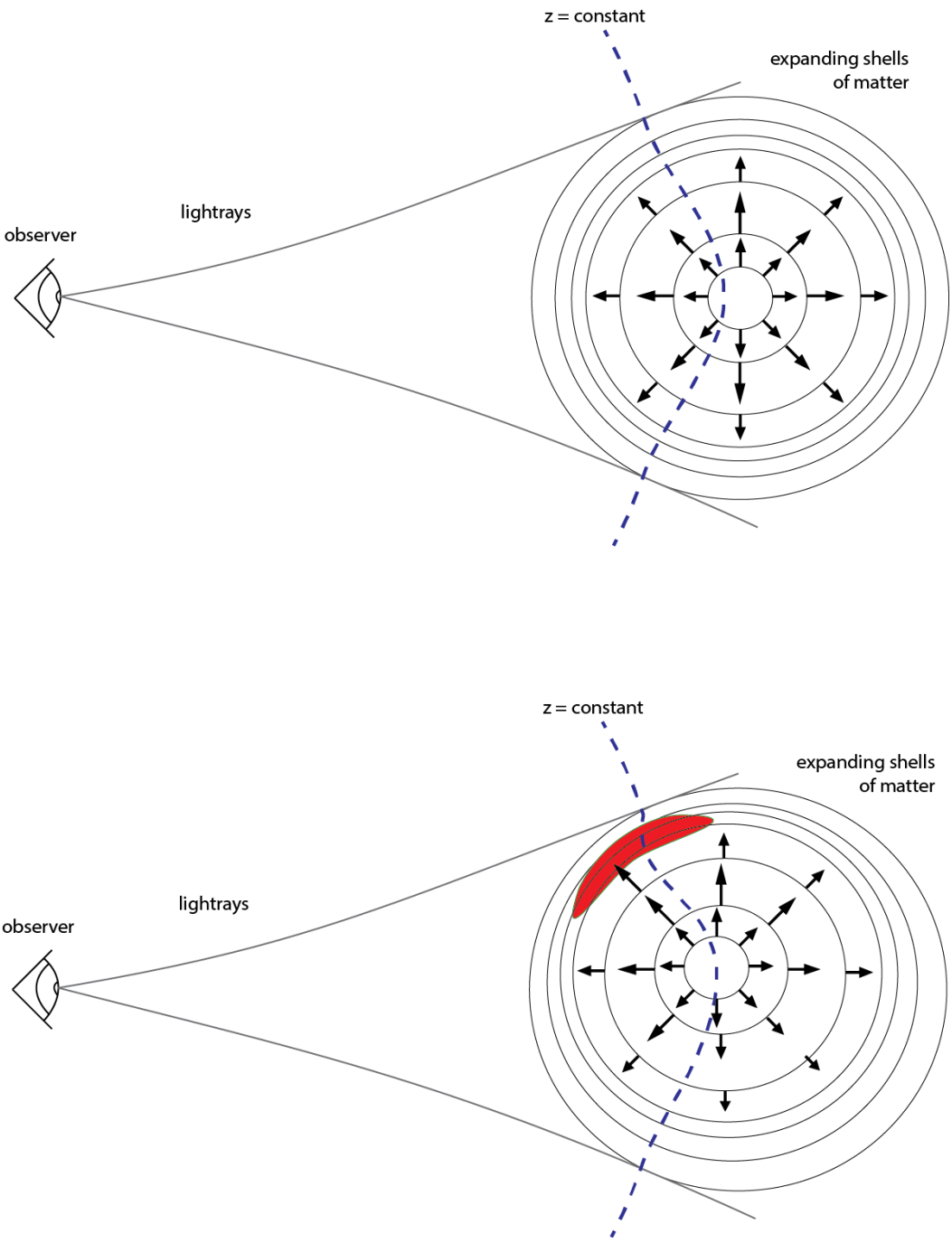

Fig. 4.21 **Fluid flow schematic for LT and Szekeres models** A schematic diagram showing an observer, two sight-lines, and fluid flow for LT (top) and Szekeres (bottom) runs. Expanding cells of matter are represented by black circles with arrows, and the dashed blue line represents a surface of constant redshift. In the LT case the observer see axial symmetry on the sky. In the Szekeres case there is a non-radial overdensity represented in red, which destroys axial symmetry from the perspective of the observer.

Chapter 5

Conclusions

The measurements of large scale bulk flows transverse to our line of sight remains an elusive goal in cosmology. Should future experiments reach the requisite sensitivity and such observations are made, it will open a new window onto the Universe through which we could potentially constrain cosmological models. In order to do this, of course, it is vital that one is able to calculate what to expect from a particular model. Here we have developed a framework for doing just this — calculating observables for an arbitrarily placed observer, in an arbitrary spacetime, in coordinates that are natural to the observer. This involved setting up a coordinate system at the observer, propagating the basis down the PNC with the geodesic deviation equation, and then constructing the observables from the result. In particular, we have derived expressions for the flow across the observer's sky as a function of redshift, which may be useful if we are ever confronted with transverse bulk flow data from future experiments. We also incorporated into our framework an expression for the area distance from the literature.

To investigate a concrete example, we have applied our method to the Szekeres metric and developed code in MATLAB to implement the procedure numerically. This involved solving 20 very messy 2^{nd} order ODEs, subject to 40 initial conditions. Using the code we performed a number of simulation runs, calculating observables in all directions on the observer's sky, out to some chosen redshift. From this we are able to inspect the output along a line of sight or over the whole sky on a particular redshift slice.

We tested our code on a number of FLRW models with different geometries and for various metric coordinate choices, and found good agreement with analytic solutions. For all lines of sight down the PNC the apparent motion was numerically zero, as

expected in FLRW, and the redshift versus affine parameter agreed with analytics (within the tolerance of the numerical integrator)[1].

Although no comparisons with analytics were done for LT models, we did find qualitative agreement with what one would expect. That is, central void models appeared to be expanding for an off-centre observer. Moreover, we see axial symmetry on the sky, as expected for a off-centre observer in a spherically symmetric model. In the void model, which was a relatively weak void, we found some appreciable flows across the sky, while the area distance showed little deviation between the rays. This seems to hint that transverse flows are very sensitive to the surrounding matter density, and is encouraging for potential future observations of cosmic flow.

We investigated a few Szekeres model setups with no symmetries. Although for these models there are no known analytic solutions and so knowing exactly what to expect is tricky, we do find the on-sky patterns made by the observables look somewhat like what one might expect in the $\epsilon = +1$ case. That is, the breaking of spherical symmetry. In the $\epsilon = -1$ case know what to expect is even less obvious. And although what we found in the simulations didn't differ greatly from the $\epsilon = +1$ case, there is scope for further exploration of these models, to see wether any novel observational features present themselves. Exploring models built from realistic initial/final data may provide valuable insight into what patterns on the sky to expect, and weather they will be observable.

To summarise, we have developed a framework to calculate the observables in a arbitrary spacetime, applied it to the Szekeres metric, and implemented it in numerical code. The code was validated with FLRW analytic solitons, and appears to be working correctly. We investigated some LT model setups, and these qualitatively agree with what we expect. This leaves many interesting possibilities to investigate using the code in future. Some of them may include drawing comparisons with perturbation theory in order to quantify non-linear GR effects, investigating non-spherical collapse, or even the effect of large scale structure on observations. It will also aid in model building, allowing for proposed models of structure to be tested, and refined or eliminated, directly from observations. For example, if a Szekeres model is constructed from some initial and final data, using the process of [85], so that it is in agreement with CMB constraints and present day statistics, one could determine its appearance for

[1]We also spent some time deriving an expression for the diameter distance in terms of our propagated basis vectors, with which we found nice agreement with FLRW analytic solutions. But when moving to LT models, we found this expression began to fail. We then realised that this is because the diameter distance will suffer from aberration in a spacetime that is not maximally symmetric, and so decided to work with the area distance, which does not share the same flaw.

comparison with observations of similar structures. And in the long term, should one embark on a "Metric of the Cosmos" approach using Szekeres models, our program would provide valuable input data for the inverse problem, allowing one to asses the efficacy of such a method.

Part II

To Kill a Surfer

Chapter 6

Introduction

By building on the solid foundation of General Relativity (GR), and including a cosmological constant as dark energy and weakly interacting particles as dark matter, the Λ-Cold-Dark-Matter model (ΛCDM) has done an astounding job of explaining all cosmological observations with a minimal amount of parameters. Its strong predicitvity and relative simplicity has thus seen it emerge as the standard model of cosmology. Currently numerous cosmological experiments are being designed to test the predictions of ΛCDM to unprecedented accuracy. There is, of course, the possibility the these experiments will reveal new degrees of freedom in the gravitational sector, and this has led to much research in "beyond-the-standard-model" physics. Among the simplest modifications to GR is to add a single scalar degree of freedom to the theory, in which case the gravitation force is mediated not only by a spin-2 graviton, but also a spin-0 scalar which couples to matter. Light scalar fields have indeed become quite ubiquitous in many theoretical cosmological models aimed at explaining the dark sector.

The existence of these scalars in Nature is typically motivated from two viewpoints; "top-down" and "bottom-up". In the bottom-up view, scalars are simply introduced ad-hoc into a theory to resolve some discrepancy between the predictions of the theory and ones observations. A good example of this is the late time acceleration of the Universe, which requires some ingredient beyond GR in order for predictions to agree with observation. While adding a cosmological constant to GR does seem to do the job, there are several examples where an additional scalar degree of freedom can achieve similar agreement [113]. In this case the scalars are assumed to exist in the low-energy effective field theory (EFT) of some unknown ultraviolet (UV) completion of gravity. In the top-down view, scalars are seen to emerge quite naturally from a number of more fundamental high energy theories. For example, in the low energy limit of string theory,

scalars manifest as light moduli which couple to gravity after string compactification [114].

Whatever the motivation, adding a scalar degree of freedom to the gravitational sector will necessarily alter dynamics of any gravitationally interacting system. This is because the scalar will affect spacetime geometry, and thus the path which particles will follow. If these additional fields are to play any important role in cosmology they must be relatively light, with a mass on the order of the Hubble scale or less in order to evade Yukawa suppression. This ensures the field can mediate long range forces. At first sight it seems this possibility should not be allowed, since light scalars that couple to matter with gravitational strength cause $\mathcal{O}(1)$ deviations from GR which is in direct conflict with local test of gravity. Solar system tests have placed extremely tight constraints on gravity, with the Cassini spacecraft constraining deviations from GR to $\mathcal{O}(10^{-5})$. And in laboratory experiments possible deviations from Newtonian gravity are contained to be $\mathcal{O}(10^{-12})$ [115]. Thus, if light scalar fields are to play an important role in gravitational interactions on cosmological scales they must possess some mechanism that enables them to evade local tests.

Originally conceived to solve the moduli stability problem in string theory, chameleon theory [116, 117] is one of a few scalar-tensor theories to receive much attention in recent years, owing to it appealing screening mechanism. Chameleons were constructed using a bottom-up approach, with the form of the potential and the matter coupling chosen in such a way to give the desired screening effect. A conformal coupling to matter ensures that the potential felt by the chameleon field depends not only on the bare self-interaction potential $V(\phi)$, but also on a contribution from the local matter density, ρ. This produces a density dependant minimum in the effective potential, and from which it follows, the field acquires a large mass in regions of high density and a small mass in regions of low density. Since a small mass corresponds to a long Compton wavelength, the field can only mediate long range forces in low density regions.

Although there is no known chameleon model that can explain the late time acceleration of the Universe [118, 119], it remains an interesting tool to locally suppress the forces coming from scalars coupled to matter. The subtle ability of the chameleon to screen itself in certain environments has led to some novel experimental tests. Astrophysically, chameleons can alter the internal dynamics of some dwarf galaxies [120, 121], as well as the stellar evolution therein [122–124]. In the lab, experiments like Eot-Wash search for deviations in the inverse-square law down to $\sim 50\mu$m, and have been able to constrain the chameleon parameter space [125, 126]. More recently it has been shown that near future cold atoms experiments using atom-interferometry

have the ability to access a large proportion of the chameleon parameter space [127]. If chameleons couple to the electromagnetic field then they will undergo chameleon-photon oscillations when propagating in through a magnetic field, and lab experiments like the GAMMeV Chameleon Afterglow Search (CHASE) [128, 129] and Axion Dark Matter Experiment (ADMX) [130] look for the afterglow from these oscillations. In addition, chameleon-photon mixing can occur deep inside the Sun [131] and affect the polarisation spectrum from distant astrophysical objects [132]. Collider signatures, particularly the effect of chameleons on the production Higgs particles, has also been calculated [133]. The strongest signatures of chameleons are predicted in very low density environments where small bodies that are screened in the laboratory are expected to be unscreened. Future space based tests like the MicroSCOPE [134] mission and STE-QUEST [135] will test the Equivalence Principal to an accuracy of $\mathcal{O}(10^{-15})$, and are expected to give the tightest constraints on the model.For a nice synopsis of the current constrains on the parameter space see [136].

In order for any particular cosmological theory to be accepted as a viable model it is important that it satisfy some philosophical considerations, such as naturalness and the fine tuning of initial conditions. One should be able to show that the relevant cosmological solutions are stable in both the classical and quantum sense, and that they are attractors for a wide range of initial conditions. It is not desirable for a theory to need very specific initial conditions to explain observations. This is considered a fine tuning problem. It has been shown that Big Bang Nucleosynthesis (BBN) constraints on the variation of particle masses, in the context of chameleon theory, impose the further requirement that the chameleon field find the minimum of its effective potential by the onset of BBN [137]. This limits viable initial conditions of the theory.

In the radiation dominated epoch one might naively assume that the scalar essentially decouples from matter since its evolution is sourced by the trace of the energy momentum tensor. However, in a more realistic model of the early Universe the quantity $\Sigma = (\rho - 3p)/\rho$, which we refer to as the *kick* function, can temporarily become non-zero whenever a massive particle species becomes non-relativistic. When one accounts for all Standard Model (SM) particles, this generates four distinct *kicks* in the trace of the energy momentum tensor as a function of Jordan frame temperature [137, 138]. Peaks in the kick function occur at when the temperature of the radiation bath is approximately equal to the mass of a particular particle species. At temperature higher than the mass, the particle is relativistic and does not contribute to Σ, and at temperatures less than the mass, the particle is Boltzmann suppressed and does not

contribute to Σ. At the peak of the kick the deviation away from zero can be $\mathcal{O}(0.1)$, and therefore can significantly affect the evolution of the field.

Chameleon cosmology was first considered in [137], where it was shown that $\phi = \phi_{\min}(t)$ is a stable dynamical attractor, and by considering the effect of the kicks, the authors showed that the attractor is approached for a wide range of initial conditions. This was however not quite the full picture. Later on in [138, 139] it was pointed out that the dependance of Σ on Jordan frame temperature permits another cosmological solution to the equation of motion for the scalar, the *surfer solution*, which has an adverse effect on chameleon cosmology. The solution is characterised by constant Jordan frame temperature which has the effect of prolonging the kick function, and driving the field to the minimum of its effective potential a high velocity. Once the minimum is reached the chameleon starts to climb up bare potential, causing rapid variation in the mass of the field and the excitation of high energy modes. This signals the breakdown of the effective field theory (EFT). Analyses indicate that the surfer is a stable dynamical attractor for a wide range of initial conditions, which cast doubt on any classical treatment of chameleon cosmology in the early Universe.

One might take the view that the chameleon EFT is not valid as far back as BBN, and thus the analysis of [138, 139] does not apply. However, we take the view that any viable alternative to GR must be valid as far back as BBN and thus consider a high energy correction to the chameleon action. The purpose of this work is to demonstrate that a consistent UV correction to the chameleon action can stabilise the evolution of the scalar in the presence of SM kicks, thereby alleviating any need to strongly constrain the matter coupling. We consider a UV correction of the Dirac-Born-Infeld (DBI) type, and emphasise that the structure is stable against quantum corrections, even when non-linearities become important. It is cruicial that the corrections we add to the action represent a healthy EFT, since we are trying to address the breakdown in calculability.

The outline of this part of the thesis is as follows: Some basic ideas and problems of modern cosmology are presented in §7, including the cosmological constant problem and dark energy, some principal of EFT and scalar-tensor gravity, and screening mechanisms. Basic principals of chameleon gravity are presented in §8 and the cosmological implications thereof in §9. The DBI modification to the chameleon is presented in §10 and the results from numerical simulations in §11.

Chapter 7

Some Preliminary Considerations

Here we review some basic concepts common in modern cosmology, as well as some problems, with the intention of providing some context to the material presented in the following sections.

7.1 Effective Field Theories

While QFT predicts non-gravitational phenomena very accurately, and classical GR does really well for gravitational systems, these two pillars of modern theoretical physics have proven really difficult to unite in to single framework. Such a unified framework is indeed necessary if one wishes to quantify the effects quantum mechanical processes have on any classical theory of gravitation. In the modern view, it is the language of EFTs that allow one to do this.

The most appealing feature of EFTs is that they provide useful insight into the low-energy phenomena of some full theory, without having to resolve the high-energy behaviour. The key to understanding how this works is noting that predictions are made in the context of a *low energy expansion*. Techniques that exploit the low-energy approximation are best expressed using effective Lagrangian methods. These take advantage of the simplicity of the low energy limit as early in the calculation as possible - from the action. This can greatly simplify calculations that would otherwise be really difficult. There are also conceptual benefits to this method - it clearly separates effects at different scales. It does however rely on the existence of a certain decoupling limit, which separates high from low energy phenomena.

After fields are promoted to operators, such expansions are typically written in powers of E/Λ_{UV}, the ratio of operator energy to the high energy cutoff. So long as the expansion variable remains small, $E/\Lambda_{UV} \ll 1$, the expansion is valid and the theory

remains predictive. In addition, the expansion can be truncated to encapsulate only the relevant terms. Consider the action [140]

$$\mathcal{L}_{\text{EFT}} \sim \mathcal{L}_{\text{low-energy}} + \sum_{n>4} c_n \frac{\mathcal{O}_n}{\Lambda^n} \Lambda^4 \tag{7.1}$$

where the operator $\mathcal{O}_n$ has dimensions [mass]^n with $n > 4$. Operators that scale like $(E/\Lambda)^\alpha$, for some α, are said to be suppressed by the strong coupling scale, and are thus dubbed *irrelevant* in the low-energy limit. On the other hand, operators contained in $\mathcal{L}_{\text{low-energy}}$ that are not suppressed by the strong coupling scale are said to be *relevant*. In this case, $\mathcal{L}_{\text{low-energy}}$ will sufficiently describe the low-energy behaviour of the theory, and the higher order terms can be neglected.

Thus, any QFT should be interpreted as an *effective* theory describing phenomena only up to some ultra-violet energy cutoff, Λ_{UV}, and above some length scale ${\Lambda_{UV}}^{-1}$. In the context of Early Universe cosmology, this implies a given theory is only valid as far back as when energy densities were on the order of ${\Lambda_{UV}}^4$. Beyond these cutoffs the effective theory no longer makes sense and cannot be trusted as new degrees of freedom are expect to become relevant. At this point a more fundamental theory is needed. Even GR should be viewed effective theory valid up to a high energy cutoff, namely, the Planck scale M_{Pl}. In the low energy regime of GR, the size of the quantum corrections are very small and can consistently be neglected. However, near black holes and cosmological singularities, where energies are high, quantum corrections are expected to become significant [141]. Extending classical GR plus a scalar field past the Planck scale, one begins to run into conflict with quantum field theory (QFT). This is because the RMS energy contained in vacuum fluctuations of the scalar field goes like $E \sim 1/R$, and extending the theory below $R \lesssim M_{\text{Pl}}^2 R$ implies that energy within a small region goes like $E \gtrsim R M_{\text{Pl}}^2$. Now R is below the Schwarzschild radius, meaning that spacetime is strongly curved - corresponding to the existence of black holes. This is unavoidable and there seems to be no way of handling this spacetime foam within the context of GR and field theory [142]. For this reason it has become the modern view that theories of gravity are effective ones, even GR.

7.2 The Problem with Concordance

Observations over recent years have provided much convincing experimental evidence for the accelerated expansion of the Universe. These include the observation of distant supernovae [143–146], analysis of the cosmic microwave background [147–149], and

of the large scale structure [150–153]. It has become quite hard to dispute that we are undergoing a phase of accelerated expansion. While all these observations are fit well within standard ΛCDM paradigm, some persisting theoretical concerns about concordance cosmology remain. One such concern is that theory is only concordant with the observations if the value of cosmological constant is set to be $\Lambda_{\rm obs} \sim M_{\rm Pl} H_0 \sim (10^{-3}{\rm eV})^4$, which translates to

$$\Lambda_{\rm obs} \sim 10^{-120} M_{\rm Pl}^4 \tag{7.2}$$

in natural units. This exceedingly small value is referred to as the cosmological constant problem. It's not just that $\Lambda_{\rm obs}$ is small in natural units, but rather, it does not posses a mechanism which makes its stable against quantum corrections. To contrast, in the case of the mass of the electron, which is also small in the applicable units, chiral symmetry suppresses quantum corrections by factors proportional to the mass, and so do not come to dominate over the small bare value. The small value of the bare mass is then said to be technically natural (in the t'Hooft sense). This is not the case for the cosmological constant. The SM particles that are known to exist are expected to produce a large contributions to Λ in the form $\langle T^{\mu\nu} \rangle \sim \langle \rho \rangle g^{\mu\nu}$ [154]. The size of this contribution can be estimated by modelling the SM fields as a collection of simple harmonic oscillators, and summing over their zero-point energies. This gives $\langle \rho \rangle \sim {\Lambda_{UV}}^4$, where Λ_{UV} is the high cutoff for the standard model of particle physics. Choosing the cutoff based on SM matter experiments to be $\Lambda_{UV} \sim 1{\rm TeV}$, one finds that the expected size of the quantum corrections to the bare cosmological constant are approximately

$$\Lambda_{\rm theory} \sim 10^{-60} M_{\rm Pl}^4. \tag{7.3}$$

This is some 60 orders of magnitude larger than the observed value. One possible resolution is if the quantum corrections coming from SM matter fields exactly cancels the bare value of the CC, to 60 decimal places, leaving the small residual that we infer from observations. This would be some extreme fine tuning, and seem most unlikely. In light of this rather disturbing problem, there have been many attempts to explain how the cosmological constant could be so small. A game of finding a mechanism that can make the cosmological constant small without fine-tuning. Some of these approaches exploit anthropic explanations as a way out of the problem, such a landscape cosmology and the multiverse [155–157]. While these might be an appealing resolution to some, as yet they don't produce testable predictions. The lack of dynamical solutions to this

problem in GR has led theoreticians to look "beyond the standard model" by studying extensions to the ΛCDM framework.

Related to the cosmological constant problem is the coincidence problem. The coincidence being that the energy density of the cosmological constant is very close to that of matter today. Finding a mechanism which explains that, without fine tuning, is also challenging.

7.3 Dynamical Dark Energy

It turns out that GR is quite special, and one really does need to add some more ingredient to get some new dynamics. The theory represents the only interacting, Lorentz invariant, masses, spin-2 particle. This implies that new gravitational physics requires new degrees of freedom [158]. The simplest extension is to add a Lorentz scalar to the theory, as is done in dynamical dark energy models. In these models, much like in inflationary models, a scalar field drives cosmic acceleration as it slowly rolls down its potential. Of the many dynamical dark energy models, the simplest are called quintessence [159]. The action can be written as

$$S = \int d^4x\sqrt{-g}\left[\frac{M_{\rm Pl}}{2}R - \frac{1}{2}\left(\partial\phi\right)^2 - V(\phi)\right] + S_m\left(\Psi, g_{\mu\nu}\right) \tag{7.4}$$

where ϕ is the quintessence field, $V(\phi)$ is the potential, and S_m is the SM matter action which is a function of the matter fields Ψ and the metric $g_{\mu\nu}$. Here the field *minimally couples* to the metric via the canonical kinetic term, $(\partial\phi)^2$. This alters the source term in the field equations for $g_{\mu\nu}$ to include a contribution from a "scalar fluid" with effective equation of state

$$w_\phi = \frac{\dot\phi^2 - V(\phi)}{\dot\phi^2 + V(\phi)} \approx -1 \tag{7.5}$$

in the slow roll regime. This then drives cosmic acceleration in a way very similar to the cosmological constant, whose equation of state is constant at $w_\Lambda = -1$. For a wide class of potentials these models have the desirable tracking solution, which ensures that the energy density in the field "tracks" that of matter.[1] This goes some way to explaining the coincidence problem, however fine-tuning issues still persist since one must choose a very particular form of the potential to ensure that the "cosmological constant" is at its observed value today. Generalisations of quintessence (and inflationary) models,

[1]The Rattra-Peebles potential presented in §8.1 has this property

sometimes called P(X) models, modify the kinetic term in the Lagrangian by making it a function of the canonical $(\partial\phi)^2$ term. These are often called K-essence in the context of dynamical dark energy and K-flation in the context of inflation. All cases have the field driving accelerated expansion phase.

In all these models the field must be weakly coupled to matter in order to avoid 5^{th} force constraints from the very well tested Lab and Solar System experiments. This implies that if they are to couple with gravitational strength such theories need to hide their scalar degrees of freedom in regions where stringent constraints apply. A screening mechanism is needed to suppress deviations from GR in high density environments, while light on cosmological scales so that it can drive acceleration.

7.4 Scalar-Tensor Gravity

Scalar-Tensor theories were first investigated by Jordan [160] when he embedded a 4-D curved manifold into 5-D flat space. He showed that a constraint, in the form of a 4-D scalar naturally arises when formulating projective geometry. This gave rise to a space-time dependant gravitational "constant", in line with the argument of Dirac [161], and mades links to the 5-D theory of Kaluza and Klein [162]. The Lagrangian in Jordan's action took the form [163]

$$\mathcal{L}_J = \varphi_J^{\gamma}\left(R - \frac{\omega_J}{\varphi_J^2}(\partial\varphi_J)^2\right) + \mathcal{L}_m\left(\varphi_J, \Psi\right) \tag{7.6}$$

where $\varphi_J(x)$ is the scalar field, and γ and ω are constants. Here, the matter Lagrangian, $\mathcal{L}_m$, is a function of the matter fields and the scalar field. This marked the birth of scalar-tensor gravity, with the introduction of the non-minimal coupling term φR.

Jordan's line of research was later taken over by Brans and Dicke [164]. They demanded that the matter Lagrangian be decoupled from the scalar, so that the theory respects the Weak Equivalence Principal. After some redefinition of the fields in (7.6), they proposed a Lagrangian of the form

$$\mathcal{L}_{BD} = \varphi R - \frac{\omega}{\varphi}(\partial\varphi)^2 + \mathcal{L}_m\left(\Psi\right) \tag{7.7}$$

where ω is a constant. Here, the non-minimal coupling term replaces the standard Einstein-Hilbert term of GR, $\mathcal{L}_{EH} = R/16\pi G$. By comparing the two one can see that

the scalar can be interpreted as an *effective gravitational constant*

$$\varphi = \frac{1}{16\pi G_{\text{eff}}}. \tag{7.8}$$

From this it should be clear that this action is not the same as simply adding a kinetic scalar term to the Einstein-Hilbert action, as is done in dynamical dark energy models. The non-minimal coupling now alters the left hand side of the field equations for the metric.

The action can be transformed into a form that more closely resembles GR. Consider the Jordan-Brans-Dicke action with a self-interaction potential, written in the form [165]

$$S = \int d^4x\sqrt{-g}\frac{M_{\text{Pl}}^2}{2}\left[F(\tilde{\phi})\tilde{R} - \tilde{g}^{\mu\nu}Z(\tilde{\phi})\partial_\mu\tilde{\phi}\partial_\nu\tilde{\phi} - 2U(\tilde{\phi})\right] + S_m\left[\tilde{g}_{\mu\nu}, \psi\right] \tag{7.9}$$

where $\{F, Z, U\}$ are arbitrary functions of the scalar field. Here we interpret U as the self-interaction potential. Between these three functions there are only two physical degrees of freedom, since one has freedom to redefine the scalar field. In order for the graviton to carry positive energy one must have $F > 0$. The matter action, S_m, is a function of the Jordan frame metric, $\tilde{g}^{\mu\nu}$. This means that this is the frame in which matter minimally couples to the metric, and ensures that the WEP is obeyed. This is referred to as the Jordan frame. By performing a conformal transformation,

$$g_{\mu\nu} = F(\tilde{\phi})\tilde{g}_{\mu\nu}, \tag{7.10}$$

one can eliminate the non-minimal coupling term in (7.9). This is usually called moving to the Einstein frame, where the action can be re-expressed in terms of the Einstein-Hilbert Lagrangian.[2] One finds

$$S = \int d^4x\sqrt{-g}\frac{M_{\text{Pl}}^2}{2}\left[R - 2g^{\mu\nu}\partial_\mu\phi\partial_\nu\phi - 4V(\phi)\right] + S_m\left[A^2(\phi)g_{\mu\nu}, \psi\right] \tag{7.11}$$

[2]See Ch.3 in [163] for details calculations

where the new field, ϕ, and the functions $A(\phi)$ and $V(\phi)$ are given by

$$\left(\frac{\mathrm{d}\phi}{\mathrm{d}\tilde{\phi}}\right)^2 = \frac{3}{4}\left[\frac{\mathrm{d}\ln F(\tilde{\phi})}{\mathrm{d}\tilde{\phi}}\right]^2 + \frac{Z(\tilde{\phi})}{2F(\tilde{\phi})}, \tag{7.12}$$

$$A(\phi) = F^{-1/2}(\tilde{\phi}), \tag{7.13}$$

$$2V(\phi) = U(\tilde{\phi})F^{-2}(\tilde{\phi}). \tag{7.14}$$

Now V is interpreted as the Einstein frame potential and A is referred to as the conformal factor. The strength of the coupling between the scalar field and matter is characterised by

$$\alpha(\phi) \equiv \frac{\mathrm{d}\ln A}{\mathrm{d}\phi}. \tag{7.15}$$

Now the left hand side of the field equations for $g_{\mu\nu}$, resulting from the variation of (7.11), will be the same as in GR.

Both the Einstein and the Jordan frames are useful to study. In the Jordan frame matter minimally couples to the metric, and this metric defines the length and time measured in the laboratory, giving observations their standard interpretation. In the Einstein frame the kinetic term has been diagonalised so the spin-2 and spin-0 degrees of freedom are perturbations of $g_{\mu\nu}$ and ϕ, respectively, making structure of the theory more evident. The physics between the frames is however invariant. For example, a time variation of the scalar field would be interpreted in the Jordan frame as a varying gravitational constant for particles of fixed mass. On the other hand, in the Einstein frame this would be interpreted as a fixed gravitational constant and varying particle masses. The physical observable which is Gm^2 , would however vary in the same way in both frame.

7.5 Classifying Screening Mechanisms

The mechanisms by which a theory screens 5th forces can be classified in a couple of different ways. By seeing how the fields in the Lagrangian relate to the static potential around a perturbation , one can classify them according to their force laws. Consider a Lagrangian of the from [158]

$$\mathcal{L} = -\frac{1}{2}Z^{\mu\nu}\left(\phi, \partial\phi, ...\right)\partial_\mu\partial_\nu - V\left(\phi\right) + g(\phi)T^\mu_\mu, \tag{7.16}$$

where $Z^{\mu\nu}$ schematically encodes derivative self-interactions, T^{μ}_{μ} is the trace of the matter energy momentum tensor and $g(\phi)$ is the coupling between the field and matter. Variation of the action leads to a wave equation for ϕ, which can be split in into background and perturbation bits. Assuming a non-relativistic source allows one to write the trace as $T^{\mu}_{\mu} = -\rho$. For a single point particle one can write the energy density in terms of a delta function, $\rho = \mathcal{M}\delta^3(x)$. Expanding the solution about the background, $\phi = \bar{\phi} + \varphi$, and assuming a diagonal metric, one arrives at the equation of motion for the perturbation φ, namely

$$Z\left(\bar{\phi}\right)\left(\ddot{\varphi} - c_s^2(\bar{\phi})\nabla^2\varphi\right) + m^2(\bar{\phi})\varphi = g\left(\bar{\phi}\right)\mathcal{M}\delta^3(x), \tag{7.17}$$

where c_s is the sound speed. This is just the Klein-Gordon equation for a massive scalar propagating in absence of a potential. Here the background value of the field $\bar{\phi}$ is set by other background quantities, say, the Newtonian potential Φ, or the background matter density $\bar{\rho}$. Neglecting spatial variations in $\bar{\phi}$ over the scales of interest, one finds the static potential

$$U(r) = -\frac{g(\bar{\phi})}{Z(\bar{\phi})c_s^2(\bar{\phi})}\frac{\mathcal{M}}{4\pi r}e^{-\frac{m(\bar{\phi})}{\sqrt{Z(\bar{\phi})}c_s(\bar{\phi})}r} \tag{7.18}$$

Since this potential is negative the force is positive, as it should be for a scalar. Examining above one can now see that, with all parameters $\mathcal{O}(1)$, any light scalar will mediate a long range force $F_\varphi \sim 1/r^2$. Fortunately the parameters $\{m, Z, c_s, g\}$ are all a function of the background value of the field $\bar{\phi}$, and so by making them environmentally dependant, they can help achieve screening. Three such mechanism are known to work

- Weak coupling: Screening can be achieved if the coupling to matter g is let to be function of the environment, with it being small in regions of high density and large in regions of low density. The symmetron mechanism is an example of this class.

- Large mass: Allowing the mass of fluctuations $m(\bar{\phi})$ to depend on the environment also leads to screening. If the mass becomes large in regions of high density the potential will be Yukawa-suppressed, and the scalar can only mediate very short range forces. This is exactly how the chameleon mechanisms works

- Large inertia: Making the kinetic function $Z(\phi)$ large environmentally leads to two types of screening. Kinetic screening applies when the first derivatives of

the field become important, and Vainshtein mechanism when second derivatives become important. In both cases $Z(\phi)$ becomes large, and the potential is suppressed.

Another more phenomenological scheme exploits the nature of the screening criterion to classify the screening mechanism, which is often better suited to astrophysical and cosmological observations.

- Screening set by ϕ: This class achieves screening from self interaction of the field, governed by the potential $V(\phi)$. Thus the local value of the field dictates weather or not non-linearities develop and screening occurs. This is the case for the chameleon, symmetron and dilaton screening. These are all example where the scalar develops either a high mass, weak coupling or strong self-interactions in region of high Newtonian potential. Thus the scalar force is suppressed in region where the local Newtonian potential is above some critical value $\Phi > \Lambda$. Mapping out the gravitational potential smoothed over some scale thus gives an indication of which regions are likely to be screened.

- Screening set by $\partial\phi$: In this class screening happens when derivative self-interactions become important, i.e. when $\partial\phi \geq \Lambda^2$. Example of this include K-mouflage and DBI type P(X) theories. The scalar force is thus suppressed in regions where the acceleration $a = -\nabla\Phi$ is above some critical value. That is $|\nabla\Phi| \geq \Lambda^2$. Thus, mapping the gravitational acceleration gives insight into which regions will be screened. These theories have been used in attempts to construct a relativistic MOND theory [166].

- Screening set by $\partial^2\phi$: Here, second derivatives become important to the dynamics, $\partial^2\phi \geq \Lambda^3$, while higher order derivatives remain small. This includes the Vainshtein mechanism. The fifth force shuts off when the density or curvature $R \sim \nabla^2\Phi$ is above some critical value . That is $\nabla^2\Phi \geq \Lambda^3$. Thus mapping the curvature smoothed over some scale will indicate weather a region is screened or not.

As one might expect, the DBI chameleons presented in this work will exhibit screening properties that fall into the first and second classes above.

Chapter 8

Chameleon Gravity

Some of the basic features of the chameleon model are reviewed in this section, going from the action to the equations of motion, highlighting some features applicable to cosmology along the way. Much of the contents in this section will inform the derivation of the DBI-chameleon in §10.

8.1 Action and Frames

Broken into its component Lagrangian densities, the Chameleon action in the *Einstein frame* takes the form [116, 117]

$$S = \int d^4x\sqrt{-g}\left(\mathcal{L}_{EH} + \mathcal{L}_{\phi}\right) - \int d^4x\mathcal{L}_m\left(\psi_m^{(i)}, \tilde{g}_{\mu\nu}^{(i)}\right) \tag{8.1}$$

with

$$\mathcal{L}_{EH} = \frac{M_{\rm Pl}^2}{2}R, \tag{8.2}$$

$$\mathcal{L}_{\phi} = -\frac{1}{2}\partial_\mu\phi\partial^\mu\phi - V\left(\phi\right), \tag{8.3}$$

where $M_{\rm Pl}$ is the reduced Planck mass, $V(\phi)$ is the self-interaction potential, g is the determinant of the Einstein frame metric $g_{\mu\nu}$, which is associated with the Ricci scalar R. $\mathcal{L}_{EH}$ is the standard Einstein-Hilbert term which gives rise to GR, and $\mathcal{L}_{\phi}$ is the Lagrangian for a scalar field in a potential, with canonical kinetic term $(\partial\phi)^2$. $\mathcal{L}_m$ is the Lagrangian density for the various SM matter fields, $\psi^{(i)}$, which are a function of the metric $\tilde{g}_{\mu\nu}^{(i)}$. This is to say that particles (i.e. excitations of the matter fields) follow geodesics of the Jordan frame metric $\tilde{g}_{\mu\nu}^{(i)}$. It is related to the Einstein frame

metric $g_{\mu\nu}$ by the conformal transformation

$$\tilde{g}^{(i)}_{\mu\nu} = e^{2\beta_i \phi/M_{\rm Pl}} g_{\mu\nu}, \tag{8.4}$$

where β_i a dimensionless coupling constant. This coupling can, in principal, be different for each matter species. In this case there are many Jordan frame metrics, one for each species, which explicitly violates the WEP. Although it is most common to consider universally coupled chameleons, as we do in §9, in this section we will remain as general as possible and keep the subscript-i for the various matter species.

It is typically assumed that $V(\phi)$, is of the *runaway* form, i.e. monotonically decreasing and satisfying

$$\lim_{\phi\to\infty} V = 0, \qquad \lim_{\phi\to\infty} \frac{V_\phi}{V} = 0, \qquad \lim_{\phi\to\infty} \frac{V_{\phi\phi}}{V} = 0, \tag{8.5}$$

and

$$\lim_{\phi\to 0} V = \infty, \qquad \lim_{\phi\to 0} \frac{V_\phi}{V} = \infty, \qquad \lim_{\phi\to 0} \frac{V_{\phi\phi}}{V} = \infty. \tag{8.6}$$

In addition, it has been noted that $V(\phi)$ can behave like an effective cosmological constant, driving the late time cosmic acceleration [137]. One such potential that satisfies the conditions above is the inverse power law, or Ratra-Peebles potential. It has the form

$$V(\phi) = M^4 \left(\frac{M}{\phi}\right)^n, \tag{8.7}$$

where M has dimensions of mass and $n > 0$. With this potential, common in Quintessence modes, the energy density in the scalar has the neat ability to track the matter/radiation energy density at early times, and come to dominate at late times. By choosing M and n appropriately one can tune the potential to match current observations of the dark energy scale. Another common choice is the exponential potential

$$V(\phi) = M^4 \exp\left[\left(\frac{M}{\phi}\right)^n\right], \tag{8.8}$$

where M is as above, and directly sets the dark energy scale. This potential is however considered to suffer from the same fine tuning issues as the cosmological constant, since M is chosen "by hand" to match observations [167].

8.2 Field Equations

Applying the principle of least action to (8.1), the variation can be written

$$\begin{aligned}\delta S &= \delta S_{EH} + \delta S_\phi + \delta S_m \\ &= \left(\frac{\delta S_{EH}}{\delta g^{\mu\nu}} + \frac{\delta S_\phi}{\delta g^{\mu\nu}} + \frac{\delta S_m}{\delta g^{\mu\nu}}\right)\delta g^{\mu\nu} + \left(\frac{\delta S_{EH}}{\delta \phi} + \frac{\delta S_\phi}{\delta \phi} + \frac{\delta S_m}{\delta \phi}\right)\delta\phi. \end{aligned} \tag{8.9}$$

When we demand the variation be zero, each set of terms in brackets in (8.9) will yield *Field Equations*, one for the tensor field describing the geometry, $g_{\mu\nu}$, and one the scalar field, ϕ, describing the chameleon. We will see that the field equations for the geometry will resemble the EFEs with an additional source term coming from the EMT of the scalar, and the scalar field equation will resemble the Klein-Gordon equation.

8.2.1 Geometry Part

The first bracket of (8.9) gives the tensor field equations. Variation of the Einstein-Hilbert term with respect to the inverse metric yields

$$\begin{aligned}\frac{\delta S_{EH}}{\delta g^{\mu\nu}} &= \int d^4x \frac{\delta\left(\sqrt{-g}\mathcal{L}_{EH}\right)}{\delta g^{\mu\nu}}, \\ &= \int d^4x \left\{\frac{M_{\rm Pl}^2}{2}\frac{\delta\left(\sqrt{-g}R\right)}{\delta g^{\mu\nu}}\right\}, \\ &= \int d^4x\sqrt{-g}\left\{\frac{M_{\rm Pl}^2}{2}\left(\frac{1}{\sqrt{-g}}\frac{\delta\sqrt{-g}R}{\delta g^{\mu\nu}} + \frac{\delta R}{\delta g^{\mu\nu}}\right)\right\}, \\ &= \int d^4x\sqrt{-g}\left\{\frac{M_{\rm Pl}^2}{2}\left(R_{\mu\nu} - \frac{1}{2}g_{\mu\nu}R\right)\right\}. \end{aligned} \tag{8.10}$$

This is just the Einstein tensor $G_{\mu\nu}$ from GR. Since SM matter fields do not couple to the Einstein frame metric directly, but rather to the Jordan frame metric via the conformal transformation (8.4), the variation of the matter action is now different from

GR. One finds

$$\begin{aligned}\frac{\delta S_m}{\delta g^{\mu\nu}} &= \int d^4x \frac{\delta \mathcal{L}_m}{\delta g^{\mu\nu}}, \\ &= \int d^4x \left\{ \frac{\delta \mathcal{L}_m}{\delta \tilde{g}^{\mu\nu}} \frac{\delta \tilde{g}^{\mu\nu}}{\delta g^{\mu\nu}}, \right\} \\ &= \int d^4x \left\{ \sum_i -\frac{1}{2}\sqrt{-\tilde{g}}\tilde{T}^{(i)}_{\mu\nu} e^{-2\beta_i\phi/M_{\rm Pl}} \right\}, \\ &= \int d^4x \sqrt{-g} \left\{ \sum_i -\frac{1}{2}\tilde{T}^{(i)}_{\mu\nu} e^{2\beta_i\phi/M_{\rm Pl}} \right\}, \end{aligned} \tag{8.11}$$

where $\tilde{T}^{(i)}_{\mu\nu}$ is defined as in (D.3). Variation of the scalar sector with respect to the metric follows straight from the definition (D.11). One finds

$$\begin{aligned}\frac{\delta S_\phi}{\delta g^{\mu\nu}} &= \int d^4x \frac{\delta\left(\sqrt{-g}\mathcal{L}_\phi\right)}{\delta g^{\mu\nu}}, \\ &= \int d^4x \sqrt{-g} \left\{ \frac{1}{\sqrt{-g}} \frac{\delta\left(\sqrt{-g}\mathcal{L}_\phi\right)}{\delta g^{\mu\nu}} \right\}, \\ &= \int d^4x \sqrt{-g} \left\{ -\frac{1}{2} T^\phi_{\mu\nu} \right\}, \end{aligned} \tag{8.12}$$

where $T^\phi_{\mu\nu}$ is given explicitly by the last line of (D.11). Collecting together all of the terms (8.10) (8.11) (8.12) with (8.9), and demanding that the variation of the action with respect to the inverse metric is zero, one finds a familiar field equation for the geometry,

$$M^2_{\rm Pl} G_{\mu\nu} = T^\phi_{\mu\nu} + \sum_i \tilde{T}^{(i)}_{\mu\nu} e^{2\beta_i\phi/M_{\rm Pl}}, \tag{8.13}$$

where

$$G_{\mu\nu} \equiv R_{\mu\nu} - \frac{1}{2} g_{\mu\nu} R \tag{8.14}$$

is the Einstein tensor of GR. While (8.13) resembles the Einstein Field Equations, the main difference is that the evolution of the geometry is sourced not by SM matter, but rather, by a combination of scalar field "matter" and conformally coupled SM matter.

8.2.2 Scalar Part

Since the Ricci scalar is purely a function of the Einstein frame metric and its derivatives, one finds that the first term in the scalar part is zero, i.e.

$$\frac{\delta S_{EH}}{\delta \phi} = 0. \tag{8.15}$$

The second term depends of the particular form of the Lagrangian density for the scalar field. For a canonical scalar of the from (8.3), one finds the variation to be

$$\begin{aligned}
\delta S_\phi &= \int d^4x\sqrt{-g}\delta\mathcal{L}_\phi \\
&= \int d^4x\sqrt{-g}\delta\left\{-\frac{1}{2}\nabla_\mu\phi\nabla^\mu\phi - V\right\} \\
&= \int d^4x\sqrt{-g}\left\{-\frac{1}{2}\delta\left(\nabla_\mu\phi\right)\nabla^\mu\phi - \frac{1}{2}\nabla_\mu\phi\delta(\nabla^\mu\phi) - V_{,\phi}\,\delta\phi\right\} \\
&= \int d^4x\sqrt{-g}\left\{-\nabla_\mu\phi\delta\left(\nabla^\mu\phi\right) - V_{,\phi}\,\delta\phi\right\} \\
&= \int d^4x\sqrt{-g}\left\{-\nabla_\mu\phi\nabla^\mu\delta\phi - V_{,\phi}\right\}\delta\phi,
\end{aligned} \tag{8.16}$$

where we assumed symmetric metric, and used fact that the variation commutes with the derivative operator. Integrating the first term in (8.16) by parts, and setting the variation of the field to zero at the boundary, allows one to isolate the variation $\delta\phi$ from the derivative operator. Doing so yields

$$\begin{aligned}
\int d^4x\sqrt{-g}\left(-\nabla_\mu\phi\nabla^\mu\delta\phi\right) &= \oint d^3x\sqrt{-g}\left(-\nabla_\mu\phi\delta\phi\right) - \int d^4x\sqrt{-g}\left(-\nabla_\mu\nabla^\mu\phi\delta\phi\right) \\
&= \int d^4x\sqrt{-g}\left(\nabla_\mu\nabla^\mu\phi\delta\phi\right).
\end{aligned} \tag{8.17}$$

Substituting the result (8.17) into (8.16) allows one to write the variation of the scalar term with respect to the field as

$$\frac{\delta S_\phi}{\delta\phi} = \int d^4x\sqrt{-g}\left\{\nabla_\mu\nabla^\mu\phi - V_{,\phi}\right\}. \tag{8.18}$$

The last term in (8.9) would be zero in the case of a minimally coupled scalar, since the matter action would be purely a function of the geometry. However, owing to conformal coupling (8.4), the matter fields in the Einstein frame are now a function of

ϕ, and thus the variation is non-zero. One finds

$$\begin{aligned}\frac{\delta S_m}{\delta\phi} &= \int d^4x \frac{\delta\mathcal{L}_m}{\delta\phi} \\ &= \int d^4x \left\{ \frac{\delta\mathcal{L}_m}{\delta\tilde{g}^{\mu\nu}} \frac{\delta\tilde{g}^{\mu\nu}}{\delta\phi} \right\} \\ &= \int d^4x \left\{ \sum_i -\frac{1}{2}\sqrt{-\tilde{g}}\tilde{T}^{(i)}_{\mu\nu} \frac{-2\beta_i}{M_{\rm Pl}} \tilde{g}^{\mu\nu}_{(i)} \right\} \\ &= \int d^4x \sqrt{-g} \left\{ \sum_i \frac{\beta_i}{M_{\rm Pl}} \tilde{T}^{(i)}_{\mu\nu} \tilde{g}^{\mu\nu}_{(i)} e^{4\beta_i/M_{\rm Pl}} \right\}. \end{aligned} \tag{8.19}$$

Combining (8.15), (8.18) and (8.19) with (8.9), and demanding that the variation with respect to the field is zero, yields the evolution equation for the scalar, namely

$$\nabla^\mu\nabla_\mu\phi - V_\phi + \sum_i \frac{\beta}{M_{\rm Pl}} \tilde{T}^{(i)}_{\mu\nu} \tilde{g}^{\mu\nu}_{(i)} e^{4\beta/M_{\rm Pl}} = 0. \tag{8.20}$$

Here we see difference from quintessence. The scalar is not free to evolve under its own potential, but rather, it conformally couples to the trace of the Jordan frame energy momentum tensor. Using the results from §D we can write the equation of motion for the field purely in terms of Einstein frame quantities. Substituting (D.10) into (8.20) yields

$$\nabla^\mu\nabla_\mu\phi = V_{,\phi} + \sum_i \rho_i \left(1 - 3w_i\right) \frac{\beta_i}{M_{\rm Pl}} e^{(1-3w_i)\beta_i\phi/M_{\rm Pl}}. \tag{8.21}$$

8.3 The Effective Potential

It is instructive to write equation of motion for the scalar in a more intuitive form. Defining the effective potential to be

$$V_{eff} = V\left(\phi\right) + \sum_i \rho_i e^{(1-3w_i)\beta_i\phi/M_{\rm Pl}} \tag{8.22}$$

we see that (8.21) becomes

$$\Box\phi = V_{eff,\phi}\,. \tag{8.23}$$

where $\Box \equiv \nabla^\mu\nabla_\mu$ is the covariant d'Alemtertian operator. Now the scalar can be interpreted as a free particle of unit mass moving in a one-dimensional (effective)

potential. Given bare potential,$V(\phi)$, is monotonically decreasing, and if one has β_i is positive, the effective potential (8.22) will have a minimum at a particular filed value, $\phi = \phi_{\rm min}$, which will change depending on the local energy density. See Figure 8.1 for a schematic representation of the effective potential for a single matter species. The

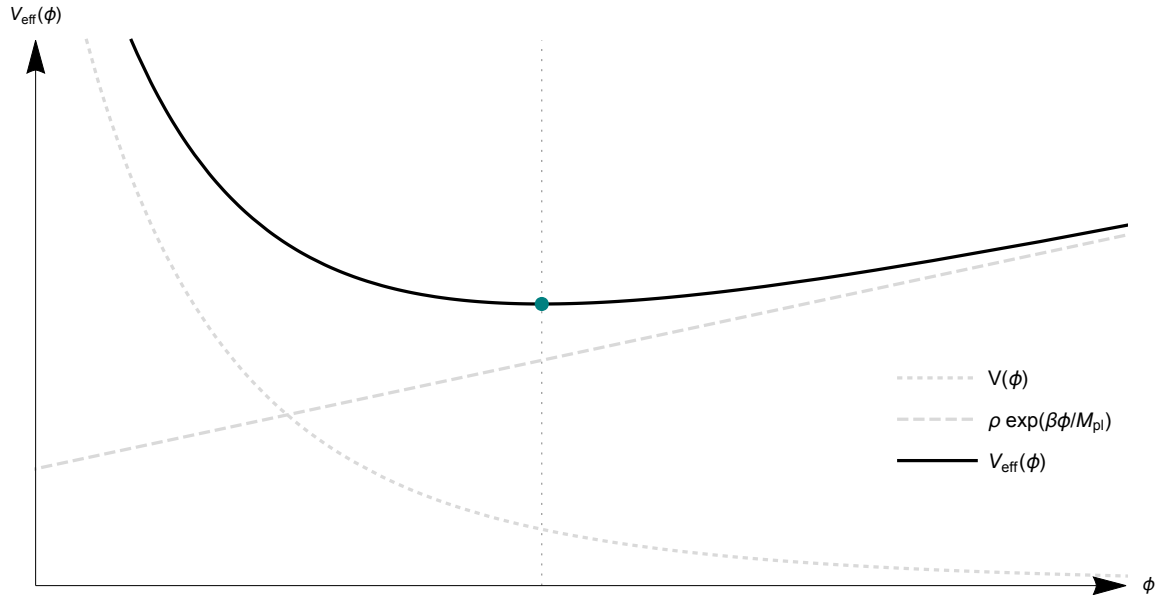

Fig. 8.1 **A schematic representation of the effective potential for a single matter coupling $\beta = \beta_i$.** The sum of the monotonically decreasing bare potential, $V(\phi)$, and the monotonically increasing matter coupling term, $\rho \exp(\beta\phi/M_{\rm Pl})$, gives an effective potential, $V_{\rm eff}(\phi)$, with a distinct minimum as a specific field value, denoted $\phi_{\rm min}$. The teal dot indicates the position of the minimum, and the light dotted line indicates the value of $\phi_{\rm min}$

location of the minimum is given by the value of $\phi_{\rm min}$ which solves

$$V_{,\phi}\left(\phi_{\rm min}\right) + \sum_i \rho_i \left(1 - 3w_i\right) \frac{\beta_i}{M_{\rm Pl}} e^{(1-3w_i)\beta_i\phi/M_{\rm Pl}} = 0. \tag{8.24}$$

If the field has relaxed to the minimum, the mass of small fluctuations about $\phi_{\rm min}$ is found by evaluating second derivative of the potential (8.22) at $\phi_{\rm min}$, which is

$$m^2 = V_{,\phi\phi}\left(\phi_{\rm min}\right) + \sum_i \frac{\beta_i^2}{M_{\rm Pl}^2} \rho_i e^{\beta_i\phi/M_{\rm Pl}}. \tag{8.25}$$

One can see that (8.24) and (8.25) imply that the location of the the minimum, $\phi_{\rm min}$, and the mass of fluctuations about that minimum, m, will be a function of the local matter density, ρ_i. Specifically, given that $V_{,\phi}$ is negative and monotonically increasing,

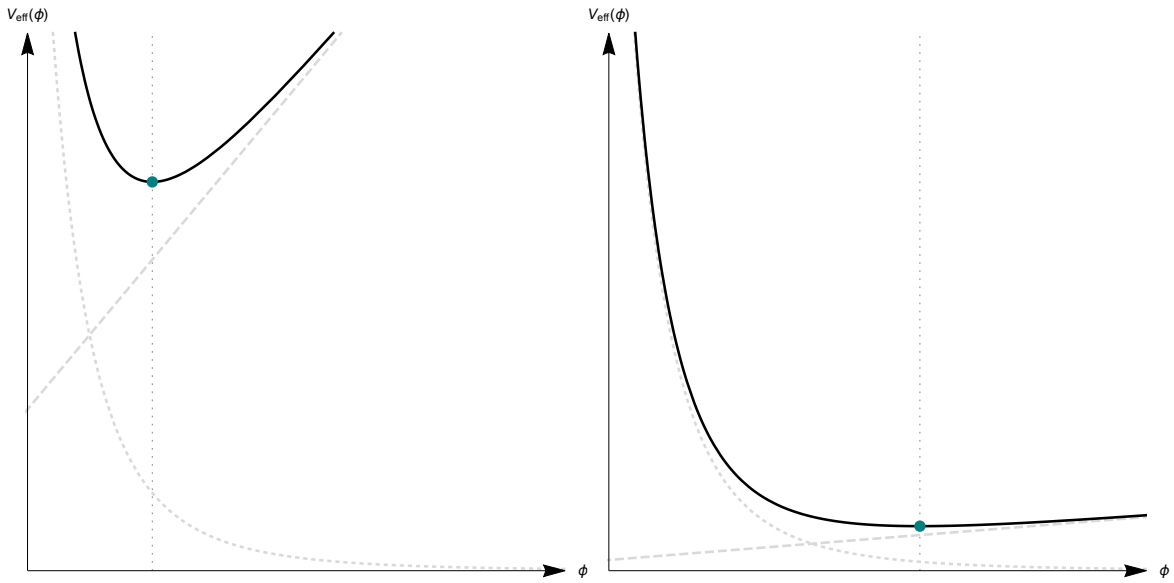

(a) High density region (b) Low density region

Fig. 8.2 **A schematic of the effective potential and its dependance on the local density.** The left pane shows the effective potential in a high density region, with the value of ϕ_{min} indicated by the light dotted line. To contrast, the right pane show the effective potential in a relatively under-dense region. Because the matter branch has become less steep, the value of ϕ_{min} has increased to larger filed values. Upon inspection one can see that the second derivative of the effective potential at the various minima, and thus mass of fluctuations, will be larger in high density regions as compared to low density ones.

while $V_{,\phi\phi}$ is positive and decreasing, it follows that larger values of ρ_i correspond to smaller ϕ_{min} and larger m. Figure 8.2 shows the effect of the local density on the effective potential. Such behaviour is crucial for the chameleon screening mechanism to be effective, since the interaction range of the fifth force decreases rapidly as m increases, as is evident in (7.18). Thus, in regions of high density (8.25) becomes large and fluctuations become Yukawa suppressed, while in low density regions the Chameleon becomes light, and can mediate long range forces.

8.4 Thin Shell Effect

The density dependance of the chameleon mass gives the theory its screening properties via the thin shell effect. This is rooted in the nonlinearity of the chameleon equation of motion. By deriving a solution for the field in the presence of a compact object one can see the thin shell behaviour manifest. Most solutions are approximations, linear or

pseudo-linear, and break down at some point. It is when these non-linearities become important that the thin shell effect comes into play. None the less instructive so derive some approximate solutions.

Consider a static, spherically symmetric body of radius R, homogeneous density ρ_c and mass $M_c = 4\pi R^3/3$, which is surrounded by a homogeneous background density ρ_∞. Under these assumptions, and choosing a single matter coupling $\beta = \beta_i$ for simplicity, (8.21) reduces to [116, 117]

$$\frac{\mathrm{d}^2\phi}{\mathrm{d}r^2} + \frac{2}{r}\frac{\mathrm{d}\phi}{\mathrm{d}r} = V_{,\phi} + \frac{\beta}{M_{\rm Pl}}\rho_m(r)e^{\beta\phi/M_{\rm Pl}}, \tag{8.26}$$

where

$$\rho_m(r) = \begin{cases} \rho_c & \text{for } r < R, \\ \\ \rho_\infty & \text{for } r > R. \end{cases} \tag{8.27}$$

The value of the field which minimises the effective potential will now be different inside and outside the body, which denote ϕ_c and ϕ_∞ respectively. Thus, from (8.24) we have the minima given by

$$V_{,\phi}\left(\phi_c\right) + \frac{\beta}{M_{\rm Pl}}\rho_c e^{\beta\phi_c/M_{\rm Pl}} = 0, \tag{8.28}$$

$$V_{,\phi}\left(\phi_\infty\right) + \frac{\beta}{M_{\rm Pl}}\rho_\infty e^{\beta\phi_\infty/M_{\rm Pl}} = 0, \tag{8.29}$$

and the corresponding mass of fluctuations about those minima, which are given by (8.25), we denote $m_c = m(\phi_c)$ and $m_\infty = m(\phi_\infty)$. Thus, if the field finds its minimum, it will have a greater mass inside the body relative to outside, provided $\rho_c > \rho_\infty$. Solving (8.26) amounts to a boundary value problem. Requiring that the solution is regular at the origin implies $\mathrm{d}\phi/\mathrm{d}r = 0$ at $r = 0$. Far from the body, $r \gg R$, we neglect all other contamination and assume the field to has relaxed the minimum of its effective potential. Since $\rho = \rho_\infty$ outside the body, it is natural to impose $\phi = \phi_\infty$ as $r \to \infty$. This ensures that the chameleon force vanishes infinitely far away from the body. Thus the boundary values are

$$\begin{aligned} \frac{\mathrm{d}\phi}{\mathrm{d}r} &= 0 \qquad \text{at} \qquad r = 0, \\ \phi &\to \phi_\infty \qquad \text{as} \qquad r \to \infty \end{aligned} \tag{8.30}$$

Solutions to (8.26) essentially fall into two classes, called *thin-shell* or *thick-shell* solutions. The applicable solution depends on the size and density of the body. By size we mean radius of the object relative to the length scale m_c^{-1}.

For small bodies the quantity $m_c R$ is small and the linear approximation is valid. Solutions can be thought of as small perturbations about the background field ϕ_∞, and thus one has $\phi \approx \phi_\infty$ everywhere. The object is not big enough for the field relax to $\phi = \phi_c$ somewhere in the core, and there are thus gradients in ϕ throughout the object. This is the so called thick-shell case.

The linear approximation starts to break down for larger, denser bodies, and non-linear effects become important when $m_c R \gg 1$. In this regime the body is necessarily much larger that the length scale $1/m_c$. One expects that all perturbations to ϕ will die off exponentially quickly over a distance of approximately $1/m_c$, and thus $\phi \approx \phi_c$ will be almost constant inside the body. And thus this region will contribute nothing to the field outside. All variation in the field will take place within a thin shell of thickness $\Delta R \approx 1/m_c$ near the surface of the body - the only region which contributes to the exterior. One can see from above that the criterion $m_c R \gg 1$ implies $\Delta R/R \ll 1$, which is the condition for the thin-shell case.

The two solutions for the field, exterior to the body, are approximately

$$\begin{aligned} \phi(r) &\approx -\left(\frac{\beta}{4\pi M_{\rm Pl}}\right)\frac{M_c e^{-m_\infty r}}{r} + \phi_\infty \qquad \text{if} \quad \frac{\Delta R}{R} < 1; \\ \phi(r) &\approx -\left(\frac{3\Delta R}{R}\right)\left(\frac{\beta}{4\pi M_{\rm Pl}}\right)\frac{M_c e^{-m_\infty r}}{r} + \phi_\infty \qquad \text{if} \quad \frac{\Delta R}{R} \gg 1, \end{aligned} \tag{8.31}$$

where the shell thickness is

$$\frac{\Delta R}{R} = \frac{\phi_\infty - \phi_c}{6\beta M_{\rm Pl}\Phi_c} \tag{8.32}$$

and $\Phi_c = M_c/8\pi M_{\rm Pl}^2 R_c$ is the Newtonian potential at the surface of the object. Given that the force on a test particle of mass M and coupling β goes like

$$F_\phi = -\frac{\beta}{M_{\rm Pl}} M \nabla\phi \tag{8.33}$$

one should interpret ϕ as the potential field for this fifth force. From (8.31) we see that both solutions have a Yukawa profile for a scalar of mass m_∞, and thus long range forces can couple to the body if ρ_∞ is sufficiently low. However, the exterior profile for a body with thin shell has a suppression factor of $3\Delta R/R$, which means that one has

$\phi \approx \phi_\infty$ outside the body, and thus the gradient is zero. In this case the body is said to be screened from fifth forces.

Although the above analysis is instructive, its not the full picture. It is important to realise that (8.23) describes the microscopic, particle-level, field theory for ϕ, while in many cases we are interested in the large scale, coarse grained, behaviour of the theory. By treating solid objects as a collection of atoms of nuclear density surrounded by vacuum, rather than some average density throughout the object, it has been shown that the chameleon mechanism becomes much stronger. Thus, properly accounting for the inherent nonlinearity of the screening mechanism opens up the possibility that light cosmological scalars can couple to matter more strongly than gravity, i.e. $\beta \gg 1$ [168].

8.5 Quantum Corrections

As discussed in §7.1, if one views the chameleon as an EFT, its important to check that quantum corrections are small in the regimes of interest, so one can reliably trust the predictions of the theory. Since the chameleon couples to gravity and matter fields, one might be concerned wether the screening mechanism is stable against radiative corrections to ϕ coming from matter/graviton loops. It has been shown that the mass correction diverges quadratically as [158]

$$\Delta m \sim \frac{\Lambda_{UV}^2}{M_{\rm Pl}}, \tag{8.34}$$

however, in practice the UV cutoff is very small, with $\Lambda_{UV} \sim 10^{-32} M_{\rm Pl}$ for chameleon and kinetic screening. This gives $\Delta m \lesssim H_0$.

Considering the corrections to $V(\phi)$ from ϕ-loops, one finds substantial contributions that limit the classical approximation. This allows on to bound the mass of the chameleon. The one-loop Coleman-Weinberg quantum corrections to the potential is [169, 170]

$$\Delta V_{1-\rm loop}(\phi) = \frac{m_\phi^4(\phi)}{64\pi^2} \ln \frac{m_\phi^2(\phi)}{\mu_0} \tag{8.35}$$

where μ_0 is an arbitrary mass scale, and the quantum corrected potential is given by $V_{1-\rm loop}(\phi) = V(\phi) + \Delta V_{1-\rm loop}(\phi)$. Choosing $\mu_0 = m_\phi^2$, so as to make the logarithm zero, does not ensure that corrections are always small. Since the mass depends of the value of the field, at other densities corrections will become important.

The size of the one-loop term can be used as a diagnostic for the breakdown of the EFT. Once it becomes as large as the tree level term, and since there is no reason to believe that the higher order terms will be suppressed, this signals the breakdown of the classical approximation. Since the one-loop correction in (8.35) goes like $\Delta V_{1-\text{loop}} \sim m_\phi^4$, quantum corrections will present problems when m_ϕ becomes large. This has allowed constraints to be placed on the maximum mass before the classical description breaks. This has been done independent of the form of the potential, in the context of lab experiments. This is because lab experiments will have large masses, and thus it is important for them to know if the theory is broken, although such bounds also apply to cosmological chameleons. Specifically, when one requires that both $\Delta V'_{1-\text{loop}}/V'$ and $\Delta V''_{1-\text{loop}}/V''$ remain small over the range of interest, this translated to a bound on mass of

$$m_\phi \lesssim \left(\frac{48\pi^2\xi^2\rho_{\text{lab}}^2}{M_{\text{Pl}}^2}\right)^{1/6} \tag{8.36}$$

where ξ is the linearised coupling strength [169].

Chapter 9

Cosmological Chameleons

If chameleons are to be a consistent theory of gravity they must adequately describe current cosmological observations. This section draws on results from §8 to derive the background equations of motion applicable to our Universe. We consider some cosmological solutions to these background equations, paying special attention to the radiation dominated phase of the early Universe, and its implications on the viability of certain initial conditions.

9.1 Background Equations

The universe is thought to be well described by the homogeneous and isotropic FLRW metric on large enough scales, with the curvature parameter has been constrained from the Planck satellite to be $|\Omega_k| \leq 0.005$, implying that the universe is very close to flat. Thus we adopt a flat FLRW background geometry, with line element

$$ds^2 = -dt^2 + a^2(t)\left(dx^2 + dy^2 + dz^2\right), \tag{9.1}$$

where $a(t)$ is the scale factor which is a function of cosmic time, t. Associated with the metric are 2 independent Christoffel connections

$$\Gamma^i_{0j} = \Gamma^i_{j0} = H\delta^i_j, \qquad \Gamma^0_{ij} = Ha^2\delta_{ij}, \tag{9.2}$$

where $H \equiv \dot{a}/a$ is the Hubble parameter, and the overdot represents a derivative with respect to cosmic time. The non-zero components of the Ricci tensor are

$$R_{00} = -3\frac{\ddot{a}}{a}, \qquad R_{ij} = \left(2H^2 + \frac{\ddot{a}}{a}\right)a^2\delta_{ij} \tag{9.3}$$

and the Ricci scalar is

$$R = 6\left(H^2 + \frac{\ddot{a}}{a}\right). \tag{9.4}$$

From this, one finds two non-zero components of the Einstein tensor, namely

$$G_{00} = 3H^2, \qquad G_{ij} = -\left(H^2 + 2\frac{\ddot{a}}{a}\right)\delta_{ij} \tag{9.5}$$

Expressions for the energy density and pressure of the scalar are found by applying the definitions (D.12) and (D.13) to the energy-momentum tensor (D.11). Assuming a comoving observer with the 4-velocity $u^\mu = (1, 0, 0, 0)$, and a spatially homogeneous field

$$\phi = \phi(t) \Rightarrow \partial_\mu \phi = \dot{\phi}, \tag{9.6}$$

one finds the usual expressions,

$$\rho_\phi = \frac{1}{2}\dot{\phi}^2 + V, \tag{9.7}$$

$$p_\phi = \frac{1}{2}\dot{\phi}^2 - V. \tag{9.8}$$

The first of the Friedmann equations comes from the 00-component of the the field equations (8.13). Under the assumptions (9.6) and (9.1), one finds

$$M_{\rm Pl}^2 G_0^0 = T_t^{\phi t} + \sum_i T_t^{(i)t} \tag{9.9}$$

$$\Rightarrow 3M_{\rm Pl}^2 H^2 = \rho_\phi + \sum_i \rho_i e^{(1-3w_i)\beta_i \phi/M_{\rm Pl}} \tag{9.10}$$

The second Friedmann equation is found by considering the spatial part of (8.13). One arrives at

$$M_{\rm Pl}^2 G_j^i = T_j^{\phi i} + T_j^{(m)i} \tag{9.11}$$

$$M_{\rm Pl}^2\left(3H^2 + \dot{H}\right) = -p_\phi - \sum_i e^{4\beta_i\phi/M_{\rm Pl}} w_i \rho_i \tag{9.12}$$

Here we see that evolution of the geometry is sourced not only by the energy-density in SM particles, as is the case in GR, but also from the energy density in the scalar field. This is essentially how quintessence fields drive cosmic acceleration. The difference with the scalar-tensor gravity is that the evolution of the scalar now coupled to SM

particles as we will see next. The first term in (8.20), in a FLRW background, can be written as

$$\begin{aligned}\nabla^\mu\nabla_\mu\phi &= \frac{1}{\sqrt{-g}}\partial^\mu\left(\sqrt{-g}\partial_\mu\phi\right)\\ &= \frac{1}{\sqrt{-g}}\partial^\mu\sqrt{-g}\partial_\mu\phi + \partial^\mu\partial_\mu\phi\\ &= -\frac{1}{a^3}\partial_t\left(a^3\right)\dot{\phi} - \ddot{\phi}\\ &= -3\frac{a^2\dot{a}}{a^3}\dot{\phi} - \ddot{\phi}\\ &= -\left(\ddot{\phi} + 3H\dot{\phi}\right)\end{aligned} \tag{9.13}$$

and thus the equation of motion for the field becomes

$$\ddot{\phi} + 3H\dot{\phi} = -V_{,\phi} - \sum_i \rho_i\left(1 - 3w_i\right)\frac{\beta_i}{M_{\rm Pl}}e^{(1-3w_i)\beta_i\phi/M_{\rm Pl}}. \tag{9.14}$$

Here we see the $3H\dot{\phi}$ term acts like friction, and thus the expansion of the Universe has the effect of slowing the acceleration of the field. Naively evaluating (9.14) for both non-relativistic and relativistic matter species, it would appear that relativistic degrees of freedom don't contribute to the evolution of the scalar field, since their equation of state parameter is $w_r = 1/3$ and thus their contribution to the trace of the EMT is zero. As will be shown in §9.2 this is not strictly true - the trace *does* receive a contribution from relativistic matter. In light of this fact, it will be useful for later sections to define a quantity

$$\Sigma \equiv \frac{\rho_r - 3p}{\rho_r} = 1 - 3w_r, \tag{9.15}$$

which we refer to as the *kick function*. Assuming $\phi \ll M_{\rm Pl}/\beta$, we can make the approximation $e^{\beta_i\phi/M_{\rm Pl}} \approx 1$, and thus the Jordan frame and Einstein frame metrics are indistinguishable, as are the energy densities $\tilde{\rho} \approx \rho$. As we will show later, this is required from BBN for the model to be viable. Moreover, we don't expect scalar tensor theory to be valid up to the Planck scale. Thus is a reasonable assumption. Further, in order to respect the universality of free fall we assuming the same coupling $\beta_r = \beta_m = \beta$. This allows one to write the governing background equations (9.10),

(9.12) and (9.14) as

$$3M_{\rm Pl}^2 H^2 = \rho_\phi + \rho, \tag{9.16}$$

$$M_{\rm Pl}^2 \left(2\dot{H} + 3H^2\right) = -p_\phi - p, \tag{9.17}$$

$$\ddot{\phi} + 3H\dot{\phi} = -V_{,\phi} - \frac{\beta}{M_{\rm Pl}}\rho_r \left(\Sigma + f_m\right), \tag{9.18}$$

where f_m is the non-relativistic matter fraction $f_m \equiv \rho_m/\rho_r$. Writing the equation of motion with these definitions is helpful, as it allows one to easily see which term dominates the dynamics. In the early Universe the non-relativistic matter fraction is tiny, $f_m \approx 10^{-6}$ around the time of BBN, while the kick function is $\Sigma \sim \mathcal{O}(0.1)$, so clearly it dominates early universe dynamics. As the energy density in radiation dilutes faster than matter, f_m grows. It reaches $f_m = 1$ at matter-radiation equality, at which point it becomes dominant, and continues to grow.

9.2 Standard Model Kicks

In order to understand the dynamics of the chameleon deep in the radiation dominated epoch of the early Universe it is necessary to consider the effect relativistic degrees of freedom have on its evolution. If a radiation bath consists purely of photons then $w_r = 1/3$ is always true and $T^\mu_\mu = 0$ always holds. In the early Universe however, there are several massive particles in thermal equilibrium with the photons, and this changes this situation significantly. At temperatures approximately equal to the mass of the particle, $T \approx m$, particle species momentarily drop out of equilibrium with the radiation bath, and one finds that the pressure decreases faster than the energy density. This causes the equation of state parameter to deviate from what one typically expects, $w \neq 1/3$, and thus produces a contribution to the trace of the energy-momentum tensor. When the radiation temperature is much greater than the mass of the particles, they are relativistic and can be well approximated by radiation. Thus their contribution to Σ is zero. And once the radiation temperature is much less than the mass of the particle, the particle is Boltzmann suppressed, and contributes nothing to Σ. These evens are referred to as "kicks". The kick function is then [171, 172, 165, 137–139]

$$\Sigma(T_J) = \sum_i \frac{\tilde{\rho}_i - 3\tilde{p}_i}{\tilde{\rho}_r} \tag{9.19}$$

where the sum is over the particles that involved, listed in Table 9.1, and ρ_r is the sum of the energy densities of all particles that are in thermal equilibrium with the radiation, including neutrinos. In the Jordan frame this is given by

$$\tilde{\rho}_r = g_*(T_J)\frac{\pi^2}{30}T_J^4 \tag{9.20}$$

where g_* is the effective number of degrees of freedom,

$$g_*(T_J) = \frac{7}{8}\sum_{\text{fermions}} g_i \left(\frac{T_i}{T}\right)^4 + \sum_{\text{bosons}} g_i \left(\frac{T_i}{T}\right)^4 \tag{9.21}$$

and T_i is the temperature of the particle. For a given species of massive particles the energy density and pressure is given by

$$\begin{aligned} \rho &= \frac{g}{2\pi^2}\int_m^\infty \frac{\sqrt{E^2-m^2}}{\exp E/T \pm 1}E^2 dE, \\ p &= \frac{g}{6\pi^2}\int_m^\infty \frac{(E^2-m^2)^{3/2}}{\exp E/T \pm 1}dE. \end{aligned} \tag{9.22}$$

where g is the number of degrees of freedom for the particle, m is the mass of the particle, and T is the temperature of the radiation bath. The +ve sign in the denominator applies to fermions, a the -ve to bosons. Using (9.22) and (9.20) with (9.19) gives the contribution to the kick function from a single particle species. One finds

$$\Sigma_i = \frac{15}{\pi^4}\frac{g_i}{g_*(T)}\left(\frac{m_i}{T}\right)^2 \int_{m_i/T}^\infty \frac{\sqrt{u^2-(m_i/T)^2}}{e^u \pm 1}du, \tag{9.23}$$

where $u \equiv E/T$ is an integration variable. The various particle species which contribute to (9.23), listed in Table 9.1, produce four distinct kicks. Detailed numerical calculations have been done in [138] to accurately model the various kicks, see Figure 5 therein.

9.3 The Old Picture: $\phi = \phi_{min}$ Attractor

As the Universe expands and matter is redshifted, the location of $\phi_{\min}$ will necessary move to larger field values (see Figure 8.2). Assuming the field is initially at the minimum, and comparing the response time of the field with the characteristic timescale associated with the evolution of $\phi_{\min}$, one can determine the wether the field is able to track the minimum of the effective potential as it evolves. Since the location of $\phi_{\min}$

Contributions to Σ

particle	g	m[GeV]	particle	g	m [GeV]
top	12	172	Higgs	1	125
bottom	12	4.2	Z	3	91
charm	12	1.3	$W^{\pm}$	6	80
tau	4	1.8			
muon	4	0.106	π^0	1	0.140
electron	4	5.11×10^{-4}	$\pi^{\pm}$	2	0.135

Table 9.1 **The various particles which contribute to the kick function** Σ**,** and their corresponding number of degrees of freedom, and mass threshold. They are ordered in decreasing mass threshold, with the left column corresponding to fermions and the right column to bosons. The top four rows occur before the electro-weak phase transition, while the bottom two occur after.

is governed by the redshifting of matter, the associated timescale is the Hubble time, H^{-1}, while the response time of the field is approximately the period of oscillation about the minimum, m^{-1}. When the response time of the field is much less than the evolution time of $\phi_{\rm min}$, one has

$$m \gg H, \tag{9.24}$$

and the field adjusts itself adiabatically and follows the minimum as it evolves. If the converse is true, $m \ll H$, the field cannot keep up with the evolution of the minimum, and will lag behind.

It has been shown that for a Ratra-Peebles potential (8.7), with n and β order unity, and $M = 10^{-3}$eV, the condition (9.24) is satisfied from the big bang (post inflationary reheating) until today. Thus if the field is initially at the minimum, it will track it as it evolves. In addition, the solution is stable, and small perturbations about the minimum decay via damped oscillations. The solution $\phi = \phi_{\rm min}(t)$ is therefore said to be a dynamical attractor. In the cosmological context this is very important, as we regularly assume that the field has found the minimum of its effective potential. However, it is not reasonable to assume that the field starts at or near the minimum, so it is crucial to show that the attractor is approached for a general set of initial conditions far from the minimum. Such initial conditions can be split into two groups: those with $\phi_i \gg \phi_{\rm min}$, and those with $\phi_i \ll \phi_{\rm min}$. Their corresponding solutions have been dubbed *Undershoot* and *Overshoot* solutions, respectively. [137]

9.3.1 Undershooting

When the initial value of the field is much greater than the minimum, $\phi_i \gg \phi_{\rm min}$, the effective potential is dominated by the matter coupling term and $V(\phi)$ can be neglected. The equation of motion (9.18) then becomes

$$\ddot{\phi} + 3H\dot{\phi} \approx -\frac{\beta}{M_{\rm Pl}}\rho_r \left(\Sigma + f_m\right), \tag{9.25}$$

Thus the evolution of the scalar is sourced by the trace of the energy momentum tensor. If one (incorrectly!) assumes that contributions to the trace from relativistic species are negligible, one would have a source term $\sim \rho_r f_m = \rho_m$. During radiation dominated era the non-relativistic matter density, ρ_m, is tiny when compared to the $3H\dot{\phi}$ term, so the field would be over-damped, pinned at its initial value ϕ_i. It would only start rolling toward the minimum around matter-radiation equality, when the energy density in matter is be comparable to the Hubble friction term. This would be problematic from the perspective of BBN constraints, since we know that we require $\phi = \phi_{min}$ by the onset BBN (See §9.3.3). This was resolved by realising that in the early Universe contributions from SM kicks to the trace of the energy-momentum tensor and are significant enough to overcome Hubble friction and drive the field towards its minimum prior to BBN. Since these kicks dominate over the non-relativistic matter contribution, one can approximate the equation of motion (9.18) as

$$\ddot{\phi} + 3H\dot{\phi} \approx -\frac{\beta}{M_{\rm Pl}}\rho_r\Sigma. \tag{9.26}$$

By modelling the kicks as a series of delta functions of the appropriate size, it has been shown numerically that the combination of all kicks will move the field by $(\Delta\phi)_{\rm tot} \approx -\beta M_{\rm Pl}$ towards the minimum. After electrons/positrons become non-relativistic ($z \sim 10^9$) there are no more kicks and the field is frozen at some value until matter-radiation equality. At that time $M_{\rm Pl}^2 H^2 \sim \rho_m \approx T^\mu_\mu$, thus the driving term becomes comparable Hubble friction, and the field rolls toward $\phi_{\rm min}$, undergoes large anharmonic oscillations and settles to $\phi_{\rm min}$. From this one might conclude that for initial conditions in the range $\phi_{\rm min} \ll \phi_i < \beta M_{\rm Pl}$, the field will be kicked sufficiently close to the minimum of its effective potential, begin oscillating, and quickly settle to $\phi_{\rm min}$ before BBN.

This is however not the full picture. By neglecting the dependance of the kick on Jordan frame temperature, and modelling it as a delta function, one misses the existence of another attractor solution. This will be addressed in §9.4 .

9.3.2 Overshooting

In the case where the initial value of the field is much less than the location of the minimum, $\phi_i \ll \phi_{\rm min}$, the effective potential is donated by the bare potential, one can neglect the matter coupling terms. The equation of motion (9.18) becomes

$$\ddot{\phi} + 3H\dot{\phi} \approx -V_{,\phi}\,. \tag{9.27}$$

This is just the equation for a minimally coupled scalar. Given that the initial value of the field is much less than the minimum, the second derivative of the potential at this ϕ_i will be much greater than the mass of oscillations about the minimum $V_{,\phi\phi}\left(\phi_i\right) \gg m_i^2$, and since $m \gg H$, this implies that $V_{,\phi\phi}\left(\phi_i\right) \gg H_i^2$. Thus the field will be underdamped, essentially behaving like a free field. The kinetic energy will quickly dominate and the field will overshoot $\phi_{\rm min}$ until the kinetic energy is sufficiently redshifted so that Hubble damping becomes important. The field then comes to a stop at

$$\phi_{stop} \approx \phi_i + \sqrt{6\Omega_\phi^{(i)}} M_{\rm Pl}, \tag{9.28}$$

where $\Omega_\phi^{(i)}$ is the fraction of total energy in the scalar. At this point the situation is exactly that of the undershoot case, with ϕ_i replaced with ϕ_{stop}.

9.3.3 Constraints on Initial Conditions

The previous two sections showed that if the field starts at, or overshoots to, a field value of $\phi > \beta M_{\rm Pl}$, it will not reach the minimum of its effective potential by the onset of Nucleosynthesis. Based on BBN constraints of the time variation of particle masses, this allows one to rule out certain initial conditions. Due to the conformal coupling (8.4) a constant mass scale in the Jordan frame, $m^{(i)}$, becomes field-dependant in the Einstein frame, $m(\phi) = e^{\beta_i \phi / M_{\rm Pl}} m^{(i)}$. As the field evolves, this leads to a time variation in the mass of SM particles, approximately

$$\left|\frac{\Delta m}{m}\right| \approx \frac{\beta}{M_{\rm Pl}} \left|\Delta\phi\right|, \tag{9.29}$$

where Δm is the mass variation and $\Delta\phi$ is the field excursion. The most stringent constraints on the variation of m between the time of BBN and now come from BBN analysis, and are on the order of 10%. Assuming the field is at its minimum today, which is much less than $M_{\rm Pl}$, this translates to a constraint on the value of the field at

BBN, ϕ_{BBN}, to be

$$\phi_{BBN} \leq 0.1 \frac{M_{\rm Pl}}{\beta}. \tag{9.30}$$

This constrains viable initial conditions in the early Universe. If the field starts at, or overshoots to, a value $\phi \geq \beta M_{\rm Pl}$, it will violate (9.30) and thus the bound on the variation of particle masses. Based on this reasoning, such initial conditions were ruled out.

9.4 A New Problem: Surfing Chameleons

The presence of SM kicks allow for another cosmological dynamical attractor, the *surfer solution*. While these SM kicks were shown to be a necessary ingredient in getting the Chameleon home to the minimum of its effective potential before BBN, we will see that the existence of the surfing solution voids this result, and has been shown to cause problems for early Universe chameleon cosmology.

9.4.1 The Surfing Solution

The surfer is best appreciated by changing the time variable to Einstein frame E-folds and making the scalar field dimensionless,

$$N \equiv \ln\left(\frac{a}{a_i}\right), \qquad \varphi \equiv \frac{\phi}{M_{\rm Pl}}, \tag{9.31}$$

where a_i is the scale factor at some fixed initial time. After some manipulation (9.16), (9.17) and (9.18) can be written (see Appendix E.1 for derivation) as [138, 139]

$$\varphi'' + \varphi'\left(1 - \frac{\varphi'^2}{6}\right) = -3\beta\Sigma(T_J)\left(1 - \frac{\varphi'^2}{6}\right), \tag{9.32}$$

where $\Sigma(T_J)$ is the kick function as defined in (9.19), which is a function of Jordan frame temperature. The Jordan frame temperature is a function of the field, and can be written

$$T_J = \left[\frac{g_{*S}(T_{J,i})}{g_{*S}(T_J)}\right]^{1/3} e^{\beta(\varphi-\varphi_i)} e^{-N}, \tag{9.33}$$

where $g_{*S} \equiv s_R[(2\pi^2/45)T_J^3]^{-1}$ and $s_R = (\tilde{\rho}_R - \tilde{p}_R)/T_J$ is the entropy density in the radiation bath . It is precisely this dependance of the Jordan frame temperature on the field that admits this new solution which was missed in the original few chameleon papers. The surfing solution is given by the ansatz

$$\varphi = \varphi_S - \frac{(N - N_S)}{\beta}, \tag{9.34}$$

where N_S is the value of N at the time surfing behaviour begins, and the value of the field at this time is

$$\varphi_S = \varphi_i - \frac{N_S}{\beta} - \frac{\lambda}{\beta}, \tag{9.35}$$

where λ is constant. Inserting the ansatz (9.34) into the expression for the Jordan frame temperature (9.33), and rearranging, one obtains

$$T_J[g_{*S}(T_J)]^{1/3} = [g_{*S}(T_{J,i})]^{1/3} T_{J,i} e^{\lambda}. \tag{9.36}$$

This implies that while the chameleon follows the surfer solution, the Jordan-frame temperature is constant. The temperature is referred to as the surfing temperature, T_S. From (9.34) we see the surfing solution has $\varphi'' = 0$ and $\varphi' = -1/\beta$. Using this with (9.32) one finds

$$\left(1 - \frac{1}{6\beta^2}\right)\left(-\frac{1}{\beta} + 3\beta\Sigma\right) = 0, \tag{9.37}$$

which is satisfied provided

$$\Sigma(T_S) = \frac{1}{3\beta^2}. \tag{9.38}$$

Numerical simulations have indicated that if $\beta > 1.82$, the surfing solution is an attractor in the presence of SM kicks, provided $\dot{\phi}^2 << \rho$ before the onset of the kicks. Thus, chameleons with $\beta > 1.82$ can "surf" the kicks from arbitrarily large initial field values - i.e, they will reach ϕ_{min} regardless of ϕ_i. The problem is that they approach the minimum with a large characteristic velocity $\varphi' = -1/\beta$. At this point the approximations of (9.32) break down and the bare potential term in (9.18) becomes important. Once the chameleon reaches the minimum it will begin to climb the bare potential until its kinetic energy has been exhausted, at which point it will turn around and roll to higher field values. This causes the effective mass of the chameleon to change

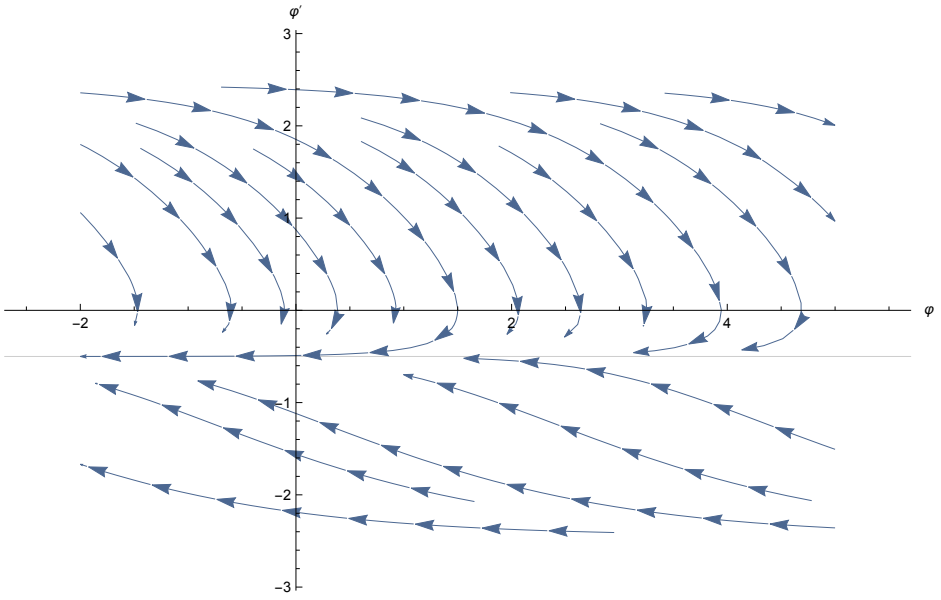

Fig. 9.1 **Phase portrait of φ vs. φ' for the simplified chameleon equation of motion.** i.e. (9.32) with $\beta = 3$ and kick function set to a constant at the critical value $\Sigma = 1/3\beta^2$. The light grey line represents the surfing solution at $-1/\beta$. One can see that all trajectories are eventually attracted toward the surfer.

significantly (see (8.25)) over a very short timescale, say Δt, and such non-adiabatic variations will in turn excite very high energy modes with $k \leq (\Delta t)^{-1}$. These modes are then expected to backreact on the on the background field, causing particle production, and leading to a breakdown of the classical treatment approximation. It is for this reason that the surfer is said to cause catastrophic consequences for the chameleon in the early Universe.[1]

9.4.2 Dynamical Systems Analysis

Subsequent to the analysis of [138, 139], we re-examined the problem in [173] using the tools of dynamical systems analysis to check for fixed points and stability. Here we summarise this analysis as the DBI analysis in §10.5 will follow directly. Neglecting the potential and rearranging (9.16) allows one to eliminate ρ from (9.18) and (9.17).

[1] Interestingly, (9.37) is also satisfied if $\beta = 1/\sqrt{6}$, corresponds to the subset of $f(R)$ models that can map into chameleon models. This condition is not mentioned in [138, 139].

Recalling that $p_\phi = \rho_\phi = \dot{\phi}^2/2$ when the potential is neglected, one finds

$$M_{\rm Pl}^2 H^2(4-\Sigma) + 2M_{\rm Pl}^2\dot{H} + \frac{(2+\Sigma)}{3}\rho_\phi = 0, \tag{9.39}$$

$$\ddot{\phi} + 3H\dot{\phi} + 3M_{\rm Pl}\beta\Sigma H^2\left(1 - \frac{\rho_\phi}{3M_{\rm Pl}^2H^2}\right) = 0. \tag{9.40}$$

By defining the variables

$$x \equiv \beta\phi + M_{\rm Pl}\ln a, \tag{9.41}$$

$$y \equiv \frac{\rho_\phi}{3M_{\rm Pl}^2H^2}, \tag{9.42}$$

$$z \equiv \dot{\phi} + M_{\rm Pl}H. \tag{9.43}$$

one can begin to look for fixed points of the system corresponding to the surfer. Here $\dot{x} = 0$ represents the characteristic property of the surfer, constant Jordan frame temperature, and y, the ratio between the energy density of the scalar and the critical density, is the typical choice for fixed point analysis in cosmology. The autonomous system can now be written

$$\dot{x} = z, \tag{9.44}$$

$$\dot{y} = \frac{1}{H_y}\left[H_z\left(3Hz - \frac{1}{2}M_{\rm Pl}H^2(1-y)\left(2+\Sigma(1-6\beta^2)\right)\right) + \frac{H^2}{2}\left(\Sigma - 4 - y(\Sigma+2)\right)\right], \tag{9.45}$$

$$\dot{z} = -3Hz + \frac{1}{2}M_{\rm Pl}H^2(1-y)\left(2+\Sigma(1-6\beta^2)\right), \tag{9.46}$$

where $H_y = \frac{\partial H}{\partial y}$, $H_z = \frac{\partial H}{\partial z}$ and $H(y,z)$ is given by

$$M_{\rm Pl}^2H^2y = \frac{\left(z - M_{\rm Pl}H\right)^2}{6\beta^2}. \tag{9.47}$$

Solving for $H(y,z)$ explicitly, one finds

$$H(y,z) = \frac{z}{M_{\rm Pl}(1 \pm \sqrt{6\beta^2 y})}. \tag{9.48}$$

Assuming the conformal factor in the matter coupling decreases with time (i.e. $\dot{\phi} < 0$) one has $z/M_{\rm Pl} - H < 0$, and thus one takes the lower root of (9.48). Inserting this expression into (9.44), (9.45) and (9.46) allows one to analyse the fixed points. If

$y \neq 1/6\beta^2$ the system will have fixed points at $z = 0$, with x and y arbitrary constants. This is of little interest as H will always be zero in this case, and thus correspond to an empty Universe. However, if

$$\Sigma = \frac{2}{6\beta^2 - 1}, \tag{9.49}$$

new fixed points appear at $y = 1/6\beta^2$, $z = 0$, with x an arbitrary constant. Since they have $\dot{x} = 0$, and place no constraint on H, they can exist in a Universe at any scale and correspond to constant Jordan frame temperature . These are the problematic points corresponding to the surfing solution of [138, 139]. Numerical simulations of (9.44), (9.45), and (9.46) indicate that when Σ is set to (9.49), all trajectories in the $(H - z)$ plane approach the $z = 0$ line for a wide range of initial conditions, even when $H \neq 0$. Thus, for certain values of β, the kick coming from SM particles (9.23) will satisfy (9.49) and the surfer will be an attractor. This confirms the results of [138, 139]. Note that the discrepancy between (9.49) and (9.38) arises as a result on the approximations made in deriving when (9.32). The results are in fact in agreement to leading order in large β.

Chapter 10

DBI Chameleons

Here we present DBI Chameleons[1], a Dirac-Born-Infeld inspired high energy modification to the chameleon action (8.1). We will see that such a theory has the desired effect of destabilising the surfing solution (see §9.4), and thus preventing the adverse effects of the SM kicks in the early Universe.

10.1 The Action

We propose a high energy modification to the original chameleon action of the from [173]

$$S = \int d^4x\sqrt{-g}\left(\mathcal{L}_{EH} + \mathcal{L}_{DBI}\right) - \int d^4x\mathcal{L}_m\left(\psi_m^{(i)}, \tilde{g}_{\mu\nu}^{(i)}\right) \tag{10.1}$$

with

$$\mathcal{L}_{EH} = \frac{M_{\rm Pl}^2}{2}R, \tag{10.2}$$

$$\mathcal{L}_{DBI} = \Lambda^4 - \Lambda^4\sqrt{1 - \frac{2X}{\Lambda^4}} - V\left(\phi\right), \tag{10.3}$$

where $X \equiv -\partial^\mu\phi\partial_\mu\phi/2$ is the canonical kinetic term, and Λ is the DBI energy scale. Expanding the action to leading order in the low energy limit $\partial\phi \ll \Lambda$, one recovers the original chameleon action (8.1).

[1]The idea for this project is credited to Antonio Padilla at the University of Nottingham. The work on this project was collaborative, with my role focusing on the numerical side. As such, the analysis in §10.2 and §10.5 is not my own, and so I quote our paper. My contribution is presented in Chapter 11, the numerical simulation.

10.2 Symmetries and Irrelevant Operators

Among the entire class of $P(X)$ theories, the DBI model has taken a leading role due to an additional symmetry that keeps non-linearities under control. This feature can be appreciated by first considering the structure of a correction that does not possess such a symmetry. For example, a generic correction to the chameleon action (8.1) of the form [173]

$$\delta\mathcal{L} \sim c_n \frac{(\partial\phi)^{2n}}{\Lambda^{4n-4}} \tag{10.4}$$

would be problematic. At energies where the first irrelevant operator becomes important, an infinite tower of higher order operators would too, causing the dynamics to be dominated by the $n \to \infty$ limit. Each of the (now important) operators would come with an arbitrary coefficient and calculability would be lost as soon as the Z factor becomes large. The DBI correction in (10.3) is different. Taking the decoupling limit of gravity ($M_{\rm Pl} \to \infty$) and neglecting the potential, the theory is built from an infinite tower of $(\partial\phi)^{2n}$ operations describing an interacting scalar propagating on a Minkowski background. Although this is exactly the structure of (10.4), the coefficient of each operator is set by an additional symmetry, namely

$$t \to \frac{1}{\sqrt{1-v^2}}\left(t - v\frac{\phi}{\Lambda^2}\right), \qquad \phi \to \frac{1}{\sqrt{1-v^2}}\left(\phi - \Lambda^2 v t\right). \tag{10.5}$$

This ensures that the structure of the theory is not spoilt by quantum corrections. As long as $\ddot{\phi}$ is kept small in the appropriate units, the theory describes a healthy EFT, even in the limit where $(\partial\phi)^2 \to \Lambda^4$, unlike a generic K-essence model.

Expanding (10.3) to quadratic order about a homogeneous background solution $\phi(t)$ gives

$$\delta\mathcal{L} \sim \frac{1}{2} Z^{\mu\nu}\partial_\mu\delta\phi\partial_\nu\delta\phi, \tag{10.6}$$

where the non-zero components of $Z^{\mu\nu}$ are

$$Z^{tt} = \left(1 - \frac{\dot{\phi}^2}{\Lambda^4}\right)^{-3/2}, \qquad Z^{ij} = \left(1 - \frac{\dot{\phi}^2}{\Lambda^4}\right)^{-1/2}\delta^{ij}, \tag{10.7}$$

and $\delta\phi$ is a small perturbation. Clearly $Z^{\mu\nu}$ gets large as $\dot{\phi} \to \Lambda^2$, which ensures that the fluctuations become weakly coupled to matter, as desired.

The symmetry that sets each coefficient is the four dimensional remnant of a fully realised five dimensional Poincaré invariance [174]. Consider a higher dimensional picture of a probe brane in Minkowski bulk, localised in the fifth dimension at $y = \phi(x^\mu)/\Lambda^2$. The four dimensional effective description of the brane depends on the induced metric,

$$\hat{g}^{\mu\nu} = \eta^{\mu\nu} + \frac{\partial_\mu\phi\partial_\nu\phi}{\Lambda^4}, \tag{10.8}$$

and gives the leading order contribution to the brane action as

$$S = -\Lambda^4 \int d^4x\sqrt{-\hat{g}} = -\Lambda^4 \int d^4x\sqrt{1 + \frac{(\partial\phi)^2}{\Lambda^4}}, \tag{10.9}$$

where Λ^4 is identified with brane tension. This action is invariant under five dimensional Lorentz transformations, which gives rise to the non-linear symmetry (10.5). However, it is truncation of the full action. Higher order corrections to (10.9) will also generate ϕ operators invariant under the symmetry (10.5), and its important to check that they remain small so that the effective description can be trusted. These corrections, involving derivatives of the induced metric, are encoded in increasing powers of the brane's extrinsic curvature K^μ_ν. Any Lorentz invariant operator built from K^μ_ν could in principal be generated by quantum corrections. Since the truncation in (10.9) is zeroth order in extrinsic curvature, we require that first order terms built from K^μ_ν be small. Thus, we require that

$$K^\mu_\nu \ll \Lambda, \tag{10.10}$$

where the extrinsic curvature is given by

$$K^\mu_\nu = \frac{\gamma}{\Lambda^2}\nabla^\mu\nabla_\nu\phi - \frac{\gamma^2}{\Lambda^6}\nabla^\sigma\phi\nabla^\mu\phi\nabla_\nu\phi\nabla_\sigma\phi, \tag{10.11}$$

and

$$\gamma = \frac{1}{\sqrt{1 + \frac{(\partial\phi)^2}{\Lambda^4}}} \tag{10.12}$$

is referred to as the "gamma-factor", akin to Lorentz factor of Special Relativity. On a flat FLRW background this translates to

$$\frac{\gamma H\dot{\phi}}{\Lambda^3} \ll 1, \qquad \frac{\gamma^3\ddot{\phi}}{\Lambda^3} \ll 1. \tag{10.13}$$

We will see that these conditions hold, and thus the truncation to the DBI square root is consistent, even in the regime where the Z factor is large and the scalar perturbations become weakly coupled to matter.

The symmetry (10.5) is however broken in the full action (10.1) by finite $M_{\rm Pl}$ and non-zero potential $V(\phi)$, and this may cause one to worry weather the structure of the theory is spoiled by loop corrections. Such corrections arising from finite $M_{\rm Pl}$ will be Planck suppressed and can consistently be neglected provided $\Lambda \ll M_{\rm Pl}$. Corrections associated with $V(\phi)$ depend on form of the potential. Assuming a runaway potential as described in §8.1, the strength of self-interactions is governed by the mass scale M, and the associated corrections enter into the action with positive powers of M. Thus the symmetry is only weakly broken when $M \ll \Lambda$, and so as long as this condition holds, symmetry breaking operators associated with $V(\phi)$ can consistently be neglected. Since Λ is set by early Universe physics, and M by late Universe physics, this condition will be naturally satisfied. Thus, provided we have

$$M \ll \Lambda \ll M_{\rm Pl}, \tag{10.14}$$

the DBI structure will be stable against loop corrections associated with the symmetry breaking operators.

10.3 Energy-Momentum Tensor for the Field

Since the scalar Lagrangian density (10.3) does not have a canonical kinetic term, the energy-momentum tensor and the resulting energy density and pressure take more complicated forms. Assuming a scalar Lagrangian density of the form

$$\mathcal{L}_{P(X)} = P - V, \tag{10.15}$$

where is $P = P(X)$ is a general function of the kinetic term $X \equiv -(\partial\phi)^2/2$, one finds a energy-momentum tensor of the form

$$\begin{aligned} T_{\mu\nu} &= -2\frac{\partial \mathcal{L}}{\partial X}\frac{\partial X}{\partial g^{\mu\nu}} + g_{\mu\nu}\mathcal{L} \\ &= P_{,X}\,\partial_\mu\phi\partial_\nu\phi + g_{\mu\nu}\left(P - V\right), \end{aligned} \tag{10.16}$$

where $_{,X} \equiv \frac{\partial}{\partial X}$. Applying the usual definitions for energy density (D.12) and pressure (D.13) to (10.16), and again assuming a comoving observer and spatially homogenous field (9.6), yields a modified expressions for the scalar field energy density

$$\begin{aligned} \rho_\phi &= P_{,X}\,\partial_\mu\phi\partial_\nu\phi u^\mu u^\nu + u^\alpha u_\alpha\left(P - V\right), \\ &= P\dot{\phi}^2 - P + V, \\ &= 2XP_{,X} - P + V, \end{aligned} \tag{10.17}$$

and scalar field pressure

$$\begin{aligned} p_\phi &= \frac{1}{3}\left\{T_{\mu\nu}u^\mu u^\nu + T_{\mu\nu}g^{\mu\nu}\right\} \\ &= \frac{1}{3}\left\{\left(2XP_{,X} - P + V\right) + P_{,X}\,\partial^\alpha\phi\partial_\alpha\phi + 4\left(P - V\right)\right\} \\ &= P - V. \end{aligned} \tag{10.18}$$

By choosing $P(X) = X \Rightarrow P' = 1$, one can see that the above expression (10.16), (10.17) and (10.18) all reduce to their canonical form (D.11), (9.7) and (9.8) , respectively. In the case of the DBI chameleon (10.1) the expressions (10.16), (10.17) and (10.18) apply with

$$P(X) = \Lambda^4\left(1 - \sqrt{1 - \frac{2X}{\Lambda^4}}\right). \tag{10.19}$$

10.4 Background Equations

One of the advantages of working in the Einstein frame is that any change to the scalar Lagrangian density (8.3) leaves the geometry part of the field equations remain largely unaltered -the only difference being a modification to the EMT sourcing the evolution. The variation of the action (10.1), and the calculation of the resulting equations of motion follow exactly the same steps as in §8.2. Again, assuming a flat FLRW metric (9.1), the background equations for the geometry can be read off (8.13), with $T^\phi_{\mu\nu}$ given

by (10.16). As before, the Friedmann equations are found to be

$$3M_{\rm Pl}H^2 = \rho_\phi + \rho, \tag{10.20}$$

$$M_{\rm Pl}^2\left(2\dot{H} + 3H^2\right) = -p_\phi - p, \tag{10.21}$$

where the energy density and pressure in the scalar are now given by (10.17) (10.18), respectively. The first term in the scalar EOM, in a FLRW background, can be written as

$$\begin{aligned}\partial^\mu\partial_\mu\left(P_{,X}\,\phi\right) &= \frac{1}{\sqrt{-g}}\partial^\mu\left(\sqrt{-g}\partial_\mu(P_{,X}\,\phi)\right),\\ &= \frac{1}{\sqrt{-g}}\partial^\mu\sqrt{-g}\partial_\mu(P_{,X}\,\phi) + \partial^\mu\partial_\mu(P_{,X}\,\phi),\\ &= -\frac{1}{a^3}\partial_t\left(a^3\right)P_{,X}\,\dot{\phi} - \partial_t(P_{,X}\,\dot{\phi}),\\ &= -\left(\partial_t(P_{,X}\,\dot{\phi}) + 3HP_{,X}\,\dot{\phi}\right),\end{aligned} \tag{10.22}$$

which allows one to then write the scalar EOM as

$$\left(P_{,X} + 2XP_{,XX}\right)\ddot{\phi} + 3HP_{,X}\,\dot{\phi} + V'(\phi) = -\frac{\beta}{M_{\rm Pl}}\rho\Sigma. \tag{10.23}$$

One can now see that taking the limit where $\Lambda \to \infty$ decouples the DBI interactions and one recovers the original chameleon theory.

10.5 Dynamical Systems Analysis

As we did §9.4.2 for the original chameleon, we perform a dynamical systems analysis of the DBI chameleon to find the fixed points. Eliminating ρ by rearranging (10.20) and then substituting into (10.21) and (10.23) yields

$$M_{\rm Pl}^2H^2(4-\Sigma) + 2M_{\rm Pl}^2\dot{H} + p_\phi - \rho_\phi + \frac{(2+\Sigma)}{3}\rho_\phi = 0, \tag{10.24}$$

$$\left(P_{,X} + 2XP_{,XX}\right)\ddot{\phi} + 3HP_{,X}\,\dot{\phi} + 3M_{\rm Pl}\beta\Sigma H^2\left(1 - \frac{\rho_\phi}{3M_{\rm Pl}^2H^2}\right) = 0. \tag{10.25}$$

Introducing the same variables (9.41), (9.42) and (9.43) from the dynamical systems analysis of §9.4.2, one can begin to look for fixed points of the system. Again, $\dot{x} = 0$ is the characteristic property of the surfer, constant Jordan frame temperature, and y is ratio between the energy density of the scalar and the critical density. One then

arrives at the following autonomous system [173]

$$\dot{x} = z \tag{10.26}$$

$$\dot{y} = \frac{1}{H_y}\left[H_z\left(3Hs^2z - \frac{1}{2}M_{\rm Pl}H^2\left[(1-y)\left(2+\Sigma(1-6\beta^2s^3)\right)\right.\right.\right.$$
$$\left.\left.\left.+3y(1-s)-6(1-s^2)\right]\right) + \frac{H^2}{2}\left(\Sigma - 4 - y(\Sigma+2) + 3y(1-s)\right)\right] \tag{10.27}$$

$$\dot{z} = -3Hs^2z + \frac{1}{2}M_{\rm Pl}H^2\left[(1-y)\left(2+\Sigma(1-6\beta^2s^3)\right) + 3y(1-s) - 6(1-s^2)\right] \tag{10.28}$$

where $s = \sqrt{1 - \dfrac{(z - M_{\rm Pl}H)^2}{\beta^2\Lambda^4}}$. And as before $H_y = \frac{\partial H}{\partial y}$, $H_z = \frac{\partial H}{\partial z}$ but now $H(y,z)$ given implicitly by the following equation

$$\left(\Lambda^4 - \frac{(z - M_{\rm Pl}H)^2}{\beta^2}\right)\left(1 + \frac{3M_{\rm Pl}^2H^2y}{\Lambda^4}\right)^2 = \Lambda^4. \tag{10.29}$$

In §9.4.2 we identified the surfer as the line $z = 0$ with y chosen so that (9.47) does not constrain H. Other fixed points corresponded to empty universes with $H = 0$ and were of no interest. In complete analogy, here we identify the generalised surfer by requiring $z = 0$ and with y chosen such that (10.29) does not constrain H. Setting $z = 0$ in (10.29) gives a polynomial in $M_{\rm Pl}H$, namely

$$\left(\frac{9y^2}{\beta^2\Lambda^8}\right)(M_{\rm Pl}H)^6 + \left(\frac{6y}{\beta^2\Lambda^4} - \frac{9y^2}{\Lambda^4}\right)(M_{\rm Pl}H)^4 + \left(\frac{1}{\beta^2} - 6y\right)(M_{\rm Pl}H)^2 = 0. \tag{10.30}$$

This will only fail to constrain H if, and only if, all the coefficients vanish. One possibility is if $\Lambda \to \infty$ and $y = 1/6\beta^2$. As mentioned earlier, this is the DBI decoupled limit. Its essentially the original chameleon theory, so its not surprising the surfer shows up here. The only other possibility is if one sets $y = 0$ and have $\beta \to \infty$. This is the strong coupling limit. Again its unsurprising the surfer emerges here, since strongly coupled SM kicks will dominate over the DBI self interactions. Apart from those two, there are no other fixed points. Since the action for the DBI-chameleon reduces to the original chameleon action (at leading order) when $\partial\phi \ll \Lambda$, the DBI corrections only become important when $\dot{\phi}^2 \sim \Lambda^4$. And since one has $\dot{\phi} = -M_{\rm Pl}H/\beta$ on a would-be surfer, its expected that the DBI corrections will spoil any surfing behaviour provided $\Lambda^2 \lesssim M_{\rm Pl}H/\beta$, where the scale $M_{\rm Pl}H$ is set by the scale at which the kicks occur.

Numerically, we expect the surfer will emerge for finite Λ, provided it is sufficiently large compared to the other energy scales involved.

Chapter 11

Numerical Simulations

Here we confirm the results of the dynamical systems analysis by performing numerical simulations[1], solving the original chameleon and DBI corrected systems of equations with realistic initial conditions, in the presence of a simplified kick function.

11.1 Equations for the Numerics

As was done in [138, 139], we make a change of variable to ones more suited to numerical simulation. We rescale the field ϕ by $M_{\rm Pl}$ and change the time variable to Einstein frame E-folds. Applying (9.31) to the equations of motion for the original chameleon theory (9.39) and (9.40) one finds

$$2\frac{H'}{H} + (4 - \Sigma) + \left(\frac{2+\Sigma}{3}\right)\frac{\varphi'^2}{2} = 0, \tag{11.1}$$

$$\varphi'' + \left(\frac{H'}{H} + 3\right)\varphi' + 3\beta\Sigma\left(1 - \frac{\varphi'^2}{6}\right) = 0, \tag{11.2}$$

[1]This part is my contribution to the collaboration [173]. I was responsible for deriving equations suited to numerical implementation, coding the simulations, choosing suitable parameter values to illustrate the effect of the DBI correction and producing the plots. We then drew conclusions on the plots, collectively, after much discussion. Thus in §11.2 I quote the results from our paper.

where in this section a prime denotes differentiation with respect to N. Similarly, the equations of motion for the DBI-chameleon (10.24) and (10.25) become

$$2\frac{H'}{H} + (4 - \Sigma) + \left[p_\phi - \rho_\phi + \left(\frac{2+\Sigma}{3}\right)\rho_\phi\right] / M_{\rm Pl}^2 H^2 = 0, \quad (11.3)$$

$$\left(P_{,X} + P_{,XX}\, M_{\rm Pl}^2 H'^2 \varphi'^2\right)\left(\varphi'' + \frac{H'}{H}\varphi'\right) + 3P_{,X}\,\varphi' + 3\beta\Sigma\left(1 - \frac{\rho_\phi}{3M_{\rm Pl}^2 H^2}\right) = 0. \quad (11.4)$$

We approximate the kick function as a Gaussian bump in terms of Jordan frame temperature, given by

$$\Sigma(T_J) = A \exp \frac{(\log T_J - \log T_{peak})^2}{\sigma^2} \quad (11.5)$$

where A, T_{peak} and σ are chosen by eye from Figure 2 in [138]. Since the Jordan frame temperature goes like $1/\tilde{a}$, the relation to Jordan frame e-folds is simply

$$T_J\left(\tilde{N}\right) = T_{J,i} \exp\left(-\tilde{N}\right) \quad (11.6)$$

where T_i is some initial temperature. The Jordan frame and Einstein frame e-folds are related by

$$\tilde{N}(N) = N + \beta\left(\varphi(N) - \varphi_i\right). \quad (11.7)$$

With (11.5) (11.6) (11.7) we get an expression for the kick function in terms of Einstein frame e-folds $\Sigma(N)$, to be used in the simulations. We note that $T_J(N)$ is not monotonically decreasing. From (11.7), we see that if φ decreases faster than N increases (i.e. faster than the critical velocity of the surfer), the Jordan frame will contract while the Einstein frame expands. We will see that this does in fact happen in our simulations.

11.2 Results

We solve the chameleon evolution equations, (11.1) and (11.2), and DBI-chameleon counterparts, (11.3) and (11.4), in the presence Gaussian kick function (11.5). To demonstrate the effect of the DBI correction on the surfing solution, we vary the value of the DBI energy scale, Λ, and investigate the resulting trajectories in phase space. In order to consistently compare and contrast with the chameleon we match the initial conditions for ϕ and $\dot{\phi}$ in each case, while maintaining $\gamma \sim \mathcal{O}(1)$ to ensure the energy

densities are comparable. In all cases we choose the initial Jordan frame temperature to be $T_{J,i} = 10^{-2}$GeV, approximately the temperature at which the electron/positron kick starts, and the matter coupling strength to be $\beta = 3$. We choose both positive and negative initial conditions for $\dot{\phi}$ and relate their energy scale to that of the kick by

$$\dot{\phi}_i = \Lambda_k^2\{0.8, -0.8\}, \tag{11.8}$$

with the energy scale of the kick given by $\Lambda_k = 10T_{peak} = 2 \times 10^{-3}$GeV. Thus, when $\Lambda \approx \Lambda_k$, we have $\dot{\phi}$ strongly in the DBI regime (with $\gamma \approx 1.7$) and we expect surfing behaviour will be destroyed. Neglecting any contribution to the energy density from non-relativistic matter, the initial energy density ρ_i is dominated by radiation and is given by

$$\rho_{r,i} = \frac{\pi^2}{30} g_* \left(T_{J,i}\right) T_{J,i}^4 e^{4\beta\varphi_i}, \tag{11.9}$$

with $g_*(T_{J,i}) = 10.75$. This closes the system of equations and allows one to calculate the three initial conditions $\varphi_i, \varphi_i', H_i$ required to solve either (11.1) and (11.2), or (11.3) and (11.4).

We perform five runs of the DBI-chameleon system with Λ values ranging between Λ_k and $10\Lambda_k$. The results are shown in Figure 11.1, with the thick black dotted line corresponding to the original chameleon, the grey broken lines (dashed, dot-dashed and dotted) corresponding to the DBI-chameleon runs that do surf, and the coloured solid lines corresponding to DBI-chameleons that don't surf. We only show trajectories for positive $\dot{\phi}_i$, as the negative ones are very similar, and all curves represent 15 Einstein frame e-folds. In both subplots of Figure 11.1 we see that surfing behaviour is destroyed as $\Lambda \to \Lambda_k$.

In Figure 11.1a we show the field trajectories in the $\varphi - \varphi'$ plane with the horizontal dotted grey line indicating the surfing solution at $-1/\beta$. We see that as $\Lambda \to \Lambda_k$ the field trajectories are no longer attracted to the horizontal line at $-1/\beta$, but rather, they decay to $\varphi' = 0$. In figure 11.1b we show the kick as a function of Einstein frame e-folds with the horizontal dotted grey line indicating the critical value at which the surf occurs, $2/(6\beta^2 - 1)$. Similarly, as $\Lambda \to \Lambda_k$, the kick function decays to zero in a finite time, instead of getting stuck at critical value. As a result, DBI-chameleon are only driven by the kick for a finite time, unlike the original chameleons which feel a constant kick.

The field excursion versus Jordan frame temperature is shown in Figure 11.2, with the vertical line indicating the critical temperature of the surf, T_J^c. We see that as

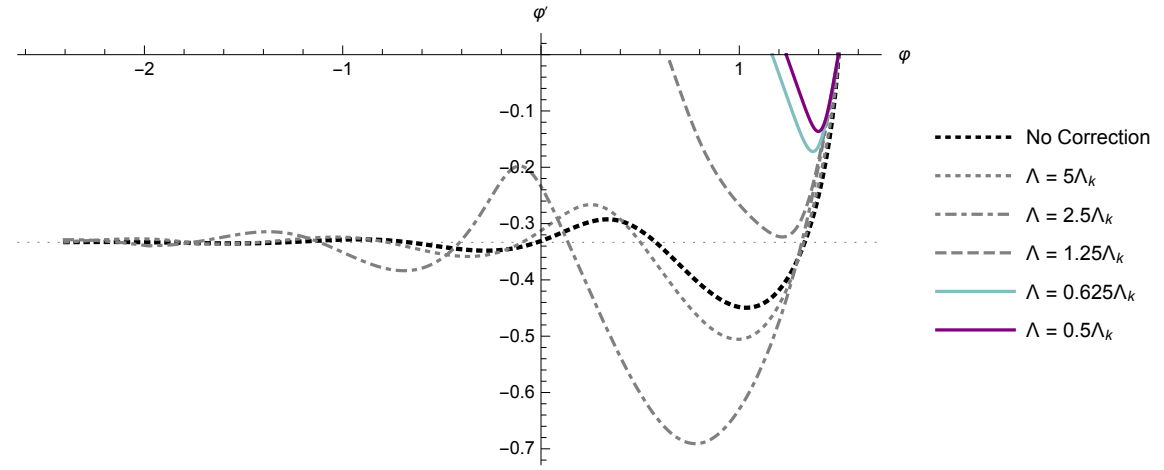

(a) Phase diagram for φ' vs. φ. Dotted light grey line indicates the surfing solution at $-1/\beta$.

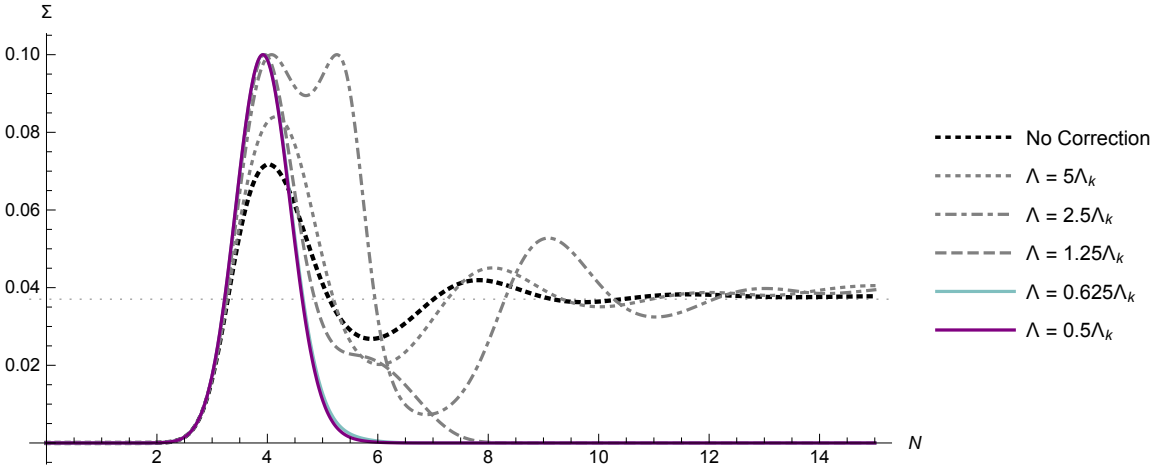

(b) The kick as a function of Einstein frame e-folds. Dotted light grey line indicates $2/(6\beta^2-1)$, the critical value of the kick at which the surf occurs. Chameleons that surf see a constant kick at this value.

Fig. 11.1 **Results from the numerical simulations for various values of Λ.** The thick black dotted line corresponds to the original chameleon without DBI correction. Grey broken lines (dashed, dot-dashed and dotted) correspond to chameleons with DBI correction that do surf. Solid lines correspond to chameleons for which the DBI correction effectively destroys surfing behaviour.

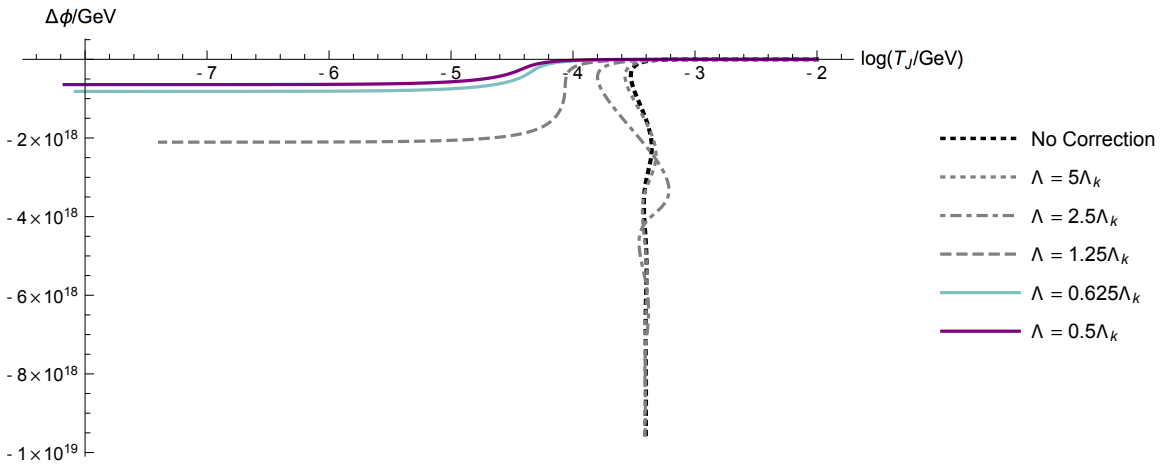

Fig. 11.2 **Field excursion vs. Jordan frame temperature for various values of Λ.** Plot legend is as in Figure 11.1. Chameleons which surf the kicks have large field excursions at approximately constant Jordan frame temperature given by T_J^c (vertical line). One can see that when the DBI correction effectively destabilises surfing behaviour, field excursions quickly become sub-Planckian

$\Lambda \to \Lambda_k$ the Jordan frame temperature doesn't get stuck at the critical temperature of the surf, but decrease below it, reducing the field excursion. The stronger the DBI correction the more the field excursion is suppressed. While one might worry that field excursions are still Planckian, its important to realise that this represents the worst case scenario, in which the DBI scale close to the kick scale, and the initial speed of the chameleon close to the speed limit. Field excursions can easily be suppressed to safe values by lowing the DBI scale by another order of magnitude. There are two mechanisms responsible for this, which we illustrate this in Figures 11.3a and 11.3b. In Figure 11.3a we hold $\dot{\phi}_i$ constant while lowering Λ, such that the γ factor increases. This weakens the effective coupling between matter and the chameleon thereby suppressing excursions generated by the kick. In Figure 11.3b we lower $\dot{\phi}_i$ and Λ in tandem, such that the γ factor remains constant. Now the effective coupling is doesn't change, but excursions are suppressed due to the "cosmic speed limit" imposed by the DBI structure. Thus, choosing $\phi_i < 0.1 M_{pl}/\beta$ before the onset of the electron kick, as required by BBN bounds, is no longer problematic. The field will not crash into the bare potential thanks to the DBI suppression of field excursions. Lastly, in Figure 11.4 we show that in all of our simulations the higher order corrections (10.13) remain suppressed, and thus we can trust the EFT description.

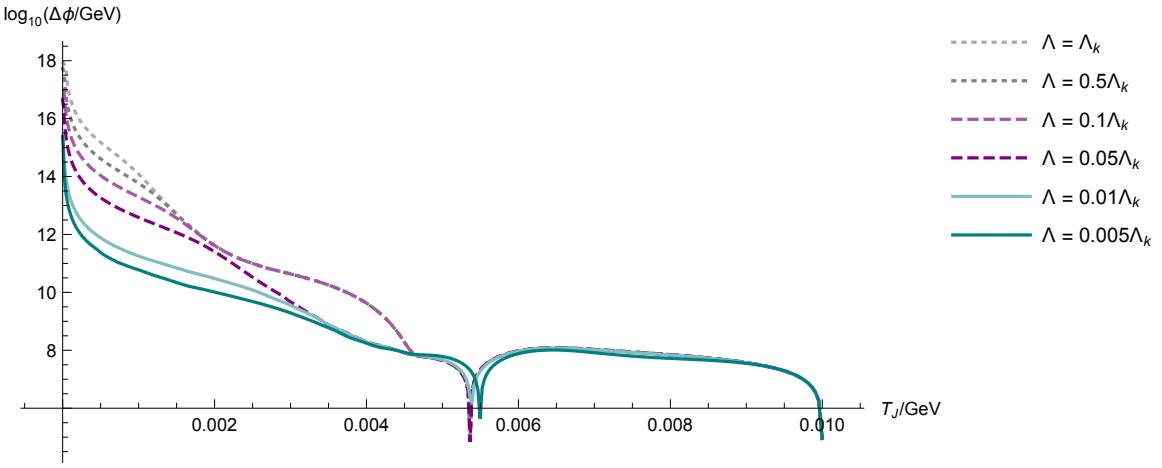

(a) Field excursions vs Jordan frame temperature, for variations in the DBI scale at fixed initial field velocity.

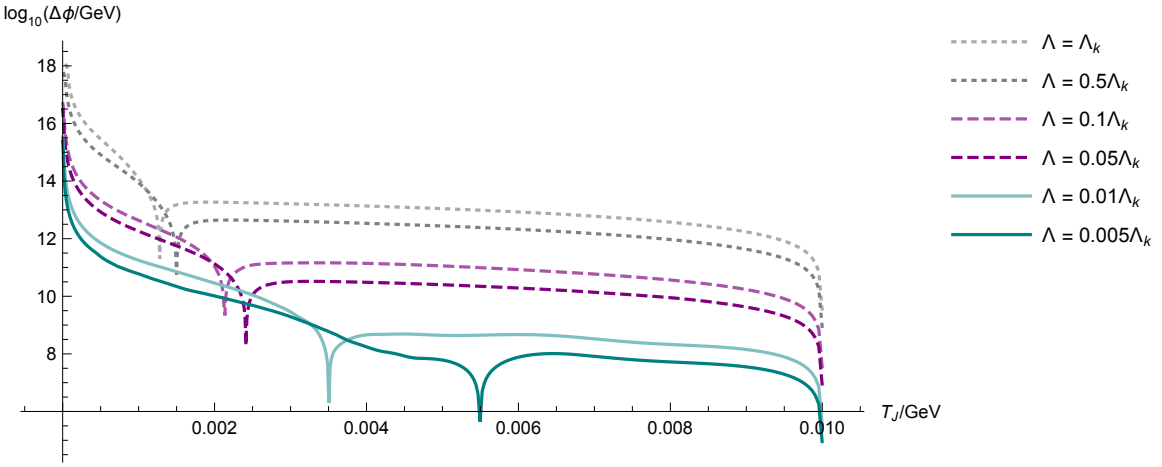

(b) Field excursions vs Jordan frame temperature for variations in the DBI scale and the initial field velocity, holding the effective coupling fixed.

Fig. 11.3 **Limiting field excursions.** Both plots shows the field excursions quickly becoming sub-Planckian. In the top plot this is due to a weakening of the effective coupling through a cosmological Vainshtein effect, whereas in the lower plot this is due to the DBI structure imposing a 'cosmic speed limit' on the scalar.

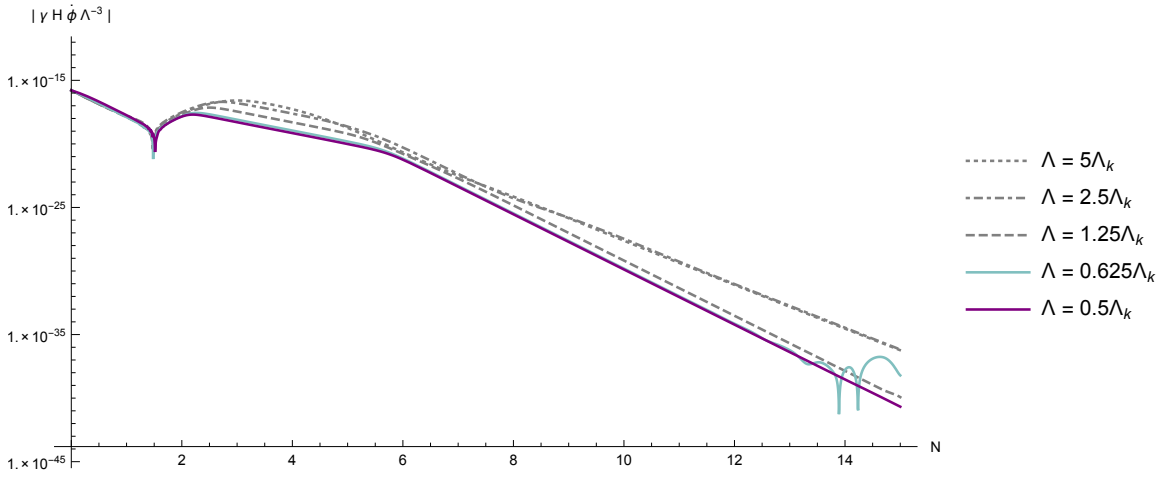

(a)

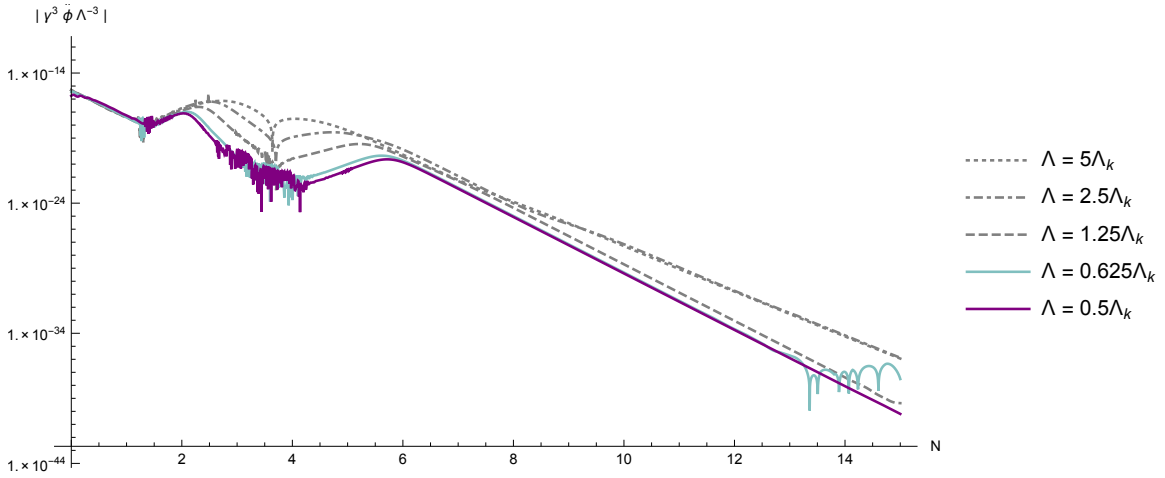

(b)

Fig. 11.4 **Conditions for the suppression of higher order operators.** All curves are $\ll 1$ and thus higher order operators can consistently be neglected.

Chapter 12

Conclusions

The chameleon model, and in particular its screening mechanism, remains an interesting tool to hide light scalar fields from detection. This has been of great interest to may theoreticians, as scalars can arise quite naturally in the low energy limit of some high energy theories.

In recent literature there have been claims that, for a wide range of initial conditions, the chameleon is not a consistent classical field theory for describing the early Universe. During radiation domination a large contribution to the trace of the stress energy tensor is produced by relativistic massive particles as they drop out of equilibrium with the radiation bath. This imparts a large amount of kinetic energy into the chameleon, causing large field excursions and driving it rapidly towards the minimum of its effective potential. As this happens the Jordan frame becomes static, thus causing the temperature to remain constant and Σ to remain non-zero until the minimum is reached. Once at the minimum the field begins to climb up (and eventually bounce back off) the bare potential, causing rapid variation in the mass of the field, and the production of highly energetic quantum fluctuations. Since perturbation theory breaks down at the bounce, this seemingly invalidates any classical treatment of the chameleon in the early Universe, and implies that the theory is not predictive as far back as BBN.

Even if predictability is not lost through the bounce, as some might argue, constraints on the variation of particle masses strongly constrain the field excursion between now and BBN. This in turn limits viable initial conditions for the model - not a desirable feature, as it raises some fine-tuning issues. All of this implies that the chameleon must be sufficiently weakly coupled to matter in order to avoid these problems.

Here we have presented DBI-chameleons. We have shown that considering a chameleon theory with a high energy DBI correction to the kinetic term destabilises

the surfing solution and protects the field from dangerously large field excursions. The DBI term has a kind of kinetic screening effect, where derivative self-interactions of the scalar dominate high energies, inducing a large Z factor on non-trivial homogeneous backgrounds, and thus dynamically weakening the coupling to matter in the early Universe.

We have re-analysed the evolution of the scalar in the presence of a single SM kick, using numerical simulations. In Mathematica, we developed code to integrate the evolution equations for various values of the DBI energy scale and initial conditions. We have shown that for suitably chosen (but technically natural) parameters

$$\frac{(\mathrm{MeV})^2}{M_{\mathrm{Pl}}} \ll \Lambda \lesssim \frac{\mathrm{MeV}}{\sqrt{\beta}} \tag{12.1}$$

the dynamics are dominated by the non-linear derivative interactions as SM particles become non-relativistic, thereby suppressing the effect of the kicks. This destabilises the surfing solution, preventing large field excursions at constant Jordan frame temperature. Decreasing the DBI scale to just an order of magnitude below the scale of the final kick sufficiently decreases the cosmic speed limit for the scalar, causing field excursions to quickly become sub-Planckian (up to factors of β), so the chameleon can easily avoid crashing into the minimum of the effective potential during BBN. This ensures that for a suitably chosen energy scale the EFT describing the DBI chameleon will not suffer from a breakdown in calculability as described in [138, 139]. We do not expect this behaviour to be unique to this particular correction which we study here, and it is conceivable that other UV corrections may possess such a behaviour. However, thanks to the additional symmetry of the DBI term, higher order operators remain suppressed and can consistently be neglected, unlike a generic k-essence model (where higher-order operations do become relevant close to the cutoff). This is the origin of the lower bound in (12.1), and translates to a bound on the matter coupling $\beta \ll 10^{21}$ - extremely mild in contrast to those of [138, 139], or even the best experimental bound which are currently set at $\beta \lesssim 10^9$ [175].

To summarise, the DBI chameleon retains the desirable screening properties of the original theory, while rendering the SM kicks of the early Universe harmless. The derivative interactions which we introduce are sub-dominant in the infrared, and so we recover the original theory in the late Universe. From this perspective we believe the DBI chameleon is better placed than the original chameleon theory to describe physics throughout our cosmic history.

Part III

Epilogue

Physical systems in Nature are often best described by systems of DEs, the solutions to which one typically seeks in order to predict the future behaviour of the system. Within the field of Cosmology many problems require an understanding of the dynamical behaviour of some gravitationally interacting system, and so will often involve solving several, possibly non-linear, coupled DEs. This can be tricky, if not impossible, using analytical methods alone. As a result, numerical methods have come to play a central role in the field. Although the solutions found using these methods are only valid for a particular initial condition, and don't make general statements about a model, they do provide a useful tool that is complimentary to analytical methods, such as dynamical systems analysis. This thesis presents two applications of numerical methods to two quite unrelated questions in contemporary cosmology. While they both essentially aim to approximate the solution to a set DEs, they are posed within different theories of gravity, and each have very different motivations.

Part one is rooted in the very well tested framework that is GR, and is motivated by a need to better understand how inhomogeneities affect observations. It is primarily concerned with structure in the late, low redshift Universe, and how it affects observations. In this case numerical methods are employed to get a particular solution to the relevant DEs, the form of which we do not know *a priori*, for a given set of initial conditions and model parameters. We used MATLAB and a built in adaptive Runge-Kutta solver to integrate 40 1st order coupled ODEs along 200 observation directions. From the solutions we constructed observable quantities along each line of sight, which we then interpolate on 20 redshift slices, and save. We then used the resulting data to construct sky maps of observables at constant redshift. This allows us to calculate the observables of a model for a given setup. It can be thought of as a tool to aid in model building, as it allows proposed models to be tested, and refined or rejected, by comparison with observations of similar structures. It is also a crucial ingredient in solving the inverse problem (i.e. going from observations to the metric of spacetime), for which one needs test data from a known model.

Part two on the other hand, presents an extension to the (perhaps more speculative) Chameleon theory gravity, dubbed DBI chameleons, and is motivated by a desire to remove a particular pathology present in the original theory. Specifically, in the early, high redshift, near homogeneous Universe, around the time of BBN. In this case we use numerical methods to confirm the behaviour, and support the conclusions, that we expected from an analytic dynamical systems analysis. We used Mathematica and its built-in ODE solver to solve 3 coupled 1st order ODEs in order to track the behaviour of the chameleon field and its DBI modification in the early Universe, for

various values of the DBI energy scale. The point of this was to compare and contrast the behaviour of the two theories, and demonstrate the efficacy of a DBI correction to the chameleon action in suppression of field excursions. We showed that this put the proposed DBI-chameleon on firmer footing than the original model, in the early Universe.

Indeed, the two projects represent two very different lines of research. In one we built a tool which can be applied to numerous different investigations, and in the other we simply demonstrated that our proposed model is well behaved in a certain regime. But both benefit from the ability of computers to approximate the solutions to complex systems of equations.

Appendix A

Propagating the Observer's Basis Using the Geodesic Deviation Equation

A.1 Geodesic Deviation Equation as a Total Derivative

The standard geodesic deviation equation uses tensor derivatives, which are ideal for physical understanding and for doing covariant calculations. But to actually integrate vector or tensor components along a path, we need to convert the absolute derivatives into total derivatives, and re-write the equation as an ordinary differential equation.

The geodesic deviation equation is

$$\frac{\delta^2 W^a}{\delta v^2} = -R^a{}_{bcd} V^b W^c V^d \ , \tag{A.1}$$

$$R^a{}_{bcd} = -\Gamma^a{}_{cb,d} + \Gamma^a{}_{db,c} - \Gamma^e{}_{cb}\,\Gamma^a{}_{de} + \Gamma^e{}_{db}\,\Gamma^a{}_{ce} \ , \tag{A.2}$$

where W^a is the deviation vector field, $V^a = \mathrm{d}x^a/\mathrm{d}v$ is the vector field for a geodesic congruence, and v is the affine parameter along V^a, while (A.2) applies to a coordinate basis. The requirements for the geodesic deviation construction are that V^c is geodesic, and it commutes with W^d,

$$\frac{\delta V^a}{\delta v} = \frac{\mathrm{d}V^a}{\mathrm{d}v} + V^b \Gamma^a{}_{bc} V^c = 0 = V^b \nabla_b V^a \tag{A.3}$$

$$V^b \nabla_b W^a - W^b \nabla_b V^a = 0 \tag{A.4}$$

However, in using (A.1) to propagate W^c along a geodesic congruence, we actually need the variation of the components of W^b, that is $\mathrm{d}^2W^a/\mathrm{d}v^2$. Thus

$$\frac{\delta W^a}{\delta v} = V^b\Big(\partial_b W^a + \Gamma^a{}_{bc}W^c\Big) \tag{A.5}$$

$$= \frac{\mathrm{d}W^a}{\mathrm{d}v} + V^b\Gamma^a{}_{bc}W^c \tag{A.6}$$

$$\frac{\delta}{\delta v}\frac{\delta W^a}{\delta v} = V^b\left(\partial_b\frac{\delta W^a}{\delta v} + \Gamma^a{}_{bc}\frac{\delta W^c}{\delta v}\right) \tag{A.7}$$

$$= V^b\left(\partial_b\left\{\frac{\mathrm{d}W^a}{\mathrm{d}v} + V^d\Gamma^a{}_{dc}W^c\right\} + \Gamma^a{}_{bc}\left\{\frac{\mathrm{d}W^c}{\mathrm{d}v} + V^d\Gamma^c{}_{de}W^e\right\}\right) \tag{A.8}$$

$$= \left\{\frac{\mathrm{d}^2W^a}{\mathrm{d}v^2} + \frac{\mathrm{d}V^d}{\mathrm{d}v}\Gamma^a{}_{dc}W^c + V^bV^d\Gamma^a{}_{dc,b}W^c + V^d\Gamma^a{}_{dc}\frac{\mathrm{d}W^c}{\mathrm{d}v}\right\} + \left\{V^b\Gamma^a{}_{bc}\frac{\mathrm{d}W^c}{\mathrm{d}v} + V^b\Gamma^a{}_{bc}V^d\Gamma^c{}_{de}W^e\right\} \tag{A.9}$$

$$= \frac{\mathrm{d}^2W^a}{\mathrm{d}v^2} + \Gamma^a{}_{bc}\left(W^c\frac{\mathrm{d}V^b}{\mathrm{d}v} + 2V^b\frac{\mathrm{d}W^c}{\mathrm{d}v}\right) + V^bW^cV^d\Big(\Gamma^a{}_{dc,b} + \Gamma^a{}_{be}\,\Gamma^e{}_{dc}\Big) \tag{A.10}$$

(by (A.1)) $$= -R^a{}_{bcd}V^bW^cV^d = V^bW^cV^d\Big(\Gamma^a{}_{cb,d} - \Gamma^a{}_{db,c} + \Gamma^e{}_{cb}\,\Gamma^a{}_{de} - \Gamma^e{}_{db}\,\Gamma^a{}_{ce}\Big) \tag{A.11}$$

$\therefore$ $$\frac{\mathrm{d}^2W^a}{\mathrm{d}v^2} = -\Gamma^a{}_{bc}\left(W^c\frac{\mathrm{d}V^b}{\mathrm{d}v} + 2V^b\frac{\mathrm{d}W^c}{\mathrm{d}v}\right) + V^bW^cV^d\Big(\Gamma^a{}_{cb,d} - \Gamma^a{}_{db,c} - \Gamma^a{}_{dc,b} + \Gamma^e{}_{cb}\,\Gamma^a{}_{de} - \Gamma^e{}_{db}\,\Gamma^a{}_{ce} - \Gamma^a{}_{be}\,\Gamma^e{}_{dc}\Big) \tag{A.12}$$

$$= -\Gamma^a{}_{bc}\left(W^c\frac{\mathrm{d}V^b}{\mathrm{d}v} + 2V^b\frac{\mathrm{d}W^c}{\mathrm{d}v}\right) - V^bW^cV^d\Big(\Gamma^a{}_{db,c} + \Gamma^e{}_{db}\,\Gamma^a{}_{ce}\Big) \tag{A.13}$$

$$= -2\Gamma^a{}_{bc}V^b\frac{\mathrm{d}W^c}{\mathrm{d}v} - V^bW^cV^d\Gamma^a{}_{db,c} - \Gamma^a{}_{ec}W^c\left(\frac{\mathrm{d}V^e}{\mathrm{d}v} + V^bV^d\Gamma^e{}_{db}\right) \tag{A.14}$$

(by (A.3)) $$\frac{\mathrm{d}^2W^a}{\mathrm{d}v^2} = -V^b\left(2\Gamma^a{}_{bc}\frac{\mathrm{d}W^c}{\mathrm{d}v} + W^cV^d\Gamma^a{}_{db,c}\right) \tag{A.15}$$

For completeness, we repeat the calculation for a covariant W_b, since g_{ab} does not commute with $\mathrm{d}/\mathrm{d}v$:

$$\frac{\delta W_a}{\delta v} = V^b(\partial_b W_a - \Gamma^c{}_{ba} W_c) \tag{A.16}$$

$$= \frac{\mathrm{d}W_a}{\mathrm{d}v} - V^b \Gamma^c{}_{ba} W_c \tag{A.17}$$

$$\frac{\delta}{\delta v}\frac{\delta W_a}{\delta v} = V^b \left(\partial_b \frac{\delta W_a}{\delta v} - \Gamma^c{}_{ba} \frac{\delta W_c}{\delta v} \right) \tag{A.18}$$

$$= V^b \left(\partial_b \left\{ \frac{\mathrm{d}W_a}{\mathrm{d}v} - V^d \Gamma^c{}_{da} W_c \right\} - \Gamma^c{}_{ba} \left\{ \frac{\mathrm{d}W_c}{\mathrm{d}v} - V^d \Gamma^e{}_{dc} W_e \right\} \right) \tag{A.19}$$

$$= \left\{ \frac{\mathrm{d}^2 W_a}{\mathrm{d}v^2} - \frac{\mathrm{d}V^d}{\mathrm{d}v} \Gamma^c{}_{da} W_c - V^b V^d \Gamma^c{}_{da,b} W_c - V^d \Gamma^c{}_{da} \frac{\mathrm{d}W_c}{\mathrm{d}v} \right\} - \left\{ V^b \Gamma^c{}_{ba} \frac{\mathrm{d}W_c}{\mathrm{d}v} - V^b \Gamma^c{}_{ba} V^d \Gamma^e{}_{dc} W_e \right\} \tag{A.20}$$

$$= \frac{\mathrm{d}^2 W_a}{\mathrm{d}v^2} - \Gamma^c{}_{ba} \left(W_c \frac{\mathrm{d}V^b}{\mathrm{d}v} + 2V^b \frac{\mathrm{d}W_c}{\mathrm{d}v} \right) - V^b W_c V^d \left(\Gamma^c{}_{da,b} - \Gamma^e{}_{ba} \Gamma^c{}_{de} \right) \tag{A.21}$$

$$= -R_{ab}{}^c{}_d V^b W_c V^d = -R^c{}_{dab} V^b W_c V^d \tag{A.22}$$

$$= V^b W_c V^d \left(\Gamma^c{}_{ad,b} - \Gamma^c{}_{bd,a} + \Gamma^e{}_{ad} \Gamma^c{}_{be} - \Gamma^e{}_{bd} \Gamma^c{}_{ae} \right) \tag{A.23}$$

$$\frac{\mathrm{d}^2 W_a}{\mathrm{d}v^2} = +\Gamma^c{}_{ba} \left(W_c \frac{\mathrm{d}V^b}{\mathrm{d}v} + 2V^b \frac{\mathrm{d}W_c}{\mathrm{d}v} \right) + V^b W_c V^d \left(\Gamma^c{}_{da,b} + \Gamma^c{}_{ad,b} - \Gamma^c{}_{bd,a} - \Gamma^e{}_{ba} \Gamma^c{}_{de} + \Gamma^e{}_{ad} \Gamma^c{}_{be} - \Gamma^e{}_{bd} \Gamma^c{}_{ae} \right) \tag{A.24}$$

$$\text{(by (A.3))} \qquad = \Gamma^c{}_{ba} \left(W_c \left\{ -V^e V^d \Gamma^b{}_{ed} \right\} + 2V^b \frac{\mathrm{d}W_c}{\mathrm{d}v} \right) + V^b W_c V^d \left(2\Gamma^c{}_{ad,b} - \Gamma^c{}_{bd,a} - \Gamma^e{}_{bd} \Gamma^c{}_{ae} \right) \tag{A.25}$$

$$\frac{\mathrm{d}^2 W_a}{\mathrm{d}v^2} = V^b \left(2\Gamma^c{}_{ba} \frac{\mathrm{d}W_c}{\mathrm{d}v} + W_c V^d \left(2\Gamma^c{}_{ad,b} - \Gamma^c{}_{bd,a} - 2\Gamma^c{}_{ea} \Gamma^e{}_{bd} \right) \right) \tag{A.26}$$

A.2 Consistency of Basis Propagation DEs

We here check the basis propagation equation (A.15) with an obvious special case: the propagation of $\hat{e}^a_\chi = k^a$ should be consistent with the geodesic equation. We

differentiate the radial geodesic equation (3.10) to get

$$\frac{\mathrm{d}k^a}{\mathrm{d}\chi} = -\Gamma^a{}_{bc}k^b k^c \tag{A.27}$$

$$\frac{\mathrm{d}^2k^a}{\mathrm{d}\chi^2} = -\frac{\mathrm{d}}{\mathrm{d}\chi}\Big(\Gamma^a{}_{bc}k^b k^c\Big) = -k^d\partial_d\Big(\Gamma^a{}_{bc}k^b k^c\Big) \tag{A.28}$$

$$= -k^d\Big(\Gamma^a{}_{bc,d}k^b k^c + 2\Gamma^a{}_{bc}k^b\partial_d k^c\Big) \tag{A.29}$$

$$= -k^d\Gamma^a{}_{bc,d}k^b k^c - 2k^d\Gamma^a{}_{bc}k^b\Big(\nabla_d k^c - \Gamma^c{}_{de}k^e\Big) \tag{A.30}$$

$$= -k^d\Gamma^a{}_{bc,d}k^b k^c + 2k^d\Gamma^a{}_{bc}k^b\Gamma^c{}_{de}k^e \tag{A.31}$$

$$= -k^d\Gamma^a{}_{bc,d}k^b k^c + 2k^d\Gamma^a{}_{be}k^b\Gamma^e{}_{dc}k^c \tag{A.32}$$

$$= -k^b k^c k^d\Big(\Gamma^a{}_{bc,d} - 2\Gamma^a{}_{be}\Gamma^e{}_{dc}\Big)\ ; \tag{A.33}$$

while (A.15), with the substitutions $V^a = k^a = W^a$ & $v = \chi$ — that is (3.15), becomes

(by (A.3))
$$\frac{\mathrm{d}^2k^a}{\mathrm{d}\chi^2} = -k^b\Big(2\Gamma^a{}_{bc}\frac{\mathrm{d}k^c}{\mathrm{d}\chi} + k^c k^d\Gamma^a{}_{db,c}\Big) \tag{A.34}$$

$$= -2k^b\Gamma^a{}_{be}\frac{\mathrm{d}k^e}{\mathrm{d}\chi} - k^b k^c k^d\Gamma^a{}_{db,c} \tag{A.35}$$

$$= -2k^b\Gamma^a{}_{be}\Big(-\Gamma^e{}_{dc}k^d k^c\Big) - k^b k^c k^d\Gamma^a{}_{db,c} \tag{A.36}$$

$$= +2k^b\Gamma^a{}_{be}\Gamma^e{}_{dc}k^d k^c - k^c k^d k^b\Gamma^a{}_{bc,d} \tag{A.37}$$

$$= k^b k^c k^d\Big(2\Gamma^a{}_{be}\Gamma^e{}_{dc} - \Gamma^a{}_{bc,d}\Big)\ . \tag{A.38}$$

The agreement of (A.33) & (A.38) supports the validity of (A.15).

Appendix B

Commutators of the Observer's Basis

If the propagated basis $\hat{\mathbf{e}}_\alpha$ is to be a coordinate basis, then its commutators must all be zero. By construction, that is by (3.12) and (3.13), we already have all the $[\hat{\mathbf{e}}_{\hat{\chi}}, \hat{\mathbf{e}}_\alpha] = 0$ for $\hat{\mathbf{e}}_{\hat{\chi}} = \mathbf{k}$ and all α. By the Jacobi identity, the remaining commutators are preserved by Lie dragging along the PNC — that is, their values on O's worldline are preserved. Near O we find

$$[\hat{\mathbf{e}}_{\hat{\tau}}, \hat{\mathbf{e}}_{\hat{\vartheta}}] = \hat{\chi}\Big(\cos\hat{\vartheta}\cos\hat{\varphi}\,[\overline{\mathbf{e}}_{\overline{\tau}}, \overline{\mathbf{e}}_1] + \cos\hat{\vartheta}\sin\hat{\varphi}\,[\overline{\mathbf{e}}_{\overline{\tau}}, \overline{\mathbf{e}}_2] - \sin\hat{\vartheta}\,[\overline{\mathbf{e}}_{\overline{\tau}}, \overline{\mathbf{e}}_3]\Big) \tag{B.1}$$

$$[\hat{\mathbf{e}}_{\hat{\tau}}, \hat{\mathbf{e}}_{\hat{\varphi}}] = -\hat{\chi}\Big(\sin\hat{\vartheta}\sin\hat{\varphi}\,[\overline{\mathbf{e}}_{\overline{\tau}}, \overline{\mathbf{e}}_1] + \sin\hat{\vartheta}\cos\hat{\varphi}\,[\overline{\mathbf{e}}_{\overline{\tau}}, \overline{\mathbf{e}}_2]\Big) \tag{B.2}$$

$$[\hat{\mathbf{e}}_{\hat{\vartheta}}, \hat{\mathbf{e}}_{\hat{\varphi}}] = -\hat{\chi}^2\sin\hat{\vartheta}\Big(\cos\hat{\vartheta}\,[\{\overline{\mathbf{e}}_{\overline{\tau}} - \overline{\mathbf{e}}_1\}, \overline{\mathbf{e}}_2] - \sin\hat{\vartheta}\sin\hat{\varphi}\,[\overline{\mathbf{e}}_1, \overline{\mathbf{e}}_3] + \sin\hat{\vartheta}\cos\hat{\varphi}\,[\overline{\mathbf{e}}_2, \overline{\mathbf{e}}_3]\Big) \tag{B.3}$$

and

$$[\hat{\mathbf{e}}_{\hat{\tau}}, \hat{\mathbf{e}}_{\hat{\chi}}] = \sin\hat{\vartheta}\cos\hat{\varphi}\,[\overline{\mathbf{e}}_{\overline{\tau}}, \overline{\mathbf{e}}_1] + \sin\hat{\vartheta}\sin\hat{\varphi}\,[\overline{\mathbf{e}}_{\overline{\tau}}, \overline{\mathbf{e}}_2] + \cos\hat{\vartheta}\,[\overline{\mathbf{e}}_{\overline{\tau}}, \overline{\mathbf{e}}_3] \tag{B.4}$$

$$[\hat{\mathbf{e}}_{\hat{\chi}}, \hat{\mathbf{e}}_{\hat{\vartheta}}] = \hat{\chi}\Big(\cos\hat{\varphi}\,[\overline{\mathbf{e}}_{\overline{\tau}}, \overline{\mathbf{e}}_3] - \sin\hat{\varphi}\,[\overline{\mathbf{e}}_2, \overline{\mathbf{e}}_3] - \cos\hat{\varphi}\,[\overline{\mathbf{e}}_1, \overline{\mathbf{e}}_3]\Big) \tag{B.5}$$

$$[\hat{\mathbf{e}}_{\hat{\chi}}, \hat{\mathbf{e}}_{\hat{\varphi}}] = \hat{\chi}\sin\hat{\vartheta}\Big(-\sin\hat{\vartheta}\,[\overline{\mathbf{e}}_{\overline{\tau}} - \overline{\mathbf{e}}_1, \overline{\mathbf{e}}_3] - \cos\hat{\vartheta}\sin\hat{\varphi}\,[\overline{\mathbf{e}}_{\overline{\tau}} - \overline{\mathbf{e}}_1, \overline{\mathbf{e}}_3] - \cos\hat{\vartheta}\cos\hat{\varphi}\,[\overline{\mathbf{e}}_2, \overline{\mathbf{e}}_3]\Big) \tag{B.6}$$

The first list need to be all zero (near O), but the second list do not, since they are not preserved by Lie dragging. Note that (B.1)-(B.3) all go to zero on O where $\hat{\chi} = 0$, and (B.3) is second order in $\hat{\chi}$. The zero values of these commutators at O are then preserved by the Lie dragging, so the constructed basis is a coordinate basis. Such a

coordinate system can always be set up near a single worldline. Indeed, there should be no problem setting up the orthonormal basis near O's worldline so that all the commutators $[\mathbf{e}_a, \mathbf{e}_b]$ are locally zero to first order.

For the Szekeres basis (3.33) we find the non-zero commutators are

$$[\overline{\mathbf{e}}_i, \overline{\mathbf{e}}_j] = \overline{\gamma}^k{}_{ij}\overline{\mathbf{e}}_k \tag{B.7}$$

$$\left.\begin{aligned} \overline{\gamma}^2{}_{02} = \frac{\dot{R}}{R} = \overline{\gamma}^3{}_{03}\ , \qquad & \overline{\gamma}^1{}_{01} = \frac{\dot{R}' - \dot{R}E'/E}{R' - RE'/E} \\ \overline{\gamma}^2{}_{32} = \frac{E_q}{R}\ , \qquad & \overline{\gamma}^1{}_{21} = \frac{E_p' - E_pE'/E}{R' - RE'/E} \\ \overline{\gamma}^3{}_{23} = \frac{E_p}{R}\ , \qquad & \overline{\gamma}^1{}_{31} = \frac{E_q' - E_qE'/E}{R' - RE'/E} \\ & \overline{\gamma}^2{}_{21} = \frac{\sqrt{\epsilon + f}}{R} = \overline{\gamma}^3{}_{31} \end{aligned}\right\} \tag{B.8}$$

These are all finite at a general point, i.e. for a generic observer. The only divergencies occur at a Szekeres "origin", $R = 0$. Should the observer pass through $R = 0$, we can take $\hat{\chi} \sim R$ nearby, so the commutators of the observer's PNC coordinates remain zero.

Appendix C

List of Functions

We list the MATLAB functions we developed below:

all_christoffel2_tensor.m: Accepts a row vector of coordinates, x^a, and returns a tensor object containing all the Christoffel symbols (of the second kind) at x^a. Function calls *input_funcs all_E2* and *all_R2*

allDEs.m: Returns all the RHS functions of the propagation equations (3.10) and (3.15), to be used in conjunction with *ode45*. Accepts a 1×40 row vector containing all the RHS variables, namely x^a k^a e^a_α $de^a_\alpha/d\chi$, and returns a column vector of the values corresponding derivatives $dx^a/d\chi$ $dk^a/d\chi$ $de^a_\alpha/d\chi$ $d^2e^a_\alpha/d\chi^2$. Function calls *all_christoffel2_tensor* and *christoffel_derivatives*.

allE2.m: Accepts a position (r, p, q) and returns the value of $E(r, p, q)$ and derivatives $E_{,r}$ $E_{,p}$ $E_{,q}$ $E_{,rr}$ $E_{,rp}$ $E_{,rq}$ $E_{,pp}$ $E_{,qq}$ $E_{,rrr}$ $E_{,rrp}$ $E_{,rrq}$ $E_{,rpp}$ $E_{,rqq}$. Function calls *input_funcs*.

allR2.m: Accepts two row vectors of t and r values, and returns row vectors corresponding to the values of $R(t, r)$, $\dot{R}(t, r)$, $R'(t, r)$, $\dot{R}'(t, r)$, $R''(t, r)$, $\ddot{R}(t, r)$, $\ddot{R}'(t, r)$ and $R'''(t, r)$. Function calls *input_funcs*.

apparent_motion.m: Accepts three $N \times 4$ vectors corresponding to the inverted propagated basis vectors e^τ_a $e^{\hat{\theta}}_a$ $e^{\hat{\phi}}_a$ and returns two $N \times 1$ vectors $d\tilde{\theta}/d\tilde{\tau}$ $d\tilde{\phi}/d\tilde{\tau}$. Function calls *redshift*.

area_distance.m: Accepts $N \times 4$ vectors corresponding to x^a k^a $e^{\hat{\tau}}_a$ $e^{\hat{\theta}}_a$ $e^{\hat{\phi}}_a$ along the light ray, and returns a $N \times 1$ column vector corresponding to the area distance, d_A. Function calls *metric_cpt*.

createPP.m: Creates piece-wise polynomials corresponding to the parametric evolution equations (2.12) (2.7), to be used in conjunction with the MATLAB function *ppval*.

elip_phase.m: Accepts a position (t, r) and returns the value of the phase parameter η for an elliptic region. Performs the interpolation described in §4.1.2. Function calls *input_funcs*.

hyp_phase_T.m: Accepts a position (t, r) and returns the value of the phase parameter T for a hyperbolic region. Performs the interpolation described in §4.1.2. Function calls *input_funcs*.

input_funcs.m: Contains the all metric functions ϵ $M(r)$ $f(r)$ $t_b(r)$ $S(r)$ $P(r)$ $Q(r)$, and their 'radial' derivatives, which define the Szekeres spacetime (to be specified by the user). Accepts a row vector of r values and a character string identifying the function of interest, and returns row vectors corresponding to that and its derivatives.

Obs_Basis_Setup.m Returns the components of the initial tangent vector, k^a, the observer basis vectors and their derivatives given some position, x^a, and on-sky direction $(\hat{\theta}, \hat{\phi})$. Function calls *input_funcs all_R2 all_E2* and *all_christoffel2_tensor*.

propagate.m: Solves the radial null geodesic equation for the path of the light ray, and propagates the observer basis vectors along the path with the geodesic deviation equation. Accepts a initial position vector, x^a, an on-sky direction, $(\hat{\theta}, \hat{\phi})$, and an integration range for the affine parameter χ, and returns the column vectors corresponding to the values of χ, x^a, k^a, $e^a_{\hat{\tau}}$, $e^a_{\hat{\chi}}$, $e^a_{\hat{\theta}}$, $e^a_{\hat{\phi}}$ along the light ray. Function calls *Obs_Basis_Setup* and *allDEs* (in conjunction with *ode45*).

redshift.m: Accepts a $N \times 4$ vector corresponding to $e^a_{\hat{\tau}}$ along the light ray, and returns the redshift.

metric_cpt.m: Accepts row vectors of t r p q values and a character string identifying the component of interest, and returns a row vector of metric component values.

sz_Magnitude.m: Calculates the magnitude of a vector, v^a. Accepts two row vectors containing the components x^a and v^a, and returns a row vector corresponding to the values of $v^a v_a$. Function calls *metric_cpt*.

Appendix D

Frame Relations, Energy and Momentum

Examining the action (8.1), one can see that the geometry part, $\mathcal{L}_{EH}$, and scalar part, $\mathcal{L}_{\phi}$, are defined in terms of the Einstein frame metric, while the SM matter part, $\mathcal{L}_{m}$, is defined in terms of the Jordan frame metric. Since we wish to perform our analysis in a single frame, it is useful to show the conformal transformations for relating various quantities in the resulting field equations. Using the conformal transformation (8.4) one can calculate how such quantities relate between the Einstein and Jordan frames. Amongst this simplest conformal relations is the inverse metric, which transforms like

$$\tilde{g}^{\mu\nu} = e^{-2\beta_i\phi/M_{\rm Pl}} g^{\mu\nu}, \tag{D.1}$$

and the determinant of the metric, which transforms like

$$\tilde{g} = e^{8\beta_i\phi/M_{\rm Pl}} g, \tag{D.2}$$

where we used $\det(cA) = c^N \det(A)$, where A is any matrix of dimension N and c is a conformal factor. Since the SM matter fields couple directly to the Jordan frame metric, the energy-momentum tensors for the various species, $\psi_m^{(i)}$, are defined in the Jordan frame in the standard way, i.e.

$$\tilde{T}^{(i)}_{\mu\nu} \equiv -\frac{2}{\sqrt{\tilde{g}}} \frac{\delta \mathcal{L}_m}{\delta \tilde{g}^{\mu\nu}_{(i)}}. \tag{D.3}$$

In the cosmological context this is typically assumed to be a isentroptic perfect fluid of the form

$$\tilde{T}^{(i)}_{\mu\nu} = (\tilde{\rho}_i + \tilde{p}_i)u_\mu u_\nu + \tilde{p}_i \tilde{g}^{(i)}_{\mu\nu}. \tag{D.4}$$

If the matter fields do not interact then energy-momentum is conserved for each individual species in this frame, i.e. $\tilde{\nabla}_\mu \tilde{T}^{\mu\nu}_{(i)} = 0$. This is not true of the Einstein frame however, as the scalar mixes with matter fields, and it is only the total EMT that is conserved. The Einstein frame energy density must obey the continuity equation, $\rho \sim a^{-3(1+w_i)}$, and thus is defined in terms of the Jordan frame energy density by

$$\rho_i \equiv e^{3(1+w_i)\beta_i \phi/M_{\rm Pl}} \tilde{\rho}_i. \tag{D.5}$$

Here we see that the Einstein frame energy density is manifestly a mixture of the Jordan frame energy density and the scalar field. Using (8.4) and (D.2) one can relate the Einstein frame energy-momentum tensor to that in the Jordan frame by

$$\begin{aligned} T^{\mu\nu}_{(i)} &\equiv -\frac{2}{\sqrt{-g}} \frac{\partial \mathcal{L}}{\partial g_{\mu\nu}} \\ &= -\frac{2}{\sqrt{-\tilde{g} e^{-8\beta_i \phi/M_{\rm Pl}}}} \frac{\partial \mathcal{L}}{\partial \tilde{g}_{\mu\nu}} \frac{\partial \tilde{g}^{\mu\nu}}{\partial g^{\mu\nu}} \\ &= -\frac{2}{\sqrt{-\tilde{g}}} \frac{\partial \mathcal{L}}{\partial \tilde{g}_{\mu\nu}} e^{6\beta_i \phi/M_{\rm Pl}} \\ &= \tilde{T}^{\mu\nu} e^{6\beta_i \phi/M_{\rm Pl}}. \end{aligned} \tag{D.6}$$

Assuming SM matter energy-momentum tensor takes the form (D.4), the trace can be written as

$$\begin{aligned} \tilde{T}^{\mu\nu}_{(i)} \tilde{g}^{(i)}_{\mu\nu} &= \left[(\tilde{\rho} + \tilde{p})\, u^\mu u^\nu + \tilde{p} \tilde{g}^{\mu\nu}_{(i)} \right] \tilde{g}^{(i)}_{\mu\nu}, \\ &= (\tilde{\rho} + \tilde{p})\, u^\mu u_\mu + 4\tilde{p}, \\ &= -\tilde{\rho} + 3\tilde{p}, \\ &= -(1 - 3w)\, \tilde{\rho}, \end{aligned} \tag{D.7}$$

where we have defined the equation of state parameter $w_i \equiv \tilde{p}_i/\tilde{\rho}_i$. Rearranging (D.7) for $\tilde{\rho}_i$ and substituting it into (D.5), and using (D.2), gives an expression for the

Einstein frame energy density in terms of the Jordan frame energy momentum tensor

$$\begin{aligned}
\rho_i &= -e^{3(1+w_i)\beta_i\phi/M_{\rm Pl}}\frac{1}{(1-3w_i)}\tilde{T}^{\mu\nu}_{(i)}\tilde{g}^{(i)}_{\mu\nu}, \\
&= e^{3(1+w_i)\beta_i\phi/M_{\rm Pl}}\frac{1}{(1-3w_i)}\frac{2}{\sqrt{-g^{(i)}}}\frac{\partial\mathcal{L}_m}{\partial\tilde{g}^{(i)}_{\mu\nu}}, \\
&= e^{3(1+w_i)\beta_i\phi/M_{\rm Pl}}\frac{1}{(1-3w_i)}\frac{2}{\sqrt{-ge^{8\beta_i\phi/M_{\rm Pl}}}}\frac{\partial\mathcal{L}_m}{\partial\tilde{g}^{(i)}_{\mu\nu}}, \\
&= e^{-(1+3w_i)\beta_i\phi/M_{\rm Pl}}\frac{1}{(1-3w_i)}\frac{2}{\sqrt{-g}}\frac{\partial\mathcal{L}_m}{\partial\tilde{g}^{(i)}_{\mu\nu}}.
\end{aligned} \tag{D.8}$$

The 00-component of the Einstein frame SM energy momentum tensor can then be written in terms of the Einstein frame energy density as follows. Recalling that $\tilde{T}^{00}\tilde{g}_{00} = -\tilde{\rho}$, and using (8.4), one can write the 00-component of (D.6) as

$$\begin{aligned}
T^{00}_{(i)} &= \tilde{T}^{00}\tilde{g}_{00}\frac{e^{6\beta_i\phi/M_{\rm Pl}}}{\tilde{g}_{00}} \\
&= \tilde{\rho}e^{4\beta_i\phi/M_{\rm Pl}} \\
&= \rho_i e^{(1-3w_i)\beta_i\phi/M_{\rm Pl}}.
\end{aligned} \tag{D.9}$$

Using (D.5) (D.6) (D.7) the trace of the Einstein frame energy-momentum tensor can be written in terms of the Einstein frame energy density. One finds

$$\begin{aligned}
T^{\mu\nu}_{(i)}g^{(i)}_{\mu\nu} &= \tilde{T}^{\mu\nu}e^{6\beta_i\phi/M_{\rm Pl}}\left(\tilde{g}_{\mu\nu}e^{-2\beta_i\phi/M_{\rm Pl}}\right) \\
&= \tilde{T}^{\mu\nu}\tilde{g}_{\mu\nu}e^{4\beta_i\phi/M_{\rm Pl}} \\
&= -(1-3w_i)\tilde{\rho}_i e^{4\beta_i\phi/M_{\rm Pl}} \\
&= -(1-3w_i)e^{-3(1+w_i)\beta_i\phi/M_{\rm Pl}}\rho_i e^{4\beta_i\phi/M_{\rm Pl}} \\
&= -(1-3w_i)\rho_i e^{(1-3w_i)\beta_i\phi/M_{\rm Pl}}
\end{aligned} \tag{D.10}$$

The energy-momentum tensor for the scalar is defined in a way entirely analogous to (D.3), and its form can be calculated explicitly from the definition. Expanding (D.3),

and substituting in (8.3) one finds

$$\begin{aligned} T^{\phi}_{\mu\nu} &= -\frac{2}{\sqrt{-g}}\frac{\delta S_\phi}{\delta g^{\mu\nu}} \\ &= -\frac{2}{\sqrt{-g}}\frac{\delta\left(\sqrt{-g}\mathcal{L}_\phi\right)}{\delta g^{\mu\nu}} \\ &= -2\frac{\delta\mathcal{L}_\phi}{g^{\mu\nu}} + g_{\mu\nu}\mathcal{L}_\phi, \\ &= \partial_\mu\phi\partial_\nu\phi - \left(\frac{1}{2}\partial_\alpha\phi\partial^\alpha\phi + V\right)g_{\mu\nu}. \end{aligned} \tag{D.11}$$

This allows one to define the energy density and pressure of the scalar field, again, analogous to the definition for "normal" matter. Rearranging (D.4) give us the definitions

$$\rho_\phi \equiv T^{\phi}_{\mu\nu}u^\mu u^\nu, \tag{D.12}$$

$$p_\phi \equiv T^{\phi}_{\mu\nu}\frac{(u^\mu u^\nu + g^{\mu\nu})}{3}. \tag{D.13}$$

Appendix E

Numerical Equations for the Chameleon

It will be useful to rewrite the system in a form that better lends itself to numerical analysis, and makes the surfing solution manifest. Defining Einstein frame E-folds and the dimensionless scalar field,

$$N \equiv \ln\left(\frac{a}{a_i}\right), \qquad \varphi \equiv \frac{\phi}{M_{\rm Pl}}, \tag{E.1}$$

where a_i is the scale factor at some fixed initial time. One can then write

$$\frac{\mathrm{d}N}{\mathrm{d}t} = H, \tag{E.2}$$

and

$$\frac{\mathrm{d}}{\mathrm{d}\phi} = \frac{1}{M_{\rm Pl}}\frac{\mathrm{d}}{\mathrm{d}\varphi} \tag{E.3}$$

The first derivative of the field can then be written as

$$\begin{aligned}\dot{\phi} &= \frac{\mathrm{d}\phi}{\mathrm{d}N}\frac{\mathrm{d}N}{\mathrm{d}t} \\ &= \frac{\mathrm{d}}{\mathrm{d}N}\left(\varphi M_{\rm Pl}\right)\frac{\mathrm{d}N}{\mathrm{d}t} \\ &= M_{\rm Pl} H \varphi', \end{aligned} \tag{E.4}$$

where $'$ denotes differentiation with respect to N. The second derivative of the field then becomes

$$\begin{aligned}\ddot{\phi} &= \frac{\mathrm{d}}{\mathrm{d}N}\left(\dot{\phi}\right)\frac{\mathrm{d}N}{\mathrm{d}t} \\ &= \frac{\mathrm{d}}{\mathrm{d}N}\left(M_{\mathrm{Pl}}H\varphi'\right)H \\ &= M_{\mathrm{Pl}}H\left(H'\varphi' + H\varphi''\right) \\ &= M_{\mathrm{Pl}}HH'\varphi + M_{\mathrm{Pl}}H^2\varphi''. \end{aligned} \tag{E.5}$$

These variables will also be useful for then numerical analysis to come.

E.1 Rewriting the Einstein Frame EOM

Using the Friedmann Equations (9.16) (9.17), along with some redefinitions of the field and time variables, one should be able to get (9.18) into the form of Equation (15) in [138]. We transform the EOM of the field (9.18) by plugging in (E.3) (E.4) (E.5), which gives

$$\begin{aligned} M_{\mathrm{Pl}}H^2\varphi'' + M_{\mathrm{Pl}}HH'\varphi' + 3H^2M_{\mathrm{Pl}}\varphi' &= -\frac{\mathrm{d}V/\mathrm{d}\varphi}{M_{\mathrm{Pl}}} - \frac{\beta}{M_{\mathrm{Pl}}}\rho_r\left(\Sigma + f_m\right) \\ \Rightarrow \varphi'' + \left(\frac{H'}{H} + 3\right)\varphi' &= -\frac{\mathrm{d}V/\mathrm{d}\varphi}{M_{\mathrm{Pl}}^2H^2} - \frac{\beta}{M_{\mathrm{Pl}}^2H^2}\rho_r\left(\Sigma + f_m\right) \end{aligned} \tag{E.6}$$

Rearranging (9.16) one can write

$$\frac{\rho_r}{M_{\mathrm{Pl}}^2H^2} = 3\left(1 - \frac{\varphi'^2}{6} - \frac{V}{3M_{\mathrm{Pl}}^2H^2}\right)\left(1 + f_m\right)^{-1}. \tag{E.7}$$

Noting that the factor on the right can be written

$$\begin{aligned}\frac{1}{1+f_m} &= \frac{1-f_m}{(1+f_m)(1-f_m)} \\ &= \frac{1-f_m}{1-f_m^2} \\ &\approx 1 - f_m, \end{aligned} \tag{E.8}$$

where we have dropped the $\mathcal{O}(f_m^2)$ term. This gives

$$\frac{\rho_r}{M_{\rm Pl}^2 H^2} \approx 3\left(1 - \frac{\varphi'^2}{6} - \frac{V}{3M_{\rm Pl}^2 H^2}\right)(1 - f_m)\,. \tag{E.9}$$

Using (E.9) with (E.6) one finds

$$\begin{aligned}\varphi'' + \left(\frac{H'}{H} + 3\right)\varphi' &= -\frac{\mathrm{d}V/\mathrm{d}\varphi}{M_{\rm Pl}^2 H^2} - 3\beta\left(1 - \frac{\varphi'^2}{6} - \frac{V}{3M_{\rm Pl}^2 H^2}\right)(1 - f_m)(\Sigma + f_m) \\ &\approx -\frac{\mathrm{d}V/\mathrm{d}\varphi}{M_{\rm Pl}^2 H^2} - 3\beta\left(1 - \frac{\varphi'^2}{6} - \frac{V}{3M_{\rm Pl}^2 H^2}\right)(\Sigma + f_m - \Sigma f_m)\,, \end{aligned} \tag{E.10}$$

again dropping the $\mathcal{O}(f_m^2)$ term. Clearly need to eliminate H'. Can get an expression from the second Friedmann Equation. Noting that $\ddot{a}/a = H'H + H^2$ one can write expression for H'/H from (9.12) as

$$\frac{H'}{H} + 3 = \frac{V}{3M_{\rm Pl}^2 H^2} - \frac{\varphi'^2}{6} + \frac{\rho_r}{3M_{\rm Pl}^2 H^2}\left(\frac{\Sigma - f_m}{2} - 1\right) + 2. \tag{E.11}$$

Using (E.9) in (E.11) then yields

$$\begin{aligned}\frac{H'}{H} + 3 &= \frac{V}{3M_{\rm Pl}^2 H^2} - \frac{\varphi'^2}{3} + \left(\frac{\Sigma - f_m}{2} - 1\right)(1 - f_m)\left(1 - \frac{\varphi'^2}{6} - \frac{V}{3M_{\rm Pl}^2 H^2}\right) + 2, \\ &= \frac{V}{3M_{\rm Pl}^2 H^2} - \frac{\varphi'^2}{3} + \left(\frac{\Sigma + f_m}{2} - \frac{\Sigma f_m}{2} - 1\right)\left(1 - \frac{\varphi'^2}{6} - \frac{V}{3M_{\rm Pl}^2 H^2}\right) + 2 \\ &= \frac{2V}{3M_{\rm Pl}^2 H^2} - \frac{\varphi'^2}{6} + 1 + \left(\frac{\Sigma + f_m}{2}\right)\left(1 - \frac{\varphi'^2}{6} - \frac{V}{3M_{\rm Pl}^2 H^2}\right), \\ &= \left(1 + \frac{\Sigma + f_m}{2}\right)\left(1 - \frac{\varphi'^2}{6}\right) + \frac{2V}{3H^2 M_{\rm Pl}^2}\left(1 - \frac{\Sigma + f_m}{4}\right). \end{aligned} \tag{E.12}$$

Here we have dropped terms $\mathcal{O}(f_m^2)$ and set $1 + \Sigma f_m \approx 1$. Inserting (E.12) into (E.10) gives

$$\begin{aligned}\varphi'' + \left[\left(1 + \frac{\Sigma + f_m}{2}\right)\left(1 - \frac{\varphi'^2}{6}\right) + \frac{2V}{3H^2 M_{\rm Pl}^2}\left(1 - \frac{\Sigma + f_m}{4}\right)\right]\varphi' = \\ -\frac{\mathrm{d}V/\mathrm{d}\varphi}{M_{\rm Pl}^2 H^2} - 3\beta\left(1 - \frac{\varphi'^2}{6} - \frac{V}{3M_{\rm Pl}^2 H^2}\right)(\Sigma + f_m - \Sigma f_m)\,, \end{aligned} \tag{E.13}$$

which is in agreement with Equation (15) of [138]. Transforming (9.16) with (E.4) yields

$$\begin{aligned} 3H^2M_{\rm Pl}^2 &= \frac{1}{2}\left(M_{\rm Pl}H\varphi'\right)^2 + V + \rho_r\left(1+f_m\right) \\ \Rightarrow 1 &= \frac{\varphi'^2}{6} + \frac{V}{3M_{\rm Pl}^2H^2} + \frac{1}{3M_{\rm Pl}^2H^2}\rho_r\left(1+f_m\right) \\ \Rightarrow \frac{1}{M_{\rm Pl}^2H^2} &= \frac{3}{\rho_r\left(1+f_m\right)+V}\left(1-\frac{\varphi'^2}{6}\right) \end{aligned} \tag{E.14}$$

which is in agreement with Equation (16) of [138]. This can now be used to eliminate H^2 terms in (E.13). Noting that $1+f_m \approx 1$, the factor in front of the φ' term on the LHS of (E.13) becomes

$$\begin{aligned} &\left(1+\frac{\Sigma+f_m}{2}\right)\left(1-\frac{\varphi'^2}{6}\right) + \frac{2V}{3H^2M_{\rm Pl}^2}\left(1-\frac{\Sigma+f_m}{4}\right) \\ &= \left(1-\frac{\varphi'^2}{6}\right)\left[\left(1+\frac{\Sigma+f_m}{2}\right) + \frac{2V}{\rho_r+V}\left(1-\frac{\Sigma+f_m}{4}\right)\right], \\ &= \left(1-\frac{\varphi'^2}{6}\right)\left[1+\frac{2V}{\rho_r+V}\right], \end{aligned} \tag{E.15}$$

Doing the same to the RHS of (E.13) we find

$$\begin{aligned} &-\frac{{\rm d}V/{\rm d}\varphi}{M_{\rm Pl}^2H^2} - 3\beta\left(1-\frac{\varphi'^2}{6}-\frac{V}{3M_{\rm Pl}^2H^2}\right)\left(\Sigma+f_m-\Sigma f_m\right) \\ &= -3\frac{{\rm d}V/{\rm d}\varphi}{\rho_r+V}\left(1-\frac{\varphi'^2}{6}\right) - 3\beta\left[1-\frac{\varphi'^2}{6}-\frac{V}{\rho_r+V}\left(1-\frac{\varphi'^2}{6}\right)\right]\left(\Sigma\left(1-f_m\right)+f_m\right) \\ &\quad \left(1-\frac{\varphi'^2}{6}\right)\left[-3\frac{{\rm d}V/{\rm d}\varphi}{\rho_r+V} - 3\beta\left(1-\frac{V}{\rho_r+V}\right)\left(\Sigma+f_m\right)\right], \end{aligned} \tag{E.16}$$

Combining (E.15) and (E.16) with (E.13) then gives

$$\varphi'' + \varphi'\left(1-\frac{\varphi'^2}{6}\right)\left[1+\frac{2V}{\rho_r+V}\right] = \left(1-\frac{\varphi'^2}{6}\right)\left[-3\frac{{\rm d}V/{\rm d}\varphi}{\rho_r+V} - 3\beta\left(1-\frac{V}{\rho_r+V}\right)\left(\Sigma+f_m\right)\right] \tag{E.17}$$

which is in agreement with Equation (17) of [138]. Further simplification of (E.17) is done by noting that $V(\phi) << \rho_r$ while $\phi \gtrsim M$ in the early Universe. Also, assume that $\phi >> \phi_{min}$, as is the case for the range of initial conditions under consideration,

such that the driving term $dV/d\phi$ is far less than the driving from Σ. The background density of non-relativistic matter f_m is also considered to be negligible. Doing so yields

$$\varphi'' + \varphi' \left(1 - \frac{\varphi'^2}{6}\right) = -3\beta\Sigma(T_J) \left(1 - \frac{\varphi'^2}{6}\right) \tag{E.18}$$

where Σ if a function of the Jordan frame temperature.

E.2 EOM in the Jordan Frame

Next, we transform (E.17) into the Jordan Frame. The relationship between the e-folds in each frame is given by

$$\begin{aligned} \tilde{N} &= \ln\left(\frac{\tilde{a}}{\tilde{a}_i}\right), \\ &= \ln\left(\frac{e^{\beta\phi/M_{\rm Pl}}a}{e^{\beta\phi_i/M_{\rm Pl}}a_i}\right), \\ &= \beta\left(\varphi - \varphi_i\right) + N, \end{aligned} \tag{E.19}$$

and thus the differential relation is

$$\frac{\mathrm{d}N}{\mathrm{d}\tilde{N}} = 1 - \beta\frac{\mathrm{d}\varphi}{\mathrm{d}\tilde{N}}. \tag{E.20}$$

Inverting (E.20) then gives

$$\frac{\mathrm{d}\tilde{N}}{\mathrm{d}N} = \left(1 - \beta\varphi\text{`}\right)^{-1} \tag{E.21}$$

where $\text{`} \equiv \mathrm{d}/\mathrm{d}\tilde{N}$. This allows one to transform Einstein frame quantities into the Jordan frame. Derivatives of the field become

$$\begin{aligned} \varphi' &= \varphi\text{`}\left(1 - \beta\varphi\text{`}\right)^{-1}, \\ \varphi'' &= \varphi\text{“}\left(1 - \beta\varphi\text{`}\right)^{-2}. \end{aligned} \tag{E.22}$$

Using these, (E.17) becomes

$$\begin{aligned}&\varphi\text{“}\left(1-\beta\varphi\text{‘}\right)^{-2}+\left[\varphi\text{‘}\left(1-\beta\varphi\text{‘}\right)^{-1}-\frac{\varphi\text{‘}^3}{6}\left(1-\beta\varphi\text{‘}\right)^{-3}\right]\left(1+\frac{2V}{\rho_r+V}\right)\\&=\left[1-\frac{\varphi\text{‘}^2}{6}\left(1-\beta\varphi\text{‘}\right)^{-2}\right]\left[-3\frac{\mathrm{d}V/\mathrm{d}\varphi}{\rho_r+V}-3\beta\left(1-\frac{V}{\rho_r+V}\right)\left(\Sigma+f_m\right)\right]\end{aligned}\tag{E.23}$$

Multiplying (E.23) throughout by $\left(1-\beta\varphi\text{‘}\right)^2$ then gives

$$\begin{aligned}&\varphi\text{“}+\left[\varphi\text{‘}\left(1-\beta\varphi\text{‘}\right)-\frac{\varphi\text{‘}^3}{6}\left(1-\beta\varphi\text{‘}\right)^{-1}\right]\left(1+\frac{2V}{\rho_r+V}\right)\\&=\left[\left(1-\beta\varphi\text{‘}\right)^2-\frac{\varphi\text{‘}^2}{6}\right]\left[-3\frac{\mathrm{d}V/\mathrm{d}\varphi}{\rho_r+V}-3\beta\left(1-\frac{V}{\rho_r+V}\right)\left(\Sigma+f_m\right)\right]\end{aligned}\tag{E.24}$$

Similarly, transforming the simplified EOM (E.18) into the Jordan frame gives

$$\begin{aligned}&\frac{\varphi\text{“}(1-\beta\varphi\text{‘})^{-2}}{1-\frac{1}{6}\varphi\text{‘}(1-\beta\varphi\text{‘})^{-2}}+\varphi\text{‘}(1-\beta\varphi\text{‘})^{-1}=-3\beta\Sigma,\\&\Rightarrow\frac{\varphi\text{“}}{(1-\beta\varphi\text{‘})^2-\frac{\varphi\text{‘}^2}{6}}+\varphi\text{‘}(1-\beta\varphi\text{‘})^{-1}=-3\beta\Sigma.\end{aligned}\tag{E.25}$$

Taking the ansatz (9.34) and transforming it into the Jordan frame with $N=\tilde{N}-\beta(\varphi-\varphi_i)$ gives

$$\begin{aligned}\varphi&=\varphi_S-\frac{N-N_S}{\beta}\\&=\varphi_S-\frac{\tilde{N}-\beta(\varphi-\varphi_i)-[\tilde{N}_S-\beta(\varphi_S-\varphi_{Si})]}{\beta}\\&=\varphi_S-\frac{\tilde{N}-\tilde{N}_S}{\beta}+\varphi-\varphi_i-\varphi_S+\varphi_i\\&=\varphi-\frac{\tilde{N}-\tilde{N}_S}{\beta}\end{aligned}\tag{E.26}$$

Again, this seems to imply the Jordan frame e-folds are constant during the surfing solution.

References

[1] Clifford M Will. *Theory and experiment in gravitational physics*. Cambridge University Press, 1993.

[2] B. P. Abbott et al. Observation of Gravitational Waves from a Binary Black Hole Merger. *Phys. Rev. Lett.*, 116(6):061102, 2016.

[3] J. E. Forero-Romero, Y. Hoffman, S. Gottloeber, A. Klypin, and G. Yepes. A Dynamical Classification of the Cosmic Web. *Mon. Not. Roy. Astron. Soc.*, 396:1815–1824, 2009.

[4] Thomas Buchert. On average properties of inhomogeneous fluids in general relativity. 1. Dust cosmologies. *Gen. Rel. Grav.*, 32:105–125, 2000.

[5] David L. Wiltshire. Cosmic clocks, cosmic variance and cosmic averages. *New J. Phys.*, 9:377, 2007.

[6] Timothy Clifton, Kjell Rosquist, and Reza Tavakol. An Exact quantification of backreaction in relativistic cosmology. *Phys. Rev.*, D86:043506, 2012.

[7] Timothy Clifton, Daniele Gregoris, Kjell Rosquist, and Reza Tavakol. Exact Evolution of Discrete Relativistic Cosmological Models. *JCAP*, 1311:010, 2013.

[8] Morag Scrimgeour et al. The WiggleZ Dark Energy Survey: the transition to large-scale cosmic homogeneity. *Mon. Not. Roy. Astron. Soc.*, 425:116–134, 2012.

[9] David W. Hogg, Daniel J. Eisenstein, Michael R. Blanton, Neta A. Bahcall, J. Brinkmann, James E. Gunn, and Donald P. Schneider. Cosmic homogeneity demonstrated with luminous red galaxies. *Astrophys. J.*, 624:54–58, 2005.

[10] Francesco Sylos Labini, Nikolay L. Vasilyev, Luciano Pietronero, and Yurij V. Baryshev. Absence of self-averaging and of homogeneity in the large scale galaxy distribution. *Europhys. Lett.*, 86(4):49001, 2009.

[11] Roger G. Clowes, Kathryn A. Harris, Srinivasan Raghunathan, Luis E. Campusano, Ilona K. Soechting, and Matthew J. Graham. A structure in the early universe at z 1.3 that exceeds the homogeneity scale of the R-W concordance cosmology. *Mon. Not. Roy. Astron. Soc.*, 429:2910–2916, 2013.

[12] Boudewijn F. Roukema, Thomas Buchert, Jan J. Ostrowski, and Martin J. France. Evidence for an environment-dependent shift in the baryon acoustic oscillation peak. *Mon. Not. Roy. Astron. Soc.*, 448(2):1660–1673, 2015.

[13] M. Davis and P. J. E Peebles. Evidence for local anisotropy of the hubble flow. *Ann. Rev. Astron. Astrophys.*, 21:109–130, 1983.

[14] I. D. Karachentsev et al. Local galaxy flows within 5 mpc. *Astron. Astrophys.*, 398:479–492, 2003.

[15] Megan L. McClure and C. C. Dyer. Anisotropy in the Hubble constant as observed in the HST Extragalactic Distance Scale Key Project results. *New Astron.*, 12:533–543, 2007.

[16] David L. Wiltshire, Peter R. Smale, Teppo Mattsson, and Richard Watkins. Hubble flow variance and the cosmic rest frame. *Phys. Rev.*, D88:083529, 2013.

[17] Krzysztof Bolejko, M. Ahsan Nazer, and David L. Wiltshire. Differential cosmic expansion and the Hubble flow anisotropy. *JCAP*, 1606(06):035, 2016.

[18] Chris Vale. Local pancake defeats axis of evil. *Submitted to: Astrophys. J. Lett.*, 2005.

[19] Adi Nusser and Marc Davis. The cosmological bulk flow: consistency with ΛCDM and $z \approx 0$ constraints on σ_8 and γ. *Astrophys. J.*, 736:93, 2011.

[20] Stephen J. Turnbull, Michael J. Hudson, Hume A. Feldman, Malcolm Hicken, Robert P. Kirshner, and Richard Watkins. Cosmic flows in the nearby universe from Type Ia Supernovae. *Mon. Not. Roy. Astron. Soc.*, 420:447–454, 2012.

[21] Yin-Zhe Ma and Douglas Scott. Cosmic bulk flows on 50 h^{-1}Mpc scales: A Bayesian hyper-parameter method and multi-shells likelihood analysis. *Mon. Not. Roy. Astron. Soc.*, 428:2017, 2013.

[22] Guilhem Lavaux, Niayesh Afshordi, and Michael J. Hudson. First measurement of the bulk flow of nearby galaxies using the cosmic microwave background. *Mon. Not. Roy. Astron. Soc.*, 430:1617–1635, 2013.

[23] P. A. R. Ade et al. Planck intermediate results. XIII. Constraints on peculiar velocities. *Astron. Astrophys.*, 561:A97, 2014.

[24] G. Lavaux, R. Brent Tully, R. Mohayaee, and S. Colombi. Cosmic flow from 2MASS redshift survey: The origin of CMB dipole and implications for LCDM cosmology. *Astrophys. J.*, 709:483–498, 2010.

[25] Richard Watkins, Hume A. Feldman, and Michael J. Hudson. Consistently Large Cosmic Flows on Scales of 100 Mpc/h: a Challenge for the Standard LCDM Cosmology. *Mon. Not. Roy. Astron. Soc.*, 392:743–756, 2009.

[26] Jacques Colin, Roya Mohayaee, Subir Sarkar, and Arman Shafieloo. Probing the anisotropic local universe and beyond with SNe Ia data. *Mon. Not. Roy. Astron. Soc.*, 414:264–271, 2011.

[27] F. Atrio-Barandela. On the Statistical Significance of the Bulk Flow Measured by the PLANCK Satellite. *Astron. Astrophys.*, 557:A116, 2013.

[28] Yehuda Hoffman, Helene M. Courtois, and R. Brent Tully. Cosmic Bulk Flow and the Local Motion from Cosmicflows-2. *Mon. Not. Roy. Astron. Soc.*, 449(4):4494–4505, 2015.

[29] Jonathan Carrick, Stephen J. Turnbull, Guilhem Lavaux, and Michael J. Hudson. Cosmological parameters from the comparison of peculiar velocities with predictions from the 2M++ density field. *Mon. Not. Roy. Astron. Soc.*, 450(1):317–332, 2015.

[30] Obinna Umeh, Chris Clarkson, and Roy Maartens. Nonlinear relativistic corrections to cosmological distances, redshift and gravitational lensing magnification: I. Key results. *Class. Quant. Grav.*, 31:202001, 2014.

[31] Ido Ben-Dayan, Giovanni Marozzi, Fabien Nugier, and Gabriele Veneziano. The second-order luminosity-redshift relation in a generic inhomogeneous cosmology. *JCAP*, 1211:045, 2012.

[32] Enea Di Dio and Ruth Durrer. Vector and Tensor Contributions to the Luminosity Distance. *Phys. Rev.*, D86:023510, 2012.

[33] Camille Bonvin, Chris Clarkson, Ruth Durrer, Roy Maartens, and Obinna Umeh. Do we care about the distance to the CMB? Clarifying the impact of second-order lensing. *JCAP*, 1506(06):050, 2015.

[34] Chris Clarkson. The general theory of secondary weak gravitational lensing. *JCAP*, 1509(09):033, 2015.

[35] Vinicius V. L. Albani, Alvaro S. Iribarrem, Marcelo B. Ribeiro, and William R. Stoeger. Differential Density Statistics of Galaxy Distribution and the Luminosity Function. *Astrophys. J.*, 657:760–772, 2007.

[36] Alnadhief A. H. Alfedeel and Charles Hellaby. The Lemaitre Model and the Generalisation of the Cosmic Mass. *Gen. Rel. Grav.*, 42:1935–1952, 2010.

[37] M. E. Araujo, W. R. Stoeger, R. C. Arcuri, and M. L. Bedran. Solving Einstein Field Equations in Observational Coordinates with Cosmological Data Functions: Spherically Symmetric Universes with Cosmological Constant. *Phys. Rev.*, D78:063513, 2008.

[38] Marcelo E. Araujo, Sandra R. M. M. Roveda, and S. J. Stoeger, William R. Perturbed spherically symmetric dust solution of the field equations in observational coordinates with cosmological data functions. *Astrophys. J.*, 560:7–14, 2001.

[39] Marcelo E. Araujo and S. J. Stoeger, William R. Exact spherically symmetric dust solution of the field equations in observational coordinates with cosmological data functions. *Phys. Rev.*, D60:104020, 1999. [Erratum: Phys. Rev.D64,049002(2001)].

[40] W R Stoeger, G F R Ellis, and S D Nel. Observational cosmology. iii. exact spherically symmetric dust solutions. *Classical and Quantum Gravity*, 9(2):509, 1992.

[41] W R Stoeger, S J Stanley, D Nel, and G F R Ellis. Observational cosmology. v. solution of the first-order general perturbation equations. *Classical and Quantum Gravity*, 9(7):1725, 1992.

[42] W. R. Stoeger, S. D. Nel, R. Maartens, and G. F. R Ellis. The fluid-ray tetrad formulation of Einstein's field equations. *Class. Quant. Grav.*, 9(2):493, 1992.

[43] Charles Hellaby. The Mass of the Cosmos. *Mon. Not. Roy. Astron. Soc.*, 370:239–244, 2006.

[44] Charles Hellaby. Multicolor observations, inhomogeneity and evolution. *Astron. Astrophys.*, 372:357–363, 2001.

[45] Charles Hellaby and Alnadhief H. A. Alfedeel. Solving the Observer Metric. *Phys. Rev.*, D79:043501, 2009.

[46] Nazeem Mustapha, Charles Hellaby, and G. F. R. Ellis. Large scale inhomogeneity versus source evolution: Can we distinguish them observationally? *Mon. Not. Roy. Astron. Soc.*, 292:817–830, 1997.

[47] M. L. McClure and Charles Hellaby. The Metric of the Cosmos II: Accuracy, Stability, and Consistency. *Phys. Rev.*, D78:044005, 2008.

[48] Masato Tokutake and Chul-Moon Yoo. Inverse Construction of the ΛLTB Model from a Distance-Redshift Relation. *JCAP*, 1610(10):009, 2016.

[49] Giuseppe Fanizza and Fabien Nugier. Lensing in the geodesic light-cone coordinates and its (exact) illustration to an off-center observer in Lemaitre-Tolman-Bondi models. *JCAP*, 1502(02):002, 2015.

[50] Hao Wang and Tong-Jie Zhang. Constraints on Lemaître-Tolman-Bondi models from Observational Hubble Parameter data. *Astrophys. J.*, 748:111, 2012.

[51] Chul-Moon Yoo, Tomohiro Kai, and Ken-ichi Nakao. Redshift Drift in LTB Void Universes. *Phys. Rev.*, D83:043527, 2011.

[52] Chul-Moon Yoo. A Note on the Inverse Problem with LTB Universes. *Prog. Theor. Phys.*, 124:645–665, 2010.

[53] Chul-Moon Yoo, Ken-ichi Nakao, and Misao Sasaki. CMB observations in LTB universes: Part I: Matching peak positions in the CMB spectrum. *JCAP*, 1007:012, 2010.

[54] Chul-Moon Yoo, Ken-ichi Nakao, and Misao Sasaki. CMB observations in LTB universes: Part II – the kSZ effect in an LTB universe. *JCAP*, 1010:011, 2010.

[55] Chul-Moon Yoo, Tomohiro Kai, and Ken-ichi Nakao. Solving Inverse Problem with Inhomogeneous Universe. *Prog. Theor. Phys.*, 120:937–960, 2008.

[56] Juan Garcia-Bellido and Troels Haugboelle. Looking the void in the eyes - the kSZ effect in LTB models. *JCAP*, 0809:016, 2008.

[57] Juan Garcia-Bellido and Troels Haugboelle. Confronting Lemaitre-Tolman-Bondi models with Observational Cosmology. *JCAP*, 0804:003, 2008.

[58] George Lemaître. L'Univers en expansion. *Annales Soc. Sci. Brux.*, A53:51, 1933.

[59] G. Lemaître. The expanding universe. *Gen.Rel.Grav.*, 29:641–680, 1997.

[60] Richard C. Tolman. Effect of imhomogeneity on cosmological models. *Proc.Nat.Acad.Sci.*, 20:169–176, 1934.

[61] H. Bondi. Spherically symmetrical models in general relativity. *Mon.Not.Roy.Astron.Soc.*, 107:410–425, 1947.

[62] G. Lemaître. La formation des nebuleuses dans l'univers en expansion. *C.R.Acad.Sci.Paris*, 196(1085):303, 1933.

[63] Andrzej Krasinski and Charles Hellaby. Formation of a galaxy with a central black hole in the Lemaitre-Tolman model. *Phys.Rev.*, D69:043502, 2004.

[64] J.T. Firouzjaee and Reza Mansouri. Asymptotically FRW black holes. *Gen.Rel.Grav.*, 42:2431–2452, 2010.

[65] Andrzej Krasinski and Charles Hellaby. Structure formation in the Lemaitre-Tolman model. *Phys. Rev.*, D65:023501, 2002.

[66] Andrzej Krasinski and Charles Hellaby. More examples of structure formation in the Lemaitre-Tolman model. *Phys.Rev.*, D69:023502, 2004.

[67] Charles Hellaby and Andrzej Krasinski. Alternative methods of describing structure formation in the Lemaitre-Tolman model. *Phys.Rev.*, D73:023518, 2006.

[68] M. J. Fullana, J. V. Arnau, and D. Saez. On the microwave background anisotropy produced by big voids in open universes. *Mon. Not. Roy. Astron. Soc.*, 280:1181, 1996.

[69] Neil P. Humphreys, Roy Maartens, and David R. Matravers. Anisotropic observations in universes with nonlinear inhomogeneity. *Astrophys. J.*, 477:47, 1997.

[70] Kenji Tomita. Bulk flows and CMB dipole anisotropy in cosmological void models. *Astrophys. J.*, 529:26, 2000.

[71] Havard Alnes and Morad Amarzguioui. CMB anisotropies seen by an off-center observer in a spherically symmetric inhomogeneous Universe. *Phys. Rev.*, D74:103520, 2006.

[72] Krzysztof Bolejko, Chris Clarkson, Roy Maartens, David Bacon, Nikolai Meures, and Emma Beynon. Antilensing: The Bright Side of Voids. *Phys. Rev. Lett.*, 110(2):021302, 2013.

[73] David J. Bacon, Sambatra Andrianomena, Chris Clarkson, Krzysztof Bolejko, and Roy Maartens. Cosmology with Doppler Lensing. *Mon. Not. Roy. Astron. Soc.*, 443(3):1900–1915, 2014.

[74] P. Szekeres. A class of inhomogeneous cosmological models. *Comm. Math. Phys.*, 41:55–64, 1975. 10.1007/BF01608547.

[75] W.B. Bonnor, A.H. Sulaiman, and N. Tomimura. Szekeres's Space-Times Have No Killing Vectors. *Gen.Rel.Grav.*, 8:549–559, 1977.

[76] J. Plebanski and Andrzej Krasinski. *An introduction to general relativity and cosmology*. Cambridge Universiy Press, 2006.

[77] Andrzej Krasinski. *Inhomogeneous Cosmological Models*. Cambridge Universiy Press, 1997.

[78] W. B. Bonnor. Non-radiative solutions of Einstein's equations for dust. *Commun. Math. Phys.*, 51:191, 1976.

[79] W. B. Bonnor. Do freely falling bodies radiate. *Nature*, 263:301, 1976.

[80] G. M. Covarrubias. Gravitational Radiation in Szekeres's Quasispherical spacetimes. *J. Phys.*, A13:3023–3028, 1980.

[81] Charles Hellaby and Andrzej Krasinski. Physical and Geometrical Interpretation of the $\epsilon \leq 0$ Szekeres Models. *Phys.Rev.*, D77:023529, 2008.

[82] S.W. Goode and J. Wainwright. Friedmann-like singularities in Szekeres' cosmological models. *Mon.Not.Roy.Astron.Soc.*, 198:83, 1982.

[83] S.W. Goode and J. Wainwright. Singularities and evolution of the Szekeres cosmological models. *Phys.Rev.*, D26:3315–3326, 1982.

[84] C Hellaby. The Null and KS Limits of the Szekeres Metric. *Class.Quant.Grav.*, 13:2537–2546, 1996. See corrections in W.B. Bonnor's review, Math.Rev.97:4592,1997.

[85] Anthony Walters and Charles Hellaby. Constructing Realistic Szekeres Models from Initial and Final Data. *JCAP*, 1212:001, 2012.

[86] David Vrba and Otakar Svitek. Modelling inhomogeneity in Szekeres spacetime. *Gen. Rel. Grav.*, 46(10):1808, 2014.

[87] Roberto A. Sussman and I. Delgado Gaspar. Multiple nonspherical structures from the extrema of Szekeres scalars. *Phys. Rev.*, D92(8):083533, 2015.

[88] Mustapha Ishak and Austin Peel. The growth of structure in the Szekeres inhomogeneous cosmological models and the matter-dominated era. 2011.

[89] Austin Peel, Mustapha Ishak, and M. A. Troxel. Large-scale growth evolution in the Szekeres inhomogeneous cosmological models with comparison to growth data. *Phys. Rev.*, D86:123508, 2012.

[90] Krzysztof Bolejko and Roberto A. Sussman. Cosmic spherical void via coarse-graining and averaging non-spherical structures. *Phys. Lett.*, B697:265–270, 2011.

[91] Roberto A. Sussman, I. Delgado Gaspar, and Juan Carlos Hidalgo. Coarse-grained description of cosmic structure from Szekeres models. *JCAP*, 1603(03):012, 2016. [Erratum: JCAP1606,no.06,E03(2016)].

[92] Nikolai Meures and Marco Bruni. Exact non-linear inhomogeneities in ΛCDM cosmology. *Phys.Rev.*, D83:123519, 2011.

[93] Krzysztof Bolejko. The Szekeres Swiss Cheese model and the CMB observations. *Gen.Rel.Grav.*, 41:1737–1755, 2009.

[94] Krzysztof Bolejko and Marie-Noelle Celerier. Szekeres Swiss-Cheese model and supernova observations. *Phys.Rev.*, D82:103510, 2010.

[95] Anthony Nwankwo, Mustapha Ishak, and John Thompson. Luminosity distance and redshift in the Szekeres inhomogeneous cosmological models. *JCAP*, 1105:028, 2011.

[96] Austin Peel, M. A. Troxel, and Mustapha Ishak. Effect of inhomogeneities on high precision measurements of cosmological distances. *Phys. Rev.*, D90(12):123536, 2014. [Erratum: Phys. Rev.D92,no.2,029901(2015)].

[97] Mattia Villani. Taylor expansion of luminosity distance in Szekeres cosmological models: Effects of local structures evolution on cosmographic parameters. *JCAP*, 1406:015, 2014.

[98] S. M. Koksbang and S. Hannestad. Studying the precision of ray tracing techniques with Szekeres models. *Phys. Rev.*, D92(2):023532, 2015. [Erratum: Phys. Rev.D92,no.6,069904(2015)].

[99] Peter Szekeres. Quasispherical Gravitational Collapse. *Phys.Rev.*, D12:2941, 1975.

[100] B. K. Berger, D. M. Eardley, and D. W. Olson. Note on the Space-Times of Szekeres. *Phys. Rev.*, D16:3086–3089, 1977.

[101] Charles Hellaby. Modelling Inhomogeneity in the Universe. *PoS*, ISFTG:005, 2009.

[102] C. Hellaby and K. Lake. Shell crossings and the Tolman model. *Astrophys.J.*, 290:381, 1985.

[103] Charles Hellaby and Andrzej Krasinski. You can't get through Szekeres wormholes: Or, regularity, topology and causality in quasispherical Szekeres models. *Phys.Rev.*, D66:084011, 2002.

[104] Karl Schwarzschild. Über das gravitationsfeld eines massenpunktes nach der einstein'schen theorie. *Sitzungsberichte der Königlich Preussischen Akademie der Wissenschaften*, 1:189–196, 1916.

[105] P. Vaidya. The Gravitational Field of a Radiating Star. *Proc.Indian Acad.Sci.*, A33:264, 1951.

[106] P.C. Vaidya. Newtonian Time in General Relativity. *Nature*, 171:260–261, 1953.

[107] R. Kantowski and R.K. Sachs. Some spatially homogeneous anisotropic relativistic cosmological models. *J.Math.Phys.*, 7:443, 1966.

[108] R. K. Sachs. Gravitational waves in general relativity. 6. The outgoing radiation condition. *Proc. Roy. Soc. Lond.*, A264:309–338, 1961.

[109] S. W. Hawking and G. F. R. Ellis. *The Large Scale Structure of Space-Time*. Cambridge Monographs on Mathematical Physics. Cambridge University Press, 2011.

[110] Simonetta Frittelli, Thomas P. Kling, and Ezra T. Newman. Space-time perspective of Schwarzschild lensing. *Phys. Rev.*, D61:064021, 2000.

[111] V. Perlick. Gravitational lensing from a spacetime perspective. *Living Rev. Rel.*, 7:9, 2004.

[112] Nazeem Mustapha, B. A. Bassett, Charles Hellaby, and G. F. R. Ellis. Shrinking 2. The Distortion of the area distance redshift relation in inhomogeneous isotropic universes. *Class. Quant. Grav.*, 15:2363–2379, 1998.

[113] Timothy Clifton, Pedro G. Ferreira, Antonio Padilla, and Constantinos Skordis. Modified Gravity and Cosmology. *Phys. Rept.*, 513:1–189, 2012.

[114] Joseph P. Conlon. The QCD axion and moduli stabilisation. *JHEP*, 05:078, 2006.

[115] Clifford M. Will. The Confrontation between General Relativity and Experiment. *Living Rev. Rel.*, 17:4, 2014.

[116] Justin Khoury and Amanda Weltman. Chameleon cosmology. *Phys. Rev.*, D69:044026, 2004.

[117] Justin Khoury and Amanda Weltman. Chameleon fields: Awaiting surprises for tests of gravity in space. *Phys. Rev. Lett.*, 93:171104, 2004.

[118] Nemanja Kaloper. Challenging the Cosmological Constant. *Phys. Lett.*, B653:109–115, 2007.

[119] Junpu Wang, Lam Hui, and Justin Khoury. No-Go Theorems for Generalized Chameleon Field Theories. *Phys. Rev. Lett.*, 109:241301, 2012.

[120] Bhuvnesh Jain and Jake VanderPlas. Tests of Modified Gravity with Dwarf Galaxies. *JCAP*, 1110:032, 2011.

[121] Lam Hui, Alberto Nicolis, and Christopher Stubbs. Equivalence Principle Implications of Modified Gravity Models. *Phys. Rev.*, D80:104002, 2009.

[122] Philip Chang and Lam Hui. Stellar Structure and Tests of Modified Gravity. *Astrophys. J.*, 732:25, 2011.

[123] Anne-Christine Davis, Eugene A. Lim, Jeremy Sakstein, and Douglas Shaw. Modified Gravity Makes Galaxies Brighter. *Phys. Rev.*, D85:123006, 2012.

[124] Bhuvnesh Jain, Vinu Vikram, and Jeremy Sakstein. Astrophysical Tests of Modified Gravity: Constraints from Distance Indicators in the Nearby Universe. *Astrophys. J.*, 779:39, 2013.

[125] Amol Upadhye, Steven S. Gubser, and Justin Khoury. Unveiling chameleons in tests of gravitational inverse-square law. *Phys. Rev.*, D74:104024, 2006.

[126] E. G. Adelberger, Blayne R. Heckel, Seth A. Hoedl, C. D. Hoyle, D. J. Kapner, and A. Upadhye. Particle Physics Implications of a Recent Test of the Gravitational Inverse Sqaure Law. *Phys. Rev. Lett.*, 98:131104, 2007.

[127] Clare Burrage, Edmund J. Copeland, and James A. Stevenson. A Proposed Experimental Search for Chameleons using Asymmetric Parallel Plates. 2016.

[128] Jason H. Steffen, Amol Upadhye, Al Baumbaugh, Aaron S. Chou, Peter O. Mazur, Ray Tomlin, Amanda Weltman, and William Wester. Laboratory constraints on chameleon dark energy and power-law fields. *Phys. Rev. Lett.*, 105:261803, 2010.

[129] Aaron S. Chou et al. A Search for chameleon particles using a photon regeneration technique. *Phys. Rev. Lett.*, 102:030402, 2009.

[130] G. Rybka et al. A Search for Scalar Chameleons with ADMX. *Phys. Rev. Lett.*, 105:051801, 2010.

[131] Philippe Brax and Konstantin Zioutas. Solar Chameleons. *Phys. Rev.*, D82:043007, 2010.

[132] Clare Burrage, Anne-Christine Davis, and Douglas J. Shaw. Detecting Chameleons: The Astronomical Polarization Produced by Chameleon-like Scalar Fields. *Phys. Rev.*, D79:044028, 2009.

[133] Philippe Brax, Clare Burrage, Anne-Christine Davis, David Seery, and Amanda Weltman. Higgs production as a probe of Chameleon Dark Energy. *Phys. Rev.*, D81:103524, 2010.

[134] Joel Berge, Pierre Touboul, and Manuel Rodrigues. Status of MICROSCOPE, a mission to test the Equivalence Principle in space. *J. Phys. Conf. Ser.*, 610(1):012009, 2015.

[135] Brett Altschul et al. Quantum tests of the Einstein Equivalence Principle with the STE-QUEST space mission. *Adv. Space Res.*, 55:501–524, 2015.

[136] Clare Burrage and Jeremy Sakstein. A Compendium of Chameleon Constraints. *JCAP*, 1611(11):045, 2016.

[137] Philippe Brax, Carsten van de Bruck, Anne-Christine Davis, Justin Khoury, and Amanda Weltman. Detecting dark energy in orbit - The Cosmological chameleon. *Phys. Rev.*, D70:123518, 2004.

[138] Adrienne L. Erickcek, Neil Barnaby, Clare Burrage, and Zhiqi Huang. Chameleons in the Early Universe: Kicks, Rebounds, and Particle Production. *Phys.Rev.*, D89:084074, 2014.

[139] Adrienne L. Erickcek, Neil Barnaby, Clare Burrage, and Zhiqi Huang. Catastrophic Consequences of Kicking the Chameleon. *Phys. Rev. Lett.*, 110:171101, 2013.

[140] Claudia de Rham and Raquel H. Ribeiro. Riding on irrelevant operators. *JCAP*, 1411(11):016, 2014.

[141] C. P. Burgess. Quantum gravity in everyday life: General relativity as an effective field theory. *Living Rev. Rel.*, 7:5–56, 2004.

[142] David H. Lyth and Andrew R. Liddle. *The primordial density perturbation: Cosmology, inflation and the origin of structure.* Cambridge University Press, 2009.

[143] Adam G. Riess et al. Observational evidence from supernovae for an accelerating universe and a cosmological constant. *Astron. J.*, 116:1009–1038, 1998.

[144] S. Perlmutter et al. Measurements of Omega and Lambda from 42 high redshift supernovae. *Astrophys. J.*, 517:565–586, 1999.

[145] Pierre Astier et al. The Supernova legacy survey: Measurement of omega(m), omega(lambda) and W from the first year data set. *Astron. Astrophys.*, 447:31–48, 2006.

[146] N. Suzuki et al. The Hubble Space Telescope Cluster Supernova Survey: V. Improving the Dark Energy Constraints Above z>1 and Building an Early-Type-Hosted Supernova Sample. *Astrophys. J.*, 746:85, 2012.

[147] D. N. Spergel et al. First year Wilkinson Microwave Anisotropy Probe (WMAP) observations: Determination of cosmological parameters. *Astrophys. J. Suppl.*, 148:175–194, 2003.

[148] P. A. R. Ade et al. Planck 2013 results. XVI. Cosmological parameters. *Astron. Astrophys.*, 571:A16, 2014.

[149] Jonathan L. Sievers et al. The Atacama Cosmology Telescope: Cosmological parameters from three seasons of data. *JCAP*, 1310:060, 2013.

[150] Max Tegmark et al. Cosmological parameters from SDSS and WMAP. *Phys. Rev.*, D69:103501, 2004.

[151] Chris Blake et al. The WiggleZ Dark Energy Survey: mapping the distance-redshift relation with baryon acoustic oscillations. *Mon. Not. Roy. Astron. Soc.*, 418:1707–1724, 2011.

[152] Florian Beutler, Chris Blake, Matthew Colless, D. Heath Jones, Lister Staveley-Smith, Lachlan Campbell, Quentin Parker, Will Saunders, and Fred Watson. The 6dF Galaxy Survey: Baryon Acoustic Oscillations and the Local Hubble Constant. *Mon. Not. Roy. Astron. Soc.*, 416:3017–3032, 2011.

[153] Kyle S. Dawson et al. The Baryon Oscillation Spectroscopic Survey of SDSS-III. *Astron. J.*, 145:10, 2013.

[154] Steven Weinberg. The Cosmological Constant Problem. *Rev. Mod. Phys.*, 61:1–23, 1989.

[155] Raphael Bousso and Joseph Polchinski. Quantization of four form fluxes and dynamical neutralization of the cosmological constant. *JHEP*, 06:006, 2000.

[156] Leonard Susskind. The Anthropic landscape of string theory. 2003.

[157] Shamit Kachru, Renata Kallosh, Andrei D. Linde, and Sandip P. Trivedi. De Sitter vacua in string theory. *Phys. Rev.*, D68:046005, 2003.

[158] Austin Joyce, Bhuvnesh Jain, Justin Khoury, and Mark Trodden. Beyond the Cosmological Standard Model. *Phys. Rept.*, 568:1–98, 2015.

[159] Shinji Tsujikawa. Quintessence: A Review. *Class. Quant. Grav.*, 30:214003, 2013.

[160] Pascual Jordan. The present state of Dirac's cosmological hypothesis. *Z. Phys.*, 157:112–121, 1959.

[161] Paul A. M. Dirac. New basis for cosmology. *Proc. Roy. Soc. Lond.*, A165:199–208, 1938.

[162] Oskar Klein. Quantum Theory and Five-Dimensional Theory of Relativity. (In German and English). *Z. Phys.*, 37:895–906, 1926. [Surveys High Energ. Phys.5,241(1986)].

[163] Y. Fujii and K. Maeda. *The scalar-tensor theory of gravitation.* Cambridge University Press, 2007.

[164] C. Brans and R. H. Dicke. Mach's principle and a relativistic theory of gravitation. *Phys. Rev.*, 124:925–935, 1961.

[165] Alain Coc, Keith A. Olive, Jean-Philippe Uzan, and Elisabeth Vangioni. Big bang nucleosynthesis constraints on scalar-tensor theories of gravity. *Phys. Rev.*, D73:083525, 2006.

[166] Jacob D. Bekenstein. Relativistic gravitation theory for the MOND paradigm. *Phys. Rev.*, D70:083509, 2004. [Erratum: Phys. Rev.D71,069901(2005)].

[167] Thomas P. Waterhouse. An Introduction to Chameleon Gravity. 2006.

[168] David F. Mota and Douglas J. Shaw. Evading Equivalence Principle Violations, Cosmological and other Experimental Constraints in Scalar Field Theories with a Strong Coupling to Matter. *Phys. Rev.*, D75:063501, 2007.

[169] Amol Upadhye, Wayne Hu, and Justin Khoury. Quantum Stability of Chameleon Field Theories. *Phys. Rev. Lett.*, 109:041301, 2012.

[170] Justin Khoury. Chameleon Field Theories. *Class. Quant. Grav.*, 30:214004, 2013.

[171] Thibault Damour and Alexander M. Polyakov. The String dilaton and a least coupling principle. *Nucl. Phys.*, B423:532–558, 1994.

[172] Thibault Damour and Kenneth Nordtvedt. Tensor-scalar cosmological models and their relaxation toward general relativity. *Phys. Rev. D*, 48:3436–3450, Oct 1993.

[173] Antonio Padilla, Emma Platts, David Stefanyszyn, Anthony Walters, Amanda Weltman, and Toby Wilson. How to Avoid a Swift Kick in the Chameleons. *JCAP*, 1603(03):058, 2016.

[174] Claudia de Rham and Andrew J. Tolley. DBI and the Galileon reunited. *JCAP*, 1005:015, 2010.

[175] T. Jenke et al. Gravity Resonance Spectroscopy Constrains Dark Energy and Dark Matter Scenarios. *Phys. Rev. Lett.*, 112:151105, 2014.